Single top production in association with a WZ boson pair at the CMS experiment

Dissertation
zur Erlangung des Doktorgrades
an der Fakultät für Mathematik, Informatik und Naturwissenschaften
Fachbereich Physik
der Universität Wuppertal

vorgelegt von

ALBERTO BELVEDERE

Wuppertal
2025

Eidesstattliche Versicherung / Declaration on oath

Hiermit versichere ich an Eides statt, dass ich die vorliegende Dissertationsschrift selbst verfasst und keine anderen als die angegebenen Hilfsmittel und Quellen benutzt habe. Die eingereichte schriftliche Fassung entspricht der auf dem elektronischen Speichermedium. Die Dissertation wurde in der vorgelegten oder einer ähnlichen Form nicht schon einmal in einem früheren Promotionsverfahren angenommen oder als ungenügend beurteilt.

I hereby declare, on oath, that I have written the present dissertation by my own and have not used any resources and aids other than those acknowledged. The written version submitted corresponds to the one stored electronically. The dissertation presented in this form, has not already been accepted in an earlier doctoral procedure or assessed as unsatisfactory.

Hamburg, 9 September, 2025

Alberto Belvedere

Gutachter der Dissertation:	Prof. Dr. Katerina Lipka PD Dr. Roman Kogler
Zusammensetzung der Prüfungskommission:	Prof. Dr. Katerina Lipka PD Dr. Roman Kogler Prof. Dr. Christian Hoelbling Prof. Dr. Christian Zeitnitz

Abstract

This thesis presents a comprehensive study of the single top quark production in association with a WZ boson pair (tWZ), culminating in the first observation of this process. Measurements of rare processes are crucial to improve our understanding of the Standard Model (SM) and improve the sensitivity to loop-induced new physics. These represent a crucial part of the Large Hadron Collider (LHC) physics program. In this context, the tWZ process provides a unique probe of the top quark-electroweak sector of the SM and offers sensitivity to possible effects of new physics, which can be systematically studied within the Standard Model Effective Field Theory (SMEFT) framework. This thesis addresses the challenges associated with the computation of SMEFT predictions and uses them to measure constraints on the Wilson coefficients of relevant SMEFT operators, also providing their projections for the High-Luminosity LHC. A measurement of the inclusive tWZ production cross section is performed using proton-proton collisions recorded by the CMS experiment at centre-of-mass energies of 13 and 13.6 TeV, corresponding to an integrated luminosity of 200 fb^{-1}. The analysis tackles several experimental challenges, for example an efficient identification of the tWZ process with machine learning, and a precise prediction of the background from misidentified leptons. The inclusive tWZ cross section is measured independently at 13 and 13.6 TeV, and a simultaneous fit yields an observed statistical significance exceeding 5 standard deviations, thus establishing the first observation of the tWZ process.

Zusammenfassung

Diese Arbeit präsentiert eine umfassende Studie zur Produktion eines einzelnen Top-Quarks in Verbindung mit einem WZ-Bosonpaar (tWZ). Die vorgestellte Messung resultiert in der ersten Beobachtung dieses Prozesses. Messungen seltener Prozesse sind entscheidend um unser Verständnis des Standardmodells (SM) zu verbessern und die Empfindlichkeit zu neuer Physik durch schleifen-induzierte Prozesse zu erhöhen. Sie stellen einen wesentlichen Teil des Physikprogramms des Large Hadron Collider (LHC) dar. In diesem Zusammenhang bietet der tWZ Prozess eine einzigartige Möglichkeit den Top-Quark-elektroschwachen Sektor des SM zu untersuchen. Dieser Prozess ermöglicht die Erfassung von Effekten neuer Physik, die im Rahmen einer effektiven Feldtheorie mit SM Teilchen (SMEFT) systematisch untersucht werden können. Die vorliegende Arbeit befasst sich mit den Herausforderungen im Zusammenhang mit der Berechnung von SMEFT-Vorhersagen und nutzt diese, um Einschränkungen für die Wilson-Koeffizienten relevanter SMEFT-Operatoren zu messen. Es werden Projektionen für den High-Luminosity LHC bereitgestellt. Eine Messung des inklusiven Wirkungsquerschnitts für tWZ Produktion wird anhand von Proton-Proton-Kollisionen durchgeführt. Diese wurden mit dem CMS Experiment bei Schwerpunktsenergien von 13 und 13,6 TeV aufgezeichnet, was einer integrierten Luminosität von 200 fb^{-1} entspricht. Die Analyse befasst sich mit mehreren experimentellen Herausforderungen, beispielsweise der effizienten Identifizierung des tWZ Prozesses mit maschinellem Lernen und der präzisen Vorhersage des Untergrunds durch falsch identifizierte Leptonen. Der inklusive tWZ Wirkungsquerschnitt wird unabhängig bei 13 und 13,6 TeV gemessen, und ein gemeinsamer Fit an alle Daten ergibt eine beobachtete statistische Signifikanz von mehr als 5 Standardabweichungen und der ersten Beobachtung von tWZ Produktion.

Contents

Appendices

Introduction

The discovery of the Higgs boson in 2012 provided the missing piece of the minimal version of the Standard Model (SM), representing its definitive experimental confirmation. This theory was developed in the mid-1970s and offers a comprehensive description of three out of the four fundamental forces and of all known elementary particles. Over the years, numerous experimental results have confirmed the predictions of the SM. Its ability to precisely describe the characteristics and interactions of all discovered particles is remarkable. However, it cannot account for all observed phenomena in the Universe, such as neutrino masses, the matter-antimatter asymmetry, and dark matter. On the theoretical side, there are a number of free parameters in the SM, where their relation and energy-scale dependence are predicted by the model, but not their numerical values at a certain energy.

Therefore, search for physics beyond the SM (BSM) is currently the main focus of particle physics. Besides direct searches for new particles or interactions, stringent test of SM predictions have been performed with the aim of reaching the highest possible precision, since any deviation from theoretical expectations could indicate the presence of new physics. The most ambitious effort to precisely study the SM and search for possible new physics effects is the Large Hadron Collider (LHC) at CERN, the world's most powerful particle accelerator. At the LHC, proton-proton collisions at centre-of-mass energies up to 13.6 TeV are studied by different experiments located along its ring. In particular, the two general-purpose detectors, ATLAS and CMS, are designed to explore a wide range of physics processes and to provide the most precise measurement of SM observables. The LHC is often referred to as a "top quark factory," with a few hundred million of top quark antiquark pairs already produced and billions expected by the end of the High-Luminosity LHC program. As the most massive elementary particle in the SM, the top quark plays a key role in the SM and provides unique ways to probe BSM physics. Measuring the top quark properties is particularly challenging. It is the only quark to decay before hadronisation, allowing direct access to its bare properties through the analysis of its decay products. However, since it decays almost exclusively into a W boson and a b quark, its reconstruction is nontrivial, involving fully hadronic final states or final states with large missing transverse energy in the case of leptonic W decays. Nevertheless, the top quark plays a central role in Higgs boson physics and BSM searches as its large mass enhances its coupling to the Higgs field and makes it especially sensitive to possible new physics effects.

In this thesis, data from proton-proton collisions at LHC at centre-of-mass energies of 13 and 13.6 TeV, recorded by the CMS detector between 2016 and 2023, are used to search for the associated production of a single top quark with a WZ boson pair (tWZ). This very rare process offers the opportunity to probe the interaction between the top quark and the mediators of the weak interaction, the W and Z bosons. The tWZ process is particularly interesting since it has enhanced sensitivity to possible BSM effects encoded in higher dimensional operators, which can be studied within the Standard Model Effective Field Theory (SMEFT) framework. A measurement of its cross section therefore allows stringent tests of important sectors of the SM, with potential deviations pointing towards new physics.

The first chapter of this thesis introduces the SM, focusing on the description of proton-proton collisions and top quark physics. Particular attention is given to the associated production of top quarks with electroweak bosons, with a section dedicated to the tWZ process. The second chapter provides a general introduction to the SMEFT framework, including detailed studies of the sensitivity of the associated production of a top quark-antiquark pair with a Z boson ($\mathrm{t\bar{t}Z}$) and of the tWZ process to SMEFT operators that modify the SM interactions involving the top quark. The third chapter presents a SMEFT interpretation of the first measurement of the tWZ process, including projections for the High-Luminosity LHC (HL-LHC).

The fourth chapter describes in detail the LHC collider and the CMS experiment, providing an overview of the different detector components. The fifth chapter explains how the various physics objects are reconstructed using the data recorded with the CMS detector, with particular focus on the computation of the corrections needed for an accurate electron identification.

The remaining chapters present in detail the analysis that lead to the first observation of the tWZ process. In particular, the sixth chapter describes the event selection and categorisation in the different signal and control regions. The seventh chapter introduces the machine learning algorithms used for the identification of tWZ events.

The eighth chapter provides a description of the statistical methods used to measure the inclusive cross section of tWZ and presents the experimental and theoretical systematic uncertainties considered in the analysis. The ninth chapter explains how the fake lepton estimation is performed and validated to ensure an accurate description of this background. The tenth chapter presents the results of the analysis, reporting the inclusive production cross sections of the tWZ process at 13 and 13.6 TeV, as well as the simultaneous measurement of tWZ and $\mathrm{t\bar{t}Z}$, combining the Run 2 and Run 3 datasets.

Chapter 1

Theoretical framework

The physics of fundamental interactions relies on two main theories: general relativity, which describes gravity and the large scale structure of space-time, and quantum field theory, which governs the behaviour of particles and their interactions at the smallest scales. Together, these theories provide a coherent description of the observable Universe, in which visible matter consists of elementary particles interacting through fundamental forces.

The most successful example of a quantum field theory is the Standard Model (SM) of particle physics, which accurately describes the properties and interactions of all the known elementary particles. While it successfully predicts a wide range of experimental results, the SM remains incomplete, as it cannot account for all the observed phenomena in the Universe, suggesting the existence of physics beyond the SM (BSM). The Large Hadron Collider (LHC) and its experiments (ALICE, ATLAS, CMS, and LHCb) represent the most extraordinary effort to test the validity of the SM and to look for its possible extensions. The LHC collides protons accelerated to almost the speed of light to study physics phenomena at the smallest distances and test the validity of the SM by studying particles spanning several orders of magnitude in mass. In this thesis, the data collected at LHC are used to search for the production of a single top quark in association with a WZ boson pair, the tWZ process. This very rare process is highly sensitive to BSM effects; therefore, any deviation from the SM predictions could be interpreted as sign of new physics.

A broad overview of the SM can be found, e.g., in Refs. [1–3], while this chapter focuses on the elements most relevant to the work presented in this thesis. Section 1.1 introduces the particles and the interactions described by the SM, as well as its known shortcomings. In Section 1.2, the concepts relevant to understanding the physics of proton-proton collisions at high energy are explained, focusing on the parton distribution functions (PDFs) and the factorisation theorem. Section 1.3 presents the main aspects of top quark physics, describing the main production channels. Eventually, processes involving the associated production of top quarks and electroweak bosons are introduced with a particular focus dedicated to the tWZ process.

1.1 The Standard Model of particle physics

The Standard Model of particle physics is a quantum field theory in which the interactions are expressed as quantised fields, while the particles represent a quantised excitation of the underlying quantum field. The fundamental forces described by the SM are the strong, electromagnetic, and weak interactions. The gravitational force is not included in the SM theory but is described by general relativity [4] and applies at a macroscopic scale.

The SM is based on the principle of least action and is formulated using the Lagrangian formalism. The SM Lagrangian density, $\mathcal{L}$, is constructed by combining the Lagrangian densities of the SM fundamental interactions. The strong interaction is described by quantum chromodynamics (QCD) and is associated with the $\mathrm{SU}(3)_C$ symmetry, where the C index represents the colour quantum number. The electromagnetic and weak forces are described by the electroweak theory, which is governed by the $\mathrm{SU}(2)_L \times \mathrm{U}(1)_Y$ symmetry. The corresponding charges are the weak isospin I and the hypercharge Y. The index L refers to the left-chiral representation of the weak interaction. The entire gauge structure of the SM is thus given by $\mathrm{SU}(3)_C \times \mathrm{SU}(2)_L \times \mathrm{U}(1)_Y$. The SM Lagrangian density must be invariant under gauge transformations to ensure renormalizability [5], and it is also invariant under translations, rotations, and Lorentz boosts. Based on Noether's theorem [6], every local symmetry is associated with a conserved quantity, e.g., invariance under translations leads to conservation of energy and momentum, while rotational symmetry implies conservation of angular momentum.

The fundamental particles of the SM (Figure 1.1) can be divided into different categories according to their quantum numbers. Particles with spin 1/2 are known as fermions and obey the Fermi-Dirac statistics. Each fermion has a corresponding antiparticle with the same quantum number but opposite electric charge. Fermions are further classified into quarks and leptons. Quarks carry both colour and electric charge, they are therefore subject to all fundamental interactions. Leptons are divided

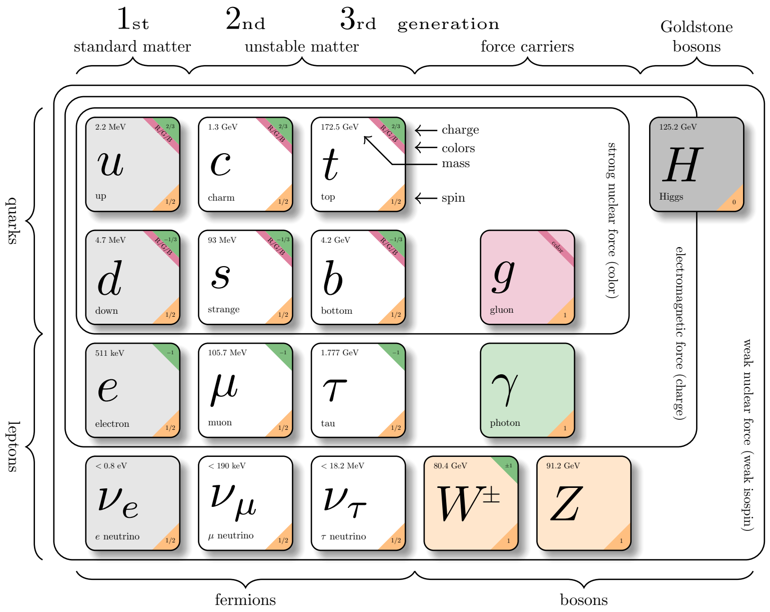

Figure 1.1: Fundamental particles of the Standard Model. Style based on Ref. [7], values from Ref. [8].

into charged leptons, which carry electric charge and interact via electromagnetic and weak interactions, and neutrinos, which are electrically neutral and only interact via the weak interaction.

Fermions are categorised into three generations. The particles' quantum numbers in each generation are the same, though their masses increase with each generation. Each generation contains three up-type quarks (u, c, t) and three down-type quarks (d, s, b), with electric charge of +2/3 and −1/3, respectively. Each generation also contains three charged leptons (e, μ) with electric charge −1 and three neutrinos. While the SM does not provide an explanation or limit for the number of generations, the number of neutrino generations has been precisely measured through the observation of the decay rates of the Z boson [9], strongly excluding the presence of a fourth generation with $m_\nu \ll m_Z/2$ ($m_Z = 91.1880 \pm 0.0020$ [8]).

Particles with integer spin are called bosons and obey the Bose-Einstein statistics; in particular, the mediator of the fundamental SM interactions are spin-1 bosons, while the Higgs boson is a spin-0 particle. The W and Z bosons mediate the weak interaction, the photon (γ) mediates the electromagnetic interaction, and the gluons (g) mediate the strong interactions. The Higgs boson (H) is the only fundamental scalar boson in the SM. It plays a crucial role in the generation of particle masses through the Brout-Englert-Higgs mechanism [10, 11], which gives mass to the EW gauge bosons and fermions via spontaneous symmetry breaking.

1.1.1 Quantum chromodynamics

The strong interaction is responsible for forming bound states of nuclear matter. It is described by quantum chromodynamics (QCD), a gauge theory based on the $\mathrm{SU}(3)_C$ group symmetry, operating with the colour charge. There are three fundamental colour charges in QCD: red (R), green (G) and blue (B). Quarks carry one of these three colour charges, antiquarks carry one of the three corresponding anticolour charges, and gluons carry combination of colour-anticolour charges. QCD describes the interaction between spinors and gauge fields that have colour quantum numbers.

The QCD Lagrangian is given by

$$\mathcal{L} = -\frac{1}{4} G^a_{\mu\nu} G^{\mu\nu}_a + \bar{Q}_i (i\gamma^\mu (D_\mu)_{ij} - m_i \delta_{ij}) Q_j, \tag{1.1}$$

where $G^a_{\mu\nu}$ represents the field strength tensor of the gluon field G^a_μ,

$$G^a_{\mu\nu} = \partial_\mu G^a_\nu - \partial_\nu G^a_\mu + g_s f^{abc} G^b_\mu G^c_\nu, \tag{1.2}$$

and D_μ is the covariant derivative,

$$D_\mu = \partial_\mu - i g_s T_a G^a_\mu. \tag{1.3}$$

The quark fields are denoted by Q_i, the quarks masses are identified by m_i, while f_{abc} represents the structure constants of the $\mathrm{SU}(3)_C$ group. The structure constants are defined by the commutation rule $[T^a, T^b] = i f^{abc} T^c$, where $a, b, c = 1, \ldots, 8$ correspond to the eight generators of the $\mathrm{SU}(3)_C$ group. A common representation of these generators is given by the Gell-Mann matrices [12], λ_a, with $T_a = \lambda_a/2$. This commutation rule highlights the non-abelian nature of QCD, which allows for the gluon self-interaction term in Eq. (1.2). Instead, the second term of Eq. (1.1) defines the interaction between quarks and gluons. Figure 1.2 displays the fundamental QCD vertices associated with these interactions.

The coupling constant of QCD, g_s, appearing in Eq. (1.2) and (1.3), is related to the strong coupling α_S through

$$\alpha_S(k^2) = \frac{g_s^2(k^2)}{4\pi}, \tag{1.4}$$

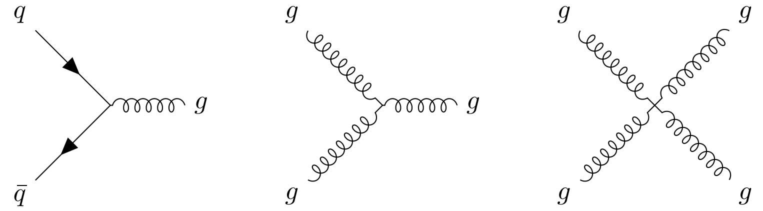

Figure 1.2: Feynman diagrams showing the fundamental QCD vertices.

where k denotes the characteristic energy scale of the process.

The energy scale dependence of α_S results from the phenomenon known as running of the coupling constant. At high energies, $k \gg \Lambda_{QCD}$ (short distances), α_S decreases logarithmically, meaning that quarks and gluons interact with a small effective coupling and can be considered as free particles in perturbative calculations. This property is known as asymptotic freedom. On the contrary, at low energies $k \lesssim \Lambda_{QCD}$(large distances), α_S increases, leading to strong interactions that confine quarks and gluons within hadrons. This behaviour is referred to as confinement. The parameter Λ_{QCD} is a characteristic scale of QCD, conventionally used to indicate the transition between the perturbative and non-perturbative regimes of the theory.

The running of the strong coupling constant is a direct consequence of the non-abelian nature of QCD, which implies the gluon self-coupling. The gluon was discovered by the PETRA experiment [13–16] via the observation of three-jet events in electron-positron collisions. Also, the energy dependence of α_S was confirmed at the PETRA experiment through measurements of multi-jet production in electron-positron collisions [17].

1.1.2 Electroweak theory

The weak interaction is mediated by the W and Z bosons and is the only SM force affecting all elementary fermions. Its charged-current component, mediated by the W boson, allows flavour-changing interactions among fermions. Another distinctive feature of the weak interaction is parity violation, which was discovered experimentally during the Wu experiment [18]. Chirality refers to the projection of a fermion's spin along its direction of motion, distinguishing left- and right-handed components. The bosons mediating the weak force interact exclusively with left-chiral fermions. In particular, left-chiral fermions form doublets under an $\mathrm{SU}(2)_L$ transformation, while right-chiral fermions are singlets. For this reason, the L index is used to denote the weak interaction symmetry group $\mathrm{SU}(2)_L$.

The electromagnetic and weak interactions are described by a unified theory named electroweak (EW) theory [19–21]. It is a non-abelian gauge theory based on the $\mathrm{SU}(2)_L \times \mathrm{U}(1)_Y$ symmetry group. The theory is spontaneously broken into the weak and electromagnetic parts below an energy scale of about $v = 246$ GeV, where v is the vacuum expectation value (vev) of the Higgs field.

The Lagrangian density of the EW theory is given by

$$\mathcal{L}_{\mathrm{EW}} = \mathcal{L}_{\mathrm{gauge}} + \mathcal{L}_{\mathrm{fermion}} = -\frac{1}{4}\left(W^a_{\mu\nu}W^{\mu\nu}_a + B_{\mu\nu}B^{\mu\nu}\right) + \bar{\psi}_L i\gamma^\mu D_\mu \psi_L + \bar{\psi}_R i\gamma^\mu D_\mu \psi_R, \tag{1.5}$$

where $W^a_{\mu\nu}$ and $B_{\mu\nu}$ are the field strength tensors,

$$W^a_{\mu\nu} = \partial_\mu W^a_\nu - \partial_\nu W^a_\mu + g f^{abc} W^b_\mu W^c_\nu, \tag{1.6}$$

$$B_{\mu\nu} = \partial_\mu B_\nu - \partial_\nu B_\mu, \tag{1.7}$$

and D_μ is the covariant derivative,

$$D_\mu = \partial_\mu - ig\hat{T}_a W^a_\mu - i\frac{g'}{2}\hat{Y} B_\mu. \tag{1.8}$$

The left-chiral fermionic fields ψ_L are doublets under $\mathrm{SU}(2)_L$ and can be written explicitly for leptons and quarks as

$$L_e = \begin{pmatrix} \nu_e \\ e^- \end{pmatrix}_L, \quad L_\mu = \begin{pmatrix} \nu_\mu \\ \mu^- \end{pmatrix}_L, \quad L_\tau = \begin{pmatrix} \nu_\tau \\ \tau^- \end{pmatrix}_L, \tag{1.9}$$

$$Q_{1st} = \begin{pmatrix} u \\ d \end{pmatrix}_L, \quad Q_{2nd} = \begin{pmatrix} c \\ s \end{pmatrix}_L, \quad Q_{3rd} = \begin{pmatrix} t \\ b \end{pmatrix}_L, \tag{1.10}$$

while the right-chiral fermionic fields ψ_R are singlets under $\mathrm{SU}(2)_L$,

$$e_R,\ \mu_R,\ \tau_R,\ u_R,\ d_R,\ c_R,\ s_R,\ t_R,\ b_R. \tag{1.11}$$

Neutrinos are predicted to be massless in the SM, and right-chiral neutrinos are not included in the theory.

In Eq. (1.8), g and g' represent the coupling constants of the interaction, while $\hat{Y}$ is the hypercharge operator and generator of the $\mathrm{U}(1)_Y$ group. The isospin generators of the $\mathrm{SU}(2)_L$ group are identified by $\hat{T}_a$ (with $a = 1,\ 2,\ 3$), a common representation of these generators is given by the Pauli matrices, σ_a, with $\hat{T}_a = \sigma_a/2$. The gauge bosons corresponding to these interactions are B_μ for $\mathrm{U}(1)_Y$ and the three W^a_μ for $\mathrm{SU}(2)_L$.

The hypercharge Y and the third component of the isospin T_3 represent the charges of the EW interaction. The linear combination

$$Q = \frac{Y}{2} + T_3 \tag{1.12}$$

gives the electric charge Q in QED. This equation is known as Gell-Mann-Nishijima relation [22, 23].

To preserve the $\mathrm{SU}(2)_L$ symmetry, the EW Lagrangian in Eq. (1.5) does not contain a mass term. However, the experimental observation of massive W and Z bosons in the UA1 and UA2 experiment at CERN [24–27] indicates that the symmetry must be broken at low energies. This process, known as spontaneous electroweak symmetry breaking (EWSB), is explained in the next section.

The experimentally observed EW gauge bosons are a linear combination of W^a_μ and B_μ. The charged current fields are given by

$$W^\pm_\mu = \frac{1}{\sqrt{2}}(W^1_\mu \mp iW^2_\mu), \tag{1.13}$$

while the neutral current field Z_μ and the electromagnetic field A_μ are defined trough the rotation

$$\begin{pmatrix} A_\mu \\ Z_\mu \end{pmatrix} = \begin{pmatrix} \cos\theta_W & \sin\theta_W \\ -\sin\theta_W & \cos\theta_W \end{pmatrix} \begin{pmatrix} B_\mu \\ W^3_\mu \end{pmatrix}, \tag{1.14}$$

where θ_W is the weak mixing angle, also known as the Weinberg angle.

The electromagnetic interaction governs the dynamics of electrically charged particles and is described by quantum electrodynamics [28] (QED). Just as QCD controls all colour charged particles, QED governs electrically charged particles.

The top part of Figure 1.3 shows the possible interactions between fermions and EW gauge bosons. The bottom part shows the Feynman diagrams depicting the EW gauge boson self-interaction. These interactions arise from the non-abelian structure of the $\mathrm{SU}(2)_L$ symmetry group and, in contrast, are absent for the photon because the $\mathrm{U}(1)$ symmetry group is abelian.

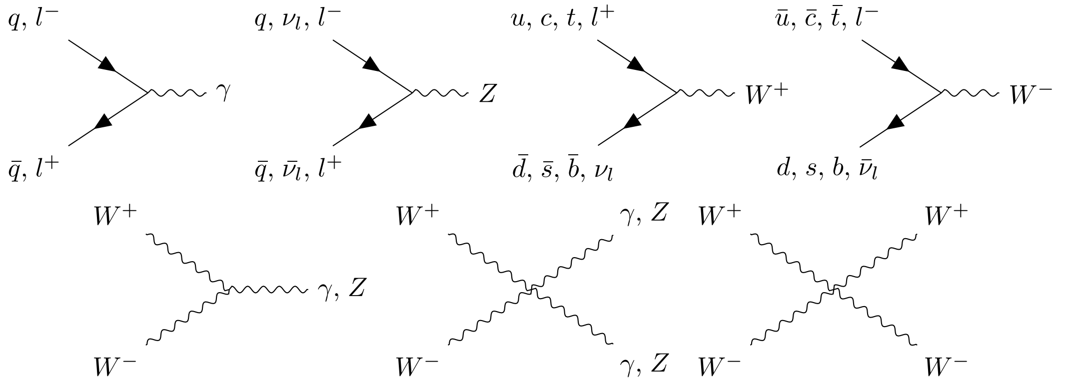

Figure 1.3: Feynman diagrams showing the fundamental EW vertices.

The weak mixing angle can be expressed as a ratio of the W to Z boson masses,

$$cos(\theta_W) = \frac{m_W}{m_Z}. \tag{1.15}$$

It also connects the definition of the g and g' coupling constants to the electromagnetic charge e,

$$e = g\ sin(\theta_W) = g'\ cos(\theta_W). \tag{1.16}$$

The most recent determination of the effective weak mixing angle [8] yields a value of

$$\sin^2(\theta_W^{\text{eff}}) = 0.23161 \pm 0.00004, \tag{1.17}$$

where *effective* indicates that the value includes loop-level corrections. The value has been obtained for fermions assuming lepton flavour universality.
Instead, the most recent determination [8] of the W and Z boson masses gives

$$m_Z = 91.1880 \pm 0.0020 \text{ GeV} \qquad m_W = 80.3692 \pm 0.0133 \text{ GeV}, \tag{1.18}$$

these results provides a stringent test of the relation in Eq. (1.15).

1.1.3 The Brout-Englert-Higgs mechanism

The Brout-Englert-Higgs mechanism [10,11] explains how particles acquire mass without violating the gauge symmetry of the $\mathrm{SU}(2)_L$ group. Introducing a new isospin doublet of scalar fields, a term $\mathcal{L}_{\text{Higgs}}$ invariant under $\mathrm{SU}(2)_L \times \mathrm{U}(1)_Y$ can be added to the EW Lagrangian Eq. (1.5),

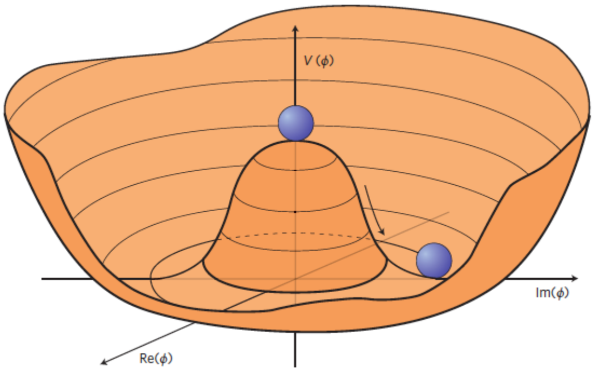

Figure 1.4: 3D representation of the Higgs potential for $\mu < 0$. The x and y axes represent the real and imaginary parts of the scalar field, respectively, while the Higgs potential is shown on the z axis. The blue sphere shows the choice of a point at the minimum of the potential, which spontaneously breaks the symmetry. Image from Ref. [29].

$$\mathcal{L}_{\text{Higgs}} = (D_\mu \phi)^\dagger (D^\mu \phi) - V(\phi), \tag{1.19}$$

where D_μ represents the covariant derivative defined in Eq. (1.8), and the Higgs potential $V(\phi)$ is given by

$$V(\phi) = -\mu^2 \phi^\dagger \phi + \lambda(\phi^\dagger \phi)^2. \tag{1.20}$$

The potential's minimum depends on the value of the parameters μ and λ. If $\lambda < 0$, the potential does not have a minimum, compromising the stability of the EW vacuum, therefore λ must be positive. The sign of μ^2 defines the shape of the potential. If $\mu < 0$, the potential has a trivial minimum at $\phi_{min} = 0$, corresponding to an unbroken EW symmetry and massless weak gauge bosons. On the other hand, if $\mu > 0$, the potential has an infinite number of minima, which are represented by a circle in the complex plane,

$$\phi_{min} = \sqrt{\frac{\mu^2}{2\lambda}} e^{i\varphi}. \tag{1.21}$$

The shape of the Higgs potential is shown in Figure 1.4, with the real and imaginary parts of the scalar field presented on the x and y axes, and the Higgs potential is shown on the z axis, respectively.

By choosing the unitary gauge, we can parametrise the Higgs field as

$$\phi = \frac{1}{\sqrt{2}} \begin{pmatrix} 0 \\ v + h(x) \end{pmatrix}, \tag{1.22}$$

with the vacuum expectation value $v = \sqrt{\mu^2/\lambda}$, while the field $h(x)$ denotes the fluctuations around the vacuum state, corresponding to the physical Higgs boson.

The mass terms for the weak gauge bosons arise from the kinetic term $|D_\mu \phi|^2$ after spontaneous symmetry breaking,

$$m_Z = \frac{1}{2} v \sqrt{g + g'} \quad \text{and} \quad m_W = \frac{1}{2} v g. \tag{1.23}$$

While the mass of the Higgs boson is given by

$$m_H = \sqrt{2\lambda} v. \tag{1.24}$$

The final confirmation of the Higgs boson's existence arrived in 2012 with its discovery by the ATLAS and CMS experiments [30, 31]. The most recent measurement of the Higgs boson mass [8] results in $m_H = 125.20 \pm 0.11$ GeV.

An interaction between the fermions and the Higgs field ϕ can be added to the SM Lagrangian density to explain the mass of the fermions. This interaction is called Yukawa interaction and is given by

$$\mathcal{L}_{\text{Yukawa}} = -\lambda_f (\bar{\psi}_L \phi \psi_R + \bar{\psi}_R \phi \psi_L), \tag{1.25}$$

where λ_f is the Yukawa coupling and is defined as

$$\lambda_f = \frac{m_f}{v}. \tag{1.26}$$

Here, m_f is the mass of the fermion, therefore the Yukawa coupling is different for each lepton.

A crucial test of the SM is the study of the Higgs boson coupling strength as a function of particle mass [32, 33]. Figure 1.5 confirms the expected linear relationship for fermions, which is verified across four orders of magnitude.

1.1.4 Fermion mixing and CKM matrix

In the SM, flavour changing interactions are only allowed if mediated by the W bosons and occur between quarks of the same generation. However, transitions between different generations have been observed experimentally. This can be explained if

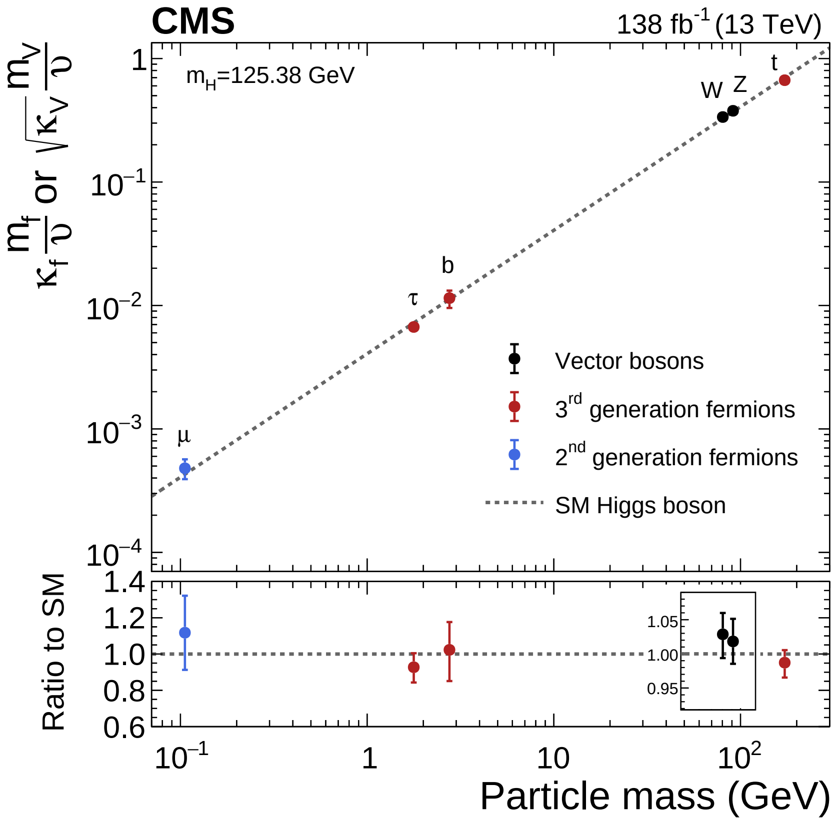

Figure 1.5: The measured coupling modifiers of the Higgs boson to fermions and heavy gauge bosons, as functions of fermion or gauge boson mass, where v is the vacuum expectation value of the Higgs field. For gauge bosons, the square root of the coupling modifier is plotted to keep a linear proportionality to the mass, as predicted in the SM. Taken from Ref. [32].

the quark EW eigenstates q' are linear combinations of their mass eigenstates q. This mixing is described by the Cabibbo-Kobayashi-Maskawa (CKM) matrix [34,35], which is a 3×3 matrix and is required to be unitary:

$$\begin{pmatrix} d' \\ s' \\ b' \end{pmatrix} = \begin{pmatrix} V_{ud} & V_{us} & V_{ub} \\ V_{cd} & V_{cs} & V_{cb} \\ V_{td} & V_{ts} & V_{tb} \end{pmatrix} \begin{pmatrix} d \\ s \\ b \end{pmatrix}. \tag{1.27}$$

The CKM matrix does not only govern the strength of the flavour changing interactions but also introduces a complex phase, which is the origin of CP violation in the quark sector of the SM. The elements of the CKM matrix have been measured with high precision for all possible generation transitions [8].

In the SM, neutrinos are predicted to be massless. However, the observation of neutrino oscillations [36] provides direct evidence that neutrinos must have mass. It is possible to include neutrino masses by extending the SM with a specific mass generation mechanism depending on whether neutrinos are Dirac or Majorana particles [37]. Similarly to the quark mixing, neutrino flavour mixing is regulated by a 3 × 3 matrix known as Pontecorvo–Maki–Nakagawa–Sakata (PMNS) matrix [38, 39].

1.1.5 Observed shortcomings of the Standard Model

The existence of finite neutrino masses is one of several phenomena that the SM cannot explain in its original formulation. Currently, only upper limits on the neutrino masses have been set. The most stringent limit, $m_\nu < 0.45$ eV [40], was imposed by the KATRIN [41] experiment. Mass differences larger than zero between different neutrino flavours have been measured in neutrino oscillation experiments [8],

$$\Delta m^2_{21} = 7.396 \times 10^{-5}\ \mathrm{eV}^2 \qquad \Delta m^2_{32} = 2.35 \times 10^{-3}\ \mathrm{eV}^2. \tag{1.28}$$

Another important shortcoming of the SM is the observed baryon asymmetry of the Universe. The Universe presumably began in a state with equal amounts of matter and antimatter, however a clear dominance of matter is observed. To generate this imbalance, a process must have occurred that satisfies the three Sakharov conditions [42]: baryon number violation, CP violation, and departure from thermal equilibrium. The SM does not allow for baryon number violation; however, CP violation has been experimentally observed in several sectors. It was first discovered in 1964 in neutral kaon meson decays [43] and over the years it has also been observed in B- and charmed-meson systems [44, 45]. More recently, CP violation was observed for the first time in the baryon sector by the LHCb experiment [46]. Nonetheless, the amount of CP violation predicted by the SM is not sufficient to account for the observed matter-antimatter asymmetry.

Additionally, the SM does not provide any suitable particle candidate to explain the existence of the dark matter. Its existence was proposed in 1933 [47] to account for the observed velocity dispersion in galaxy clusters, which visible matter alone could not explain. Therefore, dark matter candidates must interact primarily through gravity and be neutral with respect to the strong and electromagnetic interactions. Since then, numerous cosmological studies have provided evidence for the existence of dark matter, including galaxy rotation curves, gravitational lensing, and measurements of the cosmic microwave background. According to the ΛCDM model, dark matter constitutes about $(26.5 \pm 0.7)\%$ of the total energy content of the Universe, while ordinary matter contributes only $(4.93 \pm 0.06)\%$ [48]. Furthermore, the remaining $(68.5 \pm 0.7)\%$ of the Universe's energy density is attributed to dark energy, which accounts for the accelerated expansion of the Universe and is also not described by the SM [48].

For these reasons, the SM is considered to be incomplete, or often regarded as a low-energy approximation of a more fundamental theory that has yet to be discovered.

1.2 Hadron collider physics

At the LHC, the validity of the SM is tested by measuring its fundamental parameters and searching for signs of new physics phenomena. This is achieved by colliding protons at high energies and analysing the properties of the particles produced. Therefore, it is crucial to understand the internal structure of protons, the dynamics of the collision process, and the mechanisms leading to the production of the particles observed by the experiments.

1.2.1 QCD factorisation and parton distribution functions

A nucleon has a complex partonic structure, which gets resolved in high-energy collisions. The quantum numbers of the proton are described by its valence, the 2 up and 1 down quarks, while the energy of the gluons and sea quark-antiquark pairs mostly determines its mass. Altogether, gluons and quarks are called partons, and the details of the proton structure are encoded in the PDFs.

When colliding protons at high energy, the interaction occurs between two partons of the colliding protons. The QCD factorisation theorem [49] enables the calculation of a cross section $\sigma_{pp\to X}$ by separating long-distance (non-perturbative) effects from short-distance (perturbative) partonic cross sections at a factorisation scale μ_F, as

$$\sigma_{pp\to X} = \sum_{ij} f_i(x_1, \mu_F^2) f_j(x_2, \mu_F^2) \hat{\sigma}_{ij\to X}(\hat{s}, \mu_F^2, \mu_R^2) dx_1 dx_2. \tag{1.29}$$

The non-perturbative component concerns the proton's internal structure and is represented by the PDFs, $f_i(x, \mu_F^2)$. These functions describe the probability of finding a parton of flavour i carrying a momentum fraction x of the proton at an energy scale μ_F.

The perturbative component is known as partonic cross section $\hat{\sigma}_{ij\to X}$ and is computed using perturbation theory from the scattering amplitude, also referred to as the matrix element (ME). It describes the probability for a specific process X to occur between two partons i and j at a partonic centre-of-mass energy $\hat{s} = x_1 x_2 s$. The partonic cross section is also expressed as a function of the renormalisation (μ_R) and factorisation (μ_F) scales. Although the value of the cross section should be independent of the scale choice, in practice, the matrix element is computed at fixed order in perturbation theory, truncating the series at a certain order. This procedure introduces a residual scale dependence, which is typically chosen to be close to the physical scale of the process. The impact of missing higher orders is estimated by varying the values of μ_R and μ_F, and the resulting variation is taken as a systematic uncertainty in the cross section.

The scale dependence of the PDFs can be calculated in perturbative QCD using the Dokshitzer–Gribov–Lipatov–Altarelli–Parisi (DGLAP) equations [50–52].

In contrast, the x dependence of the PDFs cannot be computed perturbatively and must be determined from experimental data. Measurements from various experiments are used to extract PDFs, with deep inelastic scattering (DIS) data playing a crucial role. While the high-precision neutral- and charged-current DIS measurements at HERA [53] provide the basis for any PDF determination, the recent high-precision data at the LHC provide additional constraints on the gluon distribution and flavour separation. Particularly relevant in this context are jets and top quark pairs production measurements [54–56], as they offer large sensitivity to the gluon PDF at medium and high x.

The most widely used PDF sets include: ABMP [57], CTEQ/CT [58], HERAPDF [53], MSHT20 [59], and NNPDF [60, 61]. The analysis presented in this thesis utilises the NNPDF3.1 next-to-next-to-leading order (NNLO) PDF set [60], which is shown in Figure 1.6 for the different partons at two distinct scales.

At large x, the proton structure is dominated by the valence quarks, while at small x, sea quarks and gluons provide the main contributions. At higher scales the heavy flavour quark PDFs become accessible. The description of heavy quarks in PDFs requires a specific scheme: in the variable-flavour number scheme, heavy quarks are considered as active partons above their mass threshold, while in the fixed-flavour number scheme, only a fixed number of quarks are included as active partons. Particularly relevant in the analysis presented in this thesis is the treatment of the b quark PDF, two main fixed-flavour number schemes are commonly used. In the four-flavour scheme (4FS), the b quark is not included as an active parton in the proton, and processes with external b quarks are initiated by gluon splitting. In contrast, in the five-flavour scheme (5FS), the b quark is treated as an active parton with its own PDF.

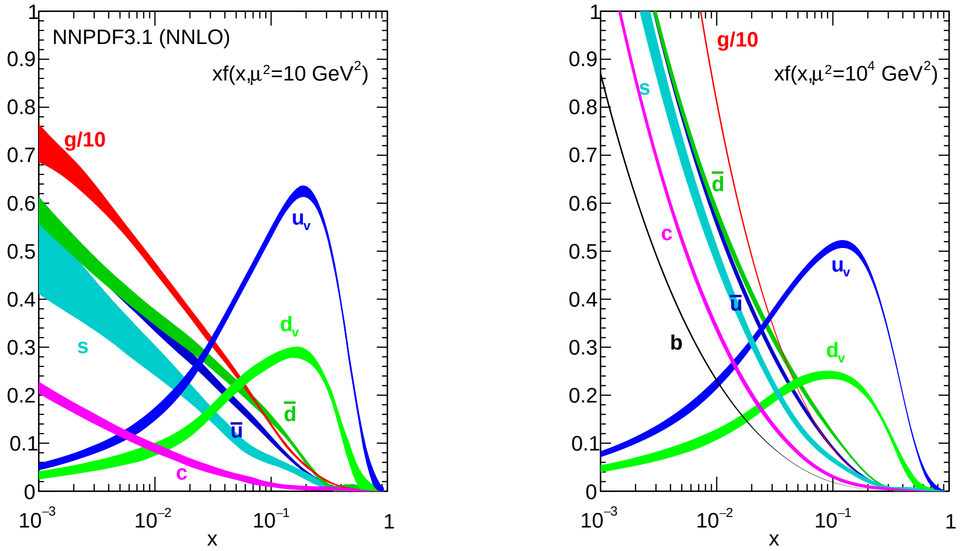

Figure 1.6: The NNPDF 3.1 NNLO PDF set, evaluated at $\mu_F^2 = 10$ GeV^2 (left) and $\mu_F^2 = 10^4$ GeV^2 (right). Taken from Ref. [60].

Both schemes are theoretically consistent and are used depending on the process and kinematic regime under study.

1.2.2 Monte Carlo simulation for pp collisions

Fixed-order calculations are not sufficient to describe pp collisions up to the formation of stable particles. In fact, it is crucial to account for soft and collinear radiation, the hadronisation of final state partons, and the decay of the produced particles. Additionally, interactions between the spectator quarks, those not involved directly in the hard scattering, must be considered. These aspects are simulated using Monte Carlo (MC) event generators, which model the entire particle interaction process up to the formation of stable final state particles. Finally, a precise simulation of the detector response is necessary to accurately reconstruct the final state particles. This approach establishes a direct connection between the reconstructed particles in the detector and the particles produced in the hard scattering, allowing precise comparisons with SM predictions.

MC generators utilise stochastic methods to simulate events according to modelled probability distributions. Figure 1.7 shows a sketch of a simulated pp collision event. The partons that interact in the hard scattering are selected probabilistically using

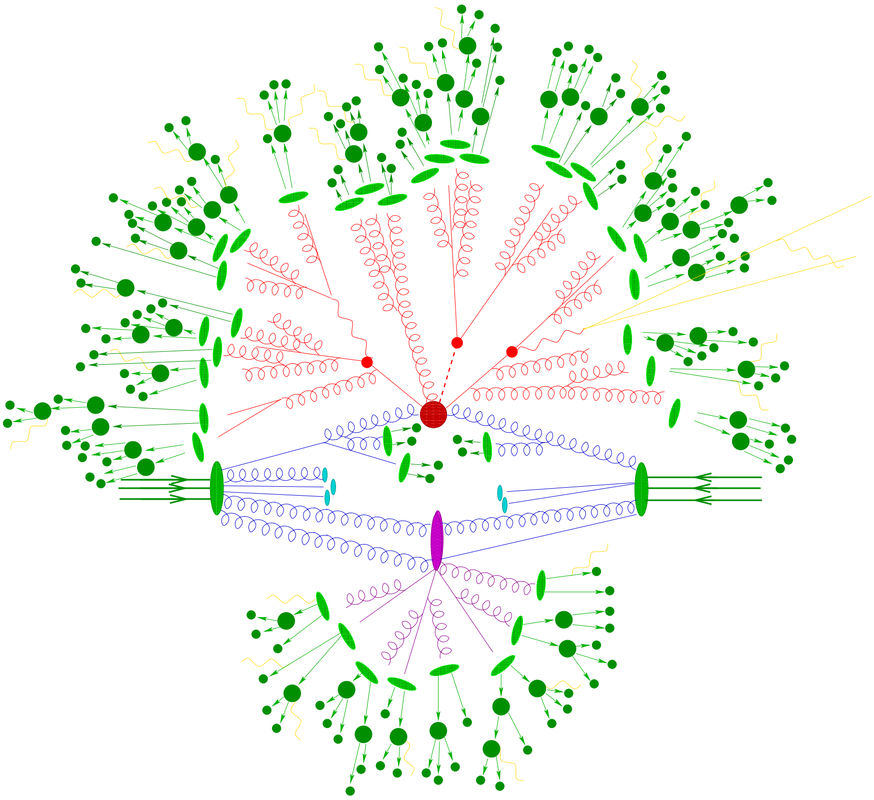

Figure 1.7: Sketch of a hadron-hadron collision as simulated by a Monte-Carlo event generator. The red circle in the centre represents the hard collision, surrounded by a tree-like structure representing Bremsstrahlung as simulated by parton showers. The purple ellipsis indicates a secondary hard scattering event. Parton-to-hadron transitions are represented by light green ellipsis, dark green circle indicate hadron decays, while yellow lines signal soft photon radiation. Taken from Ref. [62].

PDFs, while the kinematics of particles produced in the hard interaction and their decay products are computed via perturbation theory. Additional emissions of soft and collinear partons and photons are modelled by the parton shower (PS), which accounts for higher order corrections in perturbation theory. Emissions from initial state particles are known as initial state radiation (ISR), while those from final state particles are called final state radiation (FSR). While the PS describes soft and collinear emissions, the matrix element calculation determines hard emissions. To prevent double counting of emissions when combining the PS and the matrix element computation, matching and merging schemes [63–68] are employed. Partons from proton collisions that do not participate in the hard interaction are handled by phenomenological models. These models also account for multi-parton interactions (MPI). The decay products of the particles produced in the hard interactions and in the multi-parton interactions lose energy in the form of additional radiation. At this stage, the event is described at the parton level, consisting of all partons after the PS evolution but before hadronisation; after hadronisation, the stable particles define the particle level. The PS evolution is performed down to a cutoff scale, below which perturbative calculations are no longer valid. When the energy scales reach values below the PS cutoff scale, hadronization occurs. This process describes the formation of hadrons and is simulated via hadronization models [69, 70]. Finally, unstable particles decay according to their lifetimes and branching ratios, as modelled by dedicated decay algorithms integrated into event generators.

A precise detector simulation is crucial to compare measured quantities with theoretical observables. Typically, this is achieved with the GEANT4 [71] package. This tool takes the particle-level information from the MC simulation as input, and simulates the detector effects of the different components of the detector, such as the loss of energy while traversing the detector or the effect of the magnetic fields. The final objects are called detector-level objects and can be directly compared to the objects obtained from collision data.

1.3 The top quark

The existence of a third generation of fermions was postulated in 1973 by Makoto Kobayashi and Toshihide Maskawa to explain the observed CP violation in the quark sector [35]. With the observation of the τ lepton in 1975 at SLAC [72] and the discovery of the b quark in 1977 at Fermilab [73], the quest for the up-type quark of the third generation started. The top quark was directly searched for at hadron (Sp$\bar{\text{p}}$S at Fermilab) and lepton (LEP and Tristan) colliders, excluding the hypothesis of a top quark lighter than the W boson. The top quark was eventually discovered at the Tevatron collider leveraging on the leptonic decays of the W bosons produced by top quark anti-quark pairs [74, 75].

The top quark's mass is a key parameter of the SM and the most recent determination [8] gives a value of the pole mass of $m_t = 172.4 \pm 0.7$ GeV. Being the most massive elementary particle in the SM, the top quark has unique characteristics. Notably, it is the only quark that decays before hadronisation due to its extremely short lifetime, 5×10^{-25} s [8], which is shorter than the hadronisation time ($1/\Lambda_{QCD}$). This unique property allows the study of its bare properties, such as spin and electric charge, through the analysis of its decay products [76, 77]. Moreover, its large mass

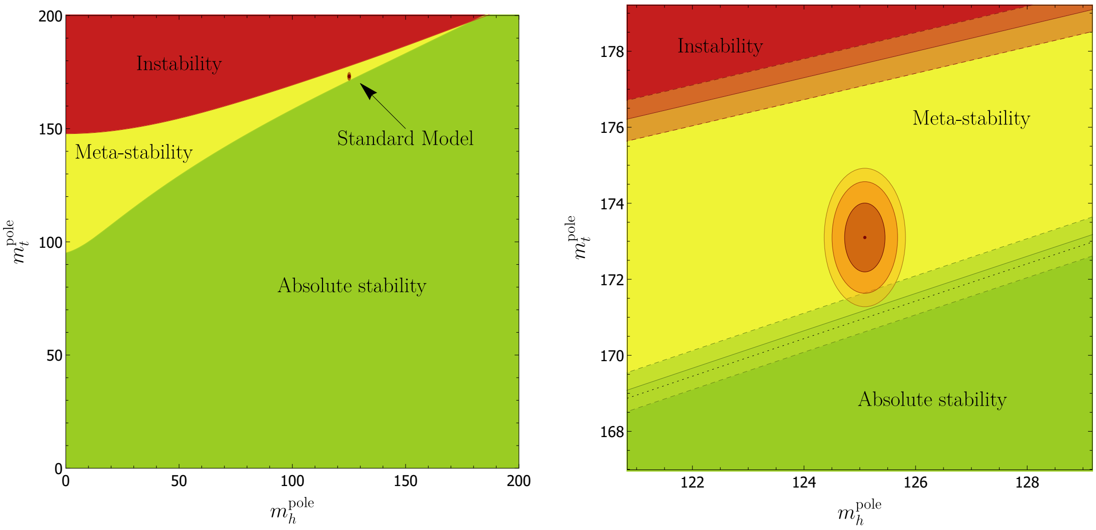

Figure 1.8: Phase diagram for stability in the m_t vs. m_h plane (left) and a closeup of the SM region (right). Ellipses show the 68%, 95% and 99% contours based on the experimental uncertainties on m_t and m_h. The shaded bands on the phase boundaries, framed by the dashed lines and centered on the solid lines, are combinations of the α_S experimental uncertainty and the theory uncertainty. Taken from Ref. [79].

also makes the top quark the particle with the strongest coupling to the Higgs boson, as the Higgs coupling is proportional to mass; therefore, the interplay between these two particles is particularly interesting. The Higgs boson Yukawa coupling to the top quark can be measured from $\mathrm{t\bar{t}}$ kinematic distributions sensitive to its value, a recent CMS measurement reported a value of $\lambda_t = 1.16^{+0.24}_{-0.35}$ [78]. Additionally, the top quark provides the largest perturbative corrections to the Higgs mass. Consequently, the top quark mass is a crucial parameter to test the stability of the SM EW vacuum. As shown in Figure 1.8, the current precision on the top and Higgs masses excludes only the hypothesis of an unstable EW vacuum. Therefore, more precise measurements of these quantities are needed to better assess the stability of the SM EW vacuum. If the vacuum is not found to be stable, extensions to the SM may be required to explain the observed stability.

1.3.1 Top quark production and decay

At hadron colliders, the dominant top quark production mode occurs via the strong interaction, resulting in top quark anti-quark ($\mathrm{t\bar{t}}$) pairs production. In pp collisions, the gluon fusion production mode (Figure 1.9) accounts for about 90% of the $\mathrm{t\bar{t}}$ cross section for collisions at a centre-of-mass energy $\sqrt{s} = 13$ TeV.

Single top quarks are produced through quark scattering or in association with a W

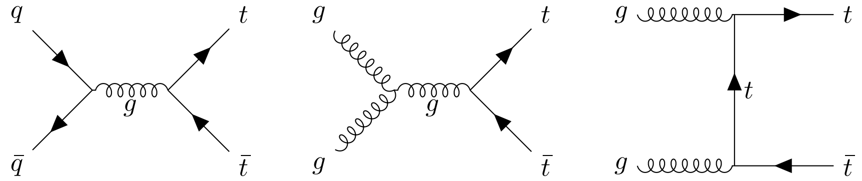

Figure 1.9: Feynman diagrams at leading order (LO) for $\mathrm{t\bar{t}}$ production at hadron colliders. The first diagram shows the production via quark-antiquark annihilation. The second and third diagrams show the production via gluon fusion in the s- and t-channel, respectively.

boson, as shown in Figure 1.10. The dominant production mode is the t-channel, which accounts for approximately 75% of the total single top quark production cross section at $\sqrt{s} = 13$ TeV. The s-channel and the W-associated production contribute roughly 5% and 20%, respectively, to the total cross section.

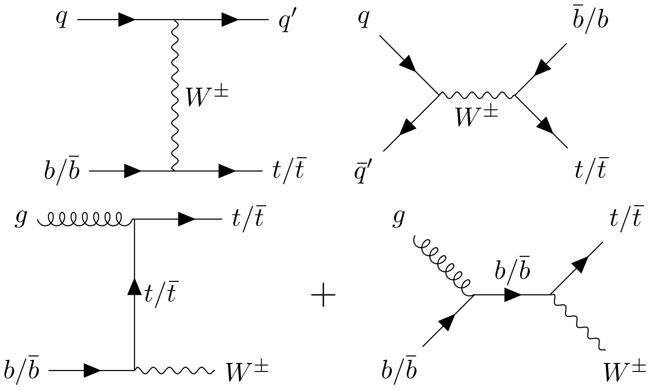

Figure 1.10: Feynman diagrams at LO for single top production at hadron colliders. The first row shows the production via t- and s-channel. While the second row illustrates the W associated production.

Since the top quark almost exclusively decays into a W boson and a b quark, the classification of its decay channels depends on the decay of the W boson. In particular, a $\mathrm{t\bar{t}}$ event is labelled as fully-leptonic if both W bosons decay into a lepton and a neutrino. Instead, $\mathrm{t\bar{t}}$ events are labelled as semi-leptonic when only one W boson undergoes such decay, while they are classified as hadronic if both W bosons decay into quark-antiquark pairs. Figure 1.11 shows the probabilities of the possible decay channels for a $\mathrm{t\bar{t}}$ event.

The hadronic and semi-leptonic final states have the largest branching fraction, however these channels suffer from significantly higher background contamination and larger systematic uncertainties due to the increased number of jets in the final state and the uncertainties associated with jets reconstruction. Although the fully-leptonic

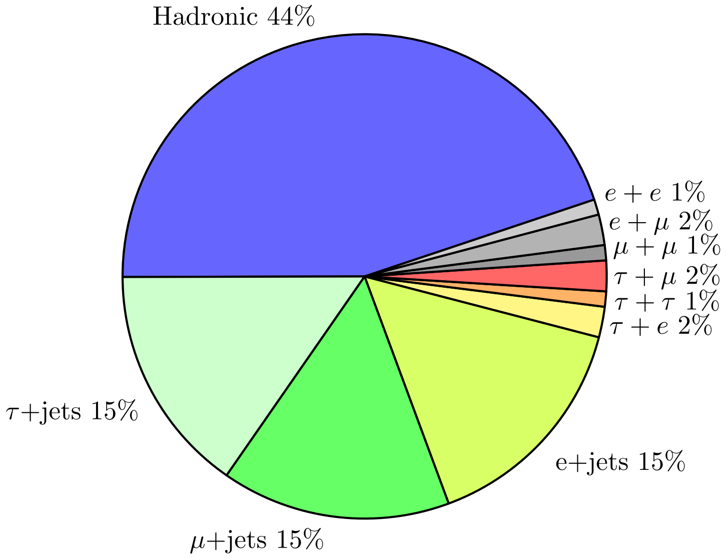

Figure 1.11: Pie chart illustrating the branching ratios [8] for the possible $t\bar{t}$ decay channels.

decay mode has the smallest branching fraction, it features the lowest background contamination, as the presence of two leptons provides a distinct signature. When considering the di-leptonic channel, only final states with electrons and muons are usually considered, including cases where they originate from the decay of a τ. This approach excludes events where the τ decays hadronically, avoiding the analysis of jets for the reconstruction and identification of leptons originating from the top quarks.

Same considerations apply to single top quark production, with the only difference being that the di-leptonic channel is available only for the W associated production, while in the s- and t-channels, at most one lepton can be present.

Figure 1.12 shows the inclusive $t\bar{t}$ cross section as a function of the centre-of-mass energy. Measurements from the ATLAS, CMS, and Tevatron experiments are compared to theoretical predictions at NNLO accuracy in QCD, NLO accuracy in EW, and next-to-next-to-Leading Logarithmic (NNLL) resummation [80–90]. The experimental measurements are obtained in the di-leptonic and semi-leptonic channels and show a good agreement with the theory predictions.

Figure 1.13 illustrates the single top inclusive cross section for the three production modes as a function of $\sqrt{s}$. Theory predictions at different orders in perturbation theory and experimental measurements from ATLAS and CMS are compared [92–98], showing good agreement.

As shown in Figures 1.12 and 1.13, the $t\bar{t}$ cross section is nearly three times larger

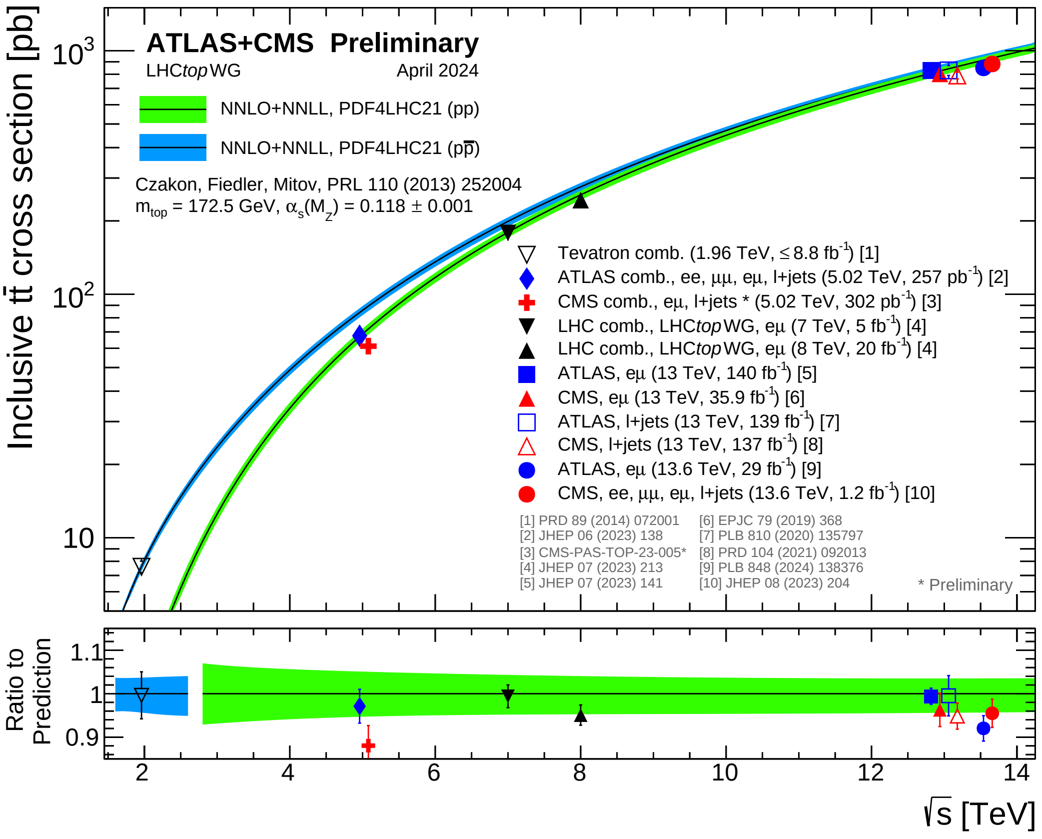

Figure 1.12: Summary of LHC and Tevatron measurements of the top-pair production cross section as a function of the centre of mass energy compared to the NNLO QCD calculation complemented with NNLL resummation. The theory band represents uncertainties due to renormalisation and factorisation scale, parton density functions and the strong coupling. The measurements and the theory calculation are quoted at $m_t = 172.5$ GeV. Measurements made at the same centre of mass energy are slightly offset for clarity. Taken from Ref. [91].

than that of single top production. Therefore, $t\bar{t}$ events usually constitute a large source of background in single top measurements.

1.3.2 Top quark production in association with electroweak bosons

CMS and ATLAS also performed measurements of top quark production in association with EW bosons. Despite being particularly challenging due to the smaller production cross section, measurements of these processes are crucial to improve our understanding of the top quark-EW interaction. In particular, the associated production of top quarks and EW bosons is a key ingredient in global Standard Model Effective Field Theory (SMEFT) fits, which test interactions of SM particles, effectively modified via

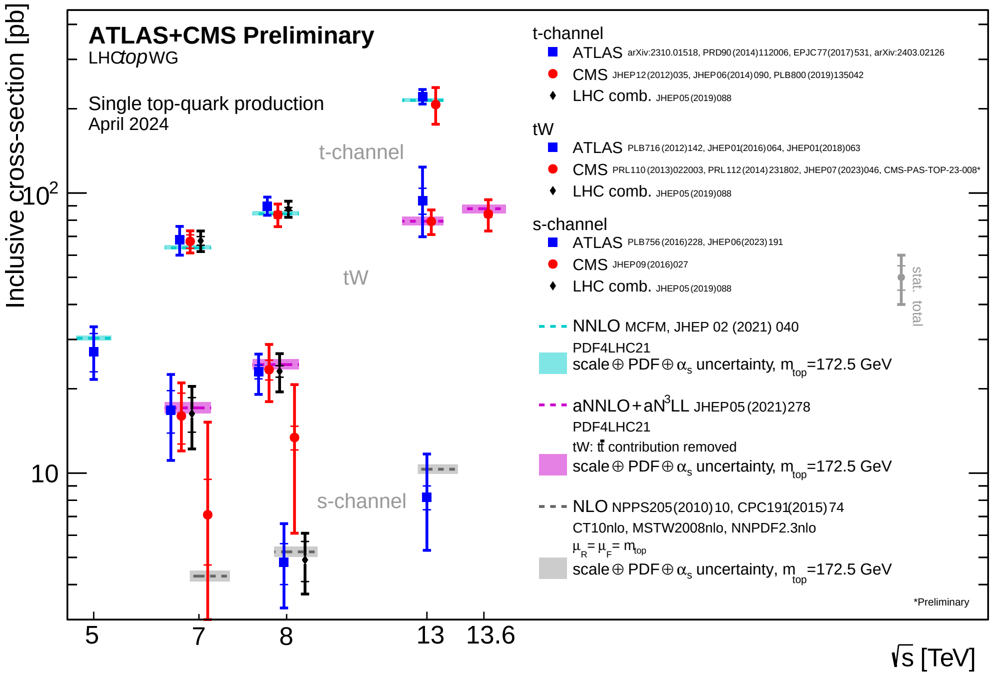

Figure 1.13: Summary of ATLAS and CMS measurements of the single top production cross sections in various channels as a function of the centre of mass energy. The measurements are compared to theoretical calculations based on: NLO QCD, aNNLO QCD complemented with aN3LL resummation and NNLO QCD. Taken from Ref. [91].

presence of new physics. This topic is extensively covered in Chapter 2.

Figure 1.14 compares theoretical and experimental cross section measurements of the most relevant processes involving the associated production of a $t\bar{t}$ pair and EW bosons. Most of these measurements reported a higher cross section with respect to the theoretical predictions. In particular, analyses [99, 100] of the associated production of a $t\bar{t}$ pair with a W boson ($t\bar{t}W$) observed a discrepancy larger than one standard deviation (s.d.), recently confirmed by the latest CMS measurement [101]. A slight tension is also observed in the CMS cross section measurement [102] of the associated production of a $t\bar{t}$ pair with a Z boson ($t\bar{t}Z$). The tension grows for the inclusive production cross section of $t\bar{t}Z$ +tWZ [103], where tWZ indicates the single top quark production in association with a W and a Z boson.

Figure 1.15 shows the cross sections of the single top production in association with EW bosons. Measurements from ATLAS and CMS are compared to the latest theory predictions computed at next-to-leading order (NLO) in QCD.

Two processes are measured in the single top t-channel production mode with an additional EW boson, a Z boson for tZq [103–105] and a photon for $tq\gamma$ [106, 107].

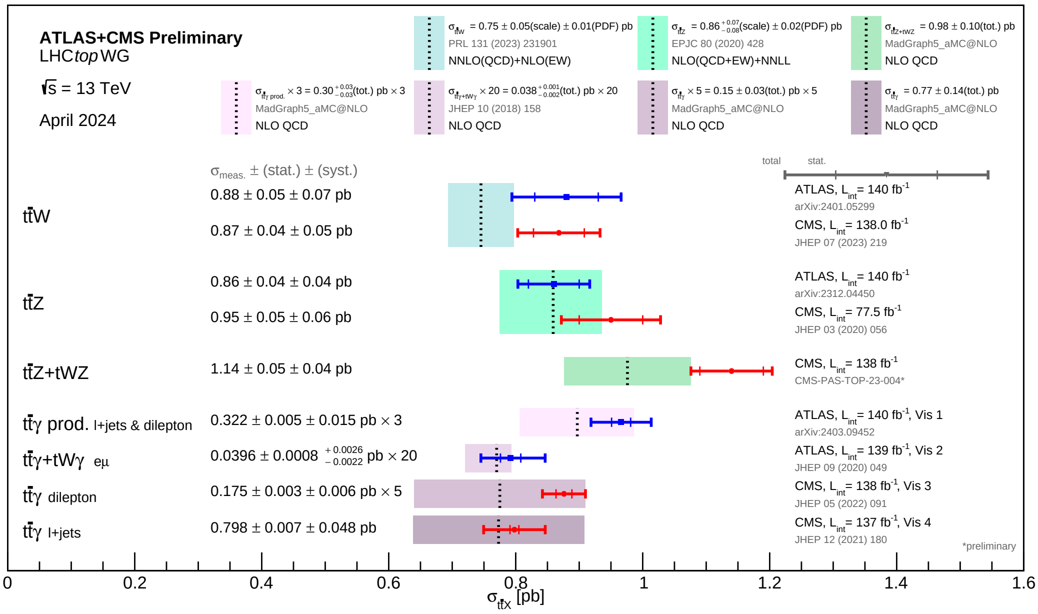

Figure 1.14: Summary of ATLAS and CMS measurements of $\mathrm{t\bar{t}} + X$ ($X = W$, Z or γ) cross sections at 13TeV. The theory predictions are calculated at different orders in QCD for the different processes. "Vis 1", "Vis 2", and "Vis 3" highlight that the relevant phase spaces used for the ATLAS and CMS $\mathrm{t\bar{t}}\gamma$ measurements are different. The theory prediction and experimental result of the ATLAS measurement of $\mathrm{t\bar{t}}\gamma$ are multiplied by a factor of 20, and the theory prediction and experimental result of the CMS measurement of $\mathrm{t\bar{t}}\gamma$ in the di-lepton channel are multiplied by a factor of 5 to allow for easy visualisation on the same scale. The theory bands represent uncertainties due to renormalisation and factorisation scales and parton density functions. Taken from Ref. [91].

These processes provide direct access to the top quark electroweak coupling in single top production and can be compared to the corresponding coupling measured in $\mathrm{t\bar{t}}$ production via the $\mathrm{t\bar{t}Z}$ and $\mathrm{t\bar{t}}\gamma$ processes. The only measurement in the W associated single top production channel is the tWZ inclusive cross section measurement by CMS [108]. While measurement and theoretical predictions of the inclusive cross section of the tZq process [103–105] agree, the latest measurement of $tq\gamma$ [106, 107] and tWZ [108] reported values significantly higher than the theoretical predictions. In particular, the ATLAS measurement of $tq\gamma$ [106], reporting the observation, and the CMS measurement of tWZ process [108], reporting the evidence, measured a two s.d. discrepancy from the theoretical predictions.

The excess observed in the tWZ measurement [108], later confirmed in the $\mathrm{t\bar{t}Z}$ +tWZ measurement [103], suggested that further studies were needed to better understand the origin of this significant discrepancy and to achieve the observation of the tWZ process. This thesis presents the latest measurement of the tWZ inclusive cross sec-

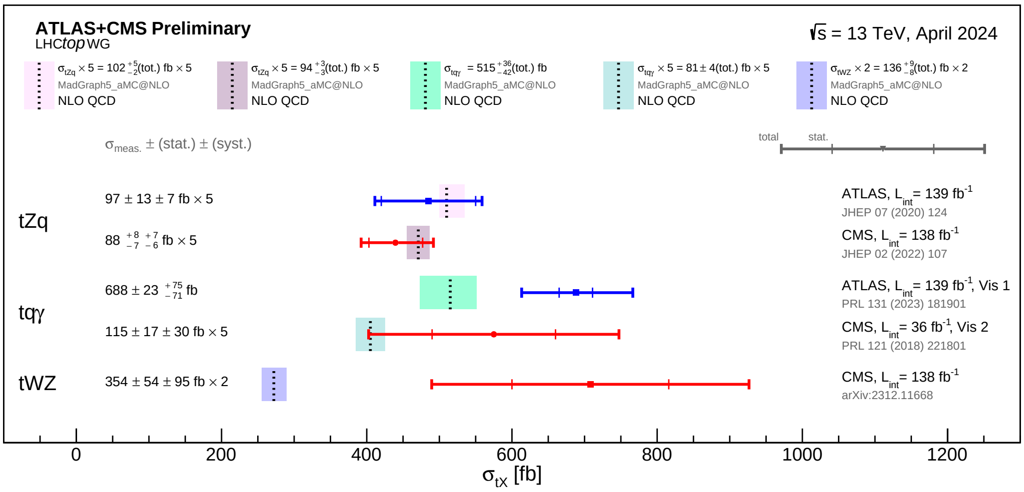

Figure 1.15: Summary of ATLAS and CMS measurements of tX ($X{=}Z$ or γ) cross sections at 13TeV. The cross section measurements are compared to the NLO QCD theoretical calculation. "Vis 1" and "Vis 2" highlight that the relevant phase space used for the ATLAS and CMS $tq\gamma$ measurements is different. The theory prediction and experimental results of tZq, and those of the CMS $tq\gamma$ measurement are multiplied by a factor of 5 to allow for easy visualisation on the same scale; those of the CMS tWZ measurement are multiplied by a factor of 2. The theory bands represent uncertainties due to renormalisation and factorisation scales and parton density functions. Taken from Ref. [91].

tion [109], reporting its observation.

1.3.3 The tWZ process

The production of a single top quark in association with a W and a Z boson is particularly sensitive to modifications of top quark electroweak coupling; therefore, it is a key process in the context of the SMEFT, as any deviation from the SM predictions could be interpreted as a sign of new physics. However, it is also a highly challenging process, both in terms of theoretical simulation and experimental identification. The similarity of its final state with that of $\mathrm{t\bar{t}Z}$ raises a problem for the operative definition of tWZ [110,111]. In fact, while at LO tWZ can be easily simulated in the 5FS through the process $gb \to tWZ$ (left image of Figure 1.16), at NLO additional diagrams featuring $gg \to tWbZ$ can appear. Some of these diagrams feature an additional on-shell top quark (resonant diagrams), which then decays to Wb; these contributions correspond to the LO simulation of $\mathrm{t\bar{t}Z}$, as depicted in the right image of Figure 1.16. Consequently, appropriate overlap removal methods must be applied to prevent double-counting of the same Feynman diagrams in different processes. Two approaches can be considered: the diagram removal (DR) and the diagram subtraction (DS). In the

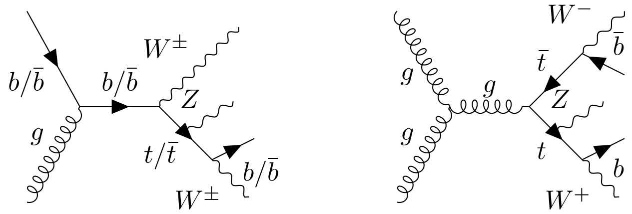

Figure 1.16: Diagrams at LO in QCD for the tWZ (left) and tt̄Z (right) processes.

DR scheme, the resonant diagrams are simply ignored. In contrast, the DS scheme introduces a gauge-invariant term that suppresses the contribution of these diagrams. Two different implementations of the DR subtraction scheme can be considered, differing in how they treat the interference between resonant and non-resonant diagrams. The squared matrix element can be expressed as

$$\begin{aligned} |\mathcal{M}|^2 &= |\mathcal{M}_{non-res} + \sum_i \mathcal{M}_{res,i}|^2 \\ &= |\mathcal{M}_{non-res}|^2 + \left|\sum_i \mathcal{M}_{res,i}\right|^2 + 2\mathrm{Re}\left(\mathcal{M}_{non-res}\sum_i \mathcal{M}_{res,i}\right). \end{aligned} \tag{1.30}$$

The DR1 scheme sets to zero both the resonant and interference terms,

$$|\mathcal{M}|^2_{DR1} = |\mathcal{M}_{non-res}|^2. \tag{1.31}$$

In contrast, the DR2 scheme considers the interference term while still removing the resonant contribution,

$$|\mathcal{M}|^2_{DR2} = |\mathcal{M}_{non-res}|^2 + 2\mathrm{Re}\left(\mathcal{M}_{non-res}\sum_i \mathcal{M}_{res,i}\right). \tag{1.32}$$

Theoretical studies [110] show that results obtained using the DS scheme typically lie between those obtained using the DR1 and DR2 schemes. Therefore, one of the two DR schemes can be considered as the operative definition of the tWZ process, with an associated uncertainty defined as the difference between the two DR schemes.

The small cross section of the tWZ process, $\sigma_{\mathrm{pp}\to\mathrm{tWZ}}$ $(\sqrt{s} = 13\,\mathrm{TeV}) = 136^{+9}_{-8}$ fb at NLO in QCD [65, 66], makes its experimental identification extremely challenging due to backgrounds with cross sections several orders of magnitude larger. Even when considering final states with three or four leptons, other processes involving the associated production of top quarks and EW bosons constitute a large source of irreducible background. In particular, the similarity of the tWZ final state with that of $\mathrm{t\bar{t}Z}$ also gives rise to problems for its identification, since the $\mathrm{t\bar{t}Z}$ cross section is much larger, $\sigma_{\mathrm{pp}\to\mathrm{t\bar{t}Z}}(\sqrt{s} = 13\,\mathrm{TeV}) = 998^{+21}_{-26}$ fb at approximate next-to-NNLO ($\mathrm{aN^3LO}$) in QCD and NLO in EW [112]. Although tWZ has a much smaller cross section and shares the same final state, this process is particularly interesting because it is produced via electroweak interactions rather than strong interactions, as in the case of $\mathrm{t\bar{t}Z}$. This makes it a valuable process for studying the top-electroweak sector and probing SMEFT interactions [110] that modify the bW → tZ vertex, illustrated in Figure 1.17. A detailed discussion of this is provided in the next chapter.

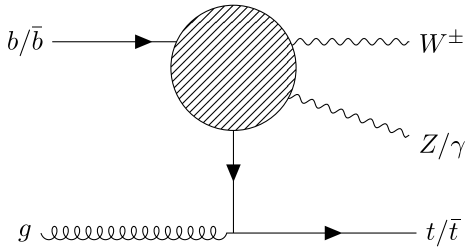

Figure 1.17: Feynman diagram for the LO production of the tWZ process introducing modified interactions, represented by the circle, affecting the bW → tZ vertex.

Chapter 2

The Standard Model Effective Field Theory

BSM searches can generally be classified as either direct or indirect. Direct searches probe specific theoretical predictions for new particles or interactions, for example by looking for new resonances. Instead, indirect searches look for deviations of the observations from the SM predictions, as they could provide evidence of BSM effects. A powerful indirect approach to exploring BSM physics is the Standard Model Effective Field Theory (SMEFT). An effective field theory extends a model by accounting for the effects of heavy particles without including them explicitly in the theory. This has the advantage of reducing the new theory to the original one at low energies, while introducing additional operators in the Lagrangian that modify the original theory at high energies. Since the scale of new physics is expected to be very high, it is possible to observe effects from very massive particles that cannot be directly produced. The main limitation of the SMEFT framework is that it is not renormalisable, unlike the SM, whose Lagrangian contains only dimension-4 operators, ensuring renormalisability at all energy scales. A classic example is Fermi's four-fermion theory [113], which successfully described beta decay before the electroweak interaction mediated by the W boson was understood. Analogously, SMEFT treats the SM as the low-energy limit of a more fundamental theory. In this way, deviations from SM predictions observed in physics measurements can be interpreted as indirect signs of BSM effects.

This chapter introduces the main elements of the SMEFT, focusing on the processes relevant for this thesis. In Section 2.1, a general introduction to the SMEFT is presented. Section 2.2 explains the main aspects of the computation of SMEFT predictions, focusing on the tWZ and $\mathrm{t\bar{t}Z}$ processes.

2.1 Standard Model Effective Field Theory

In the SMEFT, effects arising from high-energy new physics are encoded in high-dimensional operators, added to the SM Lagrangian (Eq. (2.1)). The operators are suppressed by powers of a parameter Λ, which represents the energy scale of new physics. The contribution of each high-dimensional operator is multiplied by a coefficient, known as the Wilson coefficient (WC), which acts as a coupling for the specific operator. The WCs represent the free parameters of the model and encode the strength of the contribution of each operator. A WC equal to 0 corresponds to the SM case for the considered operator.

The SMEFT Lagrangian can be written as an extension of the SM Lagrangian by the addition of $M(d)$ operators $\mathcal{O}$ with dimension d larger than four,

$$\mathcal{L}_{\mathrm{SMEFT}} = \mathcal{L}_{\mathrm{SM}}^{(4)} + \sum_{d>4} \sum_{a=1}^{M(d)} \frac{c_a \mathcal{O}^a_{(d)}}{\Lambda^{d-4}}, \tag{2.1}$$

where $\mathcal{L}_{\mathrm{SM}}^{(4)}$ is the SM Lagrangian, c_a are the WCs, and Λ represents the energy scale of the new physics.

The Lagrangian in Eq. (2.1) includes all the possible independent operators that satisfy the SM gauge symmetry. The number of operators rises drastically when increasing the dimension of the operators considered. A complete classification of dimension-5 and dimension-6 operators is provided by the Warsaw basis [114]. At dimension 5, only one operator is allowed and it encodes the effect of the existence of Majorana neutrinos [37]. At dimension 6, assuming baryon number conservation and ignoring flavour structure and Hermitian conjugations, 59 independent operators can be constructed. The set of eight operators investigated in this thesis, along with their definitions, is shown in Table 2.1. Their selection is motivated by the study in Ref. [110], which demonstrates that the tWZ process is particularly sensitive to these operators and can significantly constrain them.

In Table 2.1, θ_W indicates the weak mixing angle; Q and t denote the left-handed third generation quark doublet and the right-handed top quark singlet, respectively; $\tau^{\mu\nu} = \frac{i}{2}[\gamma^\mu, \gamma^\nu]$ is the commutator of the gamma matrices; φ is the Higgs doublet, while $\varphi^\dagger$ and $\tilde{\varphi}$ indicate its complex conjugated field, where $\tilde{\varphi}^j = \epsilon_{jk}(\varphi^k)^\star$, and ϵ_{jk} is totally antisymmetric with $\epsilon_{12} = +1$; $G^A_{\mu\nu}$, $W^I_{\mu\nu}$, and $B_{\mu\nu}$ are the field strength tensors of the $\mathrm{SU}(3)_C$, $\mathrm{SU}(2)_L$, and $\mathrm{U}(1)_Y$ gauge groups, respectively; T_A and σ_I are the generators of $\mathrm{SU}(3)_C$ and $\mathrm{SU}(2)_L$; g_s is the strong coupling constant; D_μ is the

Table 2.1: List of EFT operators considered for this thesis.

$\mathcal{O}_{tZ}$	$-\sin\theta_W \mathcal{O}_{tB} + \cos\theta_W \mathcal{O}_{tW}$
$\mathcal{O}_{tB}$	$i(\bar{Q}\tau^{\mu\nu}t)\tilde{\varphi}B_{\mu\nu}$ + h.c.
$\mathcal{O}_{tW}$	$i(\bar{Q}\tau^{\mu\nu}\sigma^I t)\tilde{\varphi}W^I_{\mu\nu}$ + h.c.
$\mathcal{O}_{tG}$	$ig_s(\bar{Q}\tau^{\mu\nu}T_A t)\tilde{\varphi}G^A_{\mu\nu}$ + h.c.
$\mathcal{O}_{\phi t}$	$i(\varphi^\dagger \overleftrightarrow{D}_\mu \varphi)(\bar{t}\gamma^\mu t)$ + h.c.
$\mathcal{O}^{(-)}_{\phi Q}$	$\mathcal{O}^{(1)}_{\varphi Q} - \mathcal{O}^{(3)}_{\varphi Q}$
$\mathcal{O}^{(1)}_{\phi Q}$	$i(\varphi^\dagger \overleftrightarrow{D}_\mu \varphi)(\bar{Q}\gamma^\mu Q)$ + h.c.
$\mathcal{O}^{(3)}_{\phi Q}$	$i(\varphi^\dagger \overleftrightarrow{D}_\mu \sigma_I \varphi)(\bar{Q}\gamma^\mu \sigma^I Q)$ + h.c.

covariant derivative and $\overleftrightarrow{D}_\mu$ is defined as $\varphi^\dagger \overleftrightarrow{D}_\mu \varphi \equiv \varphi^\dagger(D_\mu\varphi) - (D_\mu\varphi^\dagger)\varphi$; h.c. stands for Hermitian conjugate.

The $\mathcal{O}_{\mathrm{tZ}}$ operator modifies the interaction between the top quark and the Z boson and is defined as a linear combination of the $\mathcal{O}_{tB}$ and $\mathcal{O}_{tW}$ operators, which modify the interactions of the top quark with the hypercharge B and weak isospin W gauge bosons. The $\mathcal{O}_{tg}$ and $\mathcal{O}_{\phi t}$ operators modify the interactions of the top quark with the gluon and scalar fields, respectively. The $\mathcal{O}^{(-)}_{\phi Q}$ operator is defined as the difference between $\mathcal{O}^{(1)}_{\phi Q}$ and $\mathcal{O}^{(3)}_{\phi Q}$, which represent different modifications of the interactions between the scalar field and the left-handed quark doublet via neutral and charged currents.

The effects of possible SMEFT contributions can be measured across a vast range of SM processes, as they modify the interactions among all elementary particles. Probing possible SMEFT effects translates into measuring the WCs associated with the SMEFT operators. In recent years, a large variety of measurements have been performed at the LHC to measure the different WCs with increased precision. The ultimate goal is to perform a global SMEFT fit including results from a broad range of SM sectors, such as top quark physics, Higgs physics, QCD and EW measurements, to simultaneously probe the effects of as many operators as possible. Recent results from CMS, ATLAS, and the theoretical community have already probed an extensive range of SMEFT operators [115–119].

2.2 SMEFT predictions

The computation of SMEFT predictions is particularly challenging and computationally demanding. In particular, the computational cost increases significantly with the number of SMEFT operators considered, as interference effects between different operators must be taken into account.

The cross section, σ, including the effect of SMEFT operators, can be written as:

$$\begin{aligned}\sigma \propto & \left|\mathcal{M}_{\mathrm{SM}} + \frac{1}{\Lambda^2}\sum_{a=1}^{M} c_a \mathcal{M}^a_{\mathrm{EFT}}\right|^2 = \\ & = |\mathcal{M}_{\mathrm{SM}}|^2 + \frac{2}{\Lambda^2}\sum_a c_a \,\mathrm{Re}\,(\mathcal{M}^*_{\mathrm{SM}}\mathcal{M}^a_{\mathrm{EFT}}) + \frac{1}{\Lambda^4}\sum_{a,b} c_a c_b \,\mathcal{M}^{a*}_{\mathrm{EFT}}\mathcal{M}^b_{\mathrm{EFT}},\end{aligned} \tag{2.2}$$

where $|\mathcal{M}_{\mathrm{SM}}|^2$ represents the squared SM matrix element, $\frac{2}{\Lambda^2}\sum_a c_a \,\mathrm{Re}\,(\mathcal{M}^*_{\mathrm{SM}}\mathcal{M}^a_{\mathrm{EFT}})$ is the interference term between the SM and the SMEFT contributions, and $\frac{1}{\Lambda^4}\sum_{a,b} c_a c_b \,\mathcal{M}^{a*}_{\mathrm{EFT}}\mathcal{M}^b_{\mathrm{EFT}}$ is the quadratic SMEFT term.

Expanding this expression yields the cross section for the SM contribution, along with the linear and quadratic EFT terms:

$$\sigma = \sigma_{\mathrm{SM}} + \sum_{a=1}^{M} c_a \sigma^a_{\mathrm{EFT}} + \sum_{a,b=1}^{M} c_a c_b \sigma^{ab}_{\mathrm{EFT}} \tag{2.3}$$

The primary goal of an SMEFT analysis is to measure the value of the WCs of the operators relevant to the physics processes under investigation. For this purpose, the values of σ_{SM}, σ^a_{EFT}, and $\sigma^{ab}_{\mathrm{EFT}}$ are computed from theoretical predictions. This requires the simulation of K different SMEFT points, each corresponding to an arbitrary choice of the WCs for the operators considered in the analysis. The number of points must be at least equal to the number of degrees of freedom $N = 1 + M + \frac{1}{2}M(M+1)$, corresponding to one SM term, M linear EFT terms, and $\frac{1}{2}M(M+1)$ quadratic EFT terms.

The most straightforward approach to generate predictions for a specific SMEFT point is the direct simulation, which computes predictions for a specific set of operators by fixing the corresponding WCs. However, this approach becomes highly inefficient when a large number of operators is involved, since N different configurations must be considered, requiring N separate simulated datasets. Alternative strategies have been developed to reduce the computational costs and the number of simulated samples. The two most common approaches are the separated simulation and the reweighted simulation. In the separated simulation, the M linear and $\frac{1}{2}M(M+1)$ quadratic terms, used to measure to σ^a_{EFT} and $\sigma^{ab}_{\mathrm{EFT}}$ of Eq. (2.3), are simulated separately. As with the direct simulation, N different simulated datasets are required if all terms of the SMEFT contributions are considered. However, the separated simulation offers an important advantage with respect to direct simulation: the $\sigma^{a}_{\mathrm{EFT}}$ and $\sigma^{ab}_{\mathrm{EFT}}$ contributions are simulated directly as separate contributions, allowing more flexibility in the interpretation of linear and quadratic SMEFT effects. For instance, to study only the linear terms is sufficient to generate the M samples corresponding to the linear terms. Additionally, if certain interference terms between the operators are ignored, the number of required samples can be reduced to fewer than N, even when considering quadratic terms.

In the reweighted simulation, the different N SMEFT points are encoded as N different event weights, computed by evaluating the matrix element at each point. In this way, it is sufficient to generate one single sample, with all the subsequent simulation steps computed only for the reference point, significantly reducing the computational load. However, this method introduces a dependence on the choice of the reference point and may result in large weights in regions of phase space where the parton-level differential cross sections differ significantly from the reference point. Another significant drawback of the reweighting simulation is the possible presence of statistical fluctuations in poorly populated phase space regions due to large event weights.

Two different reweighting approaches exist: the helicity-aware reweighting, which preserves spin correlations by storing helicity amplitudes, and the helicity-ignorant reweighting, which averages over helicities and is therefore less accurate in capturing spin-sensitive observables.

Ref. [120] documents best practices and common pitfalls in generating SMEFT predictions, using representative physics processes as benchmarks. This thesis addresses differences between the inclusion of SMEFT effects in simulation at LO and NLO in QCD using the $\mathrm{t\bar{t}Z}$ process as a case study. Significant sensitivity of this process to SMEFT operators was demonstrated in extensive studies by ATLAS [121, 122] and CMS [123, 124]. The sensitivity to the $\mathcal{O}_{\mathrm{tZ}}$ operator is particularly relevant, as it modifies the interaction between the top quark and the Z boson (Figure 2.1).

The $\mathrm{t\bar{t}Z}$ process is simulated using MadGraph5_aMC@NLO [66], including EFT effects through the SMEFT@NLO [125] and the SMEFTsim [126] models for the NLO and LO simulation, respectively. The parton shower is modelled using Pythia8 [127] and particular attention is given to the matching procedure in the LO simulation, as the emission of an additional jet is simulated in the matrix element. Both simulations are performed in the 5FS, with renormalisation and factorisation scales set to half the sum of the transverse masses of all final-state particles at the matrix-element level.

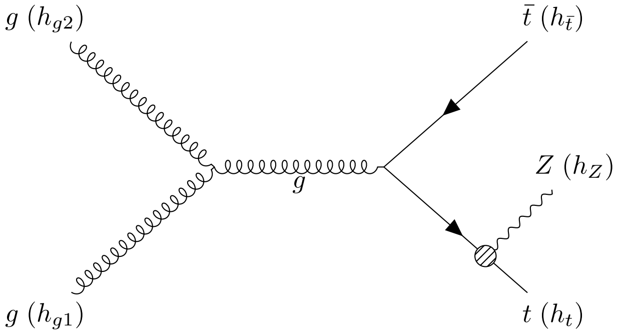

Figure 2.1: Feynman diagram for the LO production of the $\mathrm{t\bar{t}Z}$ process introducing modified interactions between the top quark and the Z boson. The terms $h_{\mathrm{g}_1}, h_{\mathrm{g}_2}, h_{\mathrm{t}}, h_{\bar{\mathrm{t}}}, h_{\mathrm{Z}}$ denote helicities of different particles.

The events are generated under the SM and $c_{\mathrm{tZ}} = 1$ hypotheses, where c_{tZ} is the Wilson coefficient associated to the $\mathcal{O}_{\mathrm{tZ}}$ operator as defined in the SMEFT@NLO model. The $\mathcal{O}_{\mathrm{tZ}}$ operator is not directly defined in the SMEFTsim model; however, the same effect can be obtained from a combination of other SMEFT operators following the translation rules between the two models, as provided in Ref. [125].

The transverse momenta (p_T) of the top quark and Z boson distributions are shown in Figure 2.2, displaying the LO simulation on the left and the NLO simulation on the right. It is not possible to simulate linear and quadratic EFT separately at NLO, therefore only the reweighted and the direct simulation are shown.

The central panels show the ratio between the EFT distributions and the SM, highlighting a significant sensitivity to EFT effects in the tails of the top quark and Z boson p_T distributions. The ratio between the different EFT generation methods is displayed in the bottom panels, showing good agreement across the entire distribution.

The Z boson p_T distribution shows larger sensitivity to EFT effects than the top quark p_T. However, the agreement between the reweighted simulation and the other two EFT prediction methods worsens in the LO results at large values of the Z boson p_T, where significant statistical fluctuations are observed. The main reason for this discrepancy is the use of helicity-aware reweighting considering the SM as a reference point. Indeed, when considering modified interactions, helicity configurations forbidden in the SM due to helicity conservation can be introduced. Therefore, it is not possible to simulate such configurations by applying a weight to SM events. To avoid this issue, it is possible to perform the helicity-ignorant reweighting, or to use a reference point different from the SM. The possible helicity configurations for the

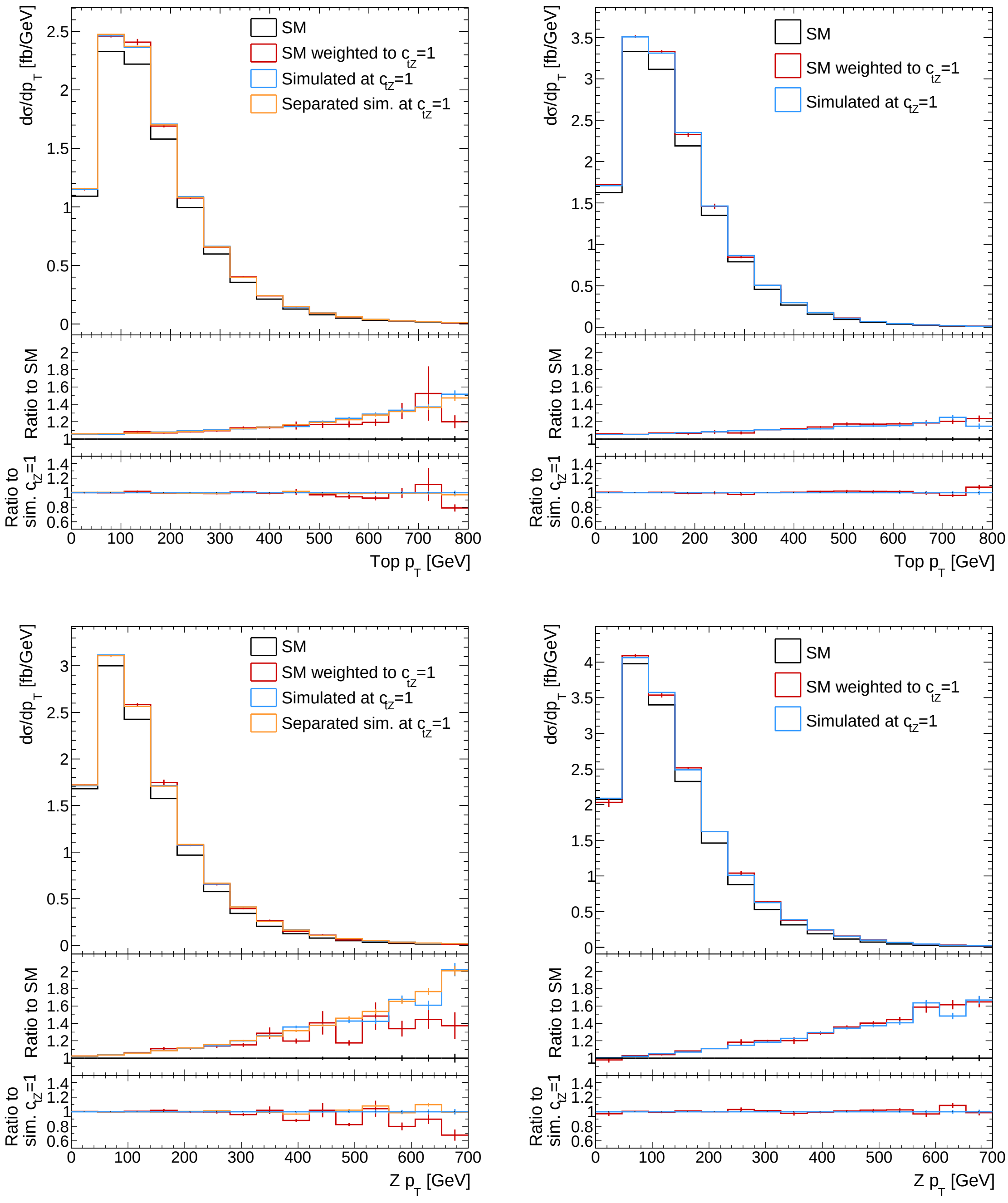

Figure 2.2: Top quark (upper) and Z boson (lower) p_T distribution simulated at LO + 1 jet (left) and at NLO (right). The SM distribution is shown in black, while the other lines represent the different available simulation methods to compute EFT predictions. The first ratio plot highlights the sensitivity to the EFT effects, while the second one shows the agreement between the direct simulation, the reweighted simulation, and the separate simulation (only for LO + 1 jet). Published in Ref. [120].

$t\bar{t}Z$ process and the corresponding contributions to the total number of events are shown in Figure 2.3 for the SM and the $c_{tZ} = 5$ hypotheses. The effect of the modified interaction is significant for specific helicity configurations where the SM contribution is zero.

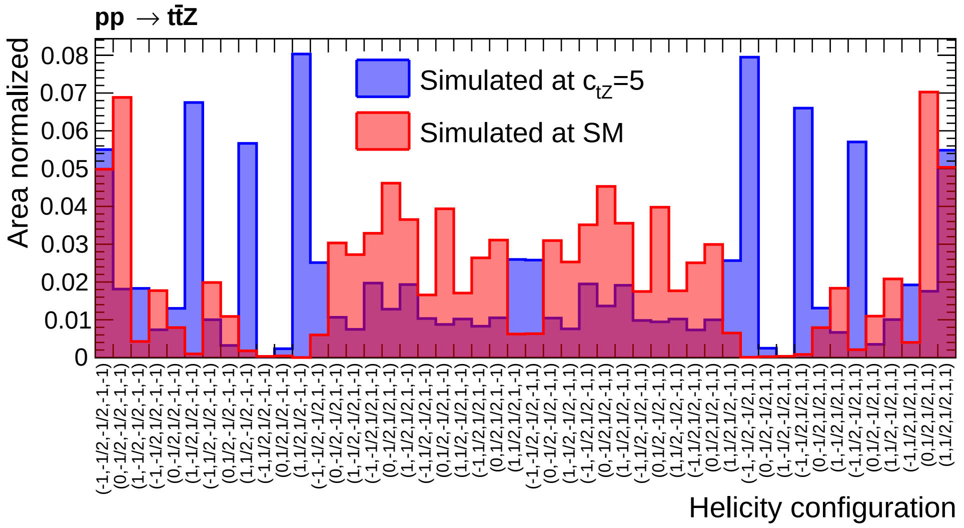

Figure 2.3: Distribution of different helicity configurations in $t\bar{t}Z$ events generated at SM and $c_{tZ} = 5$ in the partonic center-of-mass frame. Bins are labeled as $(h_Z, h_t, h_{\bar{t}}, h_{g_1}, h_{g_2})$, where h_i denotes the helicity of each particle. The plot shows that certain helicity configurations, such as those with $h_{g_1} = h_{g_2}$, are suppressed in the SM, meaning helicity-aware reweighting cannot populate those phase space regions. Published in Ref. [120]

2.2.1 Sensitivity of tWZ and $t\bar{t}Z$ to SMEFT effects

The results from the previous section are applied to study the sensitivity of the tWZ and $t\bar{t}Z$ processes to a relevant set of SMEFT operators. The simulation setup to generate the predictions for tWZ and $t\bar{t}Z$ is the same as that employed to produce the reweighted events for $c_{tZ} = 1$ at NLO; however, a larger set of operators is studied in this case. For the simulation of the tWZ predictions, the DR1 subtraction scheme is applied using the MadStr plugin [128], to remove the overlap with the $t\bar{t}Z$ process. The distributions of the top quark and Z boson p_T, normalised to the number of SM events, for the tWZ and $t\bar{t}Z$ processes are shown in Figure 2.4. The SMEFT operator contributions are obtained using the reweighting method, setting the corresponding WCs to 1.

The lower panels highlight the sensitivity to EFT effects, showing that the tWZ process is significantly more sensitive than $t\bar{t}Z$. Notably, only tWZ is sensitive to the $\mathcal{O}_{\phi Q}^{(3)}$ and

$\mathcal{O}_{tW}$ operators, with deviations from the SM predictions growing at high p_T of the top quark and Z boson. This behaviour arises from unitarity-violating effects induced by modified EW interactions affecting the $bW \to tZ$ vertex, which is absent in the t$\bar{\text{t}}$Z process. The $\mathcal{O}_{\phi Q}^{(3)}$ operator is particularly interesting, as it is connected to the Higgs boson field and is among the least constrained operators considered. Both tWZ and t$\bar{\text{t}}$Z are sensitive to the $\mathcal{O}_{tZ}$ and $\mathcal{O}_{tg}$ operators, which show large deviations from the SM, especially in the high energy tails of the distributions. Similar effects are also observed in the p_T of the decay products. As an example, the distributions of the leading jet and leading lepton p_T are shown in Figure 2.5.

The observed sensitivity to the considered SMEFT operators is consistent with the findings reported in Ref. [110], indicating that dedicated tWZ measurements including SMEFT interpretations could improve the current constraints on these operators.

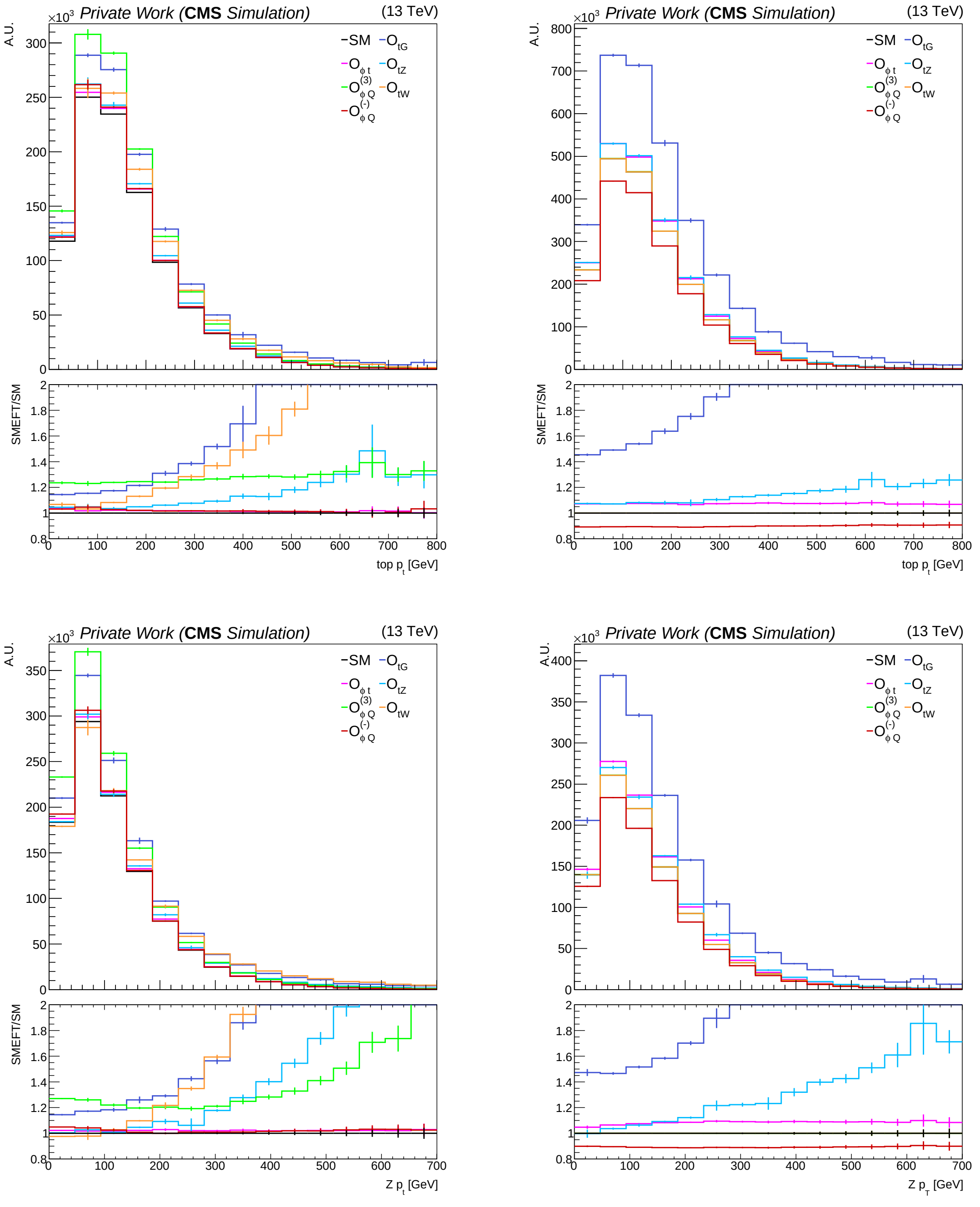

Figure 2.4: Top quark (upper) and Z boson (lower) p_T distributions normalised to the number of SM events simulated at NLO for tWZ (left) and $t\bar{t}Z$ (right). The SM distribution is shown in black, while the other lines represent the different predictions for the considered SMEFT operators. The ratio plot highlights the sensitivity to the EFT effects.

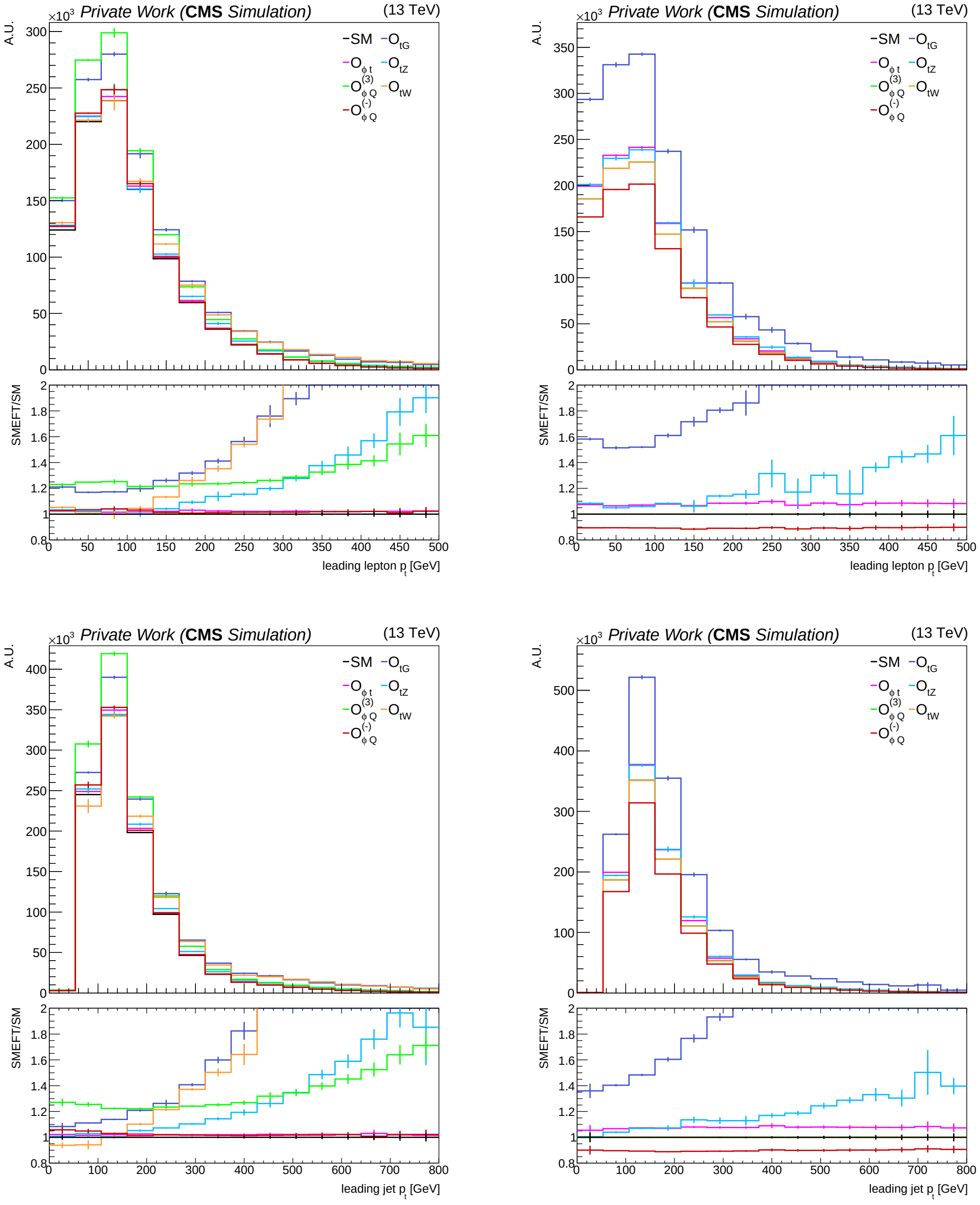

Figure 2.5: Leading lepton (upper) and leading jet (lower) p_T distributions normalised to the number of SM events simulated at NLO for tWZ (left) and t$\bar{\text{t}}$Z (right). The SM distribution is shown in black, while the other lines represent the different predictions for the considered SMEFT operators. The ratio plot highlights the sensitivity to the EFT effects.

Chapter 3

SMEFT interpretation of the tWZ measurement

The CMS collaboration recently published the first evidence for the tWZ process [108]. The tWZ cross section was measured to be 354 ± 54(stat) ± 95(syst) fb using an integrated luminosity of 138 fb^{-1}, corresponding to the data collected from 2016 to 2018 by the CMS experiment.

In Section 3.1 the results of the CMS analysis are reproduced. Section 3.2 presents an EFT interpretation of the CMS measurement focusing on the $\mathcal{O}_{tZ}$ and $\mathcal{O}_{\phi Q}^{(3)}$ operators, with projections for various scenarios with increased luminosity and improved analysis techniques.

3.1 Reproduction of the CMS results

The CMS tWZ measurement targets multi-lepton final states including 3- and 4-leptons signal regions (SRs). Events with three leptons are selected by requiring one opposite-sign same-flavour lepton pair with invariant mass within 15 GeV from the Z boson mass [8]. These events are divided into two SRs based on the number of jets: events with exactly two jets enter in the $\text{SR}_{3l,2j}$, while events with at least three jets are included in the $\text{SR}_{3l,3j}$. Additionally, the presence of at least one jet identified as originating from a b quark (b-jet) is required in both SRs. The 4-lepton SR is defined using similar selection criteria but requires exactly four leptons and at least one jet, rather than two. The CMS analysis uses Deep Neural Networks (DNNs) to distinguish signal from background. In the $\text{SR}_{3l,3j}$ a DNN with three output nodes dedicated to tWZ, $\text{t}\bar{\text{t}}\text{Z}$, and other background processes is used. This SR is further divided into two parts based on the number of b-jets: events with exactly one b-jet define a region enriched in tWZ events, while events with at least two b-jets are dominated by $t\bar{t}Z$ events. The $SR_{3l,2j}$ employs a binary DNN classifier to separate tWZ from the other background processes. The distributions of the DNN output scores for the various 3-lepton SRs, as well as the b-jet multiplicity distribution in the 4-lepton SR, are shown in Figure 3.1.

In this study, the CMS results are reproduced using the event yields included in the CMS publication. For the $t\bar{t}Z$ and tWZ processes, the MC predictions presented in Chapter 2, including SMEFT effects from the $\mathcal{O}_{tZ}$ and the $\mathcal{O}_{\phi Q}^{(3)}$ operators, are used. Realistic efficiencies and acceptances based on CMS performance are applied to reproduce the expected number of events. Table 3.1 presents the event yields for the different background processes, as well as the tWZ and $t\bar{t}Z$ event yields measured in this study and in the CMS results. In this study a 15% normalisation uncertainty is assigned to the tWZ and $t\bar{t}Z$ processes, 10% to di-boson processes, 30% to nonprompt lepton contributions, and 11% to the remaining backgrounds.

Table 3.1: Event yields in the 3ℓ and 4ℓ final states in simulation and in data.

	3ℓ		**4ℓ**	
	CMS	This study	CMS	This study
tWZ	106	108 ± 16	16	13 ± 2
$t\bar{t}Z$	781	803 ± 120	114	101 ± 15
VV(V)	504 ± 50		22 ± 2	
Nonprompt	309 ± 93		1 ± 0.3	
Other bckg	485 ± 53		24 ± 3	
CMS observed	**2312**		**180**	

The effect of the DNN algorithms used in the CMS analysis is reproduced by applying different selection efficiencies for signal and background processes. Events enter in the inclusive 3-lepton SR considered in this study with a 25% efficiency for $t\bar{t}Z$ and 50% efficiency for tWZ and the other backgrounds. The remaining events are assigned to a control region. The expected and observed signal strengths for the tWZ and $t\bar{t}Z$ processes are extracted from a simultaneous fit, and the 68%, 95%, and 99% confidence level (CL) intervals are derived. The results are shown in Figure 3.2, with the best fit values $(\mu_{\mathrm{tWZ}}, \mu_{t\bar{t}Z}) = (3, 0.92)$ in good agreement with the CMS results.

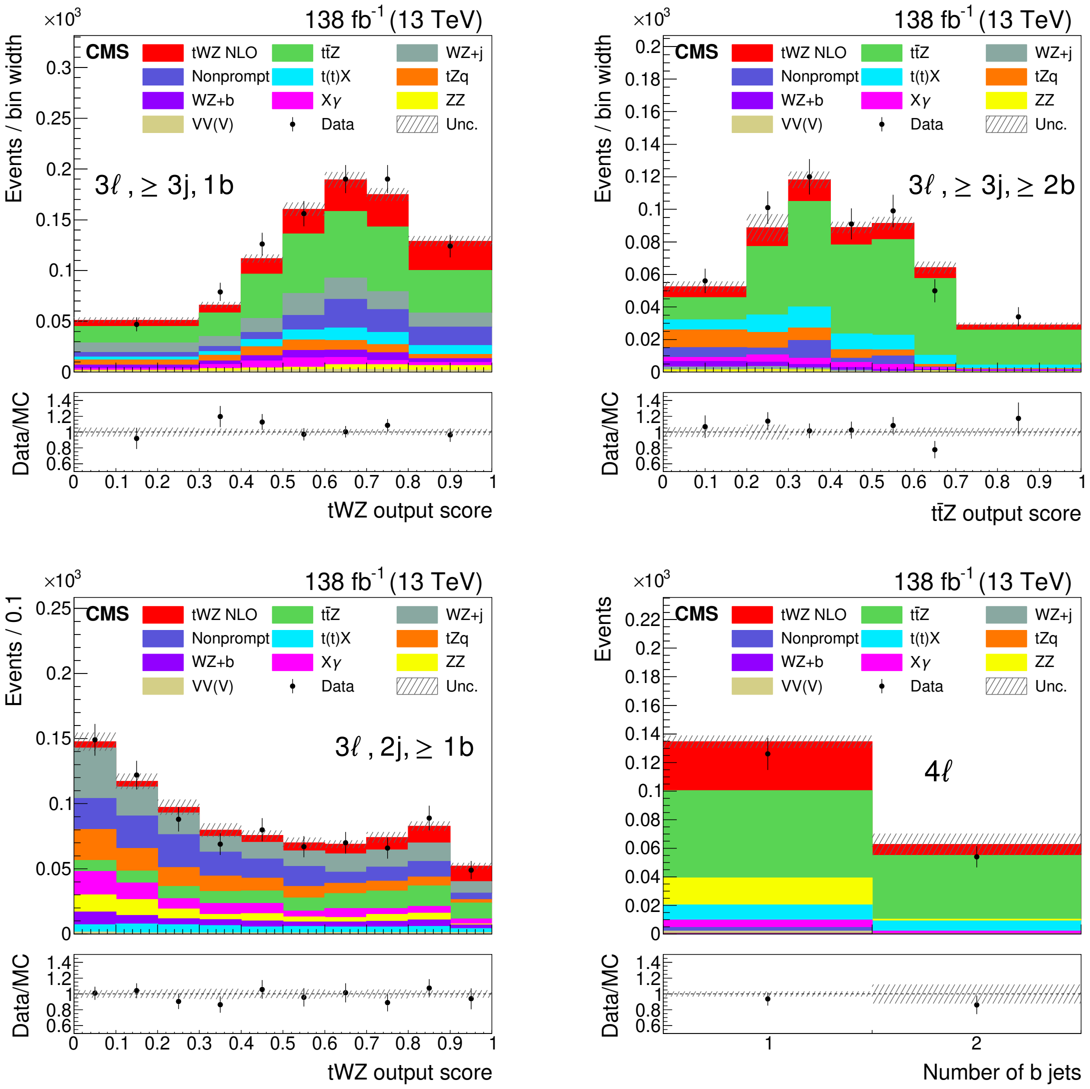

Figure 3.1: Score of the tWZ output node from the multi-class classifier in SR$_{3l,3j}$ for events with exactly one b-jet (upper left), and of the tt̄Z output node in SR$_{3l,3j}$ for events with more than one b-jet (upper right); score of the tWZ output node of the binary classifier in SR$_{3l,2j}$ (lower left), and the b-jet multiplicity in the 4-lepton SR (lower right). The VV(V) group in the legend denotes the VVV, WW, and W in association with jets backgrounds. The Nonprompt group refers to processes with at least one nonprompt lepton, estimated with data-driven methods. The dashed band shows the total uncertainty (statistical and systematic) after the fit. Taken from Ref. [108].

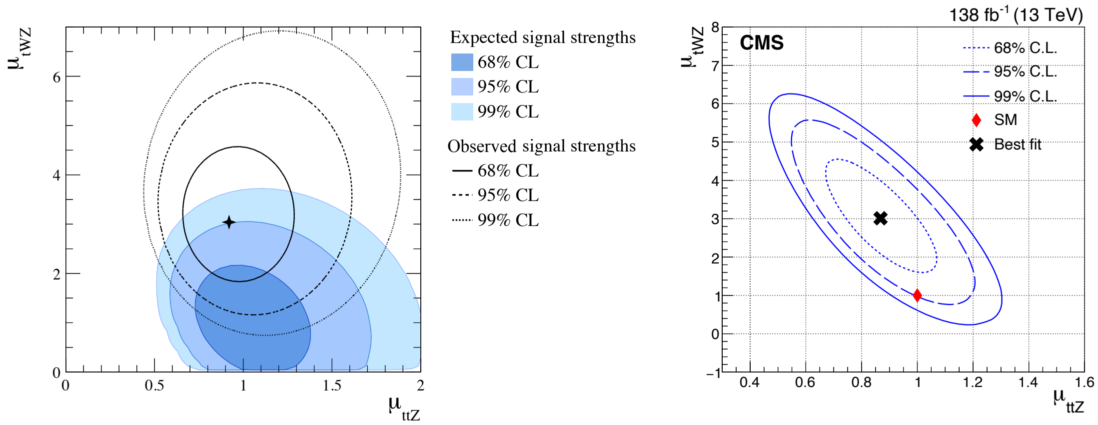

Figure 3.2: Comparison of two-dimensional likelihood scans for the tWZ and t$\bar{\text{t}}$Z signal strengths. Left: likelihood scan from this study showing the expected and observed confidence level (CL) contours for μ_{tWZ} versus $\mu_{\text{t}\bar{\text{t}}\text{Z}}$. The CL contours are shown in shades of blue for the expected limits, and as lines for the observed ones. The black marker indicates the best-fit value. Right: likelihood scan from the CMS analysis [108] showing the observed CL contours for μ_{tWZ} versus $\mu_{\text{t}\bar{\text{t}}\text{Z}}$. The black cross marks the best-fit value, and the red diamond indicates SM expectation.

3.2 SMEFT interpretation and projections for HL-LHC

These results are interpreted within the SMEFT framework performing a simultaneous measurement of the WCs associated to the $\mathcal{O}_{tZ}$ and the $\mathcal{O}_{\phi Q}^{(3)}$ operators. The resulting two dimensional likelihood scan is shown in Figure 3.3.

While the sensitivity to the $\mathcal{O}_{\phi Q}^{(3)}$ operator is not yet competitive with the current best limits, the constraint on the $\mathcal{O}_{tZ}$ operator can already provide valuable input for global SMEFT fits. However, an inclusive measurement does not fully exploit the potential of the tWZ process, as most of the sensitivity to SMEFT effects comes from unitarity-violating effects, which lead to larger sensitivity in the high energy tails of relevant distributions. Therefore, the expected results of a differential measurement of the Z boson transverse momentum are studied for various integrated luminosity scenarios. These include projections up to the full dataset expected at the High-Luminosity LHC. Systematic uncertainties are assumed to reduce following an approximate $\sqrt{L}$ scaling. Improved signal and background selection efficiencies are considered to reflect potential advancements in the analysis techniques and signal discrimination. In the final scenario, a selection efficiency of 68% is applied for the tWZ process, 18% for t$\bar{\text{t}}$Z, and 50% for the remaining background processes. The results of the inclusive and differential measurements are shown in Figure 3.4.

This study demonstrates that a differential measurement with 300 fb^{-1} would achieve

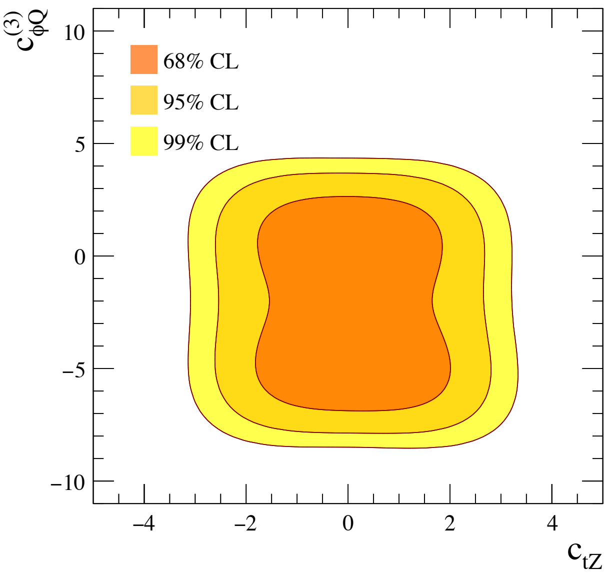

Figure 3.3: Constraints from a fit to $t\bar{t}Z$ and tWZ on the WCs of the $\mathcal{O}_{tZ}$ and $\mathcal{O}_{\phi Q}^{(3)}$ operators, for $\Lambda = 1$ TeV. The orange, light orange, and yellow shaded areas show the observed limits on the two Wilson coefficients respectively at 68%, 95%, and 99% confidence levels. Published in [129].

significantly better sensitivity than an inclusive measurement with a tenfold increase in statistical precision [130]. Therefore, these results highlight the importance of focusing future analyses on differential distributions to fully exploit the sensitivity of the tWZ process to SMEFT effects.

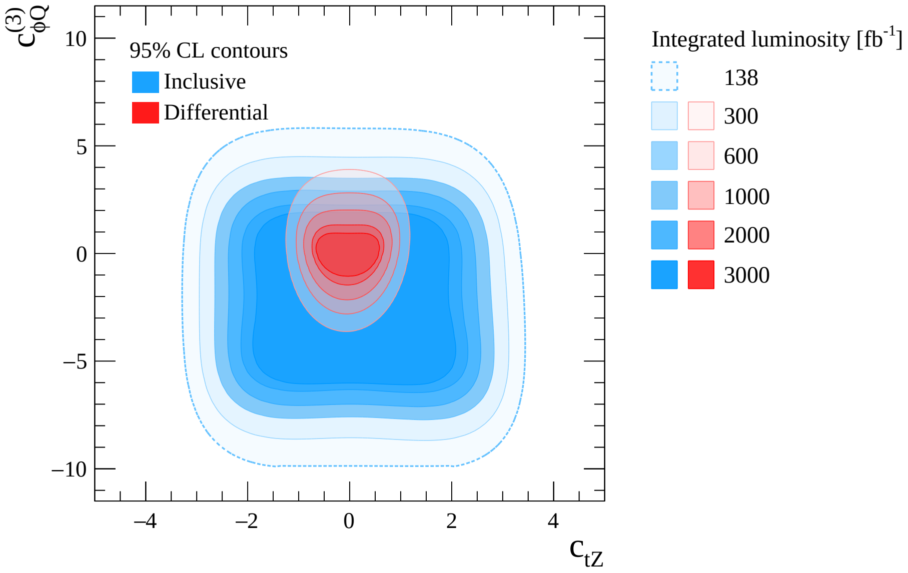

Figure 3.4: Constraints from a fit to $t\bar{t}Z$ and tWZ simulated data on the SMEFT operators $\mathcal{O}_{tZ}$ and $\mathcal{O}_{\phi Q}^{(3)}$, for $\Lambda = 1$ TeV. The blue-shaded area shows constraints from inclusive measurements, while the red-shaded area refers to constraints including differential $p_{\mathrm{T},Z}$ measurements. The outermost blue area bounded by the dashed line corresponds to expected constraints from the CMS Run 2 measurement of tWZ production [108]. Published in [130].

.

Chapter 4

The experiment

The data used in the analysis presented in this thesis were collected with the Compact Muon Solenoid (CMS), one of the four major experiments analysing the proton-proton collisions at the Large Hadron Collider (LHC). This chapter introduces the main features of the LHC in Section 4.1, and provides an overview of the four major experiments located along its ring. Section 4.2 describes the main characteristics of the CMS experiment, with a focus on the roles of the different sub-detectors.

4.1 The Large Hadron Collider

The Large Hadron Collider (LHC) [131–133] is the largest and most powerful particle accelerator in the world. It is located at the European Organisation for Nuclear Research (CERN), near Geneva, in Switzerland. The LHC is a circular accelerator situated about 100 metres underground, with a circumference of 27 km. The ring has been previously used for the Large Electron-Positron Collider [134–136], which collided electrons and positrons up to $\sqrt{s} = 209$ GeV. Major modifications were made to adapt the infrastructure for proton-proton collisions, as protons lose negligible energy through synchrotron radiation compared to electrons. This allows protons not only to reach but also to maintain much higher energies, requiring more powerful magnets to keep them on their circular trajectory.

The protons that eventually collide in the LHC are accelerated through a sequence of stages. The structure of the CERN accelerator complex is illustrated in Figure 4.1. The protons are produced in the linear accelerator (Linac4) and accelerated to 2 GeV in the Proton Synchrotron Booster (PSB). They are then injected in the Proton Synchrotron (PS), where their energy reach 26 GeV, before being accelerated to 450 GeV

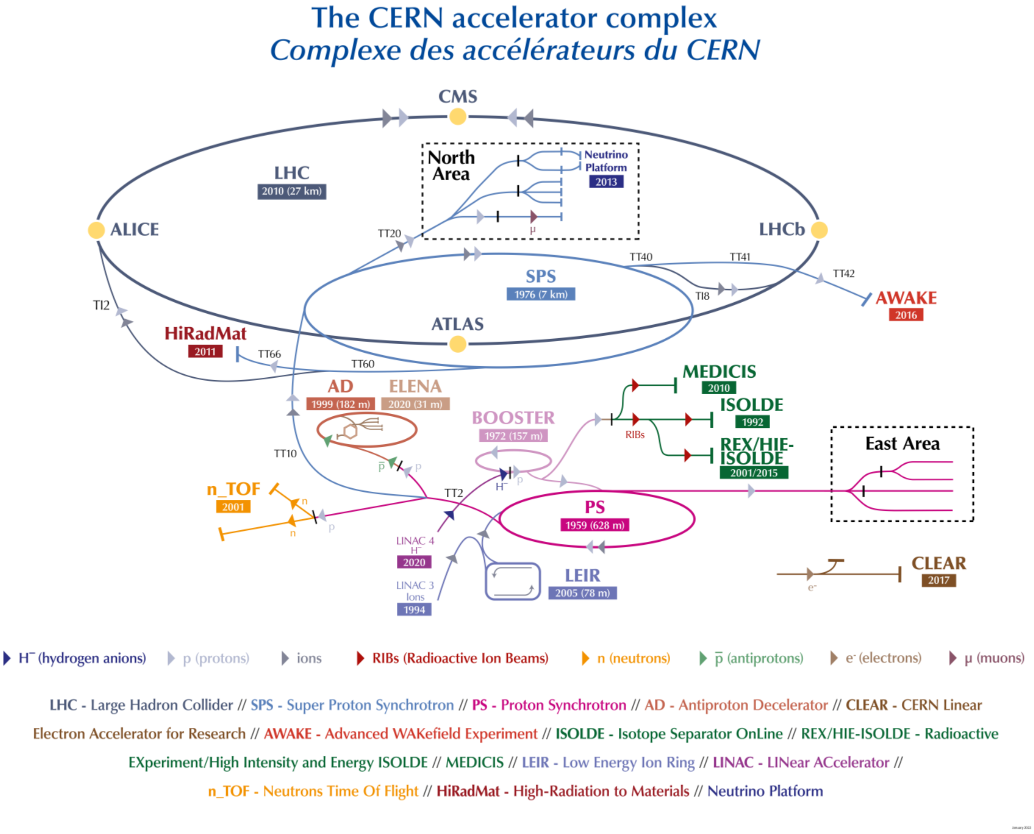

Figure 4.1: CERN accelerator complex. Image from Ref. [137].

in the Super Proton Synchrotron (SPS). Finally, the protons are transferred to the Large Hadron Collider (LHC), which is designed to accelerate the protons up to 7 TeV. The LHC can also produce collisions between ions or between protons and ions, however these datasets are not analysed in this thesis.

The protons travel in bunches of about 1.1$\times$ 10^{11} particles inside two beam pipes maintained at ultra-light vacuum. They are accelerated by eight superconducting radiofrequency cavities per beam, operating at 4.5 K. The circular trajectory of the protons is controlled by 1232 dipole magnets, which are supplemented with sextupole, octupole, and decapole magnets to correct for imperfections of the magnetic field. Additionally, quadrupole magnets are used to keep the beam focused by squeezing it horizontally or vertically. All the magnets are superconducting and operate at a temperature of 1.9 K.

The collisions between proton bunches occur at four different interaction points, cor-

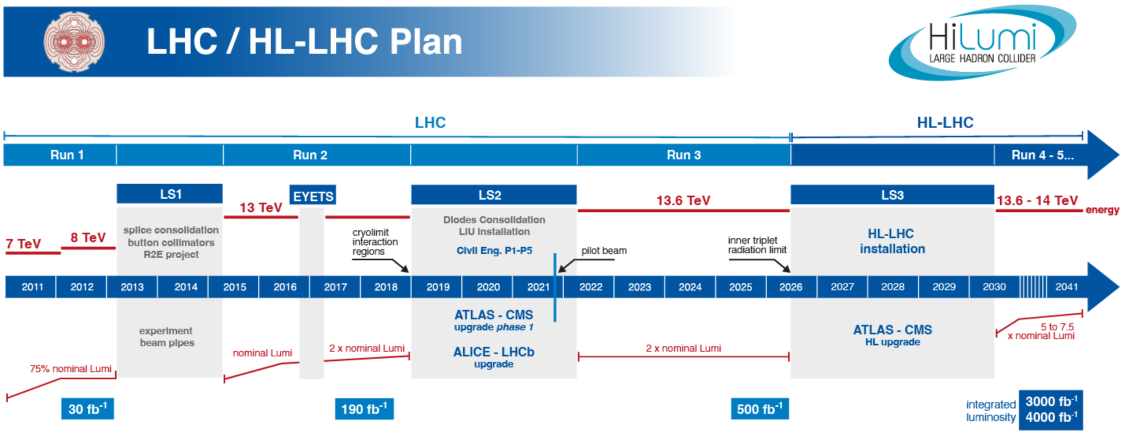

Figure 4.2: LHC schedule showing centre-of-mass energies and integrated luminosities for the different data-taking periods. Image from Ref. [142].

responding to the locations of the four major LHC experiments: A Large Ion Collider Experiment (ALICE) [138], A Toroidal LHC Apparatus (ATLAS) [139], the Compact Muon Solenoid (CMS) [140], and the Large Hadron Collider beauty (LHCb) [141]. ATLAS and CMS are general-purpose detectors, while ALICE and LHCb focus on heavy-ion collisions and b quark physics, respectively.

Proton–proton collisions at the LHC have taken place at different centre-of-mass energies over successive data-taking periods (Figure 4.2). During Run 1 (2010-2012), the centre-of-mass energy was 7 TeV (2010-2011) and 8 TeV (2012). It was increased to 13 TeV for the Run 2 period (2015-2018), and is currently at 13.6 TeV during Run 3 (2022-2026), which has been extended by two years with respect to the initial schedule. At the end of Run 3, the LHC will undergo its third long shutdown (LS3) to upgrade the accelerator and the experiments for the High-Luminosity LHC (HL-LHC) phase, during which the centre-of-mass energy is planned to reach 14 TeV.

Besides the centre-of-mass energy, another key parameter of a particle collider is the luminosity. It depends on the characteristics of the machine and the beams, and can be expressed as

$$\mathcal{L} = \frac{f n_b N_1 N_2}{4\pi\sigma_x\sigma_y}. \tag{4.1}$$

where N_1 and N_2 represent the number of particles per bunch in each beam, n_b is the number of bunches, f is the revolution frequency, and σ_x and σ_y are are the root mean square widths of the Gaussian beam profiles in the x and y directions. This expression assumes two beams with identical Gaussian proton distributions.

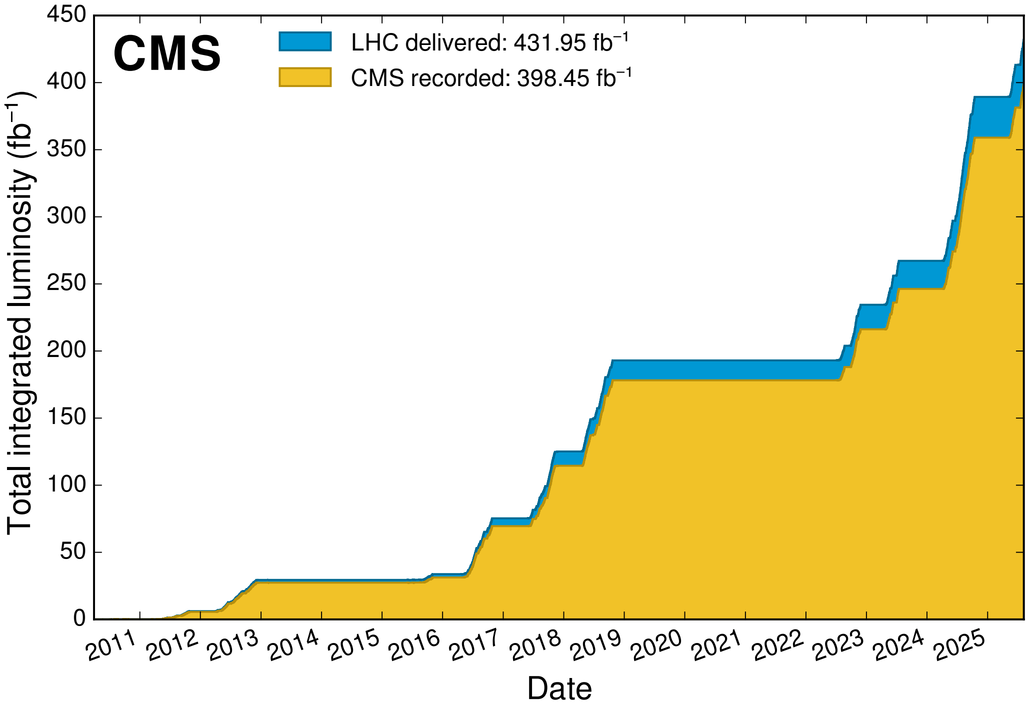

Figure 4.3: Cumulative delivered and recorded luminosity versus time for 2010-2012, 2015-2018, and 2022-2025 (pp data only). Taken from [143].

The quantity in Eq. 4.1 corresponds to the instantaneous luminosity $\frac{d\mathcal{L}}{dt}$, which relates the cross section σ of a given process to the event rate,

$$\frac{d\mathcal{L}}{dt} = \frac{1}{\sigma}\frac{dN}{dt}. \tag{4.2}$$

The integrated luminosity $\mathcal{L}_{\text{int}}$ is obtained by integrating the instantaneous luminosity over time,

$$\mathcal{L}_{\text{int}} = \int \frac{d\mathcal{L}}{dt} dt = \frac{N}{\sigma}. \tag{4.3}$$

Figure 4.3 shows the luminosity delivered by the LHC and recorded by the CMS experiment since 2010. The measurement presented in this thesis is based on data collected at $\sqrt{s} = 13$ TeV between 2016 and 2018 (Run 2) and at $\sqrt{s} = 13.6$ TeV between 2022 and 2023 (Run 3).

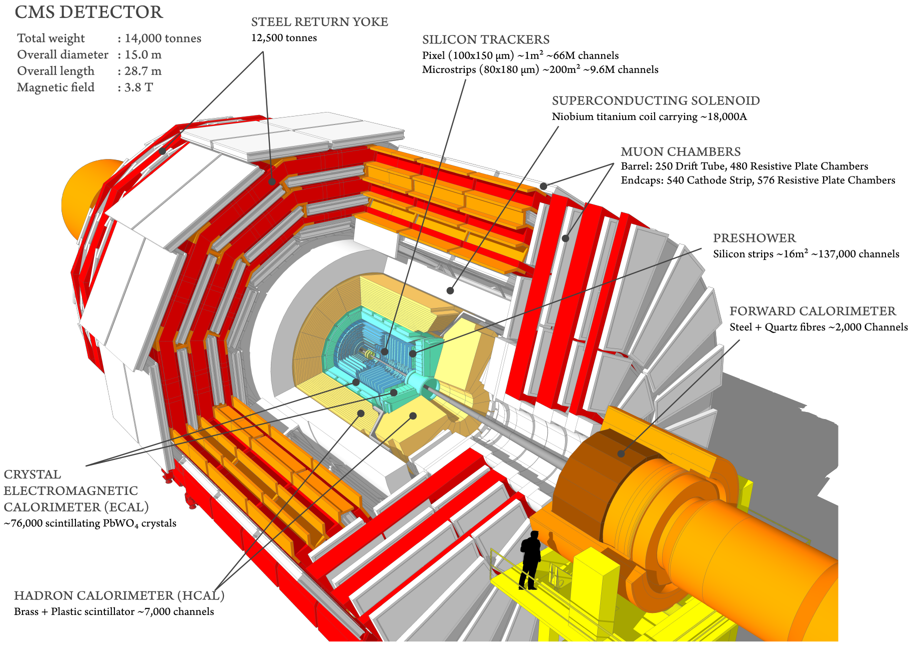

Figure 4.4: Schematic representation of the CMS detector, highlighting its different sub-detectors. Image from Ref. [144].

4.2 The Compact Muon Solenoid experiment

The CMS is the heaviest particle detector ever built. Located at Point 5 of the LHC ring, it is a general-purpose detector designed to investigate a wide range of particle physics processes. It has a cylindrical structure built around the beam pipe, with a length of 21 m, a diameter of 15 m, and a total weight of approximately 14000 tons. Figure 4.4 shows a schematic representation of the detector, highlighting its different sub-detectors. The innermost component is the tracker system, which includes pixel and silicon strip detectors. Surrounding the tracker are the electromagnetic and hadronic calorimeters. These are enclosed within the solenoidal magnet, and the outermost component is the muon system.

Figure 4.5 illustrates the role of the various sub-detectors in particle identification for a slice of the CMS detector. Charged particles produce hits in the tracker system, which are used to reconstruct their trajectory and measure their momentum analysing the curvature caused by the magnetic field. Electrons and charged hadrons deposit their energy primarily in the electromagnetic and hadronic calorimeters, respectively. By combining the information from the tracker and the calorimeters, the kinematic properties of the particles can be measured with improved precision. Neutral hadrons

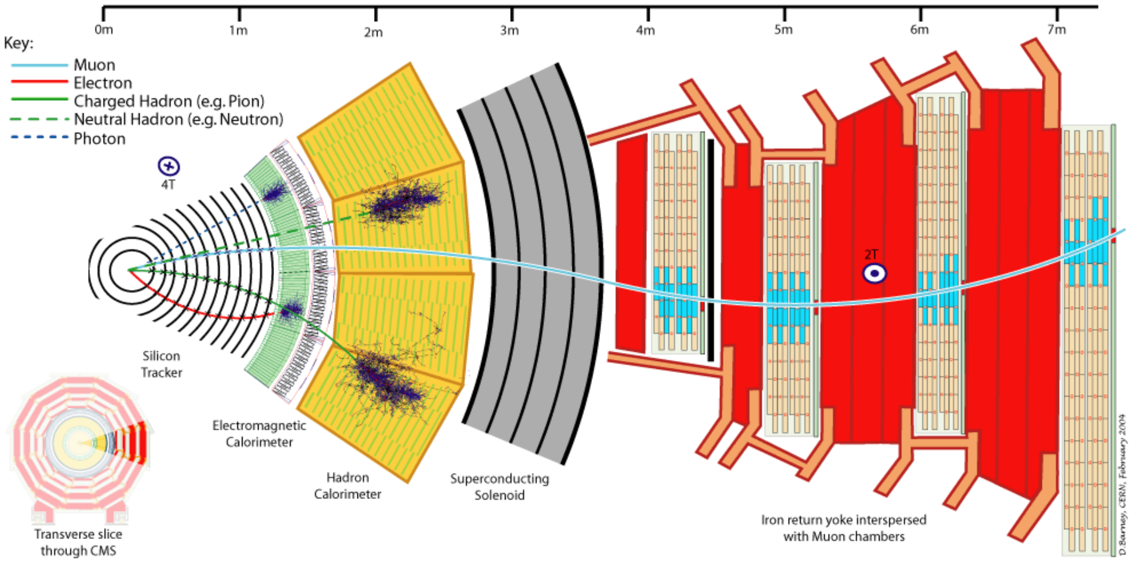

Figure 4.5: Slice of the CMS detector illustrating the role of the different sub-detectors in the particles identification. Image from Ref. [145].

and photons do not leave hits in the tracker but can be identified through energy deposits in the calorimeters. Muons traverse the entire detector, leaving information about their trajectory in the tracker and in the muon system. Neutrinos are the only particles that leave CMS undetected, however their presence can be inferred by measuring the momentum of all the detected particles in the event.

It is useful to define a coordinate system to describe the CMS detector and the reconstructed physics objects. The origin of this system is the interaction point, with the z-axis aligned along the beam pipe. The y-axis points vertically upward (towards the surface of the Earth), and the x-axis is oriented such that the coordinate system is right-handed and lies in the transverse plane. In this coordinate system, the components of a particle's momentum can be defined. The longitudinal component along the z-axis is denoted by p_z, while the transverse momentum, p_T, is defined as

$$p_T = \sqrt{p_x^2 + p_y^2}. \tag{4.4}$$

Since the proton beams do not travel in the transverse plan, the total transverse momentum of all final-state particles, including those not detected by CMS, should sum to zero. Any difference from zero can be attributed to undetected particles, typically neutrinos. This quantity is usually referred to as the missing transverse momentum vector, denoted $\vec{p}_T^{\,\text{miss}}$.

To exploit the cylindrical symmetry of the detector, it is helpful to use spherical coordinates. The azimuthal angle ϕ is defined in the transverse plane as the angle measured from the x-axis towards the y-axis. The polar angle θ is defined as the angle between the particle's momentum vector and the z-axis. However, since differences in θ are not Lorentz-invariant under boosts along the z-axis, the pseudorapidity (η) is used instead,

$$\eta \equiv -\ln\left(\tan\frac{\theta}{2}\right), \tag{4.5}$$

where $\eta = 0$ corresponds to particles emitted at $\theta = 90^\circ$ (i.e., perpendicular to the beam pipe), and $|\eta| \to \infty$ corresponds to particles emitted parallel to the beam pipe. Alternatively, the rapidity y can be used, which is defined as

$$y \equiv \frac{1}{2}\ln\left(\frac{E+p_z}{E-p_z}\right), \tag{4.6}$$

in the ultra-relativistic limit ($E \approx |\vec{p}|$), rapidity and pseudorapidity converge. However, outside this limit, rapidity is preferred because pseudorapidity differences are invariant under Lorentz boosts along the z-axis only in the ultra-relativistic limit. Finally, the angular separation between two particles in the detector is commonly quantified using the distance ΔR in the η–ϕ plane, defined as

$$\Delta R \equiv \sqrt{(\Delta\eta)^2 + (\Delta\phi)^2}, \tag{4.7}$$

where $\Delta\eta$ and $\Delta\phi$ indicate the difference in η and ϕ between the two particles.

4.2.1 Tracking system

The innermost part of the CMS detector is the tracking system [146], which is designed to perform precision measurements of the momentum of charged particles, while minimising their energy loss due to the interactions with the detector material. It is composed of multiple layers of semiconducting silicon detectors covering a region of $|\eta| < 2.5$. A schematic representation of the tracking system is shown in Figure 4.6.

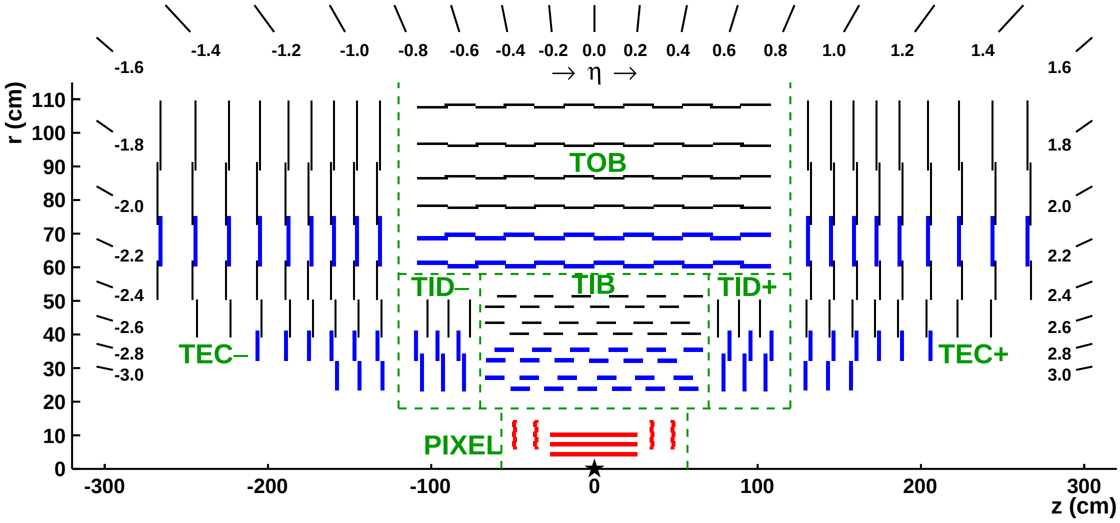

Figure 4.6: Schematic cross section of the CMS tracker before the upgrade of the PIXEL detector between 2016 and 2017. The pixel detector is depicted in red and is located close to the interaction point, indicated by a black star. The silicon strip tracker modules are depicted with black and blue lines, and are divided into four parts: TIB, TOB, TID, and TEC. Image from Ref. [147].

The core of the tracking system is the silicon pixel detector (PIXEL), which was upgraded between 2016 and 2017 to cope with higher instantaneous luminosity [148]. Before the upgrade, it consisted of three barrel layers (BPIX) and two endcap discs (FPIX). The upgraded version added one barrel layer and one additional disc per endcap. The hit resolution of the BPIX detector is measured to be 9.5 μm in the $r\phi$-direction and 22.2 μm in the z-direction [148].

The PIXEL detector is surrounded by the silicon strip detector, which is divided into four parts. The innermost part is split into barrel and endcap, referred to as the tracker inner barrel (TIB), composed of four strip layers, and the tracker inner discs (TID), which consist of three endcap discs. This structure is repeated in the outer part, comprising the tracker outer barrel (TOB), with six layers, and the Tracker Endcaps (TEC), with nine discs. For the silicon strip tracker, the position resolution ranges from 13-38 μm in the inner part to 18-47 μm in the outer part [147].

4.2.2 Electromagnetic calorimeter

The electromagnetic calorimeter (ECAL) of CMS [149] surrounds the tracking system and is designed to measure the energy of electrons and photons. These particles produce electromagnetic showers in the calorimeter material, depositing their energy and

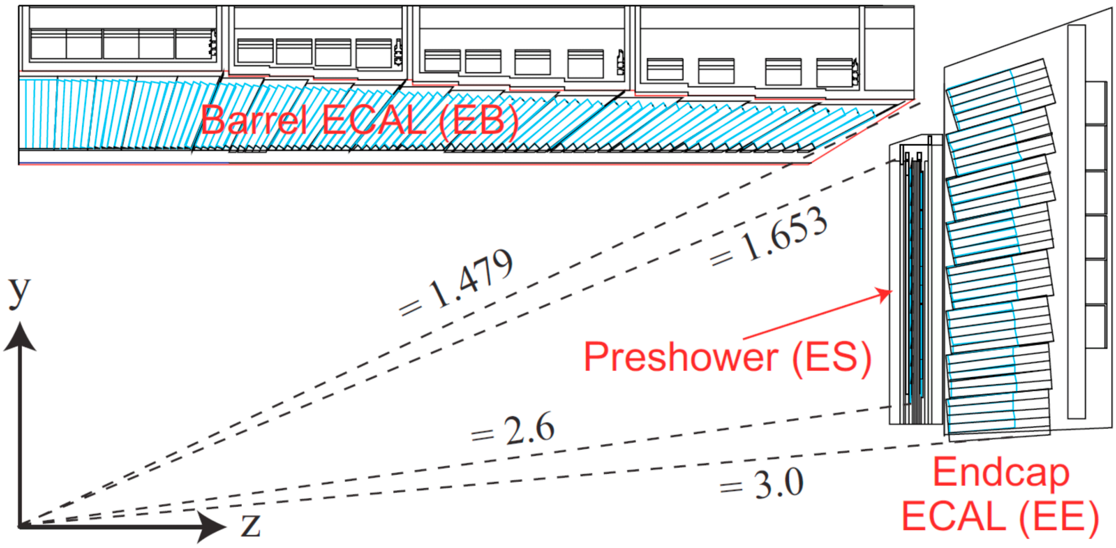

Figure 4.7: Schematic representation of one quadrant of the ECAL detector. The dotted lines indicate the η coverage of the different detector components. Image from Ref. [150].

enabling the measurement of their initial energy. Electrons and photons leave similar signatures in ECAL; however, only electrons produce energy deposits that are associated with tracks in the tracking system, allowing for their distinction from photons.
A schematic representation of the ECAL is shown in Figure 4.7. The ECAL is a homogeneous calorimeter built using lead tungstate ($PbWO_4$) crystals and provides coverage up to $|\eta| < 3$. It consists of a central barrel region (EB), which covers $|\eta| < 1.479$, and two endcaps (EE) that cover the region $1.479 < |\eta| < 3.0$. In front of the endcaps, the preshower (ES) detector is installed to increase the spatial resolution, thereby improving the identification of low-energy photons originating from π^0 decays. The $PbWO_4$ crystals have very short radiation length ($X_0 = 0.89$ cm) and quick scintillation response such that approximately 80% of the light is emitted in a time window of 25 ns, crucial to cope with a proton bunch spacing of 25 ns.
The energy resolution of the ECAL was measured in test beams [151] and is parametrised as

$$\frac{\sigma_E}{E} = \frac{2.8\%}{\sqrt{E[\mathrm{GeV}]}} \oplus \frac{12\%}{E[\mathrm{GeV}]} \oplus (0.3\%), \tag{4.8}$$

the first term represents the stochastic nature of the electromagnetic shower development, scaling with $\frac{1}{\sqrt{E}}$. The second terms accounts for noise contributions, scaling with $\frac{1}{E}$, and is therefore dominant at low energies. The third term is constant and becomes dominant at high energies, it reflects the limited accuracy in the calibration of the ECAL cells. The ECAL performance is constantly monitored to account for crystals aging and changes in transparency. The energy resolution varies across different η regions, ranging from 2% to 5% [152].

4.2.3 Hadronic calorimeter

The hadronic calorimeter (HCAL) of CMS [153] is designed to measure the energy of neutral and charged hadrons. These particles produce hadronic showers when interacting with the detector material. Hadronic showers include an electromagnetic component; however, it is not possible to fully absorb the energy of heavy hadrons in ECAL due to its limited depth. For this reason, the HCAL is placed around the ECAL. A schematic representation of the HCAL is shown in Figure 4.8.

The HCAL is a sampling calorimeter composed of alternating layers of brass absorber and plastic scintillator material. Like the ECAL, it includes a barrel (HB) and two endcaps (HE), covering the region $|\eta| < 1.4$ and $1.3 < |\eta| < 3$, respectively. An additional outer barrel (HO) is placed outside the solenoid, which is used as an additional absorber. The high-η region ($3 < |\eta| < 5.2$) is covered by the hadron forward detector (HF), which has to cope with a higher amount of radiation and is therefore built using layers of steel and quartz fibers.

The hadronic energy resolution of the combined HCAL and ECAL in the barrel region has been measured in test beams [154] and is parametrised as

$$\frac{\sigma_E}{E} = \frac{85\%}{\sqrt{E[\mathrm{GeV}]}} \oplus 7.4\%, \tag{4.9}$$

the first term represents the stochastic component of the resolution, while the second one corresponds to the constant term.

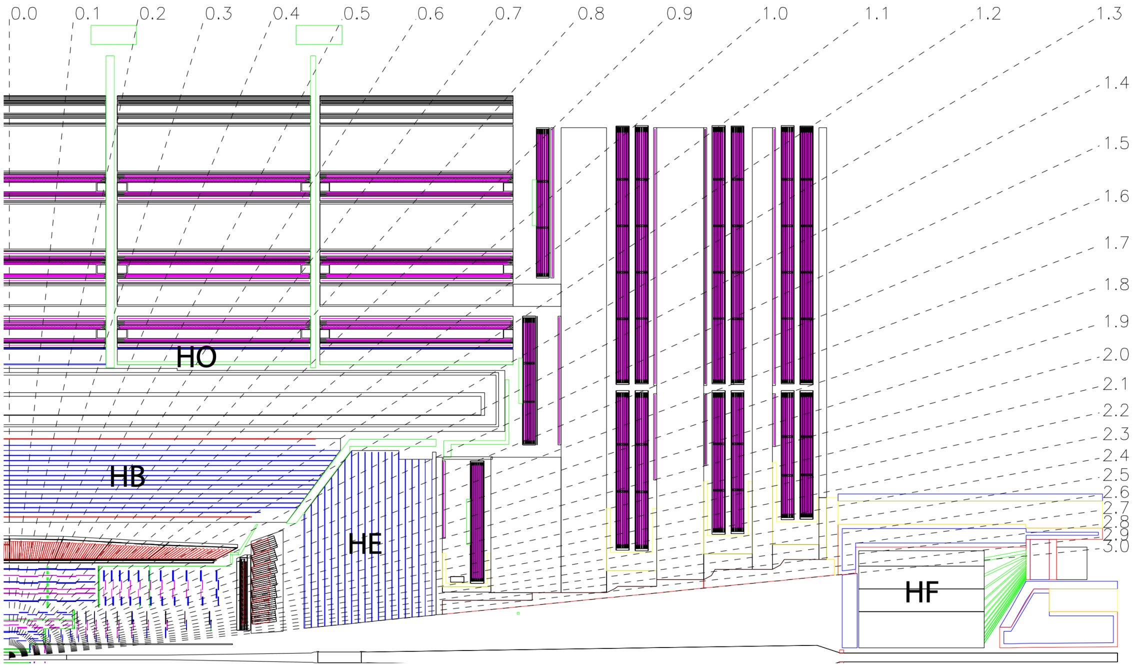

Figure 4.8: Schematic representation of one quadrant of the HCAL detector. The dotted lines indicate different values of η. Image from Ref. [140].

4.2.4 Solenoid magnet

The trajectory of charged particles bends in the presence of a magnetic field, enabling the determination of their momentum from the curvature of the trajectory. For this reason, the CMS detector employs a solenoid magnet [155] generating a magnetic field of 3.8 T. The magnet measures 12.5 m in length and 6.3 m in diameter, making it the largest solenoid ever constructed. The superconducting coil is composed of niobium-titanium (NbTi) and is maintained at a temperature of 4.7 K using a cryogenic system operating with liquid helium. Surrounding the coil is a massive steel structure that serves as the return path for the magnetic flux. This return yoke is the heaviest component of the CMS detector and provides mechanical support for the muon detectors. Additionally, it helps suppress hadronic particles that escape the calorimeters, thereby improving the quality of the muon signals.

4.2.5 Muon system

The muon system is the outermost component of the CMS detector [156]. Muons traverse all the components of CMS without being stopped, and their trajectories are

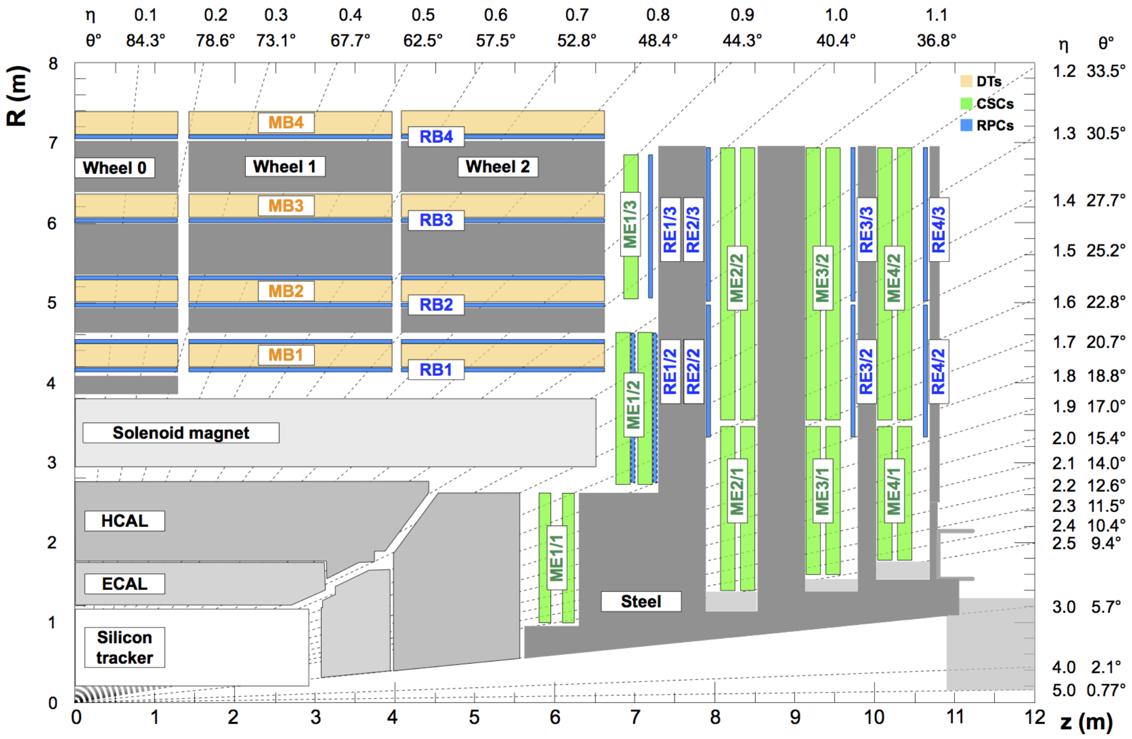

Figure 4.9: Schematic representation of one quadrant of the CMS detector. The locations of the various muon detectors are shown in different colours, while the steel flux-return disks are represented by the dark areas. Image from Ref. [157].

recorded both in the tracking system and in the muon system, allowing for a precise reconstruction of their kinematic properties.

A schematic representation of the muon system is shown in Figure 4.9. The muon system consists of three different type of detectors. Drift tubes (DT) are used in the barrel region, while cathode strip chambers (CSC) are employed in the endcap regions. Resistive plate chambers (RPC), which provide fast timing information for triggering, are installed in both barrel and endcaps. All three detector types operate within the magnetic field produced by the solenoid. However, since the muon system is located outside the solenoid, the direction of the magnetic field is reversed compared to the inner detector components, causing the particle trajectories to bend oppositely. In this outer region, the magnetic field is also weaker, with a typical strength of about 2 T. The muon system is able to reconstruct and identify muons with an efficiency greater than 95%, with a misidentification rate below 1% [157]. The momentum resolution of muons, when combining the information from both the muon and tracking systems, is about 1% in the barrel and 3% in the endcaps for muons with $p_{\mathrm{T}} < 100$ GeV, and approximately 10% for muons with p_{T} in the TeV range [157].

Chapter 5

Physics object reconstruction

The LHC delivers pp collisions with a bunch spacing of 25 ns, resulting in a nominal collision rate of 40 MHz. However, the CMS data acquisition system can't record events at such a high rate. Given that the average offline event size is approximately 1 MB, recording all collisions would correspond to a data stream of around 40 TB/s. To reduce the event rate while preserving interesting events, CMS employs a trigger system, which is described in Section 5.1. Events selected by the trigger system are subsequently reconstructed using information collected from the various CMS subdetectors. The resulting physics objects are then used in offline analyses to perform physics analyses. Section 5.2 presents the methods used to reconstruct the different physics objects, while Section 5.3 details the procedure used to derive electrons and photons corrections necessary for an accurate description of these objects.

5.1 Trigger system

The CMS trigger system is a two-tiered system [158]. The Level-1 (L1) trigger is hardware-based and must make decisions within 1 μs. For this reason, it doesn't use the full detector information, but relies on combined data from the calorimeters and the muon system. Nonetheless, the L1 trigger reduces the output rate from 40 MHz to about 100 kHz. The output rate is further reduced by the high level trigger (HLT), a software based system that has access to the complete readout of all CMS detector components. Therefore, it performs more complex event reconstruction, with performance close to that of offline analyses. The HLT reduces the event rate to approximately 1 kHZ, corresponding to a data stream of about 1 GB/s. The selected events are categorised into different datasets based on the objects identified by the

HLT and stored at the CERN Tier-0 computing centre. A first reconstruction step is then performed to convert the raw detector information into physics objects. The reconstructed datasets are transferred to Tier-1 centres, which are located in the major CMS collaborating countries. There, the data are further calibrated and reduced in size before being distributed to the Tier-2 centres, typically hosted by universities and other CMS institutes. These datasets can then be accessed by CMS analysts worldwide.

5.2 Objects reconstruction

The physics objects are identified and reconstructed by leveraging the combined information from the various CMS sub-detectors using the Particle Flow (PF) algorithm [159]. This algorithm reconstructs tracks from hits in the tracking and muon systems, and clusters from energy deposits in the calorimeters. It then links tracks and energy clusters to build physics objects corresponding to different SM particles.

5.2.1 Tracks and vertices

Tracks reconstruction in CMS relies on hits measured in the PIXEL and silicon strip detectors. These hits are combined using the combinatorial track finder (CTF) algorithm, which is based on Kalman filtering [147, 160]. The CTF algorithm runs iteratively, starting with the reconstruction of high-p_T tracks originating near the interaction point. In each iteration, a set of starting seeds is identified and a trajectory is extrapolated from each seed. All hits along a trajectory are used to perform a fit and estimate the particle's origin, direction, and transverse momentum. In successive iterations, the seeding requirements are relaxed to target low-p_T and more displaced tracks. After each iteration, tracks that pass the quality criteria are retained, and their associated hits are masked for the next iterations. The quality criteria become more stringent in later iterations to compensate for the looser seeding and reduce the number of fake tracks.

The reconstructed tracks are used to identify the primary vertices (PVs) of the collision. This is achieved using a deterministic annealing algorithm [147, 161], which identify PVs with a position resolution of approximately 20 μm and an efficiency close to 100%. Multiple PVs are typically reconstructed due to the presence of several pp collisions occurring in the same bunch crossing. In physics analyses, the PV is defined as the one with the largest sum of p_T^2 of the associated physics objects (jets and $p_{\mathrm{T}}^{\mathrm{miss}}$), and is selected after the reconstruction of all objects in the event. The remaining vertices are attributed to pileup (PU) interactions and are generally not analysed.

5.2.2 Muons

The muon reconstruction relies on hits recorded by the tracking and muon systems [157]. Three types of reconstructed muon candidates are defined: *standalone muons*, *tracker muons*, and *global muons*. *Standalone muon* tracks are reconstructed combining hits from the DT, CSC, and RPC. If a *standalone muon* can be matched to a track in the inner tracker, it is promoted to a *global muon*. *Tracker muons* are reconstructed starting from tracks reconstructed in the tracking system, which are then extrapolated to the muon system. If the track matches with at least one hit from the muon system, the candidate is considered a *tracker muon*. High p_{T} muons are generally reconstructed as *global muons*, as they leave more hits in the muon system, while low p_{T} muons ($p_{\mathrm{T}} < 10$ GeV) are usually reconstructed as *tracker muons*. If a *tracker muon* and a *global muon* share the same track they are merged. In such cases, the reconstruction efficiency is approximately 99% [157].

5.2.3 Electrons and photons

Electrons and photons are primarily reconstructed based on energy deposits measured in the ECAL [152]. Electrons can emit bremsstrahlung photons as they traverse the detector material, these photons can then convert into electron-positron pairs. For this reason, multiple energy clusters can be associated with a single electron, whereas photons typically produce more collimated electromagnetic showers. The electron and photon reconstruction begins from a *seed cluster*, defined as the ECAL cluster with the largest energy deposit. Additional ECAL clusters within a given region around the seed are combined to form a supercluster (SC). Electrons form larger SCs than photons due to the wider spread of their electromagnetic shower. The compatibility between all available tracks and the SC is tested, and the matching is performed using the Gaussian Sum Filter (GSF) algorithm [162]. The SCs with matched tracks are classified as electrons, while unmatched SCs are considered photons. Electrons can also be reconstructed using a tracker-seeded algorithm, which performs better for low-p_{T} electrons. In this case, the reconstruction is initiated from a track, whose trajectory is refitted using the GSF algorithm and matched to an ECAL SC. If the

p_{T} measured from the track is consistent with the energy of the matched SC, the candidate is classified as electron.

5.2.4 Lepton selection

The analysis presented in this thesis targets final states with three or more leptons; therefore, it is particularly sensitive to fake leptons. Specifically, reconstructed leptons can be classified as:

- Prompt leptons, that are genuine isolated leptons produced in the decay of on-shell W, Z, H, or τ decays.
- Fake leptons: nonprompt leptons coming from b-hadron decays or light-flavour jets, misidentified photons, or leptons from photon conversion.

The presence of events with fake leptons represents a source of reducible background in the region of interest for the analysis. For this reason, it is important to estimate this background directly from data to have the best possible description of this contribution, while at the same time employing a prompt lepton identification method to reduce the number of fake leptons entering the final selection. The estimation of the fake lepton background is discussed in details in Chapter 9. Regarding the second point, multivariate analysis (MVA) discriminants [152, 163] are used to increase the rejection of fake leptons. During Run 2, the TOP MVA ID [164] is used. This method consists of a Boosted Decision Tree (BDT) trained separately for 2016, 2017, and 2018, and for electrons and muons. For Run 3, the PROMPT MVA ID [165] is adopted, which uses the same ML model as in Run 2, but with a retraining that improves the performance. Before applying the identification algorithms, leptons are required to pass the same selection criteria used to define the training samples for the MVA discriminants. The details of this preselection and the cut on the identification algorithm score are provided in Table 5.1.

The variables used for the lepton preselection include a combination of kinematic, low- and high-level quantities related to the tracking system, calorimeters and muon system:

- p_{T}: Define the phase space region in which the lepton identification algorithm will be applied.
- $|\eta|$: Restricts leptons to the acceptance of the CMS barrel and endcap regions.
- $|d_{xy}|$ and $|d_z|$: Distances from the PV in the transverse and longitudinal directions.
- `lost hits`: Number of lost hits in the tracker.

Table 5.1: Summary of lepton selection.

	Run2		Run3	
	Electrons	Muons	Electrons	Muons
p_{T}	> 10 GeV	> 10 GeV	> 15 GeV	> 15 GeV
$\lvert\eta\rvert$	< 2.5	< 2.4	< 2.5	< 2.4
$\lvert d_{xy}\rvert$	< 0.05 cm	< 0.05 cm	< 0.05 cm	< 0.05 cm
$\lvert d_z\rvert$	< 0.1 cm	< 0.1 cm	< 0.1 cm	< 0.1 cm
`lost hits`	< 2	–	< 2	–
`sip3d`	< 8 cm	< 8 cm	< 8 cm	< 8 cm
$\sigma_{i\eta i\eta}$	$< 0.011/0.030$[1]	–	$< 0.011/0.030$[1]	–
H/E	< 0.10	–	< 0.10	–
$1/E - 1/p$	> -0.04	–	> -0.04	–
`miniPFRelIso_all`	< 0.4	< 0.4	< 0.4	< 0.4
`isPFcand`	True	True	True	True
`Global muon`	–	True	–	True
`Conversion rejection`	True	–	True	–
MUON CUT-BASED ID	–	Medium	–	Medium
TOPLEPTON MVA ID	> 0.81	> 0.64	–	–
PROMPT MVA ID	–	–	> 0.90	> 0.64

[1] Barrel/endcap

- `sip3d`: 3D impact parameter significance relative to the PV.
- $\sigma_{i\eta i\eta}$: ECAL crystal-based shower shape in the η direction.
- H/E: Ratio of hadronic to electromagnetic energy.
- $1/E - 1/p$: Compares the ECAL supercluster energy to the tracker momentum; useful to verify the consistency between ECAL and tracker measurements for electrons.
- `miniPFRelIso_all`: Lepton isolation based on the scalar p_{T} sum of charged particles, neutral hadrons, and photons within a cone of size R around the lepton,

  $$R = \begin{cases} 0.05 & \text{if } p_T > 200\,\text{GeV}, \\ 10\text{ GeV}/p_T & \text{if } 50 < p_T \leq 200\,\text{GeV}, \\ 0.20 & \text{if } p_T \leq 50\,\text{GeV}. \end{cases} \tag{5.1}$$

  Only charged particles originating from the PV are considered in the sum to reduce pileup effects. The isolation variable is defined as

  $$I_l = \sum_{charged} p_{\mathrm{T}} + \max\left(0, \sum_{neutrals} p_{\mathrm{T}} - \rho\mathcal{A}\left(\frac{\mathcal{R}}{0.3}\right)^2\right) , \tag{5.2}$$

  where ρ is the energy density of the neutral particles reconstructed within the geometric acceptance of the tracker, and $\mathcal{A}$ is the effective area. These variables are used to correct for residual pileup corrections in the neutral component of the isolation.
- `isPFcand`: Ensures that the lepton is a PF candidate.
- `Global muon`: Confirms that the muon is identified in both the tracker and muon system.
- `Conversion rejection`: Suppresses electrons from photon conversions.
- MUON CUT-BASED ID: Medium working point (WP) of the official CMS cut-based ID for muons.

The variables used in the preselection are also employed as input features in the training of the lepton ID algorithms. In addition, variables related to the closest jet, such as the p_{T} ratio between lepton and closest jet or the closest jet's b-tagging score, are included. In the training of the electron identification algorithms, a boolean indicating whether the lepton passes the central CMS MVA ID with 90% efficiency is also used.

The tight (medium) WP of the algorithms is chosen by requiring the BDT score to be > 0.81 (0.64) for electrons (muons) for the Top MVA ID and > 0.90 (0.64) for electrons (muons) for the Prompt MVA ID. The chosen WP for the lepton identification algorithms for Run 2 data have efficiencies of 87% and 92% for electrons and muons, respectively. A tighter WP is used for Run 3 data, resulting in lower efficiencies of 60% and 84% for electrons and muons, but with a threefold improvement in the rejection of fake leptons.

Two main changes are introduced with respect to the previous analysis [108]: lower transverse momentum requirements, and tighter WPs for the electron ID algorithms. This configuration was found to give the highest signal significance to tWZ, measured as $\frac{S}{\sqrt{S+B}}$, among several tested. The improvement is likely due to the increased signal yield achieved lowering the transverse momentum requirements, and to the enhanced rejection of fake leptons due to the tighter ID WPs.

Corrections accounting for possible discrepancies between data and simulation in the input variables of the electrons and muons reconstruction and identification algorithms are applied as functions of the reconstructed particle's p_{T} and η. The methods used to derive these corrections are described in 5.3.

5.2.5 Jets

Neutral and charged hadrons are also reconstructed using the PF algorithm by combining information from energy deposits in calorimeters and tracks in the tracking system. The reconstructed particles are then clustered to form jets, which are the result of the hadronisation of partons and are used to study the properties of quarks and gluons. At CMS, jets are reconstructed by clustering PF particles using the anti-k_T jet algorithm [166], implemented via the FastJet package [167]. The anti-k_T algorithm is infrared and collinear safe, meaning it is insensitive to soft or collinear gluon emissions. It defines a distance measure between particles i and j as

$$d_{ij} = \min\left(\frac{1}{p_{T,i}^2}, \frac{1}{p_{T,j}^2}\right)\frac{\Delta R_{ij}^2}{R^2}, \tag{5.3}$$

where R is the radius parameter controlling the size of the resulting jet, and $\Delta R_{ij}^2 = (y_i - y_j)^2 + (\phi_i - \phi_j)^2$. Rapidity is used instead of pseudorapidity because jets can be significantly massive, and the ultra-relativistic approximation does not always apply. A distance between each particle i and the beam is also defined as $d_{iB} = 1/p_{T,i}^2$. The algorithm proceeds iteratively. For each particle i, the smallest distance among all d_{ij} and d_{iB} is identified. If d_{ij} is smaller, particles i and j are clustered into a new *pseudo-jet*, and the procedure is repeated including this *pseudo-jet* instead of i and j. If d_{iB} is smaller, then particle i (or the current *pseudo-jet*) is a final jet and is removed from the list. This process continues until all particles have been clustered into jets. The jet radius parameter used in the measurement presented in this thesis is R=0.4. Jets are calibrated through a series of corrections to data, simulation, or both, to account for various effects [168]. To mitigate pileup contamination, jets are reconstructed excluding charged PF candidates not associated with the primary vertex (PV), using the charged hadron subtraction (CHS) algorithm [169]. The pileup per particle identification (PUPPI) algorithm [170, 171] is instead used to account for neutral pileup particles. The PUPPI algorithm is applied only to jets reconstructed during the Run 3 period; therefore, the contribution of neutral pileup particles in Run 2 is accounted for through an additional set of dedicated corrections. In addition to pileup mitigation, jet energy response corrections are applied to both data and simulation as a function of jet p_{T} and η, to correct for differences between the reconstructed and generated jet momenta. Residual corrections are then applied to jets in data to account for remaining mismodelling in the jet response between data and simulation, as evaluated in dijet, multijet, and Z+jets events. Finally, the jet p_{T} resolution in simulation is corrected as function of jet p_{T} and η to match that observed in data.

Jets enter in the final event selection of the analysis presented in this thesis if they satisfy the tight WP of the particle flow jet ID algorithm [172]. This requirement helps reduce the number of jets originating from reconstruction failures, detector noise, or misreconstructed leptons. Additionally, jets reconstructed during the Run 2 period with $p_{\mathrm{T}} < 50$ GeV must also satisfy a dedicated jet pileup identification algorithm [173] to further suppress jets arising from pileup interactions. Finally, only jets with $p_{\mathrm{T}} > 25$ GeV and $|\eta| < 2.5$ are accepted in the final selection, and they are cross-cleaned from leptons using a cone of $\Delta R = 0.4$.

In 2016 and 2017 data, due to problems in early L1 electron/photon triggers, uninteresting events were recorded while the subsequent interesting ones were rejected. Since this effect is present only in data, simulation events are reweighted to simulate this effect. Another problem occurred in late runs of 2018 data taking, when the power supply of two HCAL modules was damaged. For this reason, events containing jets in the affected regions are vetoed.

In Run 3, some regions of the calorimeters are observed to produce anomalously high or low jet rates. To avoid a possible bias, events with a least one *loose jet* in the affected regions are vetoed both in data and simulation. A *loose jet* is a jet that satisfies the following selection

- $p_T > 15$ GeV,
- Tight WP of the particle flow jet ID algorithm,
- Electromagnetic energy fraction (charged + neutral) < 0.9, and
- No overlap with PF muon in a cone with $\Delta R < 0.2$.

Corrected PF missing transverse momentum is used throughout the analysis. For each variation of the jet corrections, the p_{T} and η of the missing transverse momentum vector is recomputed.

5.2.6 Heavy flavour jets

Jets origination from b and c quarks are referred to as heavy-flavour jets. In particular, b jets are highly relevant in top quark physics, as the top quark decays almost exclusively into a b quark and a W boson. The identification of b jets relies on the relatively long lifetime of b hadrons, which typically travel a few millimetres in the tracking system before decaying. Therefore, they produce a secondary vertex which can be identified from the tracks of charged decay products. This information, along with other kinematic properties, is used as input to machine learning (ML) algorithms designed to identify b jets.

In the analysis presented in this thesis, jets originating from b quarks are identified using the DeepJet algorithm [174–176] during the Run 2 period, while a transformer-based algorithm [177–179] with improved performance [180,181] is employed in Run 3. Jets are tagged as b jets if they satisfy a requirement on the algorithm score corresponding to an identification efficiency of approximately 80% for true b jets, with misidentification rates of about 14% for charm jets and 1% for light-flavour and gluon jets. Dedicated corrections are applied as a function of the jet p_{T} and η to account for possible discrepancies between data and simulation introduced by the application of the algorithms.

5.3 Electron corrections

Muons, electrons, and photons used in CMS analysis are selected using dedicated reconstruction and identification algorithms. These algorithms are developed using accurate simulations of the detector response to these particles. However, small discrepancies between simulation and data can be present and must be corrected to avoid introducing biases in the comparison between data and theoretical predictions.

For this reason, correction factors are derived by comparing data and simulation in well-understood physics processes. In particular, the *tag-and-probe* method is widely used [152]. It exploits known resonances decaying into two leptons, as the Z boson or the J/Ψ meson, to extract information about potential mismodelling in the simulation. In this thesis, the results obtained using this method to compute corrections for the electron identification (ID) algorithms are presented.

In the *tag-and-probe* method, one of the two electrons from the decay of the Z boson is considered as the *tag* and is selected using tight criteria to ensure high purity, while the other electron in the event is considered as the *probe* and is used to measure the corrections. *Tag* electrons are selected using single-electron HLT paths that require $p_{\mathrm{T}} > 30$ GeV. An additional offline selection is applied, requiring $p_{\mathrm{T}} > 33$ GeV, $|\eta| < 2.17$, and passing the tight WP of the cut-based ID. The tight WP corresponds to the most stringent configuration of the cut-based ID, which consists of optimised requirements on variables that effectively discriminate against fake electrons, such as misidentified jets. The *probe* is selected by requiring opposite charge with respect to the *tag* and a few basic kinematic cuts that define the phase space for the measurement. In events where more than one *probe* is present, the one with the highest p_{T} is selected. Since no dedicated selection is applied to identify the *probe* electron, it represents an unbiased object, allowing the measurement of the efficiency of a given selection. The *probe* electrons are used to measure the efficiency of four WPs of the cut-based ID, as well as the 80% and 90% signal efficiency WPs of two MVA IDs. These MVA IDs are based on BDT algorithms trained using the cut-based ID variables along with additional features to improve rejection of fake electrons. Two versions of the algorithm are available: one includes variables related to the electron isolation (MVA-Iso), such as the ΔR to nearby particles, while the other doesn't (MVA-noIso).

The electron ID corrections are estimated by computing the ratio of the ID efficiencies measured in data and simulation in different bins of p_{T} and η. The p_{T} bins account for differences in the *probe* kinematics and background composition, which is more significant in the lowest p_{T} bin ([10, 20] GeV). The η bins account for differences in the detector conditions. In particular, the corrections are usually measured in the inner barrel ($|\eta| < 0.8$), outer barrel ($0.8 < |\eta| < 1.44$), and the endcaps, using two bins ($|\eta| = [1.57,\ 2.00]$ and $|\eta| = [2.00,\ 2.50]$). The transition region between barrel and endcap ($|\eta| = [1.44,\ 1.57]$) is typically excluded.

The efficiency of an ID for a specific bin is defined as

$$\epsilon = \frac{N_{\text{pass}}}{N_{\text{pass}} + N_{\text{fail}}}, \tag{5.4}$$

where ϵ is the efficiency of the ID and N_{pass} (N_{fail}) is the number of probes that pass (fail) the ID requirement in the considered bin.

To compute ID efficiencies, it is crucial to estimate the number of fake electrons considered as *probes*, in order to include only genuine electrons in the efficiency computation. This is straightforward in simulation, where reconstructed *probes* can be matched to gen-level electrons. In data, the background contribution is obtained by fitting the invariant mass distributions of the (tag, passing probe) and the (tag, failing probe) pairs. The fit model includes signal and background components to distinguish electrons from fakes and is performed in the mass range [60, 120] GeV, which includes the Z boson peak as well as a significant number of background events. The signal model is defined as a convolution of templates measured on gen-matched electrons in simulation with a function that accounts for residual resolution differences between data and simulation. Typically, either a Gaussian function or a Crystal Ball function with an exponential tail is used as the resolution function. The latter is defined as

$$f(x) = \begin{cases} \exp\left(-\frac{1}{2}\left(\frac{x-\mu}{\sigma_2}\right)^2\right) & \text{for } \frac{x-\mu}{\sigma} > 0, \\ \exp\left(-\frac{1}{2}\left(\frac{x-\mu}{\sigma}\right)^2\right) & \text{for } -\alpha \leq \frac{x-\mu}{\sigma} \leq 0, \\ \exp\left(-\frac{1}{2}\alpha^2 + n\left(\frac{x-\mu}{\sigma} + \alpha\right)\right) & \text{for } \frac{x-\mu}{\sigma} < -\alpha, \end{cases} \tag{5.5}$$

where x is the observable, and μ is the peak position of the distribution. The parameters σ and σ_2 represent the standard deviations of the Gaussian core on the left and right side of the peak, respectively. The transition between the Gaussian core and the exponential tail on the left is controlled by α, expressed in units of σ, while the steepness of the exponential tail is governed by the parameter n. This function is commonly used to model resolution effects with asymmetric tails, such as those arising from energy losses via bremsstrahlung or from detector and reconstruction inefficiencies.

The background component of the fit model is typically described by an exponential function, however the kinematic selection distorts the di-electron invariant mass making it better modelled by an exponential function multiplied by an error function,

$$f(x) = \text{erf}[(a-x)b]\exp[-(x-c)d], \tag{5.6}$$

where a and c are in GeV and b and d are in GeV^{-1}.

The nominal signal+background model is defined by the convolution of the templates measured in simulation with a Gaussian function for the signal and an exponential function multiplied by an error function for the background. Figure 5.1 shows the fit using the nominal signal+background model for the pass and failing probe distributions in the bin p_{T}=[20, 35] GeV and η=[0.00, 0.80].

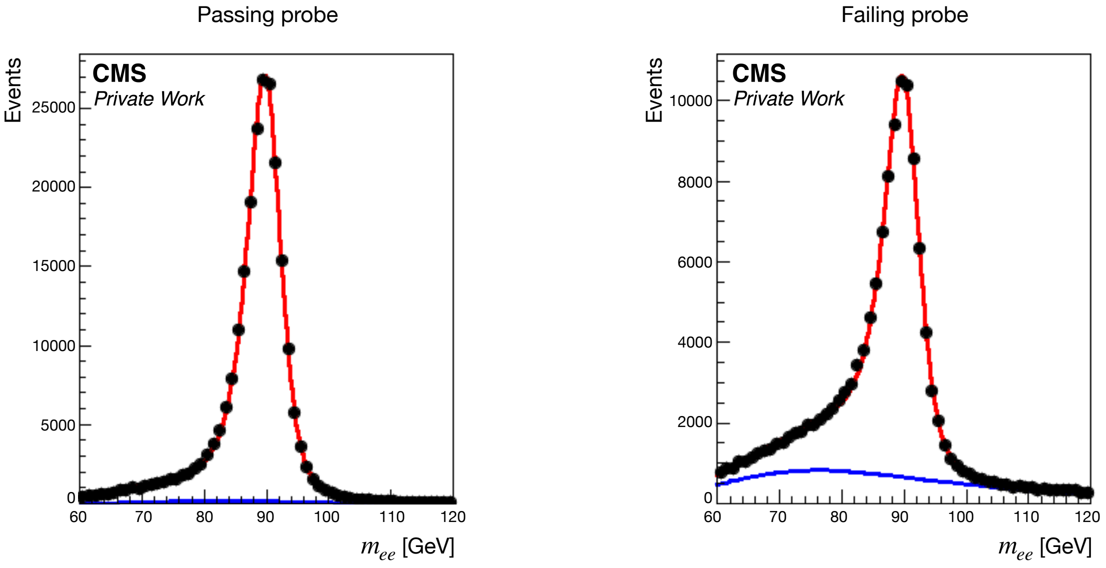

Figure 5.1: Fit of the nominal signal+background model to data for the passing (left) and failing probe (right) m_{ee} distribution. The black marker represents the data points, the blue curve shows the background function, and the red line corresponds to the signal+background model.

Alternative models are considered to estimate a systematic uncertainty on the fit model. In particular, the alternative signal model is defined using a Crystal Ball function with exponential tail as the resolution function, while the alternative background model uses a simple exponential function instead of the exponential function multiplied by an error function. Additional systematic uncertainties are included by considering different orders in QCD for the simulation and different selection criteria for the *tag*, although these have a minor impact on the overall uncertainty. The leading source of uncertainty is typically the alternative signal model in the low p_{T} region ($p_{\mathrm{T}} < 100$ GeV), while at higher p_{T} the dominant contribution comes from the statistical uncertainty.

The electron ID corrections are computed separately for each data-taking periods to account for possible differences in detector conditions. During the 2022 and 2023 data-taking periods, two different issues affected the detector performance [182]. In particular, during 2022, approximately 7% of the channels on the positive side of the ECAL endcap (EE+) were affected by a power cooling issue. As a consequence, a deficit in the number of reconstructed electrons and photons was observed in the region corresponding to the affected channels. To model this inefficiency, a dedicated simulation and two sets of corrections (preEE+ and postEE+) were derived.

Figure 5.2 shows the efficiencies and corrections for the 2022 preEE+ data-taking period using the 80% signal efficiency WP of the MVA-Iso ID as an example.

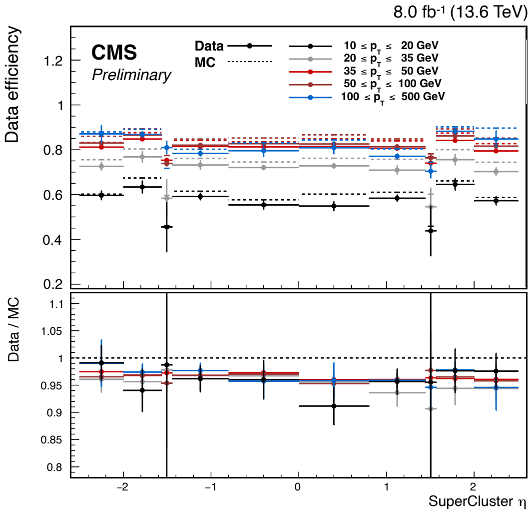

Figure 5.2: Electron identification efficiency (upper panels) and data-to-simulation efficiency ratios (lower panels) for the 80% signal efficiency MVA-Iso ID in five p_T ranges as a function of η_{SC}. The data are shown with solid markers, while the simulation is represented by dashed lines. Data collected during the first part of the year 2022 and preEE+ MC are shown. Published in [182].

The corrections are close to unity in all bins. Uncertainties are larger at low p_T due to increased background contamination, which leads to larger modelling uncertainty. At high p_T, uncertainties are also larger, but in this case primarily due to limited statistical precision.

During the 2023 data-taking year, the Quartz-controlled PLL circuit connected to 28 modules of the Barrel Pixel (BPIX) detector in layers 3 and 4 had to be excluded from a portion of the data taking. A dedicated simulation was produced to account for this issue, and two sets of corrections (preBPIX and postBPIX) were derived. The affected region corresponds to $-1.5 < \eta_{SC} < 0$ and $-1.2 < \phi < -0.8$, and therefore additional dedicated bins were added to capture the impact of this inefficiency.

Figure 5.3 shows the ID efficiencies and corrections for the 2023 postBPIX data-taking period using the 80% signal efficiency WP of the MVA-Iso ID as an example.

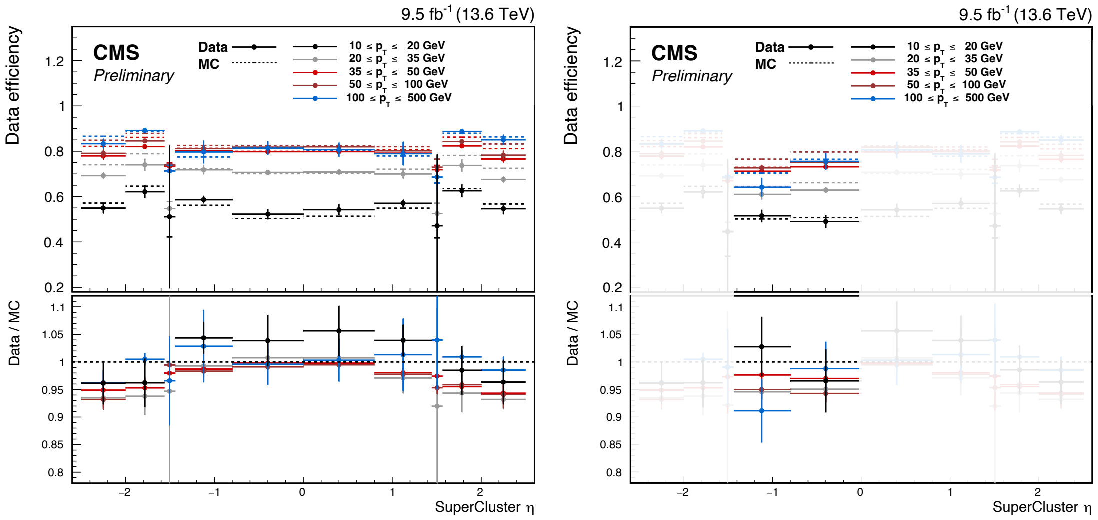

Figure 5.3: Electron identification efficiency (upper panels) and data-to-simulation efficiency ratios (lower panels) for the 80% signal efficiency MVA-Iso ID in five p_T ranges as a function of η_SC. The data are shown with solid markers, while the simulation is represented by dashed lines. Data collected during the year 2023 and postBPIX MC for the BPIX issue (non-)affected region are shown on the (left) right. Published in [182].

The corrections are close to unity in all the bins, with slightly lower values observed in the region affected by the BPIX issue. As in 2022, larger uncertainties are observed in the lowest and highest p_T ranges.

Chapter 6

Event selection and categorization

The search for rare processes is a pillar in the quest for new physics at the LHC, as it serves both to test the validity of the SM and to probe unexplored regions where new phenomena might emerge. As discussed in Section 1.3.3 and 2.2.1, the tWZ process is very interesting in this context, as it provides direct access to the EW couplings of the top quark, allowing for precise tests of the SM and studies for potential BSM effects encoded via modified interaction in the SMEFT framework.

This process is extremely challenging due to its small predicted cross section, namely 136^{+9}_{-8} fb at $\sqrt{s} = 13\,\text{TeV}$ and 147.8^{+10}_{-9} fb at $\sqrt{s} = 13.6\,\text{TeV}$ [65, 66]. Because of its rarity, experimentally identifying the tWZ process requires dedicated strategies to increase the signal to background ratio. For this purpose, multi-lepton selections and b-tagging information are exploited. Nonetheless, tWZ events make up only a very small fraction of the total selected events. Many other processes can mimic the signal, such as multi boson production or events with fake leptons, in addition to the $\mathrm{t\bar{t}Z}$ process, which represents the dominant background. For this reason, ML algorithms are used to improve the separation between signal and background.

The first analysis targeting the tWZ process was published by CMS in 2024 [108], reporting evidence for this process. It was performed using data collected at $\sqrt{s} = 13\,\text{TeV}$ during the Run 2 period and measured an excess of two s.d. with respect to theoretical predictions. A similar excess was also observed in the inclusive cross section measurement of $\mathrm{t\bar{t}Z}$ +tWZ published by CMS in 2025 [103], which used the same dataset.

This chapter introduces a new CMS measurement of the tWZ inclusive cross section [109], which includes additional data collected at $\sqrt{s} = 13.6\,\text{TeV}$ in 2022 and 2023, reaching a total integrated luminosity of 200 fb^{-1}. In Section 6.1, details on the data and the Monte Carlo simulated samples are reported, while Section 6.2 outlines the event selection and the definition of signal and control regions. The functioning and usage of the ML algorithms used in the analysis are described in Chapter 7, followed by a discussion on the systematic uncertainties in Chapter 8. Chapter 9 describes the methodology employed for the fake lepton background estimation, and the final results are presented and discussed in Chapter 10.

6.1 Data and simulated samples

The measurement presented in this thesis analyses the full CMS dataset collected during Run 2, corresponding to an integrated luminosity of 138 fb^{-1}. In addition, data collected in Run 3 during 2022 and 2023 are included, bringing the integrated luminosity to a total of 200 fb^{-1}.

Events are selected only if a combination of HLT requirements are fulfilled. Since the analysis targets multi-lepton final states, three-lepton triggers are employed in combination with double- and single-lepton triggers in order to achieve a trigger efficiency close to 100% for events passing the offline selection. A trigger logic is implemented in order to avoid double counting of events that fire more than one trigger.

The simulation of the hard scattering is performed using different MC event generators interfaced with PYTHIA8 [127] to model the PS and the hadronisation. The MLM matching [64] scheme is used for samples generated at LO accuracy in QCD, while FXFX merging [65] is applied for samples simulated at NLO. The PDF set used is NNPDF 3.1 [60] at NNLO in the 5FS, and both the factorisation and renormalisation scales are evaluated dynamically. The underlying event is modelled using the CP5 tuning parameters [183]. Minimum bias interactions, corresponding to a pp inelastic cross section of 69.2 mb, are simulated using PYTHIA8 [127] and added to the hard scattering events to emulate the effect of PU. The simulated PU distributions are then reweighted to match that observed in data.

6.1.1 Signal simulation

The generation of the tWZ process is performed at NLO accuracy in QCD in the 5FS, using MADGRAPH5_aMC@NLO [66]. The decays of the top quark and of the EW bosons are handled with MADSPIN [184], in order to preserve the spin correlations.

The overlap removal procedure, detailed in Section 1.3.3, is performed using the MADSTR plugin [128]. Specifically, the DR1 subtraction scheme is used to simulate the nominal sample, while modelling uncertainties are evaluated by comparing with samples generated using the DR2 subtraction scheme. The DS scheme is not considered, as it yields results that lie between the two diagram removal schemes.

The MadStr plugin currently support only 1 → 2 decays, leading to two important consequences:

- The overlap with the $t\bar{t}$ process is not subtracted, as this arises from a 1 → 3 decay ($t \to bW^+Z$ or $\bar{t} \to \bar{b}W^-Z$). However, in this region of $t\bar{t}$ phase space, the Z boson is typically off-shell.
- It is not possible to generate the $tW\ell\ell$ final state directly, but only tWZ when using the MadStr plugin. The impact of diagrams that do not involve an on-shell $Z \to \ell\ell$ transition is relevant only far from the Z boson peak. Nonetheless, this approximation has been verified comparing the cross section as a function of the di-lepton invariant mass for the $tW\ell\ell$ and the tWZ processes (Figure 6.1). The $tW\ell\ell$ simulation is obtained by manually removing the diagrams that overlap with the $t\bar{t}Z$ process, instead of using the MadStr plugin. Within the Z boson mass window used in the analysis, the normalisation difference is found to be below 1%.

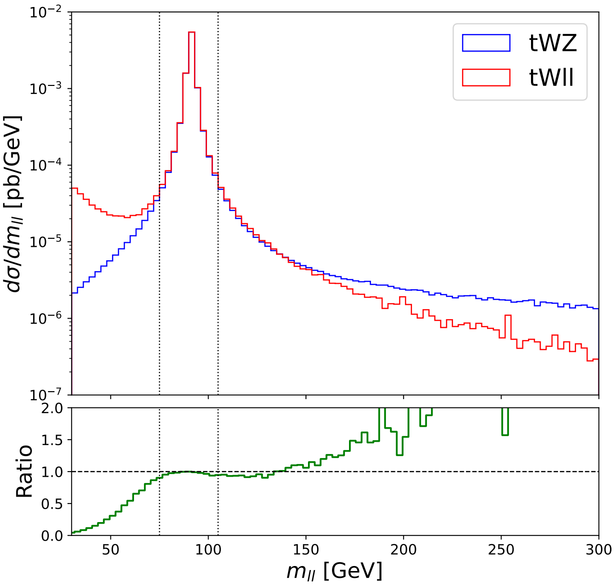

Figure 6.1: Generator level distribution of the di-lepton invariant mass for tWZ (blue) and $tW\ell\ell$ (red). The black dotted lines indicate the Z boson mass window used in the analysis.

Three signal samples are generated based on the decay modes of the W bosons. Two samples correspond to the semi-leptonic final states, where either the W boson from the top or the second W boson decays leptonically, while the other one decays hadronically. The third sample describes the fully-leptonic final state, in which both W bosons decay leptonically. The Z boson is always decayed into a pair of charged leptons. Table 6.1 shows the cross section used for the different signal samples.

Table 6.1: List of signal samples employed in the analysis.

Process	Cross section [fb] at 13 TeV	Cross section [fb] at 13.6 TeV
tWZ DR1 ($t \to \ell\nu b$ and $W \to q\bar{q}'$)	3.00	3.28
tWZ DR1 ($t \to q\bar{q}'b$ and $W \to \ell\nu$)	3.00	3.28
tWZ DR1 ($t \to \ell\nu b$ and $W \to \ell\nu$)	1.50	1.58
tWZ DR2 ($t \to \ell\nu b$ and $W \to q\bar{q}'$)	Norm. to the DR1 sample	Norm. to the DR1 sample
tWZ DR2 ($t \to q\bar{q}'b$ and $W \to \ell\nu$)	Norm. to the DR1 sample	Norm. to the DR1 sample
tWZ DR2 ($t \to \ell\nu b$ and $W \to \ell\nu$)	Norm. to the DR1 sample	Norm. to the DR1 sample

6.1.2 Background simulation

The background samples used in the analysis are generated with different MC generators. The dominant backgrounds, $t\bar{t}Z$ and tZq, are generated with MadGraph5_aMC@NLO [66], while WZ production is simulated using POWHEG [67, 68, 185–187]. The $t\bar{t}Z$ background cross section is scaled to account for aN^3LO QCD and NLO EW corrections [112].

The cross section and the MC event generator used for all the background samples employed in the analysis are reported in Table 6.2.

6.2 Event selection

The main challenge of this analysis is the discrimination of the tWZ signal from the background processes. For this reason, dedicated selections are employed to divide selected events in different signal and control regions according to the number and characteristics of the physics objects in the events. In particular, two signal regions (SRs) and four control regions (CRs) are defined. The SRs target three- and four-lepton final states, depending on whether one or both of the W bosons in the tWZ final state decay leptonically. Two of the 4 CRs are defined to constrain the ZZ and WZ processes, while the remaining two are used to estimate the contribution of the fake leptons, mainly coming from DY and $t\bar{t}$ processes.

Table 6.2: List of background processes considered in the analysis indicating cross section and MC event generator used for the simulation.

Process	Cross section [fb] at 13 TeV	Cross section [fb] at 13.6 TeV	Generator
$\mathrm{t\bar{t}Z}$ (leptonic Z)	105	141	MadGraph5_aMC@NLO
tZq (leptonic Z)	94.2	80.0	MadGraph5_aMC@NLO
$\mathrm{t\bar{t}}$ (dilepton)	88500	97400	POWHEG
$\mathrm{t\bar{t}}$ (lepton + jets)	366000	40300	POWHEG
tW	71700	88000	POWHEG
Drell-Yan + jets	6070000	6350000	MadGraph5_aMC@NLO
Drell-Yan + γ	55500	126000	MadGraph5_aMC@NLO
W+ γ	191000	662000	MadGraph5_aMC@NLO
WW	114000	123000	Pythia8
WZ (leptonic W and Z)	5050	5310	POWHEG
ZZ (both Z leptonic)	1300	1440	POWHEG
VH (H not decaying to $b\bar{b}$)	956	1010	MadGraph5_aMC@NLO
WWW	209	232	MadGraph5_aMC@NLO
WWZ	165	190	MadGraph5_aMC@NLO
WZZ	55.7	60.0	MadGraph5_aMC@NLO
ZZZ	14.0	20.0	MadGraph5_aMC@NLO
$\mathrm{t\bar{t}}\gamma$ (dilepton)	2220	-	MadGraph5_aMC@NLO
$\mathrm{t\bar{t}}\gamma$ (lepton + jets)	7510	-	MadGraph5_aMC@NLO
$\mathrm{t\bar{t}W}$ (leptonic W)	235	250	MadGraph5_aMC@NLO
$\mathrm{t\bar{t}WW}$	7.00	8.20	MadGraph5_aMC@NLO
$\mathrm{t\bar{t}WZ}$	2.45	-	MadGraph5_aMC@NLO
$\mathrm{t\bar{t}ZZ}$	1.39	1.58	MadGraph5_aMC@NLO
$\mathrm{t\bar{t}H}$ (H not decaying to $b\bar{b}$)	215	241	POWHEG
tWγ	191.1	-	MadGraph5_aMC@NLO
tttt	13.4	15.8	MadGraph5_aMC@NLO

6.2.1 Three lepton Signal Region

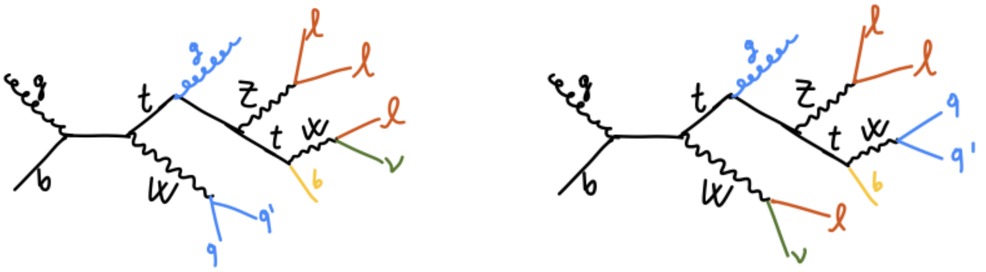

Figure 6.2: Sketch of the tWZ final states in the semi-leptonic case, including the emission of an additional gluon.

The three lepton Signal Region (3ℓ SR) features an event selection that targets the semi-leptonic final state of the signal, sketched in Figure 6.2.

It is characterised by the presence of exactly three leptons in the final state, two of which have same flavour and opposite sign, coming from the Z boson decay. Three or more jets are expected, and at least one of them is b-tagged. The event selection is then the following:

- exactly three leptons,
- two leptons must have same flavour and opposite sign, and their invariant mass must lie inside a 15 GeV window centred around the Z boson mass,
- p_{T} of the (sub)leading lepton must be $> 25(15)$ GeV,
- at least two jets, of which at least one must be b-tagged.

The composition of this region is mostly dominated by the $\mathrm{t\bar{t}Z}$ background with important contributions coming also from the tZq and WZ processes, but it retains a good amount of signal.

In the previous analysis, this region was split into two parts: one with exactly two jets and one with at least 3 jets. In this analysis a single three lepton SR is considered to benefit from the higher statistics for the ML algorithm training.

The distributions of the jet multiplicity, number of b jets, and invariant mass of the di-lepton pair with the closest invariant mass to the mass of the Z boson are shown in Figures 6.3, 6.4, 6.5, and 6.6 for the Run 2 and Run 3 periods, respectively. These distributions are used to showcase the good agreement between data and simulation. Small discrepancies are observed at high jet multiplicity, likely due to less accurate jet modelling from the PS. Comparing Run 2 and Run 3 distributions, it is possible to appreciate the increase of the signal-to-background ratio, or more generally the increase of processes with three prompt leptons and one b jet in the final state. Indeed, the contribution of the non-prompt backgrounds and the WZ process is drastically reduced thanks to the new and improved lepton identification and b-tag algorithms.

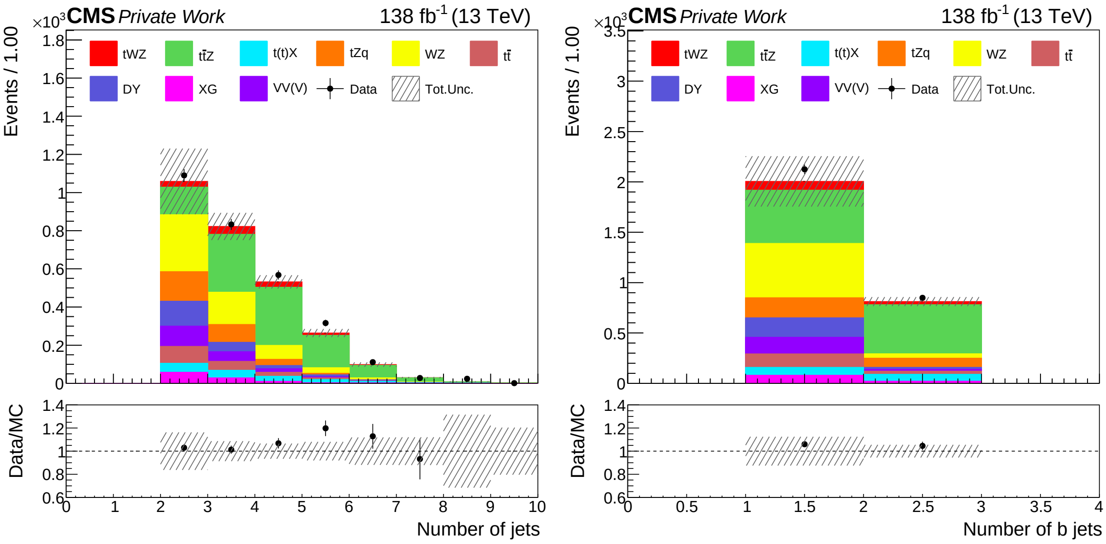

Figure 6.3: Distributions of the jet multiplicity (left) and number of b jets (right) in the 3ℓ SR for the Run 2 period. The black markers represent the data, while the solid stacked histogram shows the MC predictions for the various background processes. The dashed band indicates the total uncertainty. The lower panel displays the ratio between data and simulation.

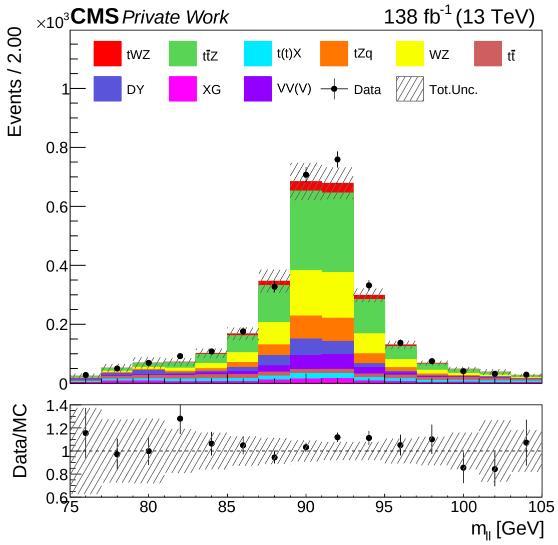

Figure 6.4: Distribution of the invariant mass of the dilepton pair with the closest invariant mass to the mass of the Z in the 3ℓ SR for the Run 2 period. The black markers represent the data, while the solid stacked histogram shows the MC predictions for the various background processes. The dashed band indicates the total uncertainty. The lower panel displays the ratio between data and simulation.

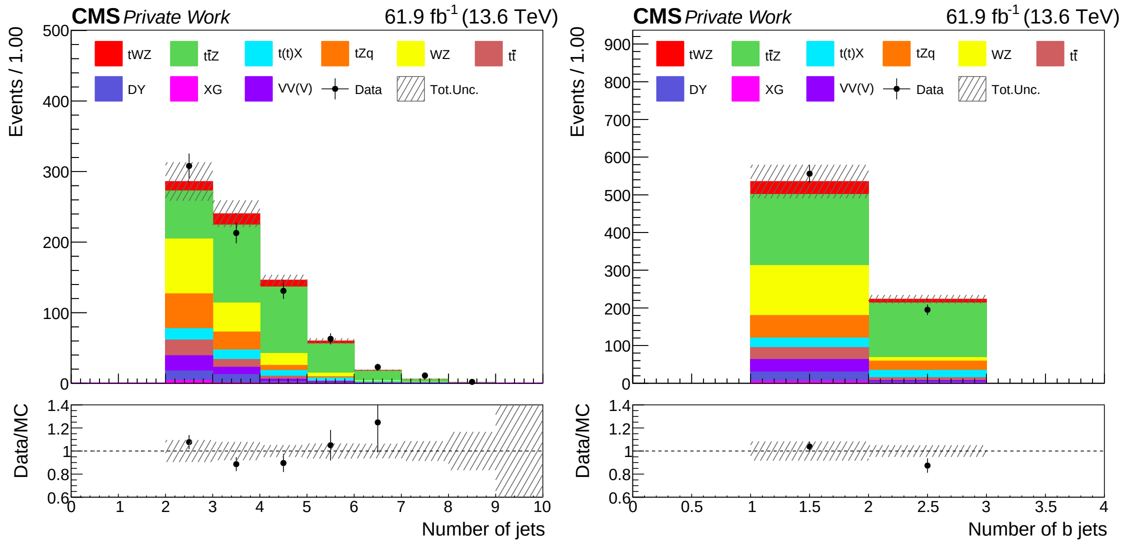

Figure 6.5: Distributions of the jet multiplicity (left) and number of b jets (right) in the 3ℓ SR for the Run 3 period. The black markers represent the data, while the solid stacked histogram shows the MC predictions for the various background processes. The dashed band indicates the total uncertainty. The lower panel displays the ratio between data and simulation.

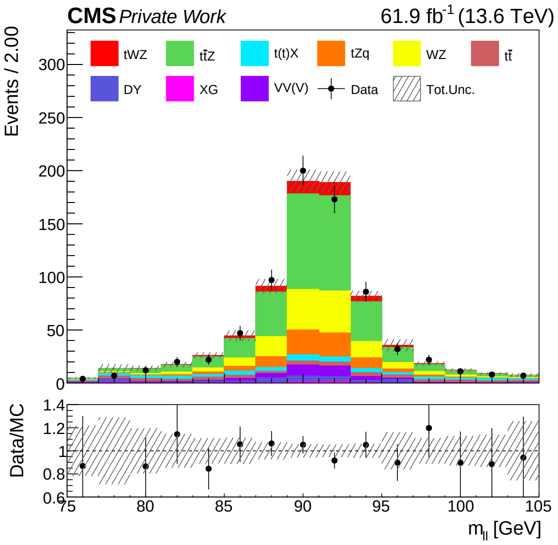

Figure 6.6: Distribution of the invariant mass of the dilepton pair with the closest invariant mass to the mass of the Z in the 3ℓ SR for the Run 3 period. The black markers represent the data, while the solid stacked histogram shows the MC predictions for the various background processes. The dashed band indicates the total uncertainty. The lower panel displays the ratio between data and simulation.

6.2.2 Four lepton Signal Region

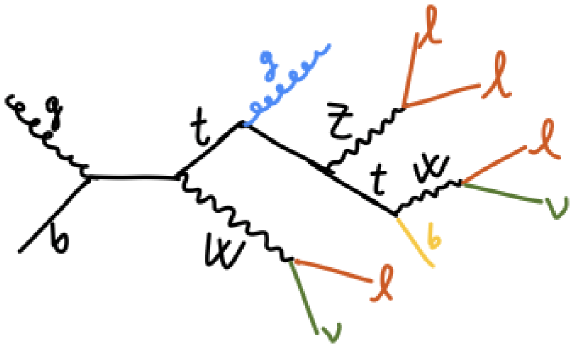

Figure 6.7: Sketch of tWZ in the fully-leptonic final state, including the emission of an additional gluon.

The topology where both W bosons decay leptonically (Figure 6.7) is investigated in the four lepton Signal Region (4ℓ SR). Because of the lower branching fraction for this process, this region has smaller statistical power compared to the 3ℓ SR. However, it has significant signal contribution and is affected by less background contamination, primarily from the $\mathrm{t\bar{t}Z}$ and ZZ processes. The following selection is required:

- exactly four leptons,
- two leptons must have same flavour and opposite sign, and their invariant mass must lie inside a 15 GeV window centred around the Z boson mass; the other lepton pair must lie outside this mass window,
- p_{T} of the (sub)leading lepton must be $> 25(15)$ GeV,
- at least one b-tagged jet.

The distributions of the jet multiplicity, number of b jets, and invariant mass of the dilepton pair with the closest invariant mass to the mass of the Z boson are shown in Figures 6.8, 6.9, 6.10, and 6.11 for the Run 2 and Run 3 periods respectively. The reduced statistical power and the smaller number of background processes compared to the 3ℓ SR is evident; in particular, statistical fluctuations are more significant in these plots. Nonetheless, good agreement between data and simulation is observed, with small deviations at high jet multiplicity, similar to the 3ℓ SR.

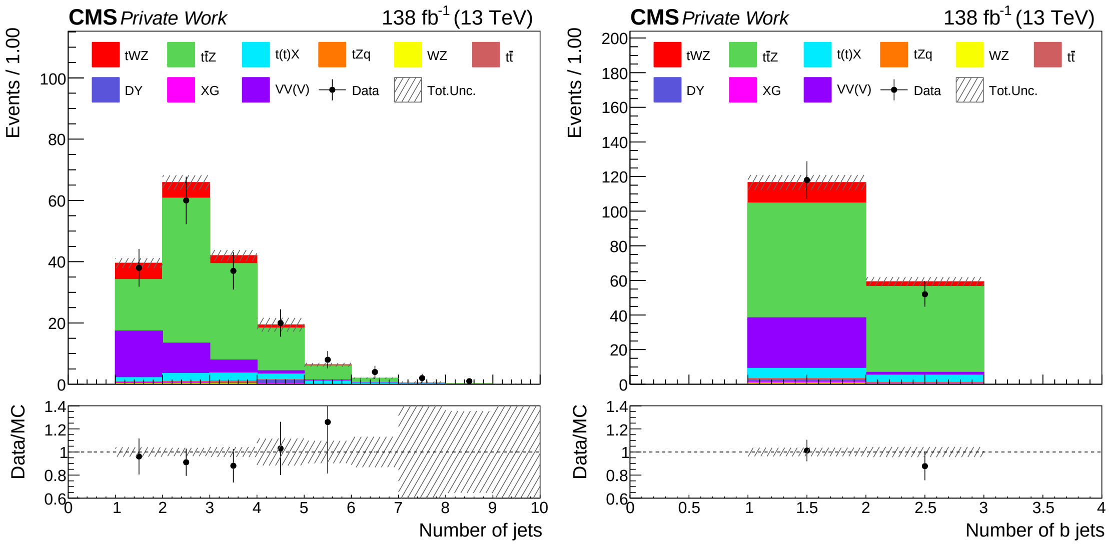

Figure 6.8: Distributions of the jet multiplicity (left) and number of b jets (right) in the 4ℓ SR for the Run 2 period. The black markers represent the data, while the solid stacked histogram shows the MC predictions for the various background processes. The dashed band indicates the total uncertainty. The lower panel displays the ratio between data and simulation.

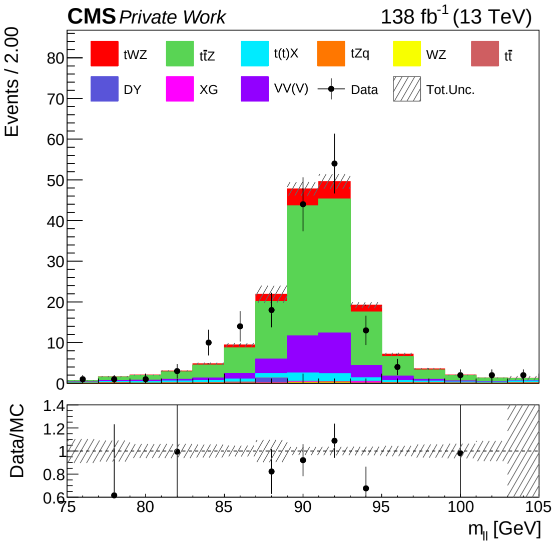

Figure 6.9: Distribution of the invariant mass of the dilepton pair with the closest invariant mass to the mass of the Z in the 4ℓ SR for the Run 2 period. The black markers represent the data, while the solid stacked histogram shows the MC predictions for the various background processes. The dashed band indicates the total uncertainty. The lower panel displays the ratio between data and simulation.

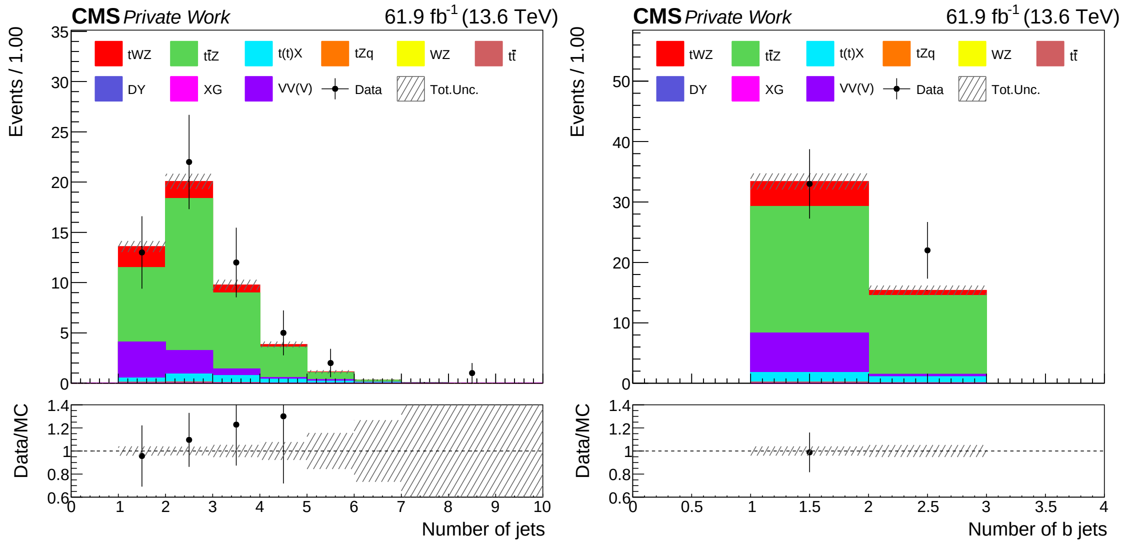

Figure 6.10: Distributions of the jet multiplicity (left) and number of b jets (right) in the 4ℓ SR for the Run 3 period. The black markers represent the data, while the solid stacked histogram shows the MC predictions for the various background processes. The dashed band indicates the total uncertainty. The lower panel displays the ratio between data and simulation.

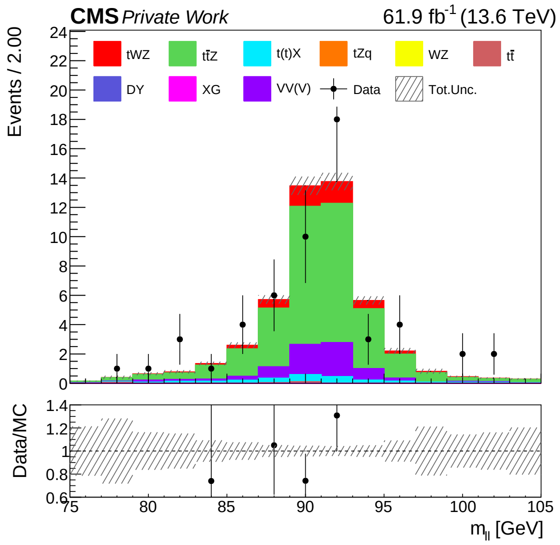

Figure 6.11: Distribution of the invariant mass of the dilepton pair with the closest invariant mass to the mass of the Z in the 4ℓ SR for the Run 3 period. The black markers represent the data, while the solid stacked histogram shows the MC predictions for the various background processes. The dashed band indicates the total uncertainty. The lower panel displays the ratio between data and simulation.

6.2.3 ZZ control region

Given the presence of the ZZ process in the signal regions, a ZZ-enriched CR is defined in order to better constrain this background in the maximum likelihood fit. The event selection consists in requiring exactly four leptons that come in pairs of two from the Z boson decay (each pair must have opposite-sign and same-flavour and the invariant mass must lie within a window of 15 GeV around the Z boson mass). The presence of at least one jet is required to have the same number of physics objects of the 4ℓ SR; in this way it is possible to test the data-MC agreement of the four lepton ML algorithm in this CR. Figures 6.12 and 6.13 show the p_{T} distributions of the leading lepton and leading jet in the ZZ CR for the Run 2 and Run 3 periods, respectively. Good agreement between data and simulation is observed both for leptons and jets, with larger statistical fluctuations in the Run 3 period due to the smaller integrated luminosity.

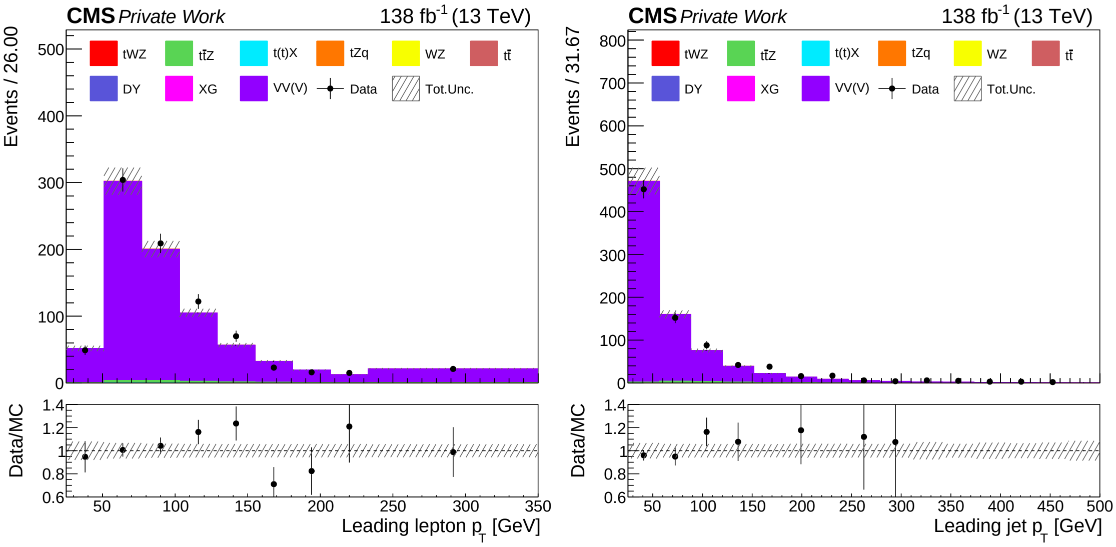

Figure 6.12: Distributions of the transverse momentum of the leading lepton (left) and leading jet (right) in the ZZ CR for the Run 2 period. The black markers represent the data, while the solid stacked histogram shows the MC predictions for the various background processes. The dashed band indicates the total uncertainty. The lower panel displays the ratio between data and simulation.

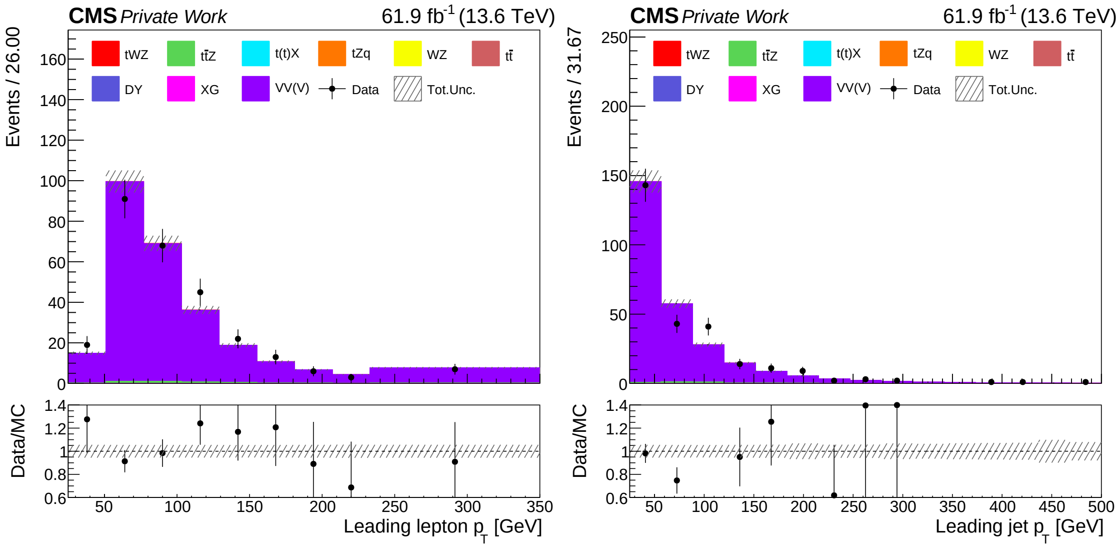

Figure 6.13: Distributions of the transverse momentum of the leading lepton (left) and leading jet (right) in the ZZ CR for the Run 3 period. The black markers represent the data, while the solid stacked histogram shows the MC predictions for the various background processes. The dashed band indicates the total uncertainty. The lower panel displays the ratio between data and simulation.

6.2.4 WZ control region

Similarly to the ZZ CR, a WZ-enriched region is defined to better constrain the WZ background in the fit. Events with exactly three leptons are selected, with the condition that one pair must originate from the Z boson decay, i.e. have opposite sign, same flavour, and an invariant mass in a window of 15 GeV around the Z boson mass. At least two jets are required in the event and, to avoid overlap with the 3ℓ SR, the presence of b jets is vetoed. Moreover, the $p_{\mathrm{T}}^{\mathrm{miss}}$ is required to be greater than 40 GeV; events with $p_{\mathrm{T}}^{\mathrm{miss}}$ smaller than 40 GeV are used in the DY CR instead. The split between these two CRs is performed applying a cut on the $p_{\mathrm{T}}^{\mathrm{miss}}$, instead of the transverse mass of the W boson, because a cut on the $p_{\mathrm{T}}^{\mathrm{miss}}$ is more efficient to separate DY from WZ. This can be observed in Figure 6.14, where the distribution of the $p_{\mathrm{T}}^{\mathrm{miss}}$ and of the W boson transverse mass are shown before applying any cut to divide the two CRs. The W boson transverse mass is defined as $M_T^{W^\pm} = \sqrt{2 \times p_{\mathrm{T}}^{\ell_W} \times p_{\mathrm{T}}^{\mathrm{miss}} \times (1 - \cos(\Delta\phi)}$, where ℓ_W is the lepton not belonging to the lepton pair within the 15 GeV window centred on the Z boson mass, and $\Delta\phi$ is the azimuthal angle between the missing transverse momentum and ℓ_W.

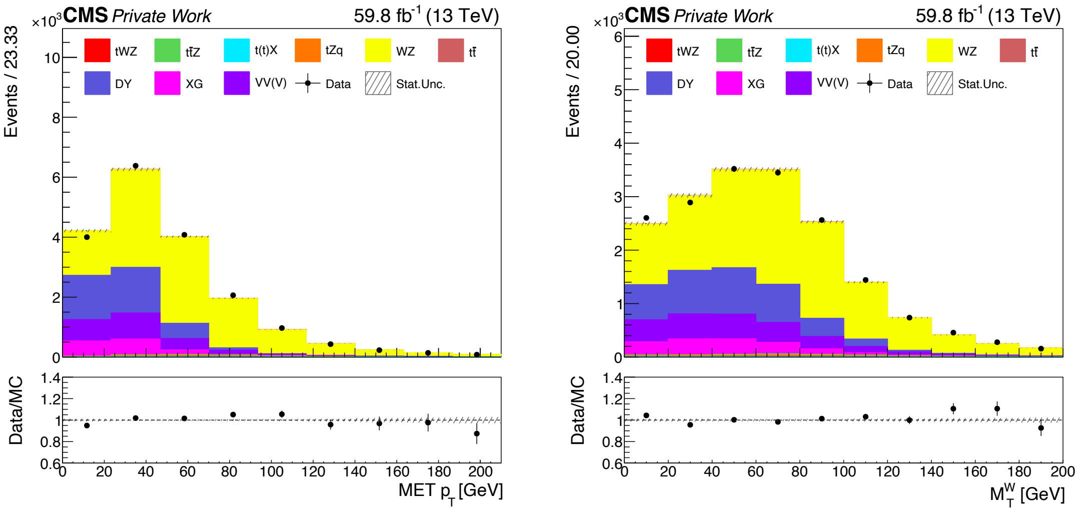

Figure 6.14: Missing transverse momentum (left) and W boson transverse mass (right) distributions for the 2018 data-taking year. The black markers represent the data, while the solid stacked histogram shows the MC predictions for the various background processes. The dashed band indicates the statistical uncertainty. The lower panel displays the ratio between data and simulation.

The data-MC agreement in the jet multiplicity distribution is not satisfactory in the WZ CR. As the presence of at least two jets is required in the 3ℓ SR, this mis-model must be addressed to avoid possible biases in the signal interpretation. For this reason a data-MC reweighting is performed in this distribution. The correction is obtained by dividing the data yields in each bin by the ones in the WZ simulation separately for the Run 2 and Run 3 data taking periods. The SF for events with more than 5 jets is computed merging the events in one single bin for the Run 2 period, a larger bin for the highest jet multiplicity SF is employed in the Run 3 period due to the smaller statistical power. Before computing the correction, the event yields of all the processes different from WZ are subtracted from the data. Eventually, the correction is applied on the WZ simulation using as template the generator level distribution of the jet multiplicity. The results of this procedure are shown in Figures 6.15 and 6.16 for the Run2 and Run 3 periods, respectively, demonstrating that the procedure fixes the observed mis-modelling.

The systematic uncertainty associated with the jet multiplicity reweighting procedure is treated as a shape uncertainty and therefore does not affect the normalisation of the WZ background. The down variation corresponds to the distribution obtained without applying the SFs, while the up variation is obtained by applying twice the SFs.

The agreement between data and simulation, after the jet multiplicity reweighting, is also verified for the leading lepton and leading jet p_{T} distributions in Figures 6.17 and 6.18 for the Run 2 and Run 3 periods, respectively.

Because of the b-veto applied in region definition, this CR comprises a different WZ background composition with respect to the signal region, where the presence of a b jet is required and therefore the main contribution from this background comes from $\mathrm{WZ} + b$.

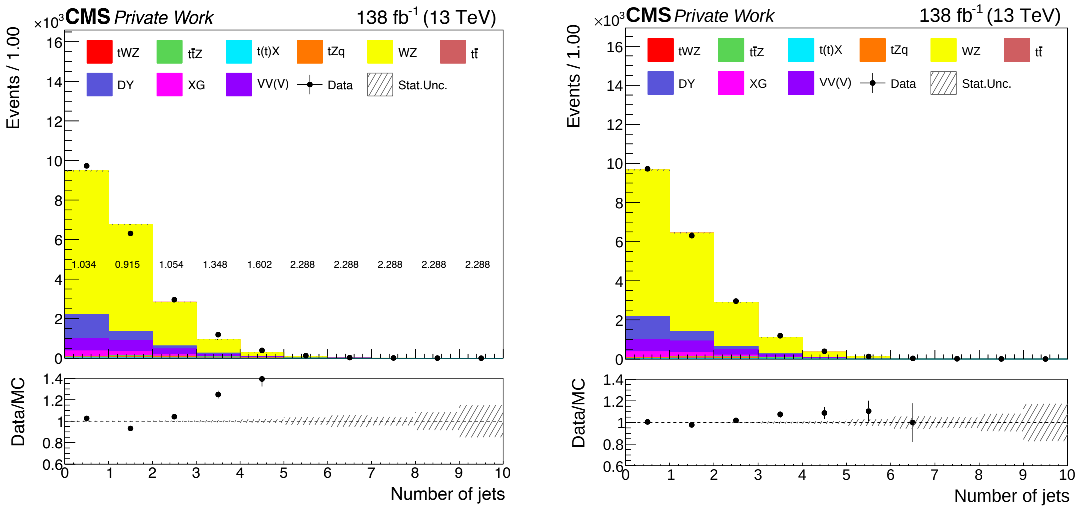

Figure 6.15: Jet multiplicity distribution before (left) and after (right) the reweighting in the WZ CR in the Run 2 period. The nominal value of the corrections is shown in the left plot for the different bins. The black markers represent the data, while the solid stacked histogram shows the MC predictions for the various background processes. The numbers in the left plot correspond the nominal values of the correction. The dashed band indicates the statistical uncertainty. The lower panel displays the ratio between data and simulation.

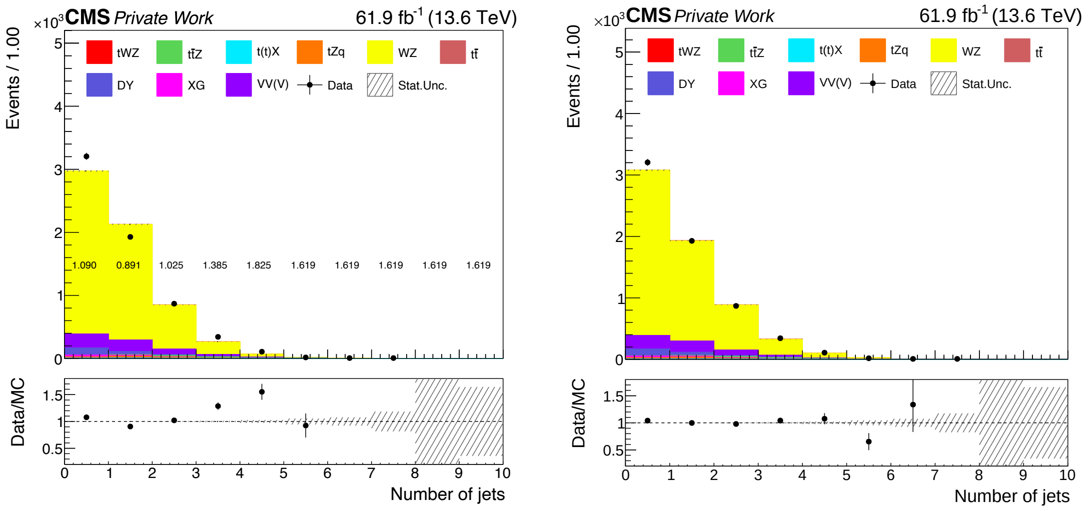

Figure 6.16: Jet multiplicity distribution before (left) and after (right) the reweighting in the WZ CR in the Run 3 period. The nominal value of the corrections is shown in the left plot for the different bins. The black markers represent the data, while the solid stacked histogram shows the MC predictions for the various background processes. The numbers in the left plot correspond the nominal values of the correction. The dashed band indicates the statistical uncertainty. The lower panel displays the ratio between data and simulation.

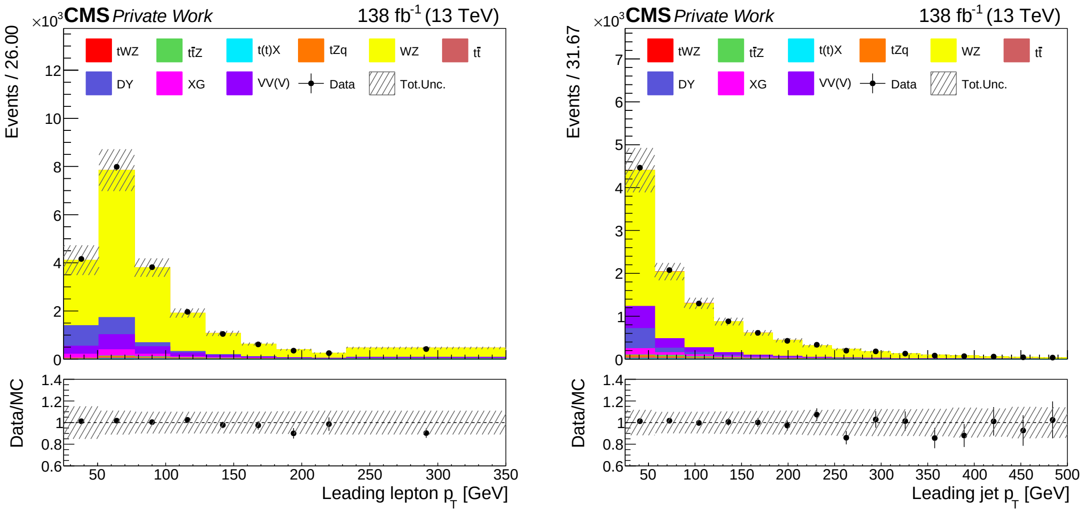

Figure 6.17: Distributions of the transverse momentum of the leading lepton (left) and leading jet (right) in the WZ CR for the Run 2 period. The black markers represent the data, while the solid stacked histogram shows the MC predictions for the various background processes. The dashed band indicates the total uncertainty. The lower panel displays the ratio between data and simulation.

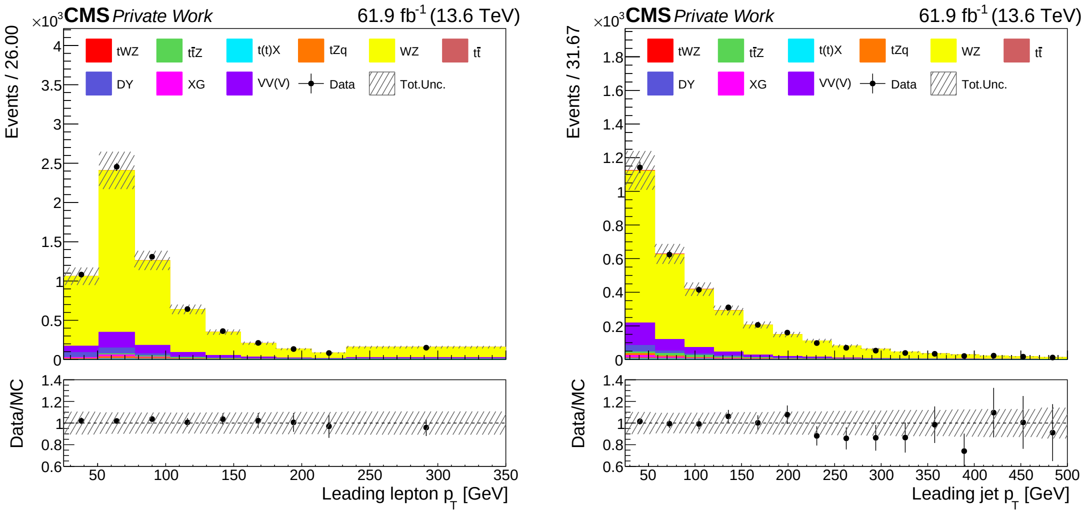

Figure 6.18: Distributions of the transverse momentum of the leading lepton (left) and leading jet (right) in the WZ CR for the Run 3 period. The black markers represent the data, while the solid stacked histogram shows the MC predictions for the various background processes. The dashed band indicates the total uncertainty. The lower panel displays the ratio between data and simulation.

6.2.5 DY control region

The DY CR is defined as starting point for the estimation of the fake leptons associated to the DY background. The definition is the same of the WZ CR but with no requirements on the number of jets and inverted cut on the $p_{\mathrm{T}}^{\mathrm{miss}}$ ($p_{\mathrm{T}}^{\mathrm{miss}} < 40$ GeV) to create an orthogonal region.

Figures 6.19 and 6.20 show the subsubleading lepton p_{T} and jet multiplicity distributions for the Run 2 and Run 3 periods. The jet multiplicity distribution is presented after the application of the reweighting for the WZ background. The same procedure is not applied to the DY background as the mis-modelling is less pronounced and DY is not a dominant background in the distributions that are sensitive to the signal. The subsubleading lepton p_{T} distribution is shown because its shape is most affected by the fake lepton contribution, which is usually more abundant at low p_{T}. Overall, good agreement between data and simulation is observed, with the dominant uncertainty coming from the fake lepton estimation. Thanks to the improvements in fake lepton rejection from the Run 3 lepton IDs, a smaller number of DY events is observed in this data-taking period. More details about the fake lepton estimation are provided in Chapter 9.

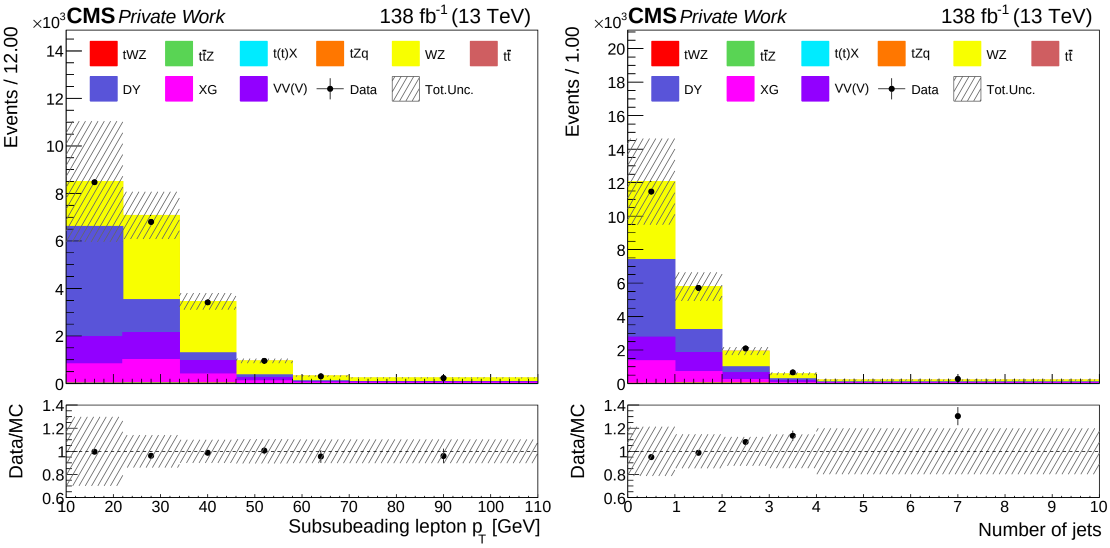

Figure 6.19: Distributions of the transverse momentum of the subsubleading lepton (left) and jet multiplicity (right) in the DY CR for the Run 2 period. The black markers represent the data, while the solid stacked histogram shows the MC predictions for the various background processes. The dashed band indicates the total uncertainty. The lower panel displays the ratio between data and simulation.

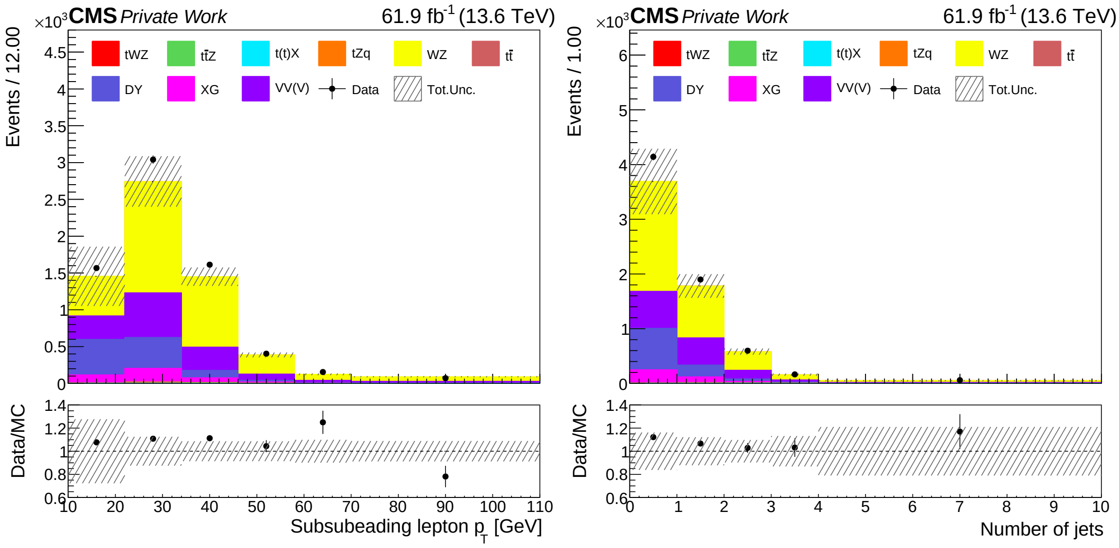

Figure 6.20: Distributions of the transverse momentum of the subsubleading lepton (left) and jet multiplicity (right) in the DY CR for the Run 3 period. The black markers represent the data, while the solid stacked histogram shows the MC predictions for the various background processes. The dashed band indicates the total uncertainty. The lower panel displays the ratio between data and simulation.

6.2.6 ttX control region

This CR is defined as starting point for the estimation of the fake leptons associated to the $t\bar{t}$ background. The definition is the same of the 3ℓ SR but rejecting any pair of leptons within the Z window to create a region that doesn't contain events from the 3ℓ SR. Since this CR has the same number of objects as the 3ℓ SR, it is also used to test the data-MC agreement of the 3 lepton ML algorithm.
Figures 6.21 and 6.22 show the p_{T} distributions of the subsubleading lepton and leading jet in the ttX CR for the Run 2 and Run 3 periods, respectively. A flat 15% excess of data is observed in the Run 2 period due to the mis-modelling introduced by the fake lepton contribution. The difference between data and MC is repaired during the fake lepton background estimation. The excess is not observed in the Run 3 period thanks to the improvements in the lepton IDs.

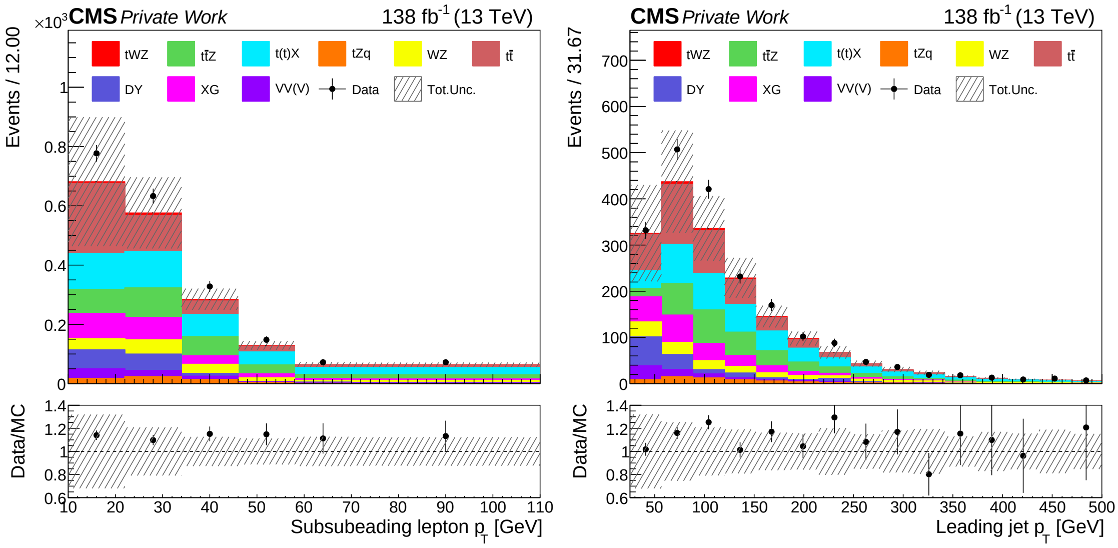

Figure 6.21: Distributions of the transverse momentum of the subsubleading lepton (left) and leading jet (right) in the ttX CR for the Run2 period. The black markers represent the data, while the solid stacked histogram shows the MC predictions for the various background processes. The dashed band indicates the total uncertainty. The lower panel displays the ratio between data and simulation.

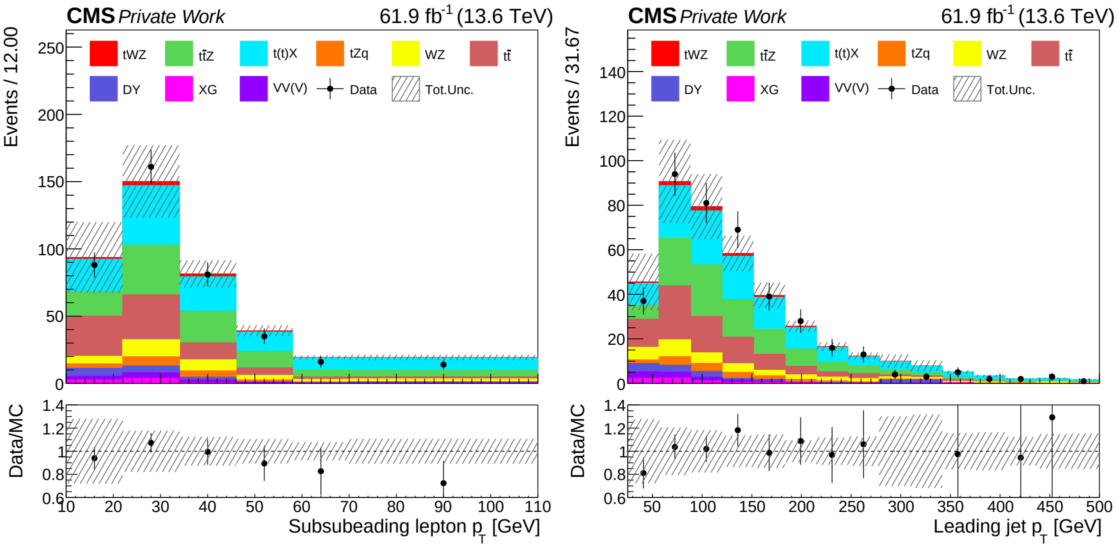

Figure 6.22: Distributions of the transverse momentum of the subsubleading lepton (left) and leading jet (right)in the ttX CR for the Run 3 period. The black markers represent the data, while the solid stacked histogram shows the MC predictions for the various background processes. The dashed band indicates the total uncertainty. The lower panel displays the ratio between data and simulation.

Chapter 7

Machine learning for tWZ identification

Machine learning refers to a class of algorithms that exploit large datasets to learn patterns or structures within the data and produce outputs useful for tasks such as classification, regression, or clustering. ML algorithms are typically categorised according to the training process:

- Supervised learning: the training dataset includes labeled examples, allowing the algorithm to learn how to map inputs to known targets.
- Unsupervised learning: the training dataset contains only input data without labels, and the algorithm attempts to identify structures or groupings within the data.

In the context of this analysis, ML algorithms are used to perform classification tasks, and supervised learning methods are used. These algorithms are trained on labelled datasets, e.g. simulated physics samples where the label is the physics process itself, enabling them to learn how input variables (features) differ between the different classes. Training involves minimising a loss function over a fixed number of iterations (epochs). For binary classification tasks, a commonly used loss function is the binary cross-entropy, defined as:

$$\mathrm{L} = -\left(y \cdot \log(\hat{y}) + (1-y) \cdot \log(1-\hat{y})\right), \tag{7.1}$$

where $y \in \{0,1\}$ is the true label and $\hat{y} \in (0,1)$ is the predicted probability for the positive class. This function penalises confident but incorrect predictions, allowing the model to improve the classification performance.

ML models have several internal parameters (hyperparameters) which depend on the specific architecture, e.g. number of decision trees in a Random Forest [188], depth of the trees in BDTs [189], or number of layers in neural networks [190–192]. The chosen values determine the structure of the algorithm and therefore significantly impacts its performance. For this reason, hyperparameters must be carefully selected through a process called hyperparameters tuning, in which different values are tested to eventually choose the set that yields the best performance.

In this work, ML algorithms are used in order to enhance the discrimination power between the signal and the background, the latter dominated by the $\mathrm{t\bar{t}Z}$ process. The performance of BDTs, neural networks and Particle Transformer (ParT) [177] has been evaluated, with the ParT algorithm outperforming the others. For this reason, the ParT algorithm has been adopted and different models have been trained for the 3ℓ SR and the 4ℓ SR. The algorithm architecture, the training and the evaluation steps are explained in details in the next sections.

7.1 The Particle Transformer algorithm

The transformer architecture was developed in 2017 [193] and since then was proven to be one of the best performing ML algorithms. The transformer architecture is used in many different fields and is playing a crucial role also in high energy particle physics. The Particle Transformer [177] algorithm is a transformer architecture specialised in high energy particle physics classification problems. Figure 7.1 illustrates the architecture of the model.

As shown in Figure 7.1 the algorithm takes as inputs two different set of variables: *Particles* ($\mathbf{x}$) and *Interactions* ($\mathbf{U}$).

The *Particles* input corresponds to a list of individual physics objects where each particle is described by a set of features. This information is represented as a matrix $\mathbf{x} \in \mathbb{R}^{N \times d}$, where N is the number of particles and d is the feature dimension. In this analysis the *Particles* input is divided into two categories: *leptons* and *jets*. The components of the four-momentum of each lepton and jet in every event are used as inputs, along with the following set of features:

- $\log(p_\mathrm{T})$,
- log(E),
- η,
- ϕ,
- b-tagging information,
- PDG-ID (only for leptons).

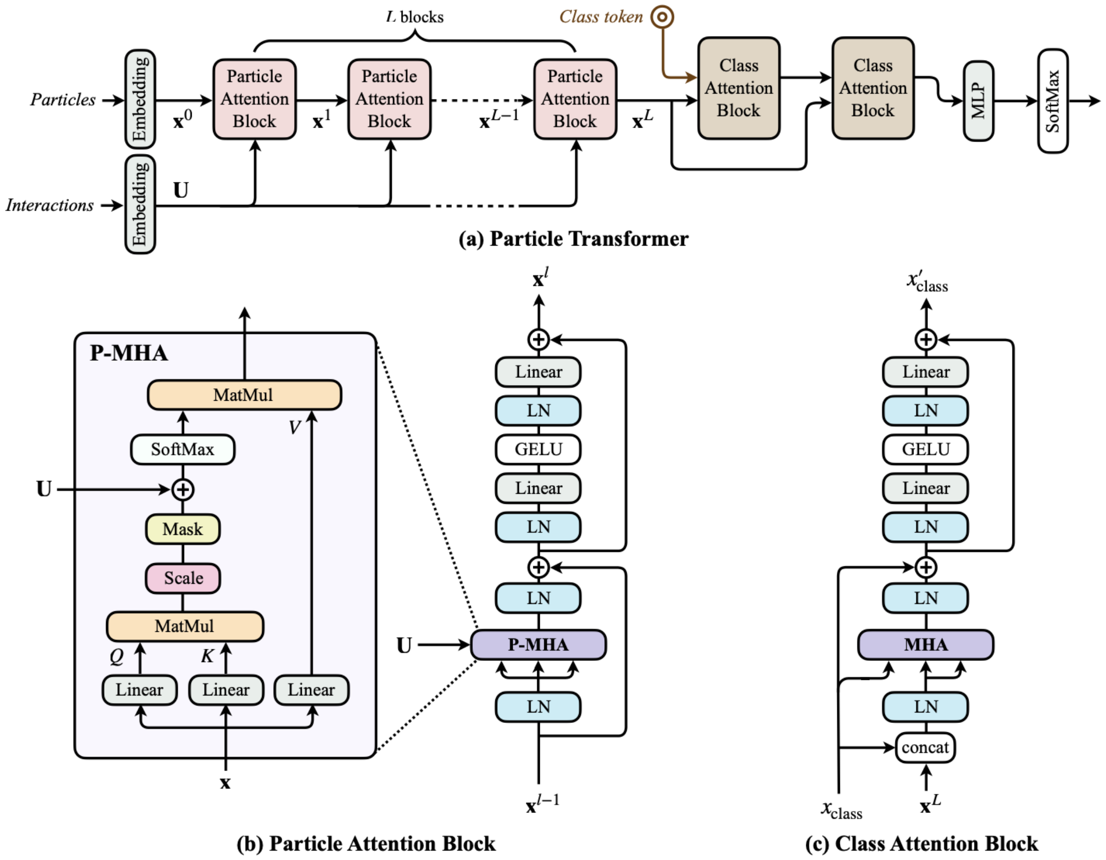

Figure 7.1: The architecture of (a) Particle Transformer (b) Particle Attention Block (c) Class Attention Block. Taken from [177].

The *Interactions* input encode interactions between pairs of particles. The variables used have been studied and implemented together with the architecture by the author of the model and their choice is motivated in Ref. [177]. In particular, they are computed considering all possible pairs of particles:

- $\Delta = \sqrt{(y_a - y_b)^2 + (\phi_a - \phi_b)^2}$,
- $k_T = \min(p_{T,a}, p_{T,b})\Delta$,
- $z = \min(p_{T,a}, p_{T,b})/(p_{T,a} + p_{T,b})$,
- $m^2 = (E_a + E_b)^2 - ||\mathbf{p}_a + \mathbf{p}_b||^2$.

Since the distributions in these variables have long-tails, the logarithmic distribution is considered as interaction for each particle pair.

As shown in Figure 7.1, the *Particles* and *Interactions* inputs are projected to a multi-dimensional embedding. The transformed inputs are then fed into L Particle

Attention Blocks, where L is chosen to be equal to 8 in the algorithms employed in this analysis. Each block uses a Particle Multi-Head Attention (P-MHA) module, which is the mechanism that updates the particle features by combining information from all other particles and their interactions. The P-MHA works as follows:

- Each particle representation $\mathbf{x}_i$ is transformed into query, key, and value vectors through linear layers.
- For a given particle i, a weight is computed for every other particle j using the scalar product between the query of i and the key of j, modified by a learnable scale and a mask derived from the interaction features $\mathbf{U}_{ij}$.
- These weights are normalised using the SoftMax function, resulting in a set of specific values, called attention weights, one for each particle j relative to i.
- The attention weights are used to compute a weighted sum with the value vectors, yielding the final representation for the particle i.

This allows each particle to incorporate information from all the other particles using both the particle features and their pairwise relationships, enabling the network to capture both local and global event characteristics.

After these layers, a special class token $\mathrm{x}_{\mathrm{class}}$ is introduced. This is a learnable vector that is concatenated to the set of particle representations. The role of this class token is to serve as a summary of the entire event. Instead of computing an average or sum over particles, the model learns how to extract the most relevant features across the event by interacting this token with the full set of particles. This interaction happens inside the two Class Attention Blocks, where the class token queries all the particle representations to obtain a condensed summary of the event. This is implemented via a standard multi-head attention mechanism, but only the class token is updated. After the Class Attention Blocks, the final value of this class token is passed through a Multi-Layer Perceptron (MLP) and a SoftMax layer to produce the final classification score.

7.2 Multiclass classifier for 3ℓ SR

The 3ℓ SR is characterised by a large contribution from the $\mathrm{t\bar{t}Z}$ background, with significant additional contributions from the WZ and tZq processes. To separate the signal from the background as effectively as possible, four classes are defined: *TWZ*, *TTZ*, *WZ*, and *others* (dedicated to the remaining backgrounds). The *TTZ* class enables the creation of a fairly pure $\mathrm{t\bar{t}Z}$ CR, which helps to constrain this background in the maximum likelihood fit. A *WZ* class is also included to reduce the impact of the WZ+b normalisation uncertainty, which is one of the leading systematic uncertainties. The four-momentum of the three leptons, along with the p_{T} and azimuthal angle of the missing transverse momentum, are used as input for the *leptons* category in the training. The four-momentum of the first six jets is used for the *jets* category. This choice was made because, although only up to four jets are simulated from the NLO matrix element of the tWZ process, a significant fraction of events contains five or six jets. The inclusion of these additional jets thus provides useful information. The fifth and sixth jets are included despite being simulated from the PS, as the data-MC agreement for the correspondent distributions is satisfactory. The input is limited to six jets because a clear drop in statistical power is observed from the seventh jet onward. Additionally, three vectors are used as input to convey the information about the three Run 2 b-tag WPs (tight, medium, and loose). Only two differences are introduced with respect to the Run 2 model implementation:

- Run 2 and Run 3 samples are both used in the training to compensate for the limited statistical power of the Run 3 dataset. An additional input variable is introduced to include the information about the data-taking period in the algorithm, accounting for possible differences between Run 2 and Run 3 due to the different centre of mass energies and reconstruction techniques.
- In addition to the three vectors representing the loose, medium, and tight b-tag WPs, a fourth vector is included to account for the extra-tight WP introduced in Run 3.

The data/MC agreement of the input variables has been validated on Run 2 and Run 3 data and the distributions are shown in Appendix A.1, where a good data-MC agreement is observed.

7.2.1 Training of the Run 2 model

The number of simulated events selected in the 3ℓ SR amounts to 9.4M for tWZ, 1.2M for $\mathrm{t\bar{t}Z}$, 132k for WZ, and 1.6M for the remaining backgrounds (grouped in the *others* class). The events are then weighted to account for the different cross sections and the corrections applied in the analysis. The absolute value of the event weights is used during training. An additional reweighting is subsequently performed to ensure that equal importance is given to the classes in the algorithm.

The dataset is split in half based on the parity of the event number. For each half, 75% of the events are used for training and validation, while the remaining 25% are reserved

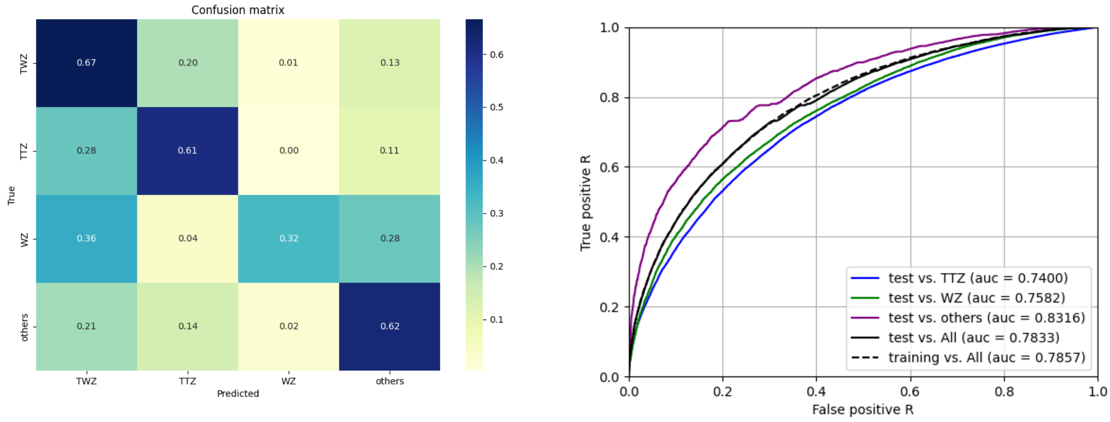

Figure 7.2: Left: Confusion matrix for the Run 2 ML algorithm. The y-axis shows the true labels for the different classes, while the x-axis shows the predicted labels assigned by the classifier. Diagonal elements represent the percentage of events correctly classified, while off-diagonal elements correspond to misclassified events. Right: ROC curves for the tWZ classification. Each curve shows the true positive rate as a function of the false positive rate for a given background: $t\bar{t}Z$, WZ, and others. The black solid curve corresponds to the overall test-vs-all ROC, while the dashed curve shows the ROC for the training set. The AUC is reported in the legend for each case.

for testing. The model trained on the even half is then used to make predictions on the odd half, ensuring no overlap between training and inference. The same procedure is applied in reverse, using the odd half for training and the even half for inference.

Several combinations of hyper-parameter values have been tested, and the algorithm's performance was found to be relatively insensitive to a specific choice. The following values have been adopted:

- Batch size: 1024
- Initial learning rate: 0.01
- Epochs: 50

The algorithm yields an area under the curve (AUC) score of 74% for tWZ vs. $t\bar{t}Z$, 76% for tWZ vs. WZ, and 83% for tWZ vs. *others*. The confusion matrix and the Receiver Operating Characteristic (ROC) curves for the Run 2 model are shown in Figure 7.2.

The algorithm is particularly effective at distinguishing tWZ from the *others* class, as the processes in this category have different kinematic properties compared to tWZ. In contrast, separating tWZ from $t\bar{t}Z$ and WZ is more challenging due to the similarity of their final states and the limited statistical power of the WZ simulated sample. Overtraining is well under control, as indicated by the minimal difference between the

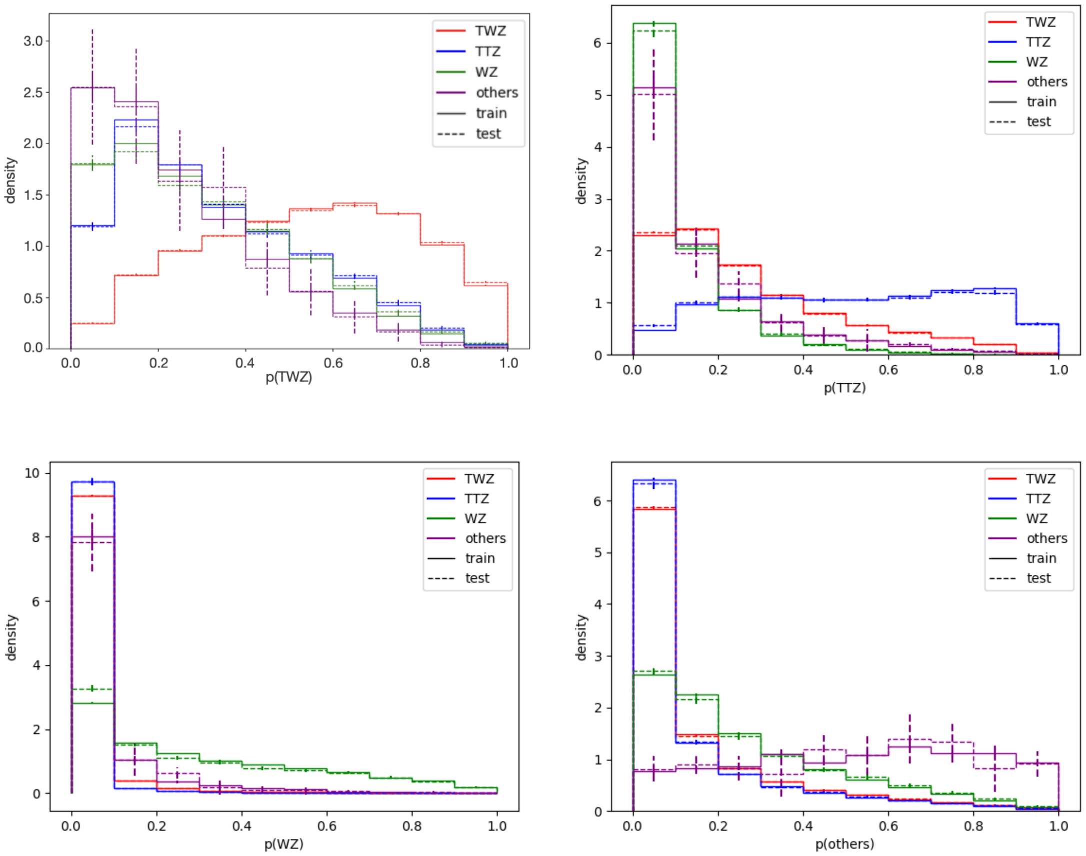

Figure 7.3: Output nodes distributions of the 3ℓ SR algorithm trained on Run 2 data. The four panels correspond to the output scores of the *TWZ* (top left), *TTZ* (top right), *WZ* (bottom left), and *others* (bottom right) nodes. For each class, the predicted probabilities are shown separately for the training (solid lines) and test (dashed lines) datasets. The colour indicates the true class of the events.

ROC curves for the training and test datasets.

The output nodes distributions are shown in Figure 7.3. The distributions for the training and test sets are compatible within statistical uncertainties across all nodes, indicating no significant overtraining.

The 3ℓ SR is eventually divided into three regions by selecting events according to the maximum score among the output nodes of the ML algorithm. In this case, the *WZ* and *others* nodes are merged due to the limited number of events classified in the *WZ* node. This approach allows for the definition of a signal-enhanced region, a region enriched in $t\bar{t}Z$ events, and a third region mostly populated by the remaining backgrounds.

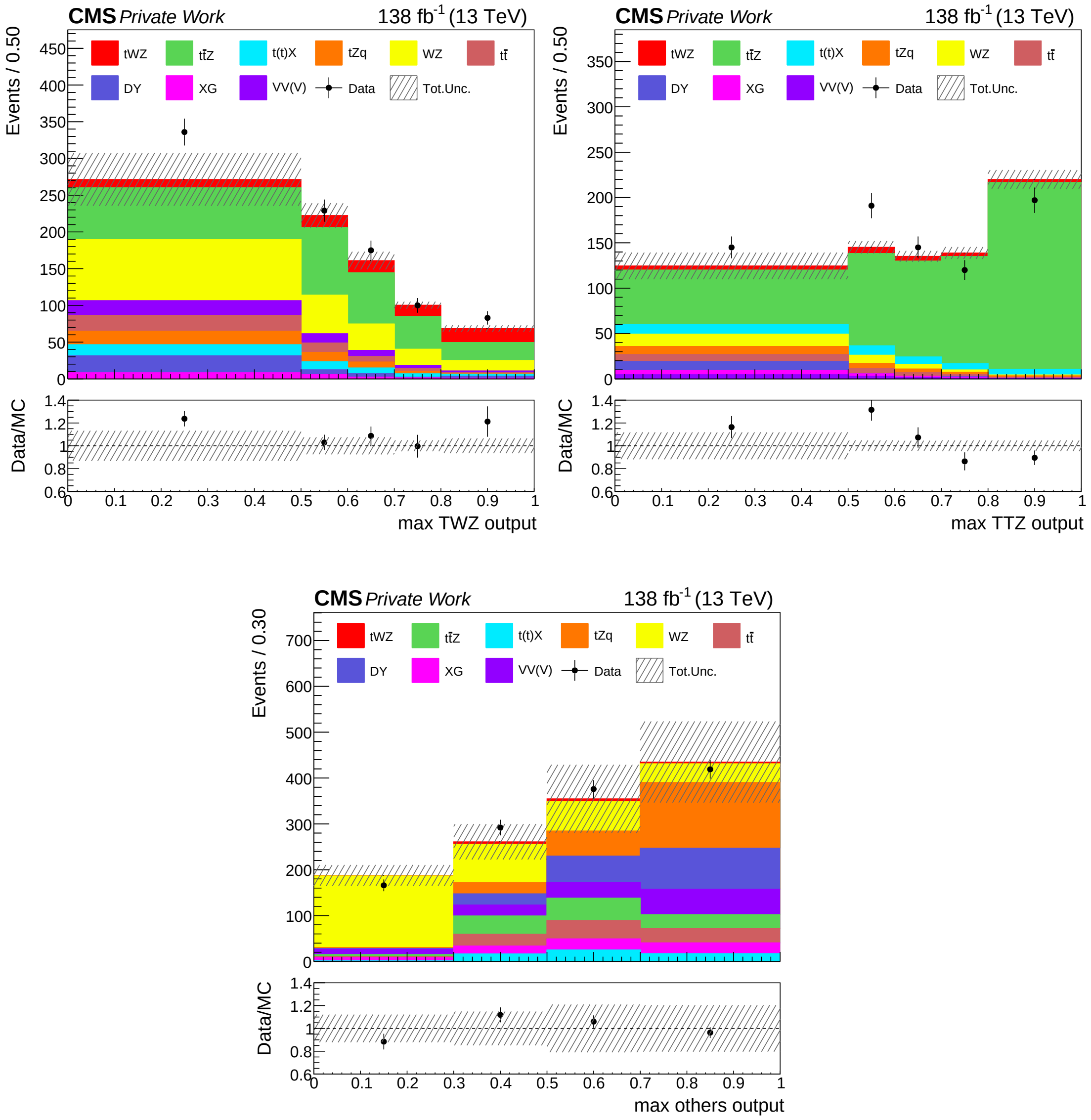

Figure 7.4: Maximum output scores of the three nodes in the 3ℓ SR for Run 2 data. The black markers represent the data, while the solid stacked histogram shows the MC predictions for the various background processes. The dashed band indicates the total uncertainty. The lower panel displays the ratio between data and simulation.

The distributions of the maximum output score for the *TWZ*, *TTZ*, and *others* nodes are shown in Figure 7.4, using the Run 2 dataset.

The width of the bins is chosen to allow sufficient statistical power to ensure a stable maximum likelihood fit. In particular, the *max TWZ output* and *max TTZ output* distributions do not contain any events below 0.25 due to how the variables are constructed; therefore, the first bin has a larger range than the others. The last two bins are merged to ensure sufficient statistical power and stability in the maximum likelihood fit. The *max TWZ output* distribution shows good separation between signal and background, while the *max TTZ output* distribution is particularly pure in $t\bar{t}Z$ events, making it useful for constraining its normalisation in the maximum likelihood fit. The *max others output* distribution is constructed to have larger WZ contributions at low values of the variable, while the remaining backgrounds are mostly concentrated at high values. For this reason, the width of the bins is symmetric with respect to the centre of the distribution. All output nodes show generally good agreement between data and simulation. While some fluctuations exceeding the uncertainty band are observed, no particular trends are present.

Figure 7.5 shows the data-MC agreement for the *max TWZ output* distribution in the ttX CR, demonstrating the absence of significant shape discrepancies and confirming that the ML algorithm does not introduce bias.

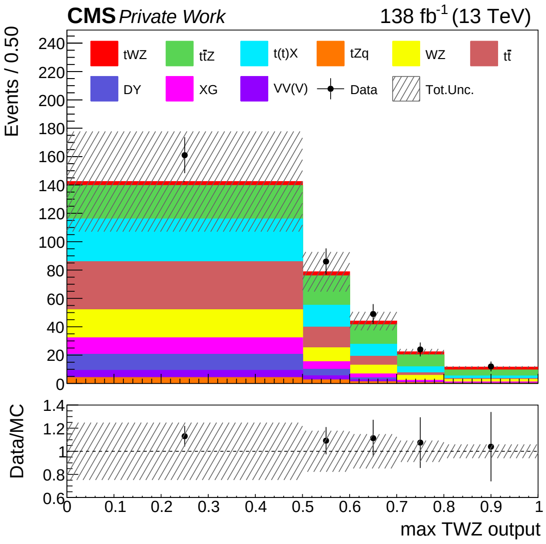

Figure 7.5: *Max TWZ output* distribution in the ttX CR for Run 2 data. The black markers represent the data, while the solid stacked histogram shows the MC predictions for the various background processes. The dashed band indicates the total uncertainty. The lower panel displays the ratio between data and simulation.

7.2.2 Training of the Run 3 model

The ML algorithm used in the 3ℓ SR on Run 3 data is trained following the same approach as in the Run 2 model. The confusion matrix and the ROC curves for the Run 3 model are shown in Figure 7.6. While the output nodes distributions are shown in Figure 7.7.

Slightly worse performance is observed for the Run 3 algorithm, primarily due to the lower statistical precision of the Run 3 samples. This limitation can't be fully compensated by including Run 2 simulated samples, as differences in kinematics and reconstruction are present. Overtraining is well under control in this case as well, as no significant differences are observed in the ROC curves or output nodes distributions between the training and test datasets.

The distributions of the maximum output score for the *TWZ*, *TTZ*, and *others* nodes are shown in Figure 7.8 for the Run 3 data.

Also in this case, the output nodes show generally good agreement between data and simulation. The *max TTZ output* distribution displays a fluctuation similar in size but in opposite direction to that observed in the same distribution for the Run 2 period, further confirming the absence of any bias induced by the ML model.

The data-MC agreement for the *max TWZ output* distribution is also verified in the

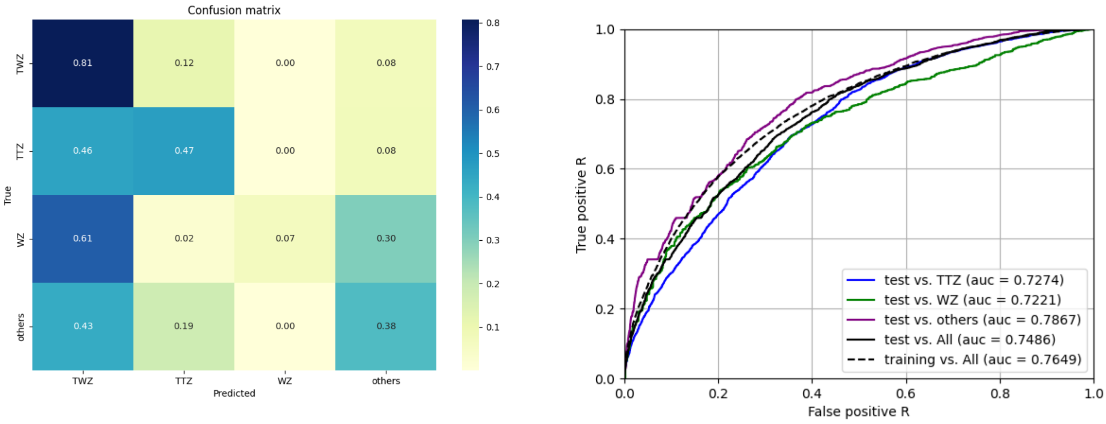

Figure 7.6: Left: Confusion matrix for the Run 3 ML algorithm. The y-axis shows the true labels for the different classes, while the x-axis shows the predicted labels assigned by the classifier. Diagonal elements represent the percentage of events correctly classified, while off-diagonal elements correspond to misclassified events. Right: ROC curves for the tWZ classification. Each curve shows the true positive rate as a function of the false positive rate for a given background: $t\bar{t}Z$, WZ, and others. The black solid curve corresponds to the overall test-vs-all ROC, while the dashed curve shows the ROC for the training set. The AUC is reported in the legend for each case.

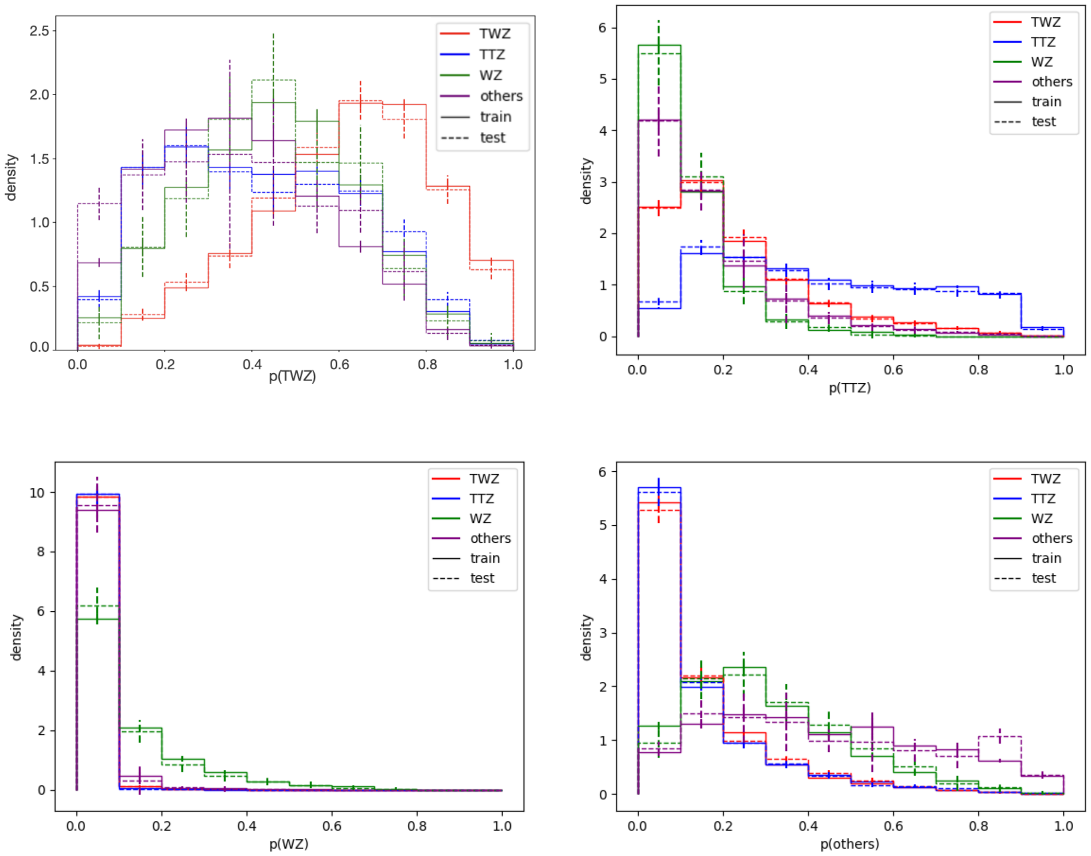

Figure 7.7: Output nodes distributions of the 3ℓ SR algorithm trained on Run 2 and Run 3 data but tested only on Run 3 data. The four panels correspond to the output scores of the *TWZ* (top left), *TTZ* (top right), *WZ* (bottom left), and *others* (bottom right) nodes. For each class, the predicted probabilities are shown separately for the training (solid lines) and test (dashed lines) datasets. The colour indicates the true class of the events.

ttX CR in Figure 7.9, confirming the absence of any significant shape effect.

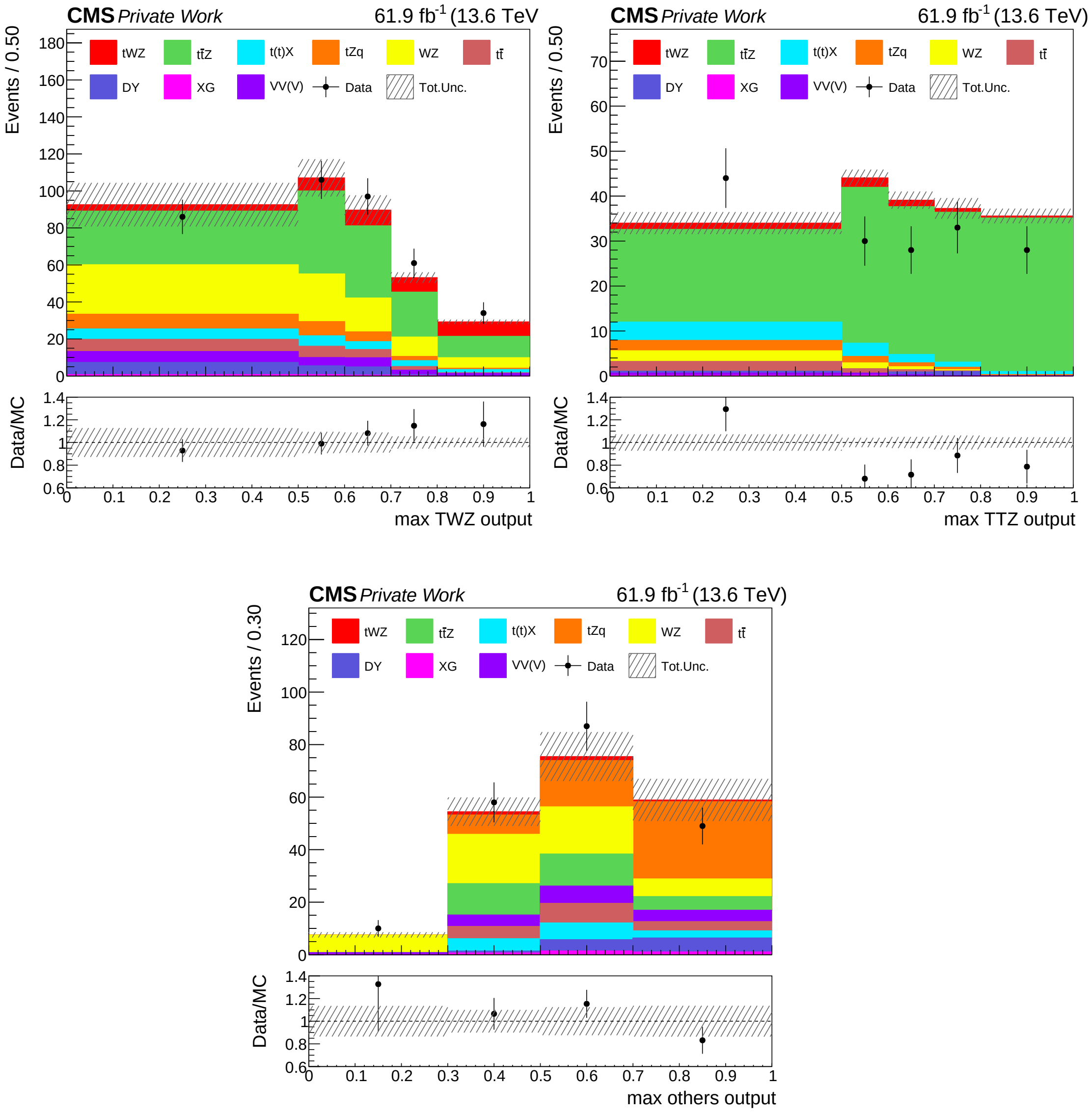

Figure 7.8: Maximum output scores of the three nodes in the 3ℓ SR for Run 3 data. The black markers represent the data, while the solid stacked histogram shows the MC predictions for the various background processes. The dashed band indicates the total uncertainty. The lower panel displays the ratio between data and simulation.

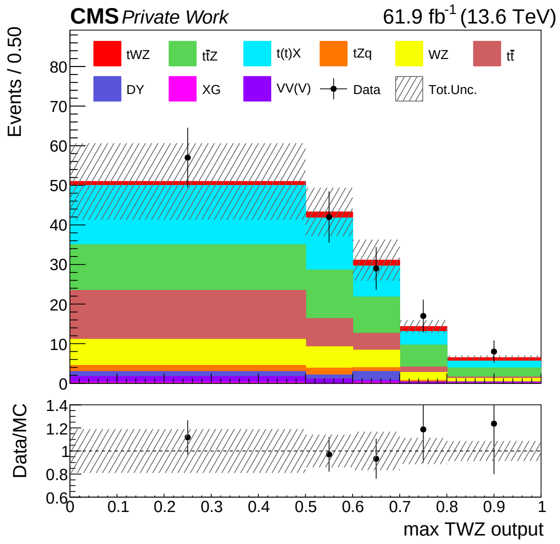

Figure 7.9: *Max TWZ output* distribution in the ttX CR for Run 3 data. The black markers represent the data, while the solid stacked histogram shows the MC predictions for the various background processes. The dashed band indicates the total uncertainty. The lower panel displays the ratio between data and simulation.

7.3 Binary classifier for 4ℓ SR

The $\mathrm{t\bar{t}Z}$ process represents the leading background in the 4ℓ SR by far. For this reason, and due to the limited statistical power, a binary classifier is employed. Given the smaller significance of this region and the smaller statistical power of the MC samples produced using Run 3 conditions, only one algorithm has been trained using exclusively Run 2 data. The four-momentum of the four leptons, together with the p_{T} and the azimuthal angle of the missing transverse momentum, are used as input for the *leptons* category. The four-momentum of the first four jets is used for the *jets* category. This choice is motivated by the fact that, even though only two jets are generated at the matrix element level for tWZ in this decay channel, a significant number of events contains additional jets, making their inclusion a valuable source of information. The input is limited to the fourth jet, as a clear reduction in statistical power is observed from the fifth jet onward. The same set of additional features used for the training of the 3ℓ SR algorithm is also employed in this case.

The data/MC agreement of the input variables has been validated on Run 2 data and the distributions are shown in Appendix A.2, where a good data-MC agreement is observed.

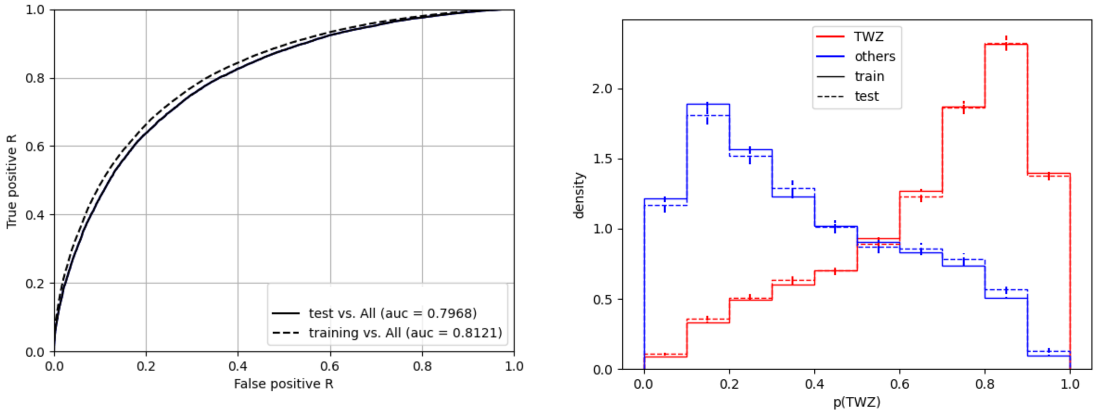

Figure 7.10: Left: ROC curves for the tWZ classification. The solid curve corresponds to the test-vs-all ROC, while the dashed curve shows the ROC for the training set. The AUC is reported in the legend for both cases. Right: Output node distributions of the 4ℓ SR algorithm. For each class, the predicted probabilities are shown separately for the training (solid lines) and test (dashed lines) datasets. The colour indicates the true class of the events.

The number of simulated events selected in the 4ℓ SR amounts to 770k for tWZ and 610k for the background processes. The same strategy adopted for the training of the 3ℓ SR algorithm is used also in this case and the following hyper-parameters values are chosen:

- Batch size: 512
- Initial learning rate: 0.01
- Epochs: 50

The ROC curves and the output nodes distribution for the final model are shown in Figure 7.10.

Both the ROC curves and the output node distributions show that the algorithm is able to achieve good separation between signal and background. No significant discrepancies are observed between training and test sets, confirming that overtraining is well under control also in this case.

The distribution of the *TWZ* output node in the 4ℓ SR and in the ZZ CR for Run 2 and Run 3 data are shown in Figures 7.11 and 7.12, respectively. Also in this case the width of the bins has been chosen to ensure enough statistical power in the last bin of the *TWZ output* distribution.

Good agreement is observed between data and simulation with larger statistical fluctuation, especially in the Run 3 period, due to the limited statistical precision of these regions.

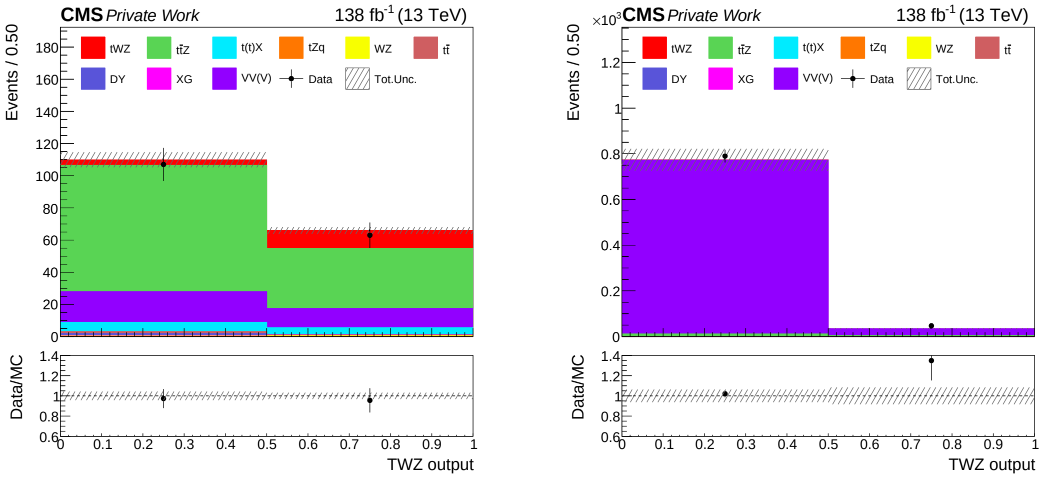

Figure 7.11: *TWZ* output node distribution in the 4ℓ SR (left) and ZZ CR (right) for Run 2 data. The black markers represent the data, while the solid stacked histogram shows the MC predictions for the various background processes. The dashed band indicates the total uncertainty. The lower panel displays the ratio between data and simulation.

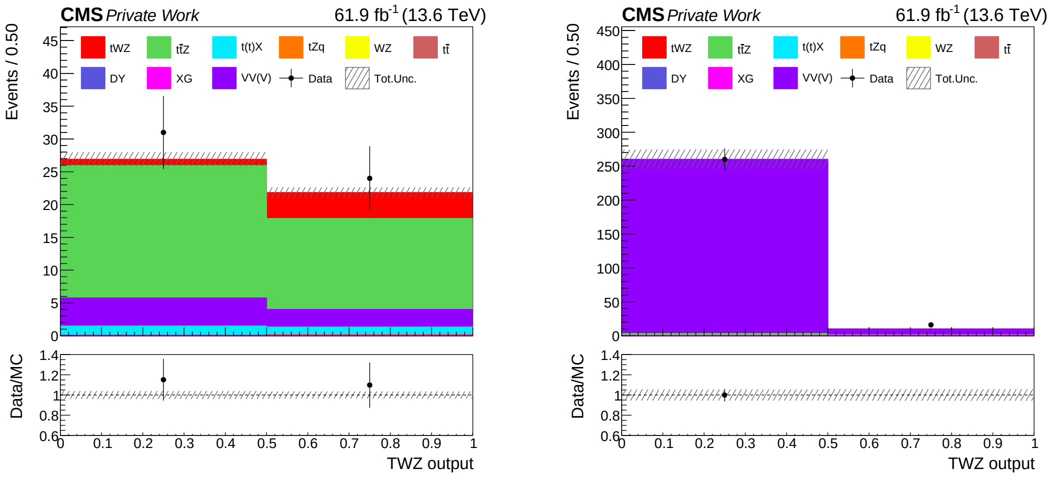

Figure 7.12: *TWZ* output node distribution in the 4ℓ SR (left) and ZZ CR (right) for Run 3 data. The black markers represent the data, while the solid stacked histogram shows the MC predictions for the various background processes. The dashed band indicates the total uncertainty. The lower panel displays the ratio between data and simulation.

Chapter 8

Statistical treatment and systematic uncertainties

Events passing the final selection are used to extract the parameters of interest (POIs) of the analysis. To measure the value of the POIs a maximum likelihood fit is performed considering all the significant systematic uncertainties. The effect of systematic uncertainties is included in the fit as they can affect both shape and normalisation of the different processes. The systematic uncertainties considered in this analysis are divided into experimental and theoretical uncertainties.

8.1 Statistical methods

The physical parameter measured in this analysis is the inclusive tWZ cross section. This parameter can be easily computed from the value of the signal strength of the tWZ process

$$\mu_{\mathrm{tWZ}} = \frac{\sigma_{\mathrm{tWZ}}}{\sigma_{\mathrm{tWZ}}^{\mathrm{SM}}}, \tag{8.1}$$

where $\sigma_{\mathrm{tWZ}}^{\mathrm{SM}}$ is the predicted tWZ inclusive cross section.
The signal strength is extracted via a maximum likelihood fit to the data, binned according to the input distributions used in the fit. The probability of observing n_i events in the data when expecting $\lambda_i(\mu)$ events, where i indicates the i-th bin out of N_{bins}, is given by the Poisson distribution

$$P_i(n_i|\mu) = \frac{\lambda_i(\mu)e^{-\lambda_i(\mu)}}{n_i!}, \tag{8.2}$$

where

$$\lambda_i(\mu) = \mu S_i + \sum_{k}^{N_{bckg}} B_{k,i}. \tag{8.3}$$

Here, S_i represents the number of signal events and $B_{k,i}$ the number of background events for the k-th source of background. The likelihood function is obtained by multiplying Eq. 8.2 for all the bins of the input distributions,

$$\mathcal{L}(\vec{n}, \mu) = \prod_{i=1}^{N_{\text{bins}}} \frac{\lambda_i(\mu) e^{-\lambda_i(\mu)}}{n_i!}, \tag{8.4}$$

where the components of the vector $\vec{n}$ represent the number of entries in each bin.
Eq. 8.4 must be extended when considering the effect of systematic uncertainties, which are included as nuisance parameters and denoted by θ. Since the value of the nuisance parameters is estimated in the fit to the data, the expected number of events depends also on their value,

$$\mathcal{L}(\vec{n}, \mu) = \prod_{i=1}^{N_{\text{bins}}} \frac{\lambda_i(\mu, \theta) e^{-\lambda_i(\mu,\theta)}}{n_i!} \prod_{j=1}^{N_{\text{nuis.}}} f(\theta_j). \tag{8.5}$$

The additional term $\prod_{j=1}^{N_{\text{nuis.}}} f(\theta_j)$ is added to consider the prior knowledge on the nuisance parameters and represents the probability distribution function that constrain the j-th nuisance parameter. In general, Gaussian distributions are used for systematic uncertainties that affect the shape of the distributions, while log normal distributions are used for systematic uncertainties affecting the normalisation to avoid negative event counts when the uncertainties are large. A uniform distribution is used when no initial constraint is applied.
The fit to data is performed by maximising the likelihood function. This corresponds to finding the values of the parameters that maximise the likelihood or equivalently, minimise $-2 \ln \mathcal{L}$ (negative log-likelihood), which is more convenient for numerical computation and allows for a direct connection with the test statistics. The tests statistics are used to verify the compatibility of a specific hypothesis with the data. In this analysis, the profiled likelihood ratio is employed, defined as

$$\Lambda_\mu = \frac{\mathcal{L}(\vec{n}|\mu, \hat{\theta}_\mu)}{\mathcal{L}(\vec{n}|\hat{\mu}, \hat{\theta})}, \tag{8.6}$$

where $\hat{\mu}$ and $\hat{\theta}$ are the values of the parameters that globally maximise the likelihood, while $\hat{\theta}_\mu$ corresponds to the value of the nuisance parameters that maximise the likelihood for a fixed value of μ. The denominator therefore corresponds to the absolute maximum of the likelihood function, and the numerator to the maximum for a specific assumed value of μ. In this context, Wilks' theorem [194] is particularly helpful. It states that, in the limit of $N_{events} \to \infty$, the distribution of $-2\ln\Lambda_{\mu}$ approaches a χ^2 distribution, with degrees of freedom equal to the difference in the number of parameters between the two hypotheses. Thus, it is possible to compute the profiled likelihood ratio from the observed data and compare it to the χ^2 distribution to derive confidence intervals and perform hypothesis tests. For this reason, the value of the POI, in this case μ_{tWZ}, is reported together with its corresponding confidence interval, which represents the probability that the interval contains the true value of the POI. In this analysis the confidence interval reported corresponds to the points where the distribution of the negative log-likelihood is equal to 1 with respect to the minimum, this corresponds to the 68% confidence level (CL) given the relation with the χ^2 distribution.

In the context of hypothesis testing, the p-value quantifies the compatibility of the observed data with a given hypothesis. It represents the probability $p(-2\ln(\Lambda_{obs})|H)$ of measuring a value of the test statistic that is at least as incompatible with the hypothesis H as the observed one, under the assumption that H is true. Therefore, the p-value for the background-only hypothesis H_0 corresponds to the probability of observing a result as discrepant as, or more discrepant than, what is predicted under H_0. It can be expressed by introducing the probability density function $f(q|H_0)$ of the background-only hypothesis

$$p_{H_0} = \int_{q_{\mathrm{obs}}}^{\infty} f(q|H_0)dq, \tag{8.7}$$

where the test statistics is defined as $q = -2\ln\Lambda$, and q_{obs} is its observed value.

In hypothesis testing, predefined thresholds are adopted to decide whether to reject a hypothesis. In high energy particle physics, two different threshold are used to reject the background-only hypothesis, corresponding to the evidence and observation of a given phenomenon. These threshold are set at 1.4×10^{-3} and 2.9×10^{-7}, corresponding to statistical significance of 3σ and 5σ, respectively, when interpreted in terms of standard deviations of a Gaussian distribution.

The agreement between the observed data and a given physics model can be quantified using the goodness-of-fit (GOF) test. It can be introduced as a hypothesis test where no specific alternative hypothesis is defined; instead, the goal is to evaluate whether the data is compatible with the assumed model.

Assuming that the number of events observed in each bin follows a Gaussian distribution, the likelihood function of the data under the model can be written as

$$\mathcal{L} = \prod_{i}^{N_{\text{bins}}} \frac{1}{\sqrt{2\pi\sigma_i^2}} \exp\left(-\frac{(x_i - \mu_i)^2}{2\sigma_i^2}\right), \tag{8.8}$$

where x_i is the observed number of events in the bin i, with an expected mean μ_i and a variance σ_i predicted by the model.

To construct a likelihood ratio test, the saturated likelihood is defined by setting the predicted mean equal to the observed value in each bin:

$$\mathcal{L}_{\text{saturated}} = \prod_{i}^{N_{\text{bins}}} \frac{1}{\sqrt{2\pi\sigma_i^2}}. \tag{8.9}$$

The saturated likelihood ratio Λ is then

$$\Lambda = \prod_{i}^{N_{\text{bins}}} \exp\left(-\frac{(x_i - \mu_i)^2}{2\sigma_i^2}\right) \tag{8.10}$$

and the corresponding test statistics is $q = -2\ln\Lambda$. Assuming Gaussian uncertainties and in the limit of $N_{\text{events}} \to \infty$, the test statistics follow a χ^2 distribution and it can be used to define a p-value. In this case a significance level of 5% is used as a threshold to determine whether the model provides an adequate description of the data. This corresponds to approximately 1.96σ in terms of Gaussian standard deviations.

Using the profile likelihood ratio, it is also possible to estimate the value of the nuisance parameters θ. Particularly interesting is the comparison between the values obtained after the minimisation of the negative log-likelihood (post-fit values) and the initial values (pre-fit values). The pull of a nuisance parameter is defined as the difference between its post-fit ($\hat{\theta}$) and pre-fit (θ_0) values divided by its pre-fit uncertainty ($\Delta\theta$):

$$\text{pull} = \frac{\hat{\theta} - \theta_0}{\Delta\theta}. \tag{8.11}$$

The constraint quantifies the reduction in uncertainty due to the fit, and is defined as the ratio between post- and pre-fit uncertainties:

$$\text{constraint} = \frac{\Delta\theta_{\text{post}}}{\Delta\theta}. \tag{8.12}$$

The impact of a nuisance parameter on the POI is computed by varying the post-fit value of that nuisance up and down by one standard deviation while keeping all other

Table 8.1: Luminosity uncertainties in percentage and their correlations for the different Run 2 data-taking periods.

Source	2016 pre-VFP	2016 post-VFP	2017	2018
Uncorrelated 2016 pre-VFP	1.0	-	-	-
Uncorrelated 2016 post-VFP	-	1.0	-	-
Uncorrelated 2017	-	-	2.0	-
Uncorrelated 2018	-	-	-	1.5
Correlated 2016pre-2016post-2017-2018	0.6	0.6	0.9	2.0
Correlated 2017-2018	-	-	0.6	0.2

nuisance parameters fixed to their post-fit values, and measuring the corresponding change for the POI. Therefore, it is defined as the difference between the nominal best-fit value $\hat{\mu}$ and the shifted values $\mu_{\text{nuis.}}$ The pull and constraint of the nuisance parameters with the largest impact on the measurement are particularly useful for studying how the fit adjusts the initial assumptions. The impact of the different nuisances helps interpret their importance in the extraction of the POI.

8.2 Experimental uncertainties

A summary is given of the experimental uncertainties considered in the analysis. All experimental uncertainties are treated as uncorrelated between Run 2 and Run 3.

- **Luminosity**. In order to account for the uncertainty on the value of the total luminosity recorded by CMS, a normalisation-only uncertainty is applied to the predicted event yields with different values and correlations across the different data-taking periods. The luminosity uncertainties used for Run 2 data [195–197] are summarised in Table 8.1. For the 2022 and 2023 data-taking years [198,199] a normalisation uncertainty of 1.4% and 1.3%, respectively, is applied.
- **Pileup**. As explained in Section 6.1, event weights are applied to all simulated events used in the analysis in order to mitigate the data/MC discrepancy that arises from not knowing exactly the mean number of interactions per bunch crossing when simulating the events. To estimate the corresponding uncertainty, the pp inelastic cross section is varied by ±4.6% and the variations are propagated to the event weights. This results in a shape uncertainty and is treated as correlated across the years but uncorrelated between the Run 2 and Run 3 periods.
- **Trigger efficiency**. As explained in Section 6.1, the trigger efficiency is very close to unity and no corrections are applied. A flat 2% uncertainty is applied to account for residual potential differences in Run 2 data. In Run 3, a flat 1%

uncertainty is applied instead. These uncertainties are considered uncorrelated across the years.

- **Lepton identification corrections**. Uncertainties coming from the lepton SFs measurement are considered and treated independently for muons and electrons by varying the lepton SFs up and down. For electrons and muons separately, the statistical and systematic uncertainties are treated as separate sources. The statistical uncertainties are uncorrelated between the years, while the systematic uncertainties are treated as fully correlated. The split in statistical and systematic part is not available in the centrally provided Run 3 SFs and given that the statistical component is significantly smaller, the uncertainty on the SFs is considered fully correlated.
- **Electron reconstruction corrections**. Uncertainties coming from the electron reconstruction corrections measurement are considered varying the scale factors up and down. The uncertainty on the SFs is considered fully correlated across the years but uncorrelated between the Run 2 and Run 3 periods.
- **Jet energy correction**. The uncertainty related to the jet energy corrections is provided as a function of the jet p_{T} and η. Events are re-analyzed after the four-momentum of the jets have been varied within uncertainties. The b-tagging efficiency corrections factor and missing transverse momentum vector are recomputed accordingly. The correlation scheme suggested for these centrally produced corrections is employed.
- **Jet energy resolution**. The uncertainty on the JER is also applied as a shape uncertainty, and is treated uncorrelated across the years.
- **Missing transverse momentum**. Type-1 corrected PF missing transverse momentum (MET) is used throughout the analysis. For each variation of the JEC, the p_{T} and ϕ of the missing transverse momentum vector is recomputed following the CMS centrally provided prescription, in order to propagate these corrections to the MET. A dedicated uncertainty on the unclustered missing energy is propagated to the MET and is treated as a shape uncertainty uncorrelated across the years.
- **B-tag corrections**. Uncertainties on the b-tag SFs are applied resulting in shape uncertainties. The sources of uncertainties are split into a correlated and an uncorrelated part, with the latter being treated as uncorrelated across the data-taking periods.
- **L1 prefiring**. Uncertainties associated to correction applied in the MC to ac-

count for early L1 electron/photon triggers. These shape uncertainties are treated as correlated between 2016 and 2017.

- **HEM1516 issue**. In late runs of 2018 data taking (era C and D), the power supply of two HCAL modules failed. This impacts the measured jet energy and MET. An uncertainty is introduced by modifying the jet energy for jets falling in the affected $\eta - \phi$ region of the detector. This uncertainty is propagated to the MET.
- **Estimation of fake lepton background**. The fake lepton background is estimated by correcting the shape and normalisation of simulated templates directly within the maximum likelihood fit. For this reason, different nuisance parameters, either unconstrained or Gaussian-constrained, are assigned to the various sources of fake leptons. The method used to estimate the fake lepton background is described in detail in Chapter 9.
- **Uncertainty on the jet multiplicity reweighting for the WZ background**. A shape uncertainty is introduced on the jet multiplicity reweighting applied to the WZ process. The down variation corresponds to the results we would obtain without applying the SFs, while the up variation is obtained by applying twice the SFs.
- **MC statistical uncertainties**. In order to account for the limited number of MC events, statistical uncertainties are considered via the Barlow-Beeston method [200].

To reduce the fluctuations in the templates associated with the HEM1516 issue, missing transverse momentum, and jet energy correction and resolution, the lowess smoothing method [201] is employed, significantly reducing statistical fluctuations. Additionally, these systematic uncertainties are not applied to the processes involved in the fake lepton estimation. This is because the MC simulation of such processes can have large event weights, leading to substantial statistical fluctuations and thus noisy templates. Since this background is estimated from data by constraining a large systematic uncertainties with flat priors (Chapter 9), jet related uncertainties have a negligible impact on the results.

8.3 Theoretical uncertainties

Theoretical uncertainties are treated as fully correlated across the years and between the Run 2 and Run 3 periods.

- **Theoretical cross section**. A normalisation uncertainty of 7% is employed for the $\mathrm{t\bar{t}Z}$ cross section [103, 122]. Two different normalisation uncertainties are considered for the WZ and ZZ processes: a 20% uncertainty is used when the boson pairs are produced in association with at least one bjet, WZ+b [105], while a 10% uncertainty is applied for the production in association with light-quark and gluon jets, WZ+j [202]. An uncertainty of 11% is used for tZq production [105], while a 10% uncertainty is used for the remaining di- and tri-boson processes, VV(V) [203, 204], and additional processes with a photon in the final state, $\mathrm{X}\gamma$ [205, 206]. A 5% uncertainty is applied to the $\mathrm{t\bar{t}}$ process [207], while a 10% uncertainty is used for the DY process [64, 66]. A 25% uncertainty is considered for the $\mathrm{t\bar{t}W}$ process [100] and a 20% uncertainty for processes in which a single top quark or a $\mathrm{t\bar{t}}$ pair is produced in association with other additional particles.
- **PDF**. The shape variations on the PDF set are considered by evaluating all the 100 eigenvectors. The variations on the coupling constant of the strong interaction, α_S, are also included, following the prescription described in Ref. [208]. These shape uncertainties are applied to the signal, as well as to $\mathrm{t\bar{t}Z}$, WZ and tZq. The PDF uncertainties and the α_S-related uncertainties are treated as correlated across processes and years. They are all properly normalised to ensure that only the shape effect is taken into account.
- **Parton shower**. The shape-only uncertainty on the parton shower simulation is accounted for by varying α_S, independently for initial and final state radiation (ISR and FSR), by factors of 1/2 and 2 for the signal samples and the backgrounds. To avoid correlation between QCD-induced and EWK-induced processes, the ISR uncertainty is treated as uncorrelated across processes, while the FSR uncertainty is considered correlated. These uncertainties are properly normalised to ensure that only the shape effect is taken into account and are applied to the signal, as well as to $\mathrm{t\bar{t}Z}$, WZ and tZq.
- **Matrix element scale**. Uncertainties on the matrix element renormalisation scale (μ_R) and factorisation scale (μ_F) are considered for the various processes. Both scales are varied by factors of 1/2 and 2, each one independently. These uncertainties are treated as uncorrelated between the different processes and are properly normalised to ensure that only the shape effect is taken into account. They are applied to the signal, as well as to $\mathrm{t\bar{t}Z}$, WZ and tZq.
- **Signal modelling**. The differences in shape due to the two different subtraction

schemes (DR1 and DR2) are evaluated and treated as a shape uncertainty for the tWZ process. This uncertainty is computed considering only one shift as systematic uncertainty, i.e. the DR2 shift is taken as up variation, while the down variation corresponds to the nominal (DR1) template. This yields a one-sided modelling uncertainty. The DS scheme is not used, as it is found to lie in between DR1 and DR2.

Chapter 9

Fake lepton estimation

When requiring a multi-lepton selection, as in the case of this analysis, events with fake leptons constitute a significant source of background. These mainly arise from DY, $\mathrm{Z}+\gamma$, and dileptonic $\mathrm{t\bar{t}}$ events with mis-identified leptons. Rates and kinematic dependencies of fake leptons are not well-modelled by the simulation and for this reason they are estimated directly from data. A detailed description of the method used in this analysis is reported in the following subsections.

9.1 Study and categorisation of the nonprompt lepton background

The fake lepton estimation method used in this analysis relies on dedicated CRs enriched in fake leptons. These regions are used to construct templates that simulate the fake leptons contribution, which is then estimated directly in the maximum likelihood fit. The key point of the method is the construction of templates capable of properly describe the fake leptons. For this purpose, the DY and ttX CRs have been created as described in section 6.2. The initial data-MC agreement is reasonably good in both the DY CR (Figures 6.19 and 6.20) and the ttX CR (Figures 6.21 and 6.22), although the latter shows a flat 15% excess of data.

Fake leptons generally originate from misidentified jets or photons, or from non-prompt leptons. In this analysis, nonprompt leptons are defined as leptons not originating from a W, Z, or Higgs boson. Leptons from external photon conversion are also considered fake leptons, even if the MC is able to describe them better than other sources of fake leptons. The origin of the fake leptons, identified via MC matching, is used to classify them into three categories: light jets, b jets, and photons. These categories

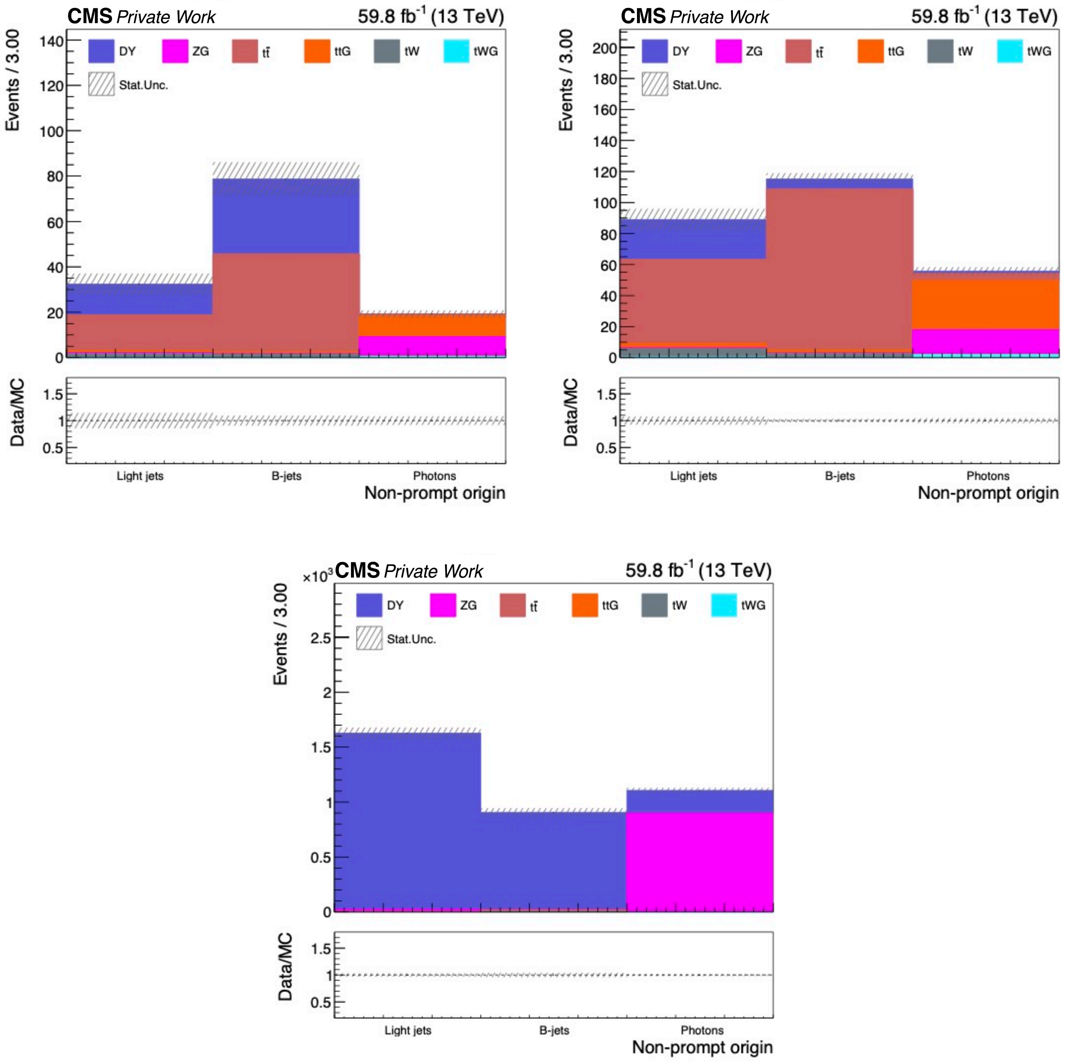

Figure 9.1: Number of simulated events for the different fake lepton categories for the 2018 dataset. The 3ℓ SR is shown in the top left, the ttX CR is in the top right, and the DY CR at the bottom.

have different kinematic properties due to their distinct production modes and may therefore require different corrections. Figure 9.1 shows the number of events for each category in the 3ℓ SR, the ttX CR, and the DY CR for the 2018 dataset.

As expected fake leptons from b jets are more abundant in 3ℓ SR and in the ttX CR, as the presence of at least one jets is requested in their definition. In contrast, in the DY CR, the more abundant category is the light jets one, while the photons category is less significant and mostly represented by the $t\bar{t}\gamma$ and $Z + \gamma$ processes.

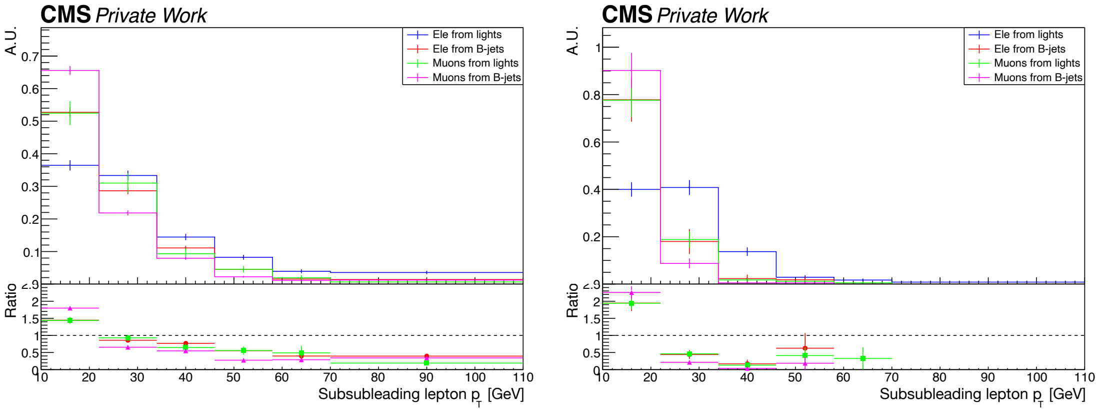

Figure 9.2: Normalised subsubleading lepton transverse momentum distribution, for the $t\bar{t}$ process in the ttX CR (left) and the DY process in the DY CR (right), for the different lepton fake categories in simulation for the Run 2 period.

In principle, the three different sources of fake leptons could have different kinematic shapes. To investigate potential shape differences, the distributions of relevant kinematic variables are studied. Figure 9.2 shows the normalised distribution of the subsubleading lepton p_{T} in the DY and ttX CR, respectively, for the DY and $t\bar{t}$ processes, for all the possible combinations of fake lepton categories. This variable was selected because it displays the largest shape differences, likely because fake leptons tend to have a softer p_{T} spectrum than prompt leptons. No significant differences among the categories were observed in the pseudorapidity distributions.

Figure 9.2 suggests that the number of categories can be reduced to two: one for electrons coming from light jets, and another for the remaining cases. The former is referred to as *light jet fakes*, while the latter is named *b jet fakes*, ignoring that this category also includes fake muons coming from light jets. This choice is justified by the fact that muons from light jets have a very similar shape to those from b jets and their overall contribution is small. Even in the DY CR, where their presence is expected to be larger, light jets account for less than 40% of the fake muons.

The up and down variations for the unconstrained nuisances associated to the *light jet fakes* and *b jet fakes* categories are defined using the subsubleading lepton p_{T} distribution as a template, scaled by factors 3 and 0. Since these are unconstrained systematics, the choice of the scaling values does not affect the results.

Although the shapes of *electrons from b jets*, *muons from b jets*, and *muons from lights* are very similar (Figure 9.2), there are small residual differences to be considered. For this reason, a shape uncertainty, referred to as *fakes shape* uncertainty, is defined. It is computed as the maximum variation from the average content of the three histograms in each bin. The largest variation measured in each bin between the DY CR and the ttX CR is considered, resulting in the following uncertainties for the six bins in the subsubleading lepton p_{T} distribution: $[\pm 15\%, \pm 42\%, \pm 67\%, \pm 54\%, \pm 27\%, \pm 39\%]$.

Leptons from external photon conversions and photons misidentified as leptons are excluded from Figure 9.2, as only fake electrons contribute to this category and a dedicated template is used. The up and down variations for the *fake photons* are defined by scaling the nominal distribution by ± 50%. In this case, a nuisance parameter with a Gaussian prior is introduced, as the MC simulation models this source of fakes more reliably than the others, thus it is reasonable to consider the nominal value as prior.

The uncertainties associated with the *light jet fakes*, *b jet fakes*, *fake photons*, and the *fake shape* uncertainty are treated as uncorrelated across the years to account for potential differences between the data-taking periods.

Figures 9.3 and 9.4 show the nominal event yields and the variations of the fake lepton nuisance parameters for the $\mathrm{t\bar{t}}$ and DY background, respectively, in the 2018 data-taking year. The two figures display the distributions of the subsubleading lepton p_{T}, the *max TWZ output*, and the *max TTZ output*. While the ML output distributions correspond to the 3ℓ SR, the subsubleading lepton p_{T} distributions correspond to the ttX CR in Figure 9.3 and to the DY CR in Figure 9.4. It is evident that the two fake lepton categories defined by the flavour of the jet faking the lepton introduce a significant shape effect in all the distributions considered. In addition, the figures highlight the relatively small statistical impact that these backgrounds have in the most sensitive bins of the ML output distributions. For examples, in the last two bins of the *max TWZ output* distribution for the 2018 data-taking year, less than 4 events from DY and $\mathrm{t\bar{t}}$ are expected, compared to more than 15 expected tWZ events.

The templates for the remaining years of the Run 2 period are shown in A.3.

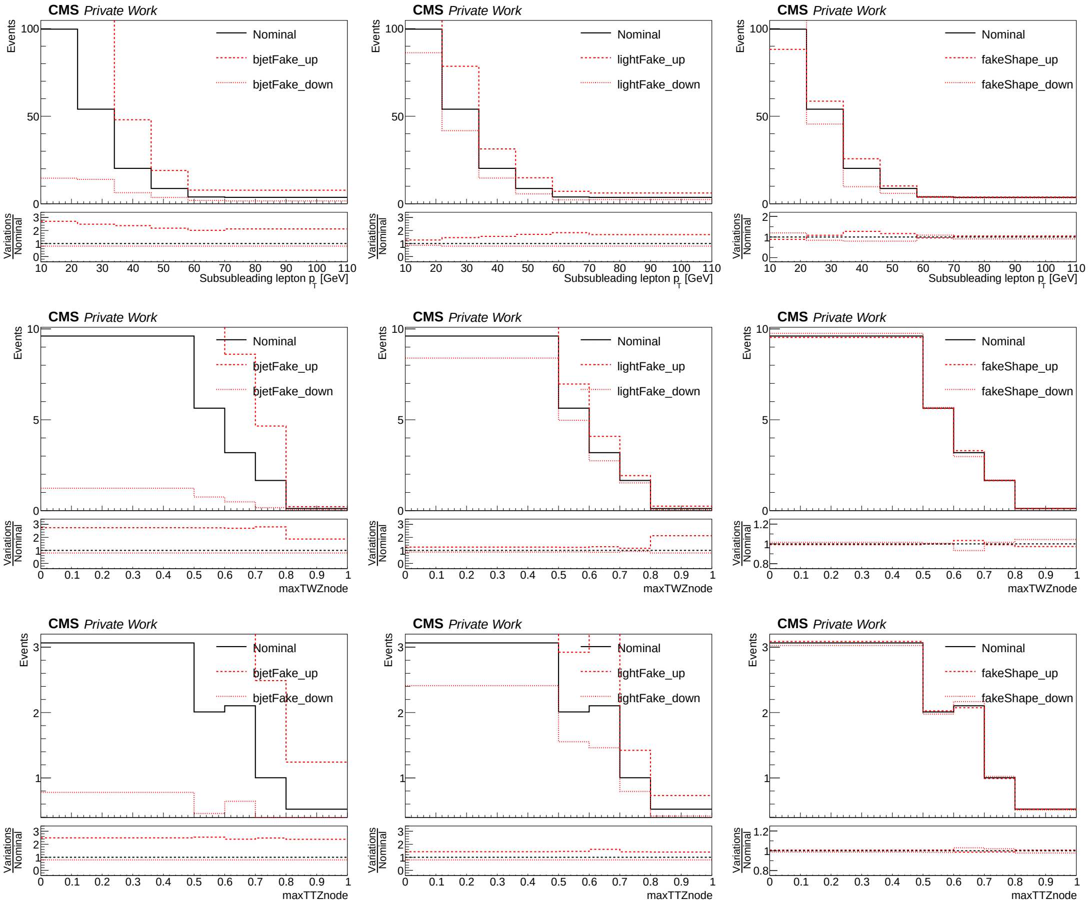

Figure 9.3: Nominal event yields and fake lepton nuisances variations for the $t\bar{t}$ background in the 2018 data-taking year. The subsubleading lepton p_T, the *max TWZ output*, and the *max TTZ output* distributions are shown from the first to the last row. The subsubleading lepton p_T distribution is presented in the ttX CR, while the ML output distributions in the 3ℓ SR. The first two columns show the templates of the *b jet fakes* and *light jet fakes* uncertainties respectively, while in the third column the templates of the *fakes shape* nuisance is presented. The black line represents the nominal distribution, while the dotted red lines indicate the up and down variations. The range in the ratio plot is adjusted to display the entire distributions.

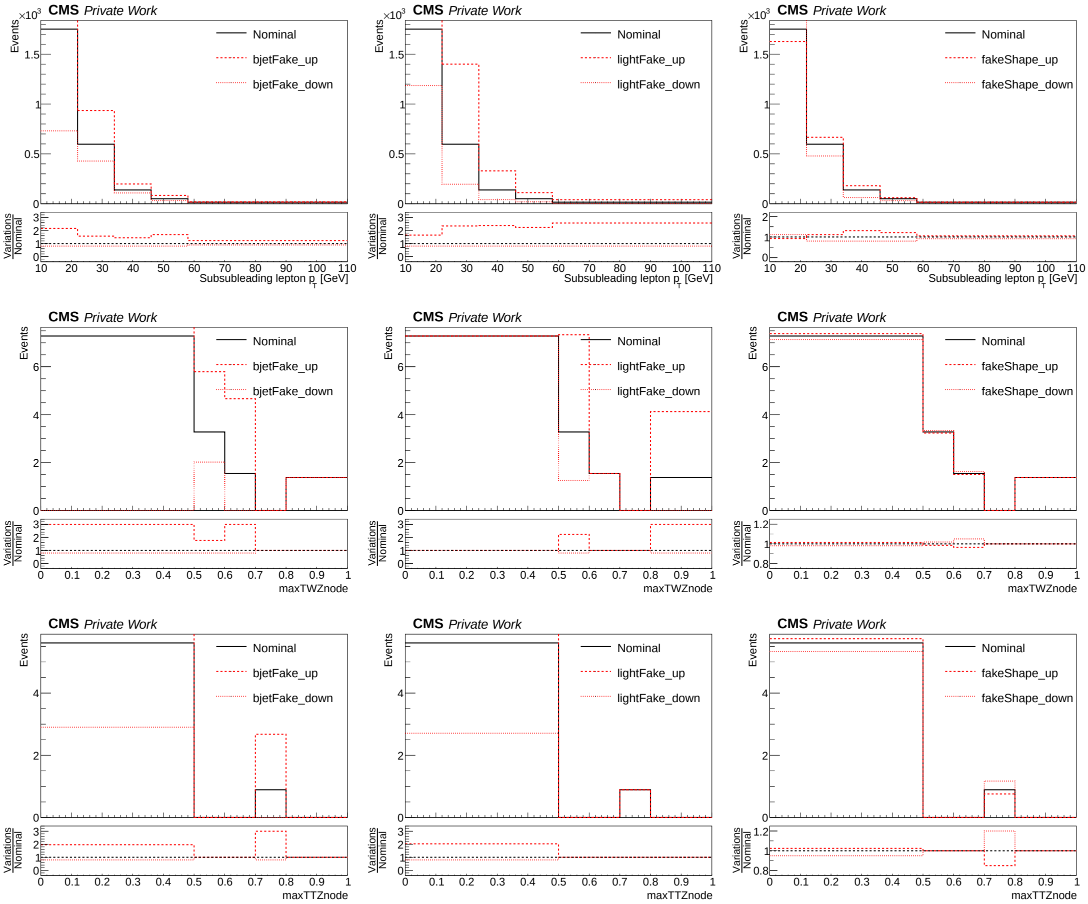

Figure 9.4: Nominal event yields and fake lepton nuisances variations for the DY background in the 2018 data-taking year. The subsubleading lepton p_{T}, the *max TWZ output*, and the *max TTZ output* distributions are shown from the first to the last row. The subsubleading lepton p_{T} distribution is presented in the DY CR, while the ML output distributions in the 3ℓ SR. The first two columns show the templates of the *b jet fakes* and *light jet fakes* uncertainties respectively, while in the third column the templates of the *fakes shape* nuisance is presented. The black line represents the nominal distribution, while the dotted red lines indicate the up and down variations. The range in the ratio plot is adjusted to display the entire distributions.

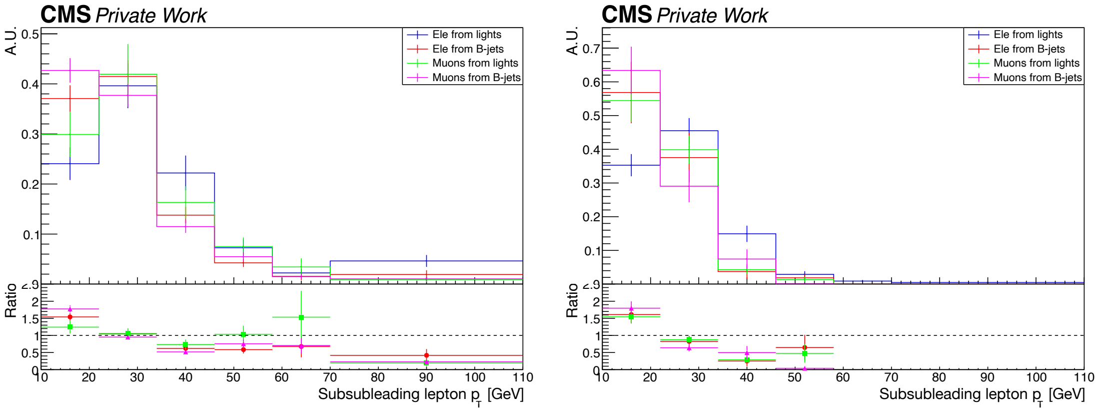

Figure 9.5: Normalised subsubleading lepton transverse momentum distribution, for the $\mathrm{t\bar{t}}$ process in the ttX CR (left) and the DY process in the DY CR (right), for the different lepton fake categories for Run 3 data.

In Run 3, the number of fake leptons is significantly reduced thanks to the improved lepton identification algorithm. This results in less than one expected event in the signal regions for the *light jet fakes* category. For this reason, it is merged with the *b jet fakes* category into a single category called *jet fakes*.

The normalised distributions of the subsubleading lepton p_{T} in the DY and ttX CR for Run 3 data are shown in Figure 9.5. These distributions include all categories before the merging into the *jet fakes* category.

The up and down variations for the unconstrained nuisances associated with the *jet fakes* category are defined using the subsubleading lepton p_{T} distribution as a template, scaled by a factor three and zero, respectively, consistent with the procedure used in Run 2. Since the *light jet fakes* category is not defined in Run 3, the *fake shape* nuisance is constructed by considering the differences among all the categories of Figure 9.5. This results in a larger shape uncertainty compared to Run 2: $[\pm33\%, \pm24\%, \pm96\%, \pm93\%, \pm57\%, \pm117\%]$. Since only an inclusive unconstrained nuisance is defined in Run 3, the *fake shape* uncertainty plays a central role in estimating potential shape effects. Additionally, in Run 3, the number of $\mathrm{t\bar{t}}$ and DY events is significantly smaller compared to Run 2 thanks to the improvements in the lepton identification algorithms.

The uncertainties associated with the *jet fakes*, *fake photons*, and the *fake shape* uncertainty are treated as uncorrelated across the years to account for potentisl differences in different taking taking periods. The nominal event yields and the variations for the fake lepton nuisance parameters for the $\mathrm{t\bar{t}}$ and DY background in the subsubleading lepton p_{T}, *max TWZ output*, and *max TTZ output* distributions for the Run 3 data-taking periods are shown in A.4.

9.2 Fit result and validation of the method

The fake lepton estimation method is tested by performing two different maximum likelihood fits on Run 2 and Run 3 data. The POI is the signal strength of the $\mathrm{t\bar{t}Z}$ process, to avoid possible bias from using directly the signal strength of the tWZ process. The fit is performed using as input variables the *max TTZ output* and *max others output* distributions in the 3ℓ SR; a one-bin template histogram for both the ZZ and WZ CRs in order to better constrain the normalisation of these processes; and the subsubleading lepton p_{T} for the ttX and DY CRs to estimate the fake lepton contribution. To avoid potential bias, the *max TWZ output* distribution in the 3ℓ SR and the *TWZ* node output in the 4ℓ SR are not used in the fit. The relevant distributions used as input in the fit are shown in Figure 9.6 for Run 2 data.

The GOF test performed using the saturated model yields a p-value of 19%, indicating that the model describes the data adequately. The impacts and pulls of the nuisance parameters (Figure 9.7) show that the unconstrained nuisances related to the fake lepton estimation are not among the dominant ones, as only three appear among those with the largest impacts (CMS_TOP24009_FAKE_B_2016PRE, CMS_TOP24009_FAKE_L_2018, and CMS_TOP24009_FAKE_B_2017). Their post-fit values are consistent with the no-corrections scenario, corresponding to a value of 0.00, and the data can constraint their uncertainties in the individual years. Larger uncertainties are observed for the *light jet fakes* category due to its lower statistical precision.

To verify that the *light jet fakes* and *b-jet fakes* unconstrained nuisances can be constrained simultaneously and that their correlation is small, a two-dimensional likelihood scan is performed, as shown in Figure 9.8. For this scan, the fake lepton nuisances are treated as correlated across years to avoid the complexity of visualising eight separate unconstrained parameters. The result confirms that both nuisances can be constrained and that their correlation is negligible.

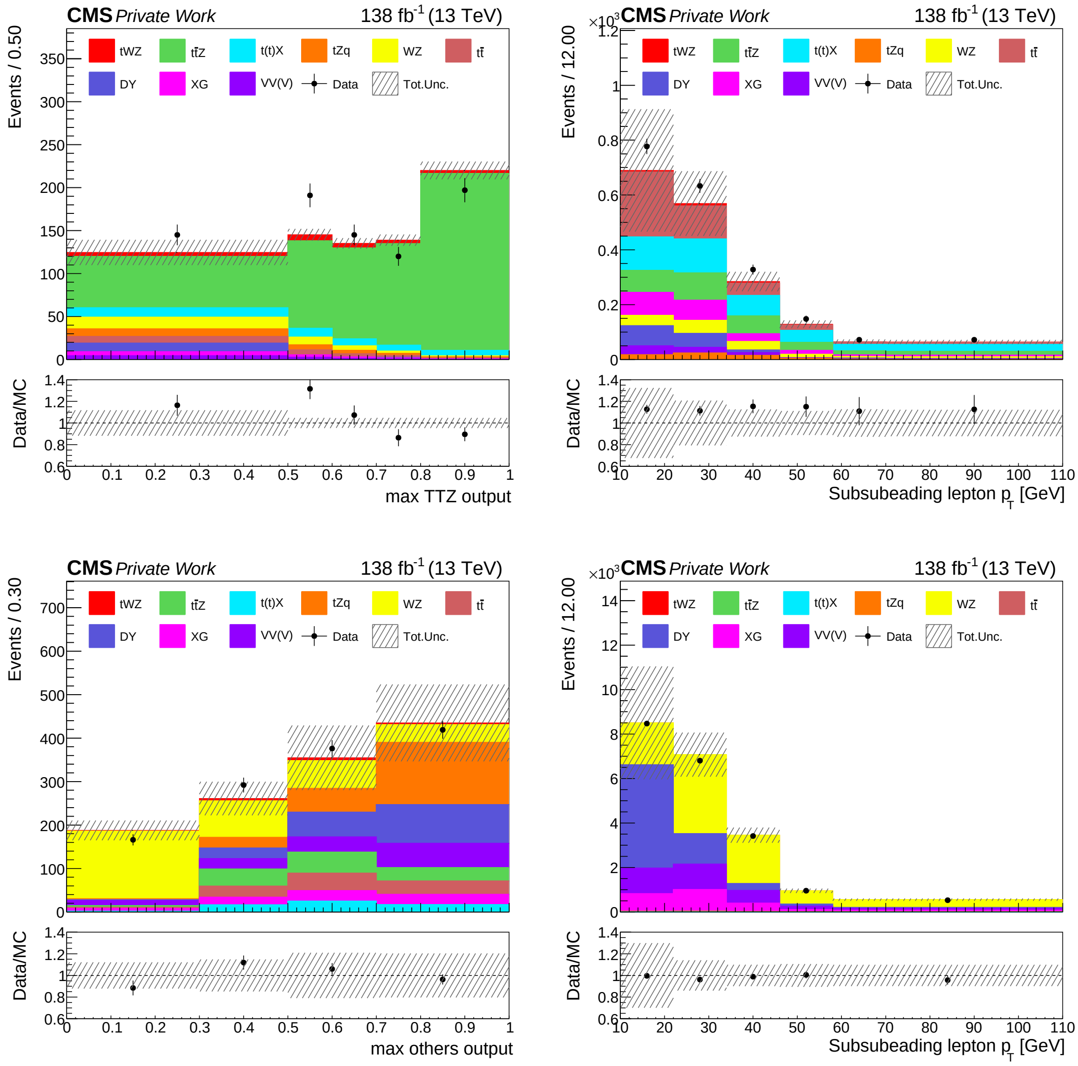

Figure 9.6: Input distribution for the maximum likelihood fit on Run 2 data. The four panels correspond to the *max TTZ output* (top left) and *max others output* (bottom left) distributions in the $3\ell SR$; and the subsubleading lepton transverse momentum distributions in the ttX CR (top right) and DY CR (bottom right). The black markers represent the data, while the solid stacked histogram shows the MC predictions for the various background processes. The dashed band indicates the total uncertainty. The lower panel displays the ratio between data and simulation.

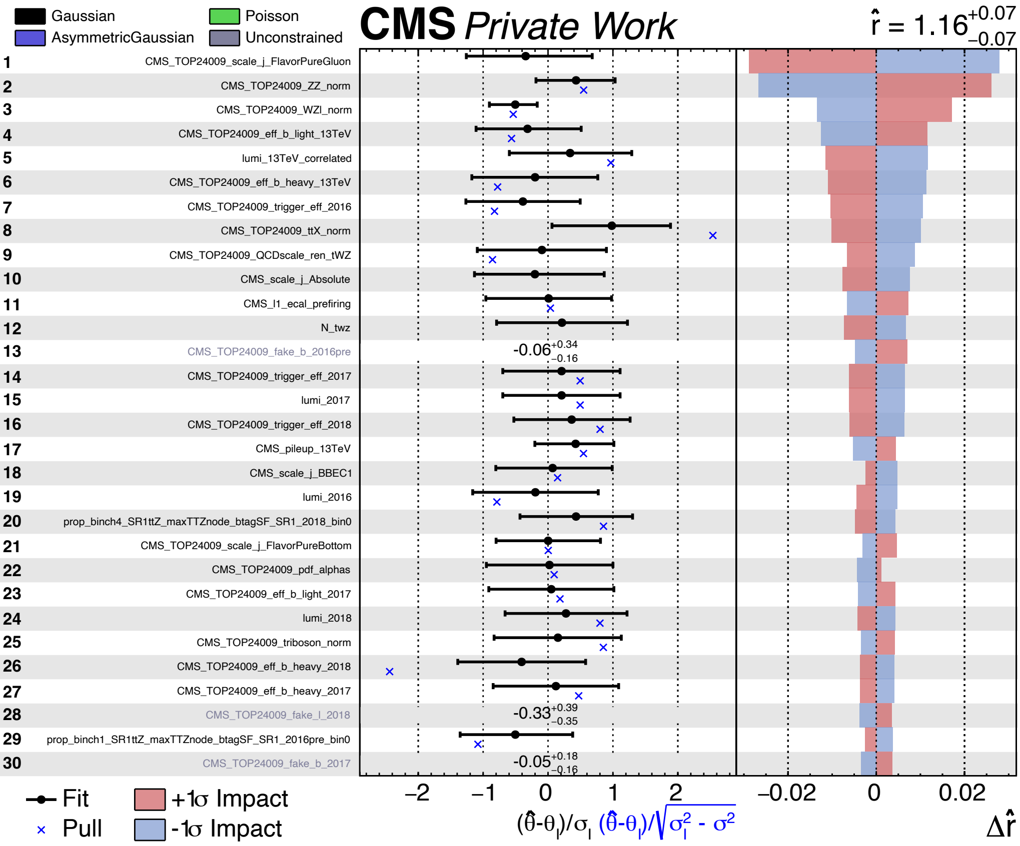

Figure 9.7: Pulls and impacts of the nuisance parameters used in the fit on Run 2 data using the signal strength of $t\bar{t}Z$ as POI.

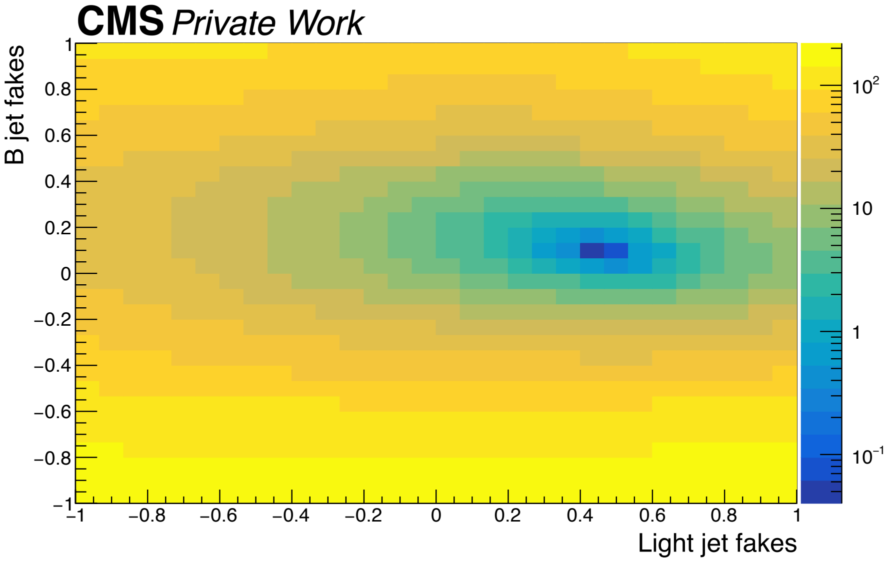

Figure 9.8: Two dimensional likelihood scan of the *light jet fakes* and *b jet fakes* nuisance parameters. The colour scale represents the change in the negative log-likelihood relative to its minimum, displayed on a logarithmic scale.

The data-MC agreement in the p_T and pseudorapidity post-fit distributions for all the leptons in the events has been verified by comparing them with the corresponding pre-fit distributions. As an example, Figures 9.9 and 9.10 show this comparison for the leading and subsubleading leptons in the DY and ttX CRs, respectively. It should be noted that only the p_T of the subsubleading lepton is used as an input to the fit. Comparing pre- and post-fit distributions illustrates how the fit constrains the large pre-fit uncertainties and improves the modelling of these distributions achieving a very good agreement between data and simulation.

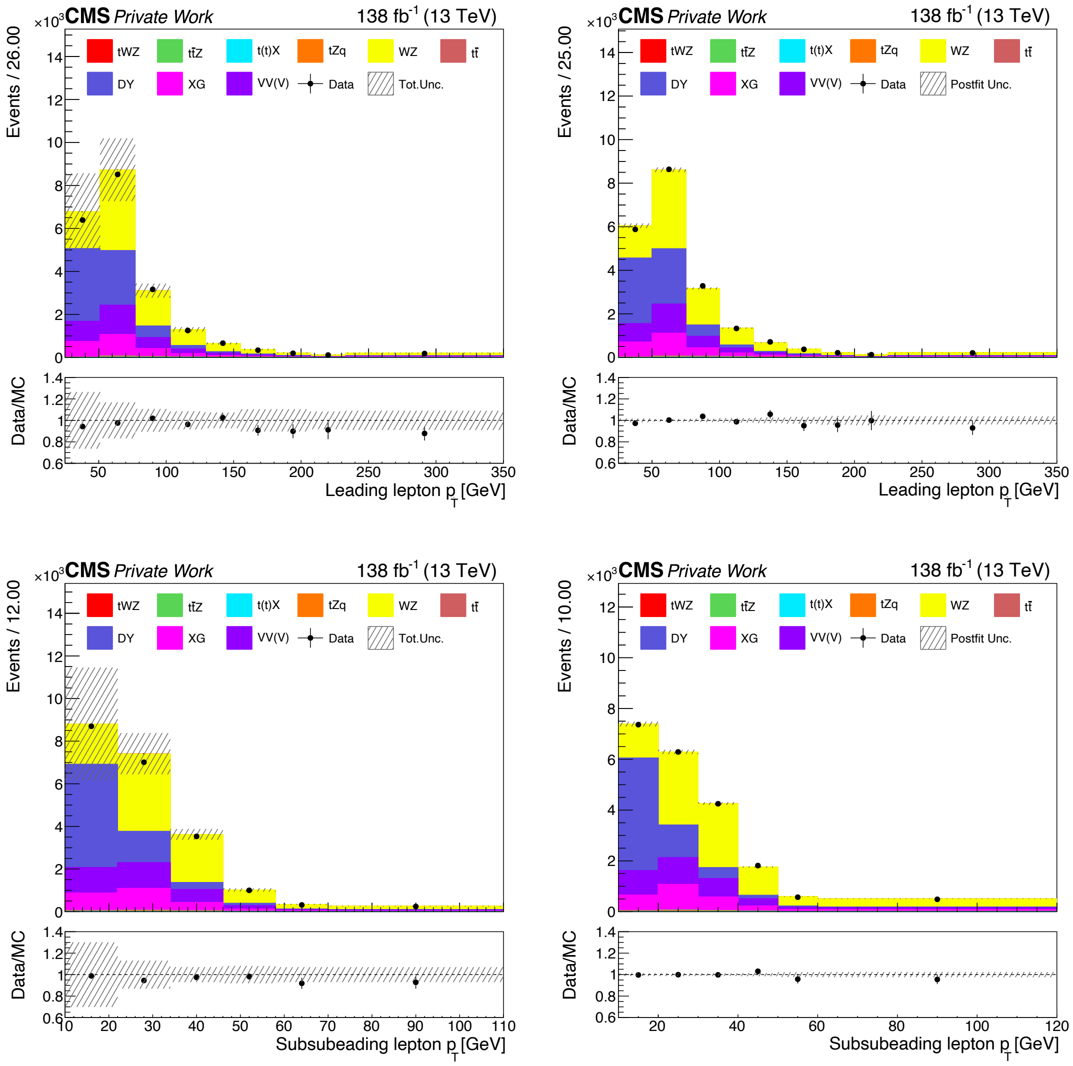

Figure 9.9: Left: Pre-fit distributions of the transverse momentum of the leading (top) and subsubleading (bottom) lepton in the DY CR for Run 2 data. The black markers represent the data, while the solid stacked histogram shows the MC predictions for the various background processes. The dashed band indicates the total uncertainty. The lower panel displays the ratio between data and simulation. Right: Post-fit distributions of the transverse momentum of the leading (top) and subsubleading (bottom) lepton in the DY CR for Run 2 data. The black markers represent the data, while the solid stacked histogram shows the MC predictions for the various background processes after the fit to data. The dashed band indicates the post-fit uncertainty. The lower panel displays the ratio between data and simulation.

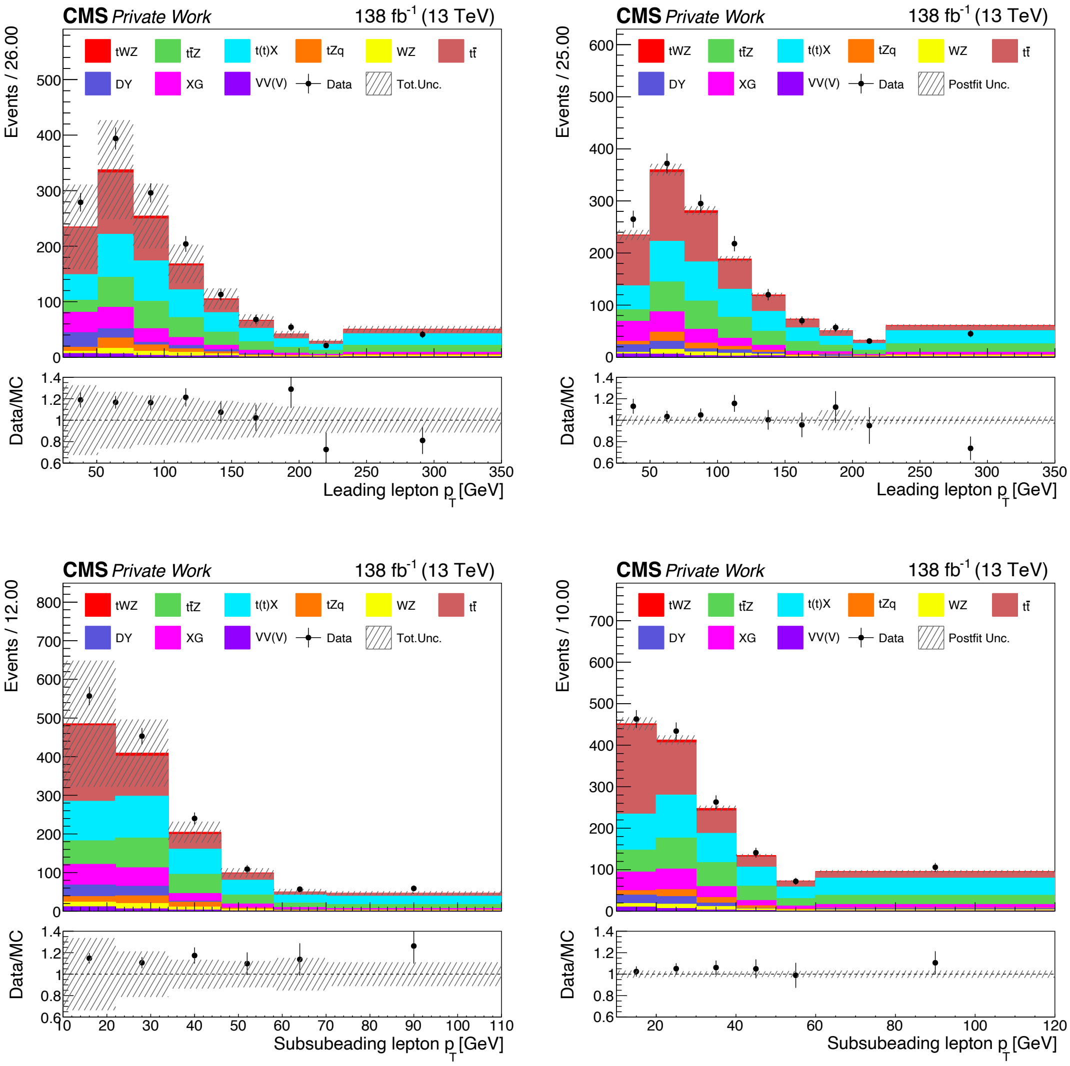

Figure 9.10: Left: Pre-fit distributions of the transverse momentum of the leading (top) and subsubleading (bottom) lepton in the ttX CR for Run 2 data. The black markers represent the data, while the solid stacked histogram shows the MC predictions for the various background processes. The dashed band indicates the total uncertainty. The lower panel displays the ratio between data and simulation. Right: Post-fit distributions of the transverse momentum of the leading (top) and subsubleading (bottom) lepton in the ttX CR for Run 2 data. The black markers represent the data, while the solid stacked histogram shows the MC predictions for the various background processes after the fit to data. The dashed band indicates the post-fit uncertainty. The lower panel displays the ratio between data and simulation.

The same procedure is also followed to perform a maximum likelihood fit on Run 3 data and the relevant distributions used as input are shown in Figure 9.11.
The model accurately describes data from the Run 3 period, as indicated by the GOF test p-value of 15%. Also in this case, the unconstrained nuisances related to the fake

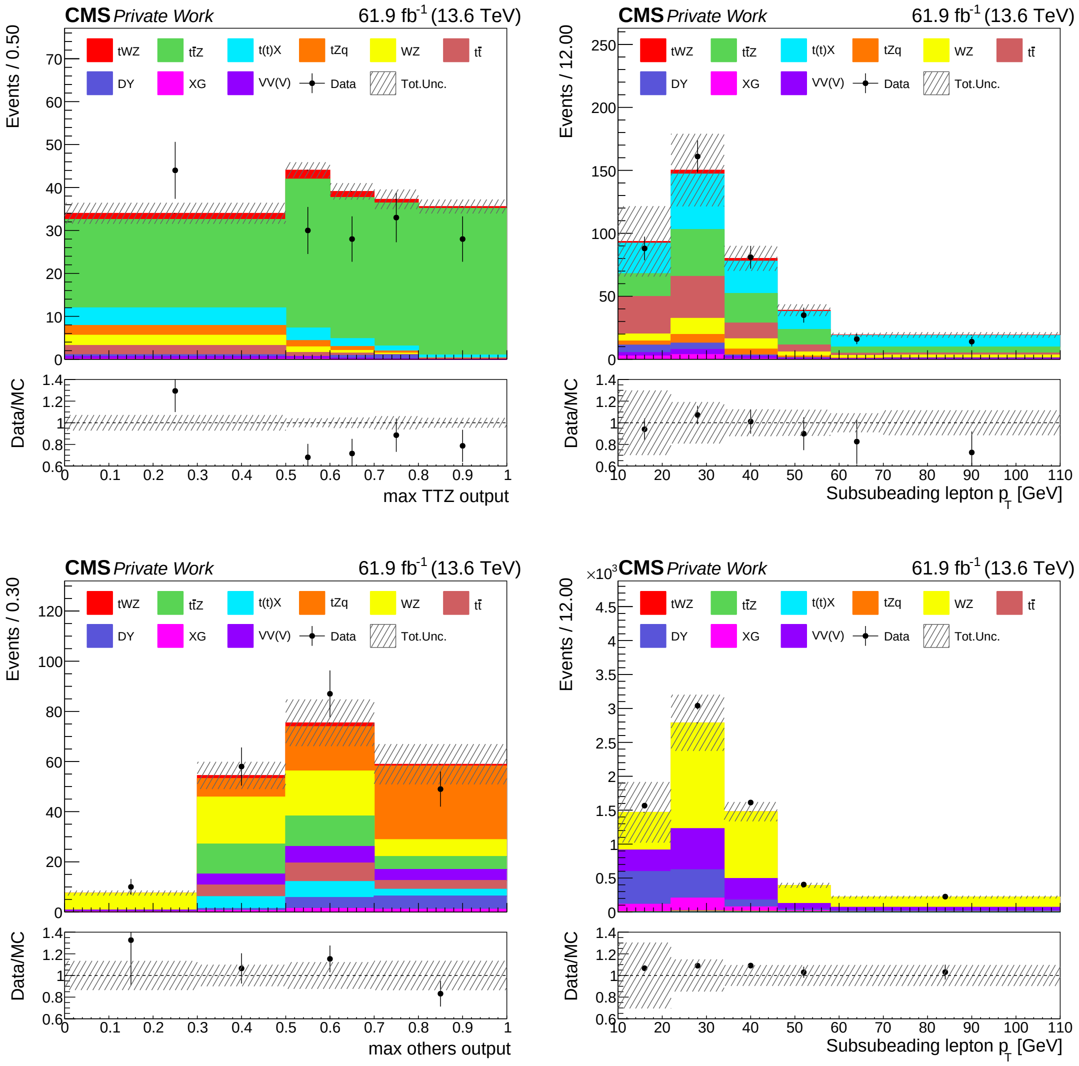

Figure 9.11: Input distribution for the maximum likelihood fit on Run 3 data. The four panels correspond to the *max TTZ output* (top left) and *max others output* (bottom left) distributions in the $3\ell SR$; and the subsubleading lepton transverse momentum distributions in the ttX CR (top right) and DY CR (bottom right). The black markers represent the data, while the solid stacked histogram shows the MC predictions for the various background processes. The dashed band indicates the total uncertainty. The lower panel displays the ratio between data and simulation.

lepton estimation have a limited impact on the result (Figure 9.12), although larger corrections are measured for the 2023 data-taking periods. To verify the accuracy of these corrections, the pre- and post-fit distributions have been validated for Run 3 data as well, and a good data-MC agreement is observed. As an example, Figures 9.13 and 9.14 display this comparison for the leading and subsubleading leptons in the DY and ttX CRs.

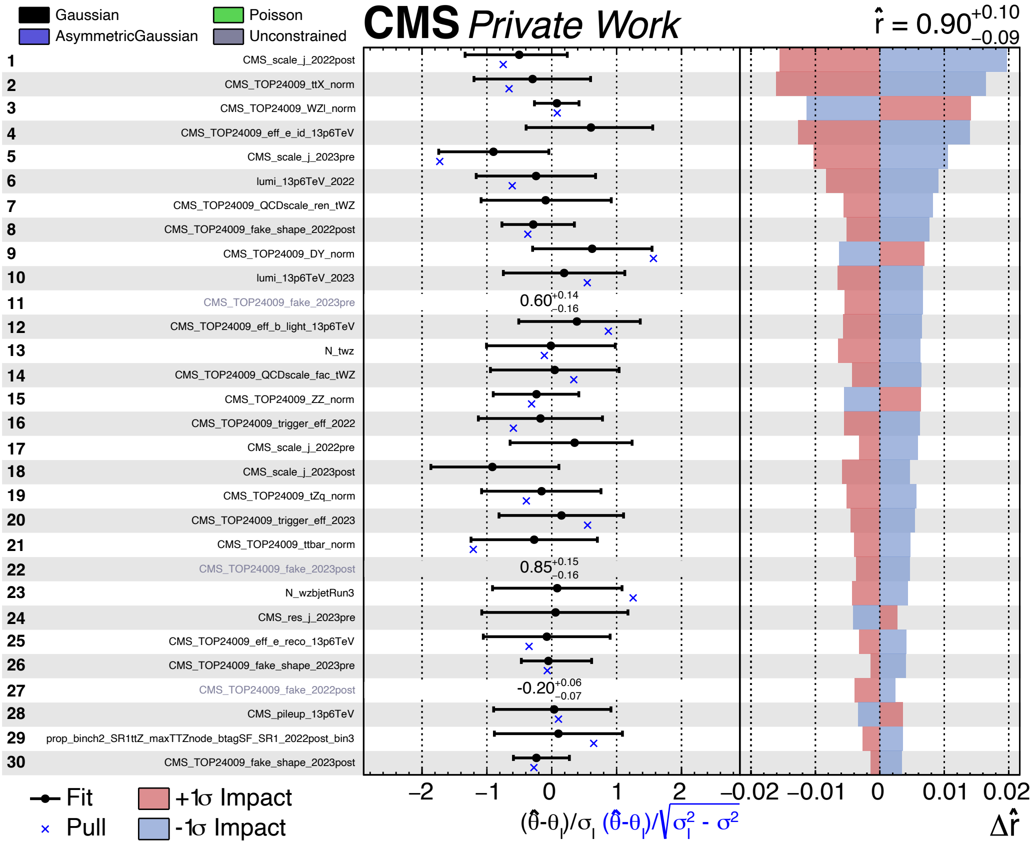

Figure 9.12: Pulls and impacts of the nuisance parameters used in the fit on Run 3 data using the signal strength of $t\bar{t}Z$ as POI.

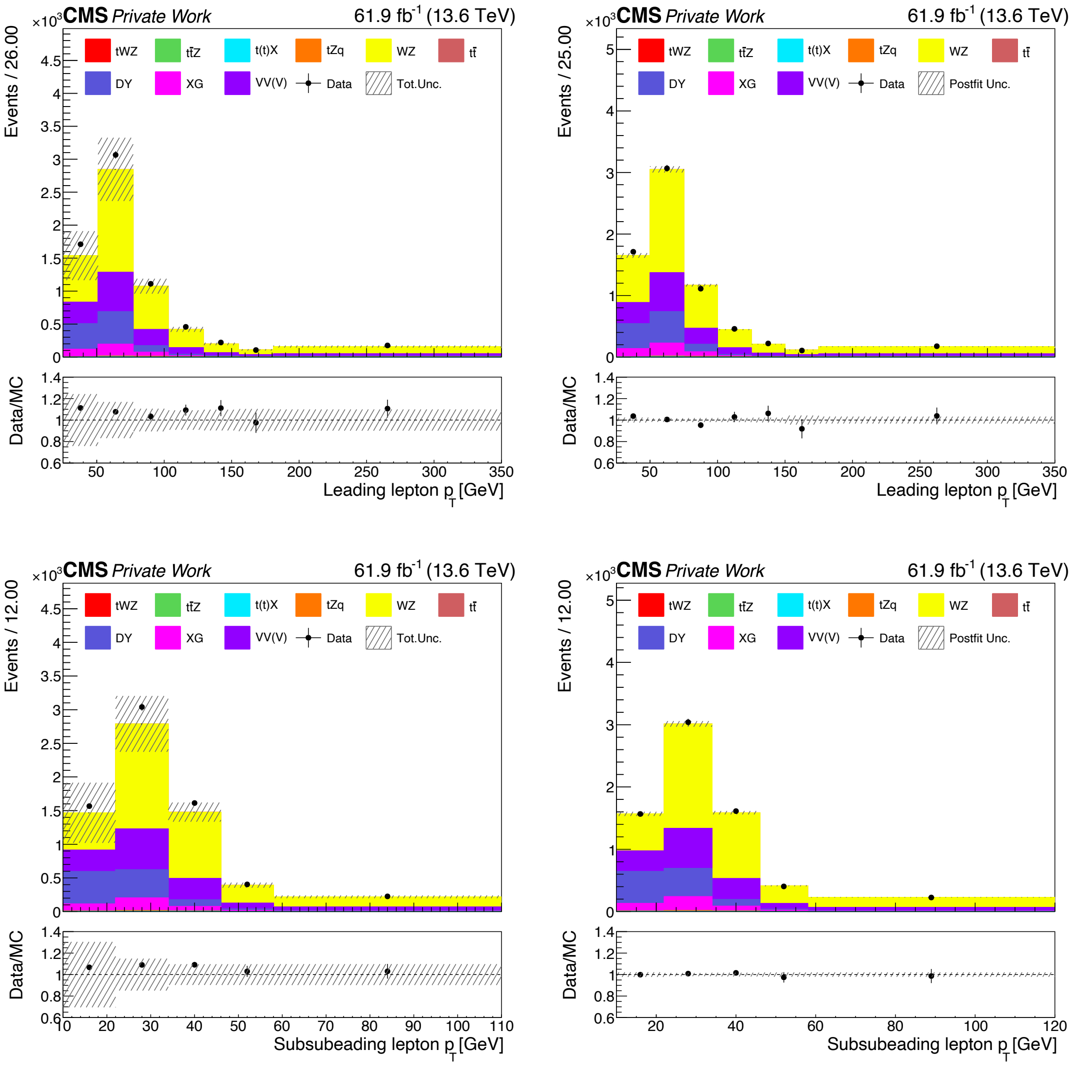

Figure 9.13: Left: Pre-fit distributions of the transverse momentum of the leading (top) and subsubleading (bottom) lepton in the DY CR for Run 3 data. The black markers represent the data, while the solid stacked histogram shows the MC predictions for the various background processes. The dashed band indicates the total uncertainty. The lower panel displays the ratio between data and simulation. Right: Post-fit distributions of the transverse momentum of the leading (top) and subsubleading (bottom) lepton in the DY CR for Run 3 data. The black markers represent the data, while the solid stacked histogram shows the MC predictions for the various background processes after the fit to data. The dashed band indicates the post-fit uncertainty. The lower panel displays the ratio between data and simulation.

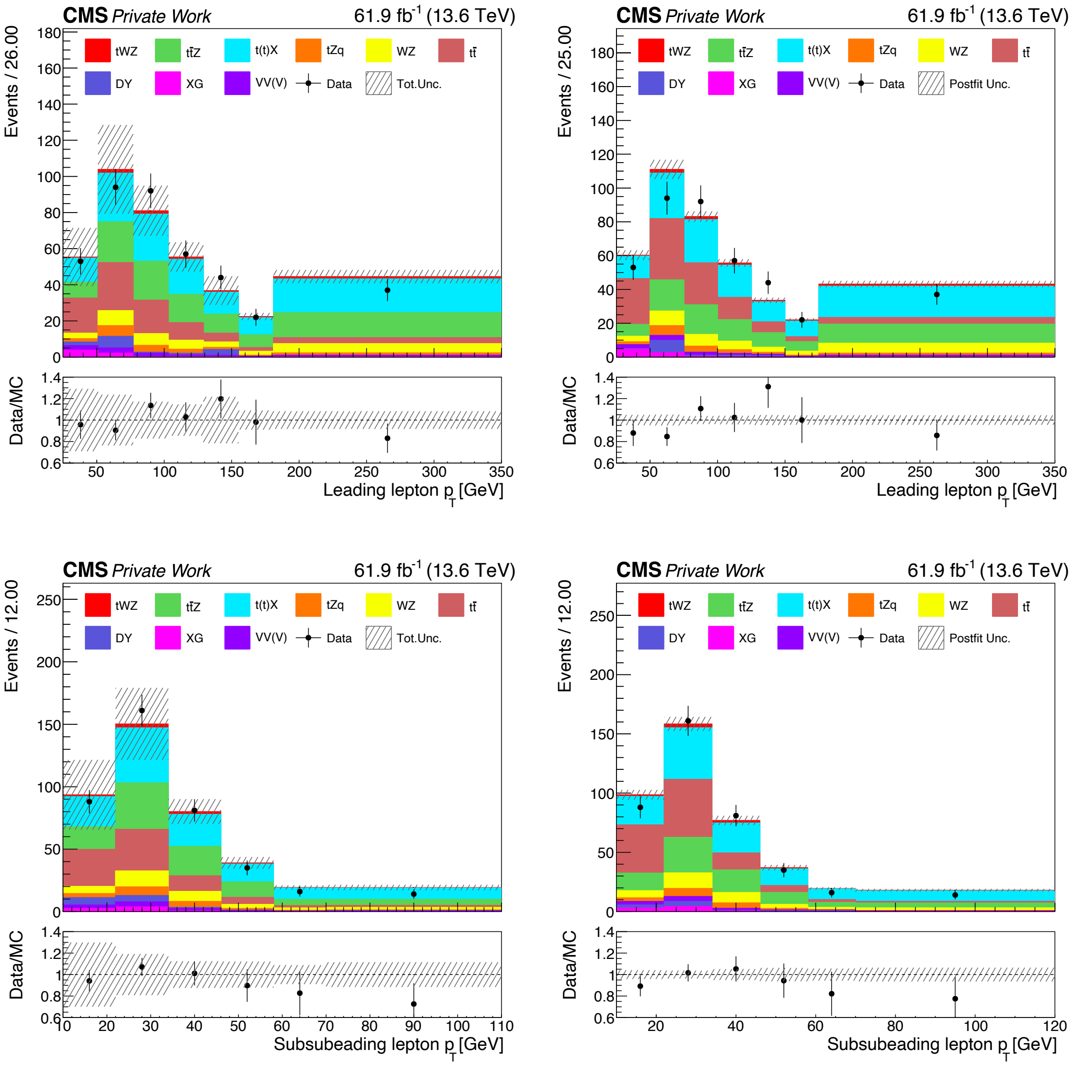

Figure 9.14: Left: Pre-fit distributions of the transverse momentum of the leading (top) and subsubleading (bottom) lepton in the ttX CR for Run 3 data. The black markers represent the data, while the solid stacked histogram shows the MC predictions for the various background processes. The dashed band indicates the total uncertainty. The lower panel displays the ratio between data and simulation. Right: Post-fit distributions of the transverse momentum of the leading (top) and subsubleading (bottom) lepton in the ttX CR for Run 3 data. The black markers represent the data, while the solid stacked histogram shows the MC predictions for the various background processes after the fit to data. The dashed band indicates the post-fit uncertainty. The lower panel displays the ratio between data and simulation.

Chapter 10

Results

Two binned maximum likelihood fits are performed in order to extract the value of the tWZ signal strength in Run 2 and Run 3 data. The results are used to compute the tWZ cross section at 13 and 13.6 TeV. A simultaneous fit of Run 2 and Run 3 data is performed to extract the tWZ signal strength and the statistical significance exploiting the larger statistical power of the combined dataset. The maximum likelihood fits are performed using as input the ParT maximum score distribution for the *TWZ*, *TTZ*, and *others* output nodes in the 3ℓ SR; the output score of the *TWZ* node in the 4ℓ SR; a one-bin template histogram for the ZZ CR in order to better constrain the normalisation of this process; the jet multiplicity distribution for the WZ CR to constrain the uncertainty on the jet multiplicity reweighting performed for the WZ background; the subsubleading lepton p_{T} for the ttX and DY CRs to estimate the fake lepton distribution.

10.1 Run 2

The pre-fit distributions for the Run 2 period are shown in A.5, while the post-fit distributions are shown in Figures 10.1 and 10.2.

Good agreement is observed in all distributions, with only small fluctuations in the *max TTZ output.* Several tests have been performed using different binning schemes to investigate this feature. In particular, the number of bins was set to 1 and to 10, yielding results compatible with those obtained with the current binning. Additionally, a χ^2 test was performed on this distribution to assess the compatibility between data and simulation, yielding a p-value of 5%. This corresponds to a deviation of about 2σ which was considered acceptable.

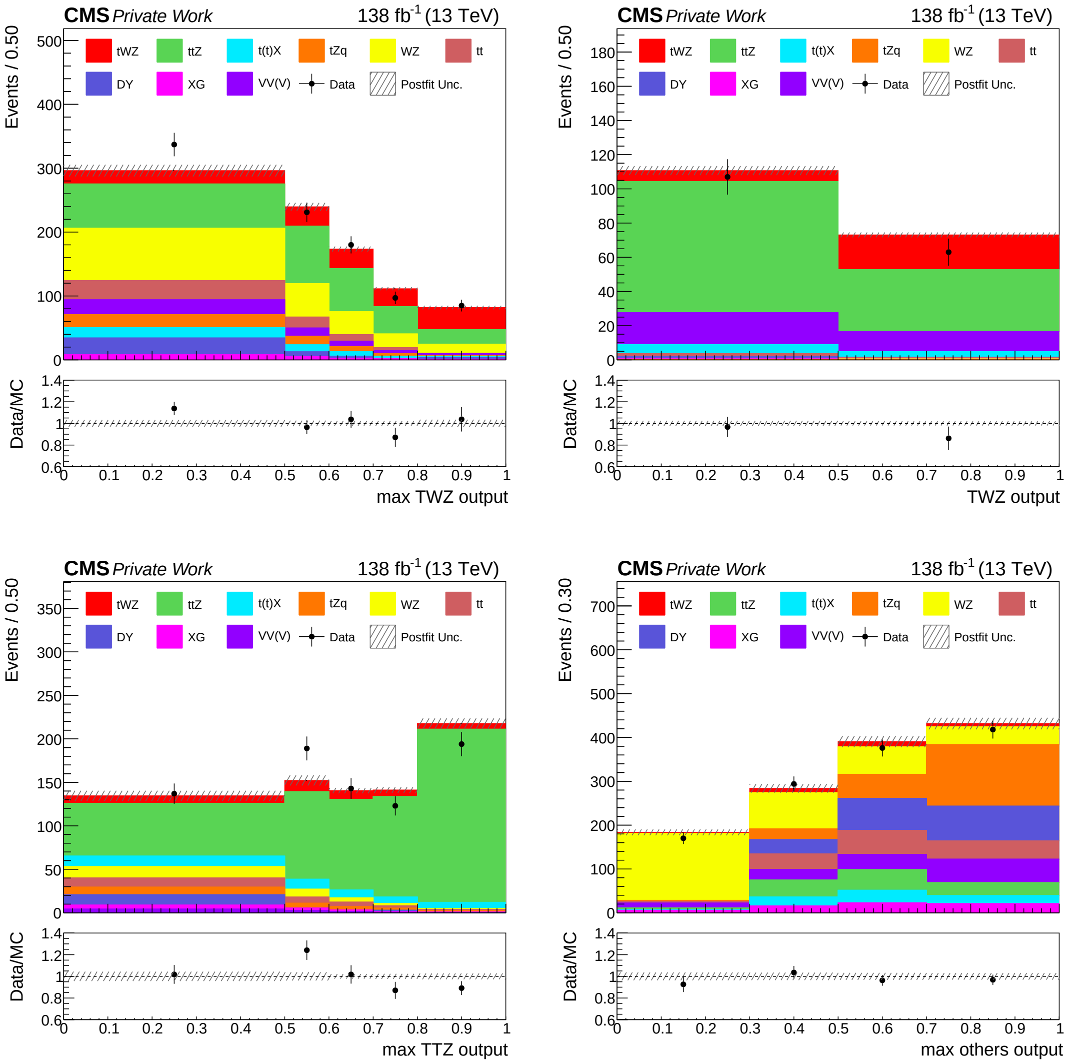

Figure 10.1: Post-fit distributions in the SRs for the fit on Run 2 data. The *max TWZ output* (top left), *max TTZ output* (bottom left), and *max others output* (bottom right) distributions are shown in the 3ℓ SR, while the tWZ ML output node distribution (top right) is shown in the 4ℓ SR. The black markers represent the data, while the solid stacked histogram shows the MC predictions for the various background processes after the fit to data. The dashed band indicates the post-fit uncertainty. The lower panel displays the ratio between data and simulation.

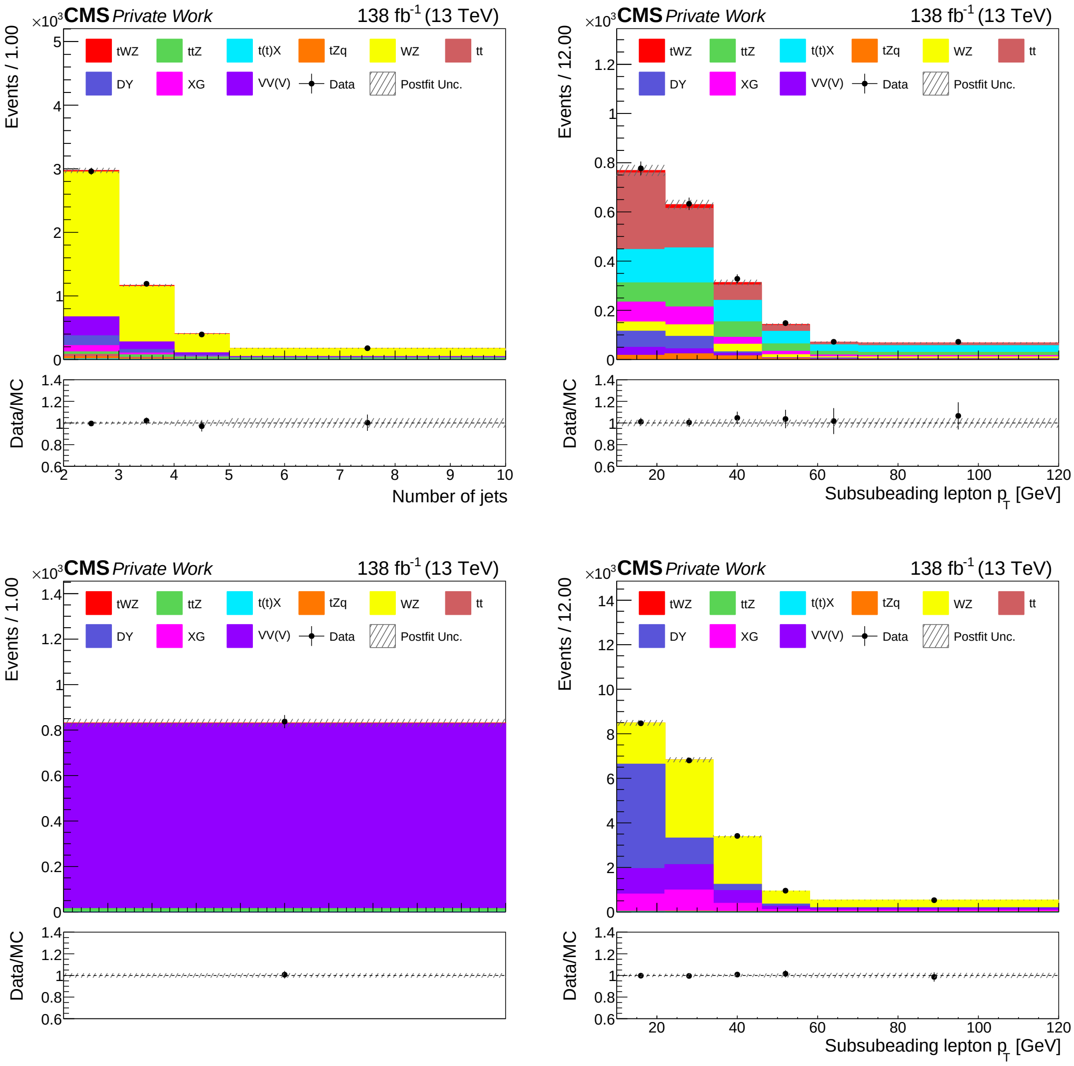

Figure 10.2: Post-fit distributions in the CRs for the fit on Run 2 data. The jet multiplicity distribution is shown in the WZ CR (top left), the event yields in the ZZ CR (bottom left), and the subsubleading lepton transverse momentum in the ttX CR (top right) and DY CR (bottom right). The black markers represent the data, while the solid stacked histogram shows the MC predictions for the various background processes after the fit to data. The dashed band indicates the post-fit uncertainty. The lower panel displays the ratio between data and simulation.

Table 10.1: Prefit and postfit yields in the different SRs in Run 2. The uncertainty on the event yields includes only the normalisation uncertainty. The tWZ process has no normalisation uncertainty, as it is the POI. Uncertainties smaller than 0.5 are omitted.

	3 ℓ SR *TWZ* node		3 ℓ SR *TTZ* node		3 ℓ SR *others* node		4 ℓ SR	
	Prefit	Postfit	Prefit	Postfit	Prefit	Postfit	Prefit	Postfit
tWZ	79	130	24	40	17	29	15	24
t$\bar{\text{t}}$Z	302 ± 21	299 ± 14	591 ± 41	587 ± 28	123 ± 9	122 ± 6	116 ± 8	115 ± 6
t(t)X	41 ± 8	46 ± 9	43 ± 9	49 ± 10	60 ± 12	70 ± 14	10 ± 2	12 ± 2
tZq	44 ± 5	45 ± 4	23 ± 2	23 ± 2	224 ± 25	217 ± 21	-	-
WZ	208 ± 21	205 ± 10	31 ± 3	31	345 ± 35	332 ± 16	1	1
t$\bar{\text{t}}$	46 ± 2	63 ± 3	21 ± 1	27 ± 1	99 ± 5	135 ± 6	2	2
DY	37 ± 4	44 ± 4	11 ± 1	13 ± 1	173 ± 17	187 ± 18	1	1
X+γ	19 ± 2	19 ± 2	10 ± 1	10 ± 1	72 ± 7	67 ± 7	1	1
VV(V)	48 ± 5	50 ± 3	10 ± 1	8 ± 1	125 ± 13	122 ± 7	31 ± 3	31 ± 2
All bkgs	745 ± 28	771 ± 21	739 ± 46	747 ± 31	1221 ± 43	1253 ± 28	161 ± 8	162 ± 7
All SM	824 ± 28	901 ± 21	763 ± 46	787 ± 31	1238 ± 43	1280 ± 28	176 ± 8	186 ± 7
Data	923	923	798	798	1253	1253	170	170

Table 10.1 shows the pre- and post-fit event yields for the 3ℓ and 4ℓ SRs in Run 2. A slight excess of data is observed in the pre-fit yields, particularly in the TWZ node of the 3ℓ SR, while the post-fit yields show improved agreement, mainly due to the increased number of tWZ events.

Also the GOF test indicates that the model describes the data accurately, yielding a p-value of 7%. The impacts and pulls of the nuisance parameters for the fit on Run 2 data are shown in Figure 10.3. The leading uncertainties arise from the uncertainties on the normalisation of the t$\bar{\text{t}}$Z and WZ+b background processes. No significant pulls are observed and, among the most significant uncertainties, only the DR modelling uncertainty has a one-sided impact, as expected by construction. The fake lepton unconstrained nuisance parameters have little impact on the analysis and remain compatible with the no-uncertainty scenario, as observed in the fake lepton estimation validation fit on Run 2 data.

The measured tWZ signal strength is 1.82 ± 0.38, corresponding to an excess of about 2 s.d. with respect to the SM prediction. The signal strength is measured with an observed statistical significance of 5.1 s.d., therefore this results marks the first observation of the tWZ process. The expected statistical significance is 3.0 s.d., representing an improvement of a factor two with respect to the previous measurement [108]. The improvement is mainly driven by the enhanced ML algorithm performance and the definition of a t$\bar{\text{t}}$Z-enriched region based on its output score, which improved the

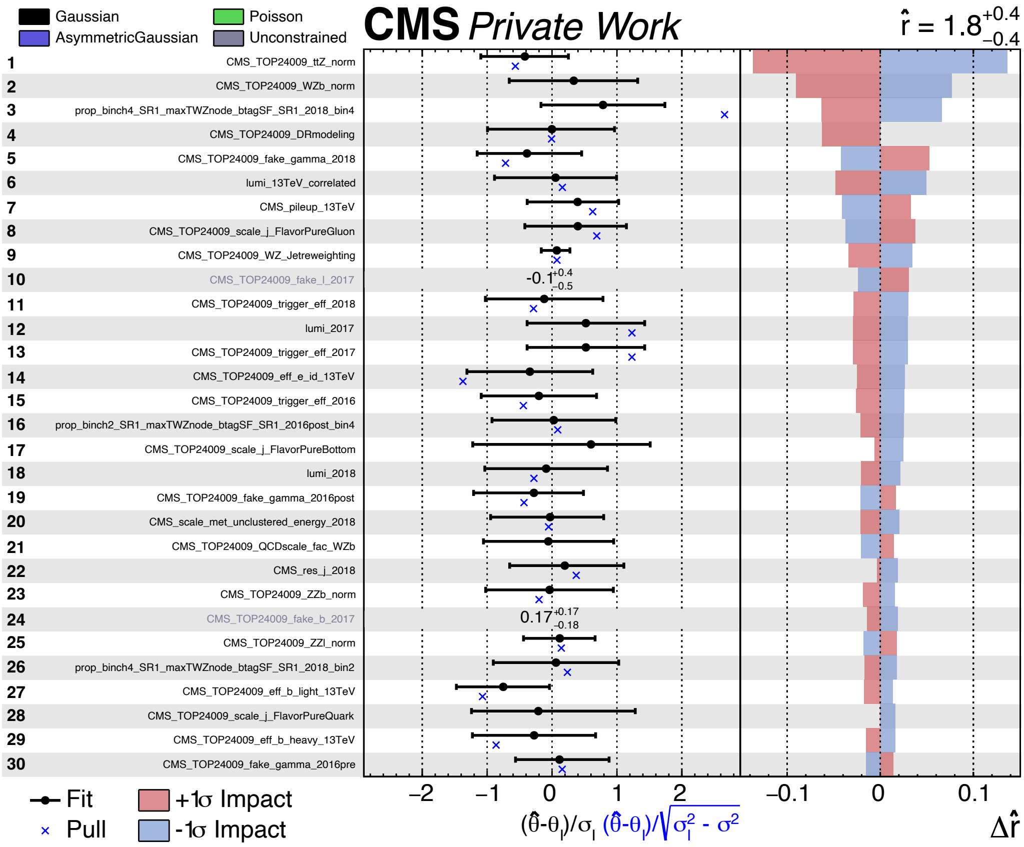

Figure 10.3: Pulls and impacts of the nuisance parameters used in the fit on Run 2 data.

constraint of the $t\bar{t}Z$ normalisation uncertainty and significantly reduced its impact compared to the previous analysis.

Figure 10.4 shows the likelihood scan of the signal strength for the fit on Run 2 data and reports the breakdown of the uncertainty into statistical and systematic components, highlighting that statistical and systematic uncertainties contribute roughly equally to the total.

The measured signal strength is used to extract the tWZ cross section at 13 TeV, yielding

$$\sigma_{\mathrm{tWZ}}(13\,\mathrm{TeV}) = 248 \pm 38\,(\mathrm{stat}) \pm 35\,(\mathrm{syst})\ \mathrm{fb}. \tag{10.1}$$

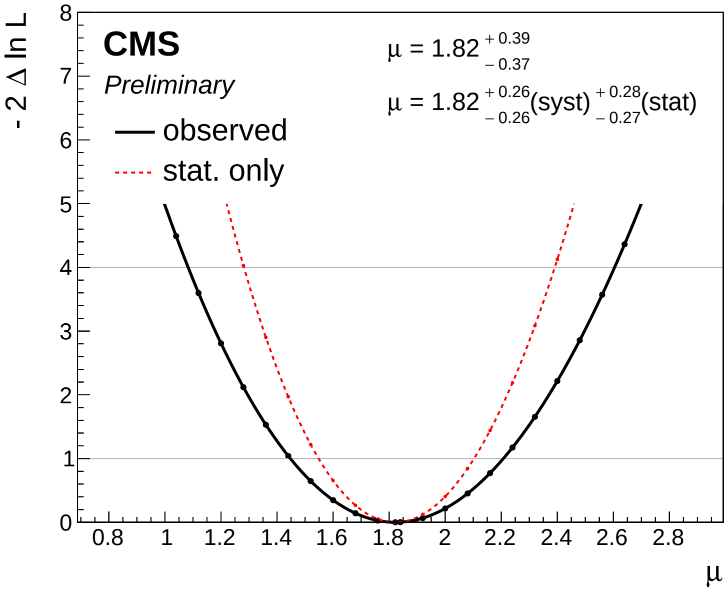

Figure 10.4: Likelihood scan of the tWZ signal strength for the fit on Run 2 data. The solid black line represents the likelihood scan considering the total uncertainty, while the dotted red line includes only the statistical component. Published in [209].

10.2 Run 3

The pre-fit distributions for the Run 3 period are shown in A.6, while the post-fit distributions are shown in Figures 10.5 and 10.6.

Good data-MC agreement is observed also in this case, with fluctuations in the *max*

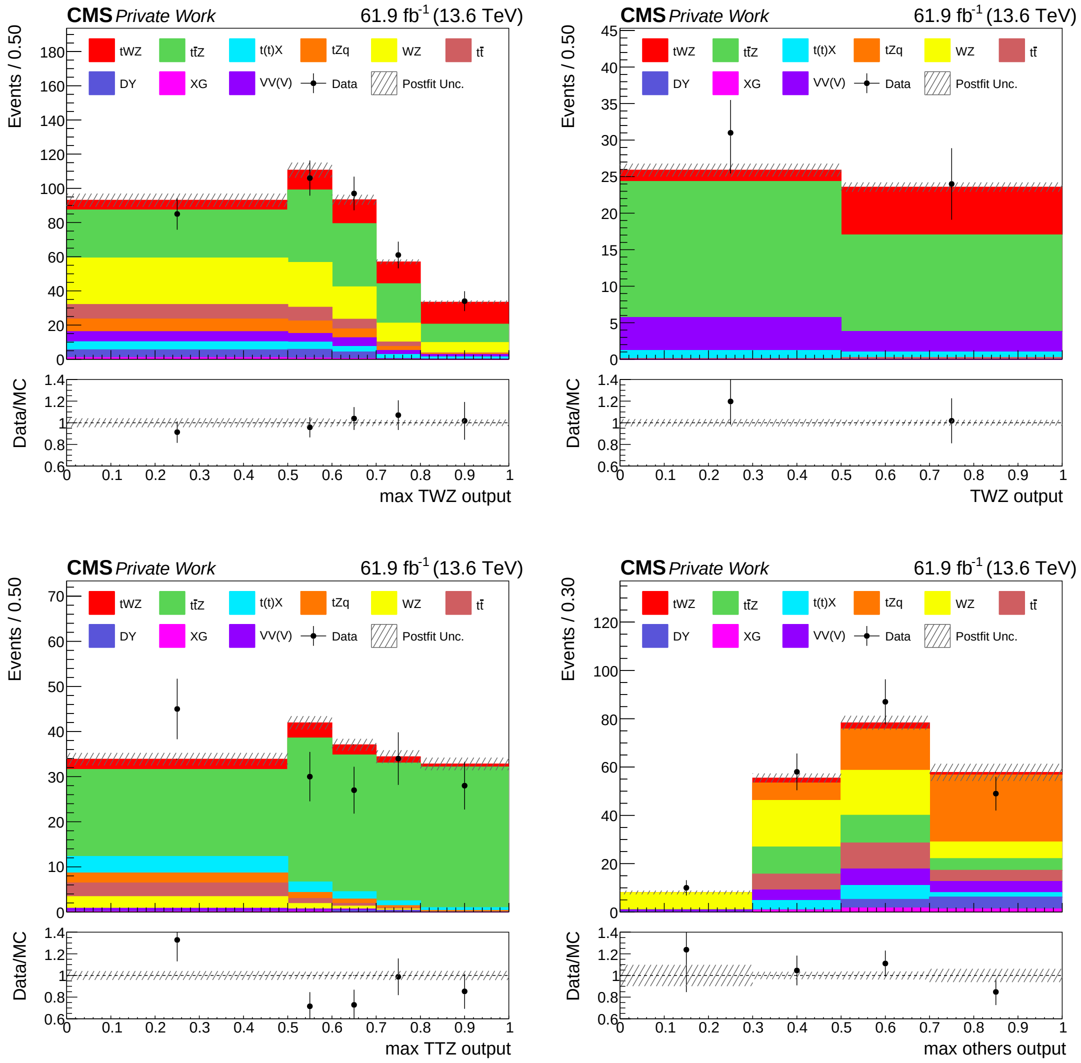

Figure 10.5: Post-fit distributions in the SRs for the fit on Run 3 data. The *max TWZ output* (top left), *max TTZ output* (bottom left), and *max others output* (bottom right) distributions are shown in the 3ℓ SR, while the tWZ ML output node distribution (top right) is shown in the 4ℓ SR. The black markers represent the data, while the solid stacked histogram shows the MC predictions for the various background processes after the fit to data. The dashed band indicates the post-fit uncertainty. The lower panel displays the ratio between data and simulation.

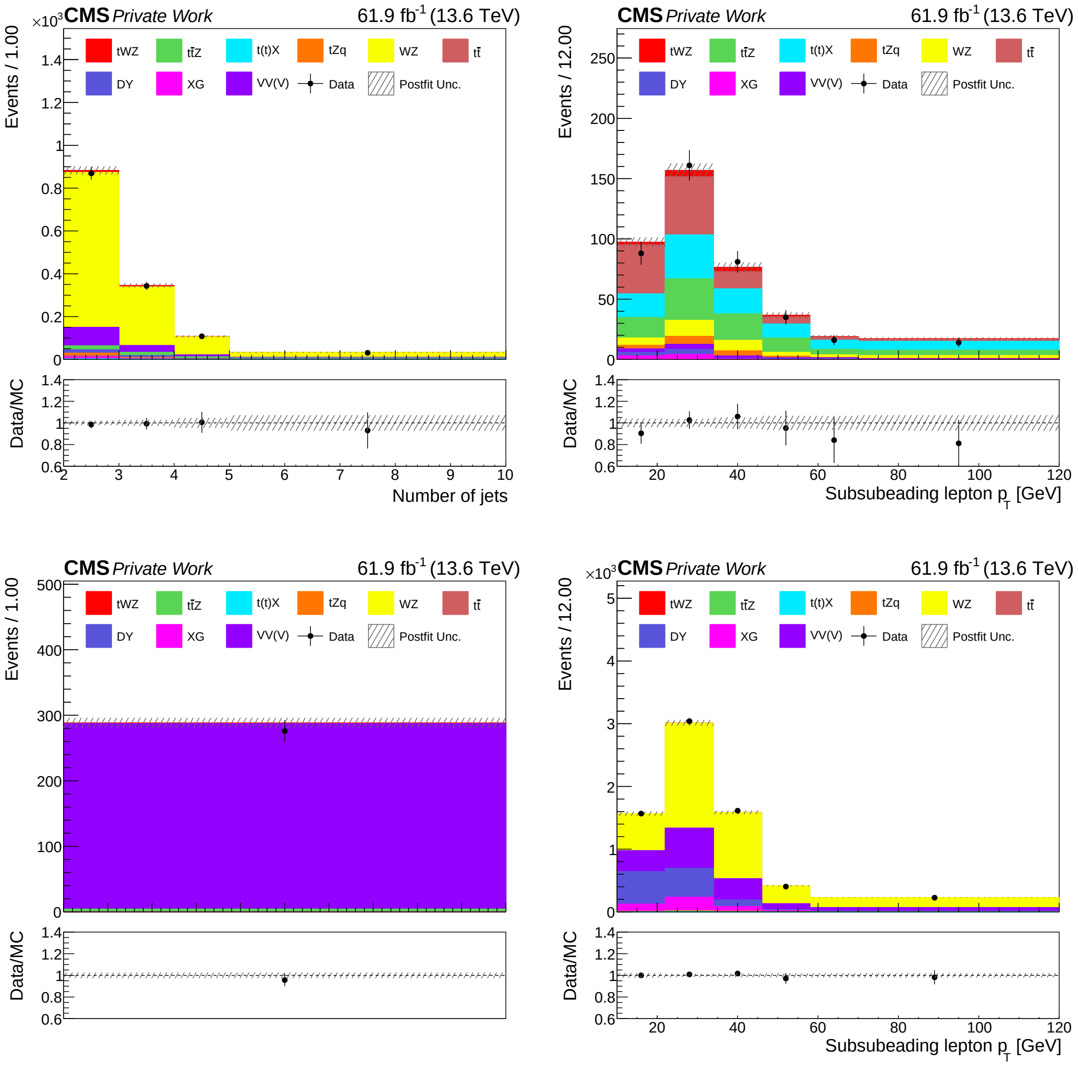

Figure 10.6: Post-fit distributions in the CRs for the fit on Run 3 data. The jet multiplicity distribution is shown in the WZ CR (top left), the event yields in the ZZ CR (bottom left), and the subsubleading lepton transverse momentum in the ttX CR (top right) and DY CR (bottom right). The black markers represent the data, while the solid stacked histogram shows the MC predictions for the various background processes after the fit to data. The dashed band indicates the post-fit uncertainty. The lower panel displays the ratio between data and simulation.

TTZ output distribution similar in size but opposite in direction to those observed in the Run 2 period. This pattern suggests statistical fluctuations rather than mismodelling in the output distribution of the ML algorithm as the reason for the observed discrepancies.

Table 10.2: Prefit and postfit yields in the different SRs in Run 3. The uncertainty on the event yields includes only the normalisation uncertainty. The tWZ process has no normalisation uncertainty, as it is the POI. Uncertainties smaller than 0.5 are omitted.

	3 ℓ SR *TWZ* node		3 ℓ SR *TTZ* node		3 ℓ SR *others* node		4 ℓ SR	
	Prefit	Postfit	Prefit	Postfit	Prefit	Postfit	Prefit	Postfit
tWZ	35	55	6	10	4	5	5	8
$t\bar{t}$Z	149 ± 10	141 ± 8	156 ± 9	142 ± 8	29 ± 2	28 ± 2	34 ± 2	32 ± 2
t(t)X	21 ± 4	20 ± 4	11 ± 2	10 ± 2	14 ± 3	13 ± 3	3 ± 1	2
tZq	24 ± 3	23 ± 2	5 ± 1	5 ± 1	54 ± 5	52 ± 5	-	-
WZ	87 ± 9	86 ± 4	5	5	50 ± 5	49 ± 2	-	-
$t\bar{t}$	19 ± 1	25 ± 1	4	5	16 ± 1	22 ± 1	-	-
DY	16 ± 2	14 ± 1	2	1	10 ± 1	8 ± 1	-	-
X+γ	2	2	-	-	3	4	-	-
VV(V)	20 ± 1	20 ± 1	2	1	17 ± 1	16 ± 1	7 ± 1	7 ± 1
All bkgs	338 ± 12	331 ± 10	184 ± 9	169 ± 7	194 ± 10	192 ± 6	44 ± 1	42 ± 1
All SM	373 ± 12	386 ± 10	190 ± 9	179 ± 7	198 ± 10	197 ± 6	49 ± 1	50 ± 1
Data	384	384	163	163	204	204	55	55

Table 10.2 reports the pre- and post-fit event yields for the 3ℓ and 4ℓ SRs in Run 3, showing good agreement even before the fit. By comparing the event yields with those from the Run 2 period, the lower statistical precision of the Run 3 dataset, mostly due to the smaller integrated luminosity, is evident.

The GOF test yields a p-value of 87%, proving that the model describes the data precisely. Figure 10.7 shows the impacts and pulls of the nuisance parameters for the Run 3 fit. The leading uncertainties are the normalisation of the $t\bar{t}$Z and WZ+b background processes, consistent with those observed in the Run 2 fit. No one-sided impacts are observed, besides the DR modelling uncertainty, and no particularly significant deviations are observed in the pulls. The $t\bar{t}$Z normalisation uncertainty has a negative pull similar in direction but larger in magnitude than that observed in Run 2. Given the 7% normalisation uncertainty associated with $t\bar{t}$Z, this pull corresponds to a decrease of about 6% in the $t\bar{t}$Z cross section. The unconstrained fake lepton nuisance parameters are not particularly significant and have similar values to those from the Run 3 fake lepton estimation validation fit.

The measured tWZ signal strength is 1.64 ± 0.52, with an observed statistical significance of 3.4 s.d., compared to an expected of 2.1 s.d.. The result is compatible with that of Run 2, although the excess with respect to the SM prediction is slightly smaller in this case.

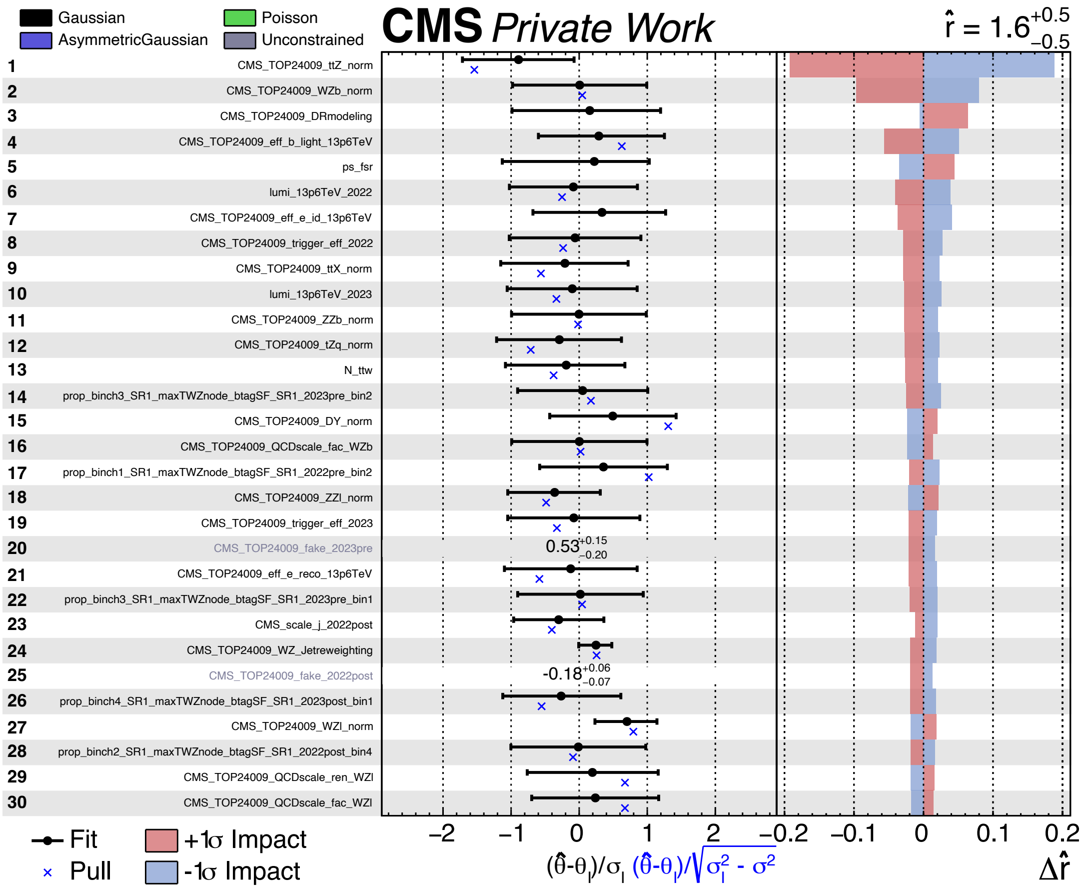

Figure 10.7: Pulls and impacts of the nuisance parameters used in the fit on Run 3 data.

Figure 10.8 shows the likelihood scan of the signal strength for the fit on Run 3 data and provides the breakdown of the total uncertainty into its statistical and systematic components. In this case, the statistical uncertainty dominates due to the smaller integrated luminosity of the Run 3 dataset.

The inclusive tWZ cross section at 13.6 TeV, extracted from the measured tWZ signal strength, yields

$$\sigma_{\mathrm{tWZ}}(13.6\,\mathrm{TeV}) = 242 \pm 62\,(\mathrm{stat}) \pm 46\,(\mathrm{syst})\ \mathrm{fb} \tag{10.2}$$

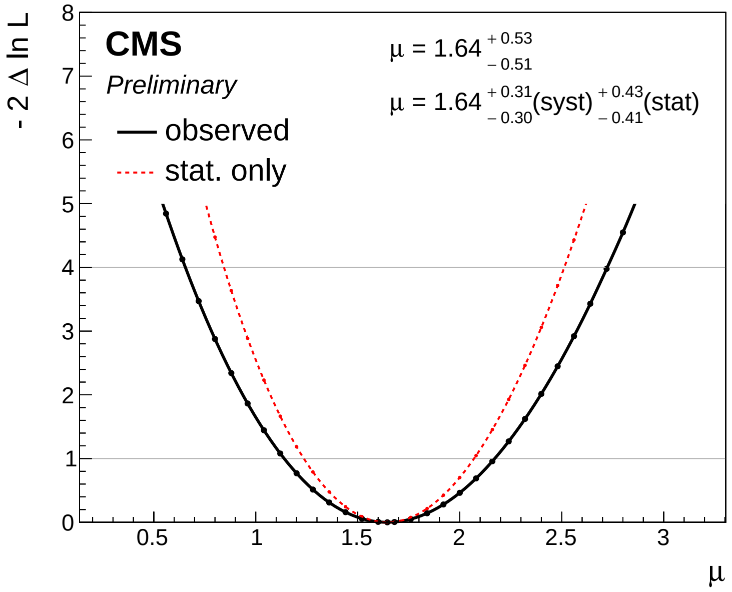

Figure 10.8: Likelihood scan of the tWZ signal strength for the fit on Run 3 data. The solid black line represents the likelihood scan considering the total uncertainty, while the dotted red line includes only the statistical component. Published in [209].

10.3 Simultaneous fit of Run 2 and Run 3

A simultaneous fit of Run 2 and Run 3 data is performed to exploit the statistical power of the combined dataset. The post-fit distributions are shown in Figures 10.9 and 10.10.

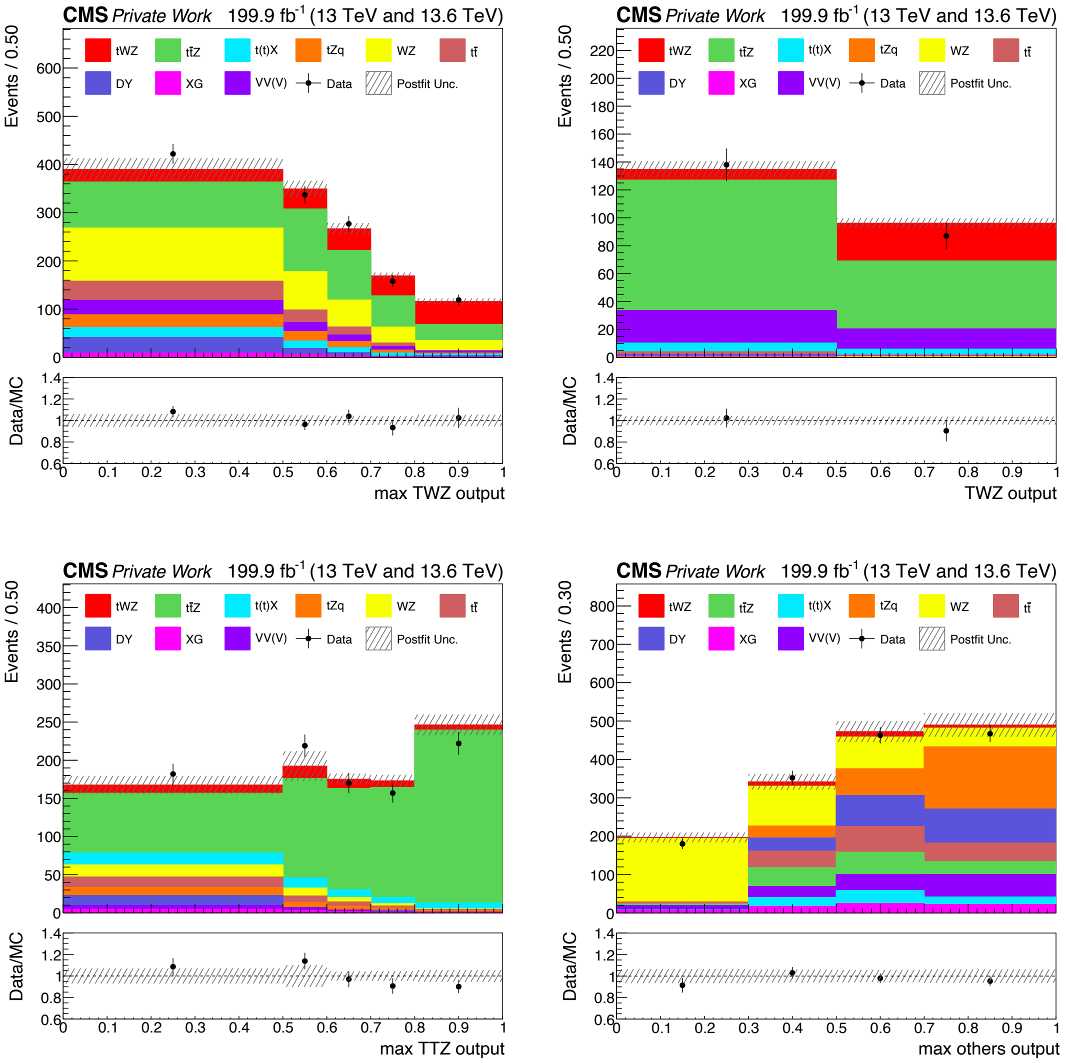

Figure 10.9: Post-fit distributions for the simultaneous fit on Run 2 and Run 3 data. The *max TWZ output* (top left), *max TTZ output* (bottom left), and *max others output* (bottom right) distributions are shown in the 3ℓ SR, while the tWZ ML output node distribution (top right) is shown in the 4ℓ SR. The black markers represent the data, while the solid stacked histogram shows the MC predictions for the various background processes after the fit to data. The dashed band indicates the post-fit uncertainty. The lower panel displays the ratio between data and simulation.

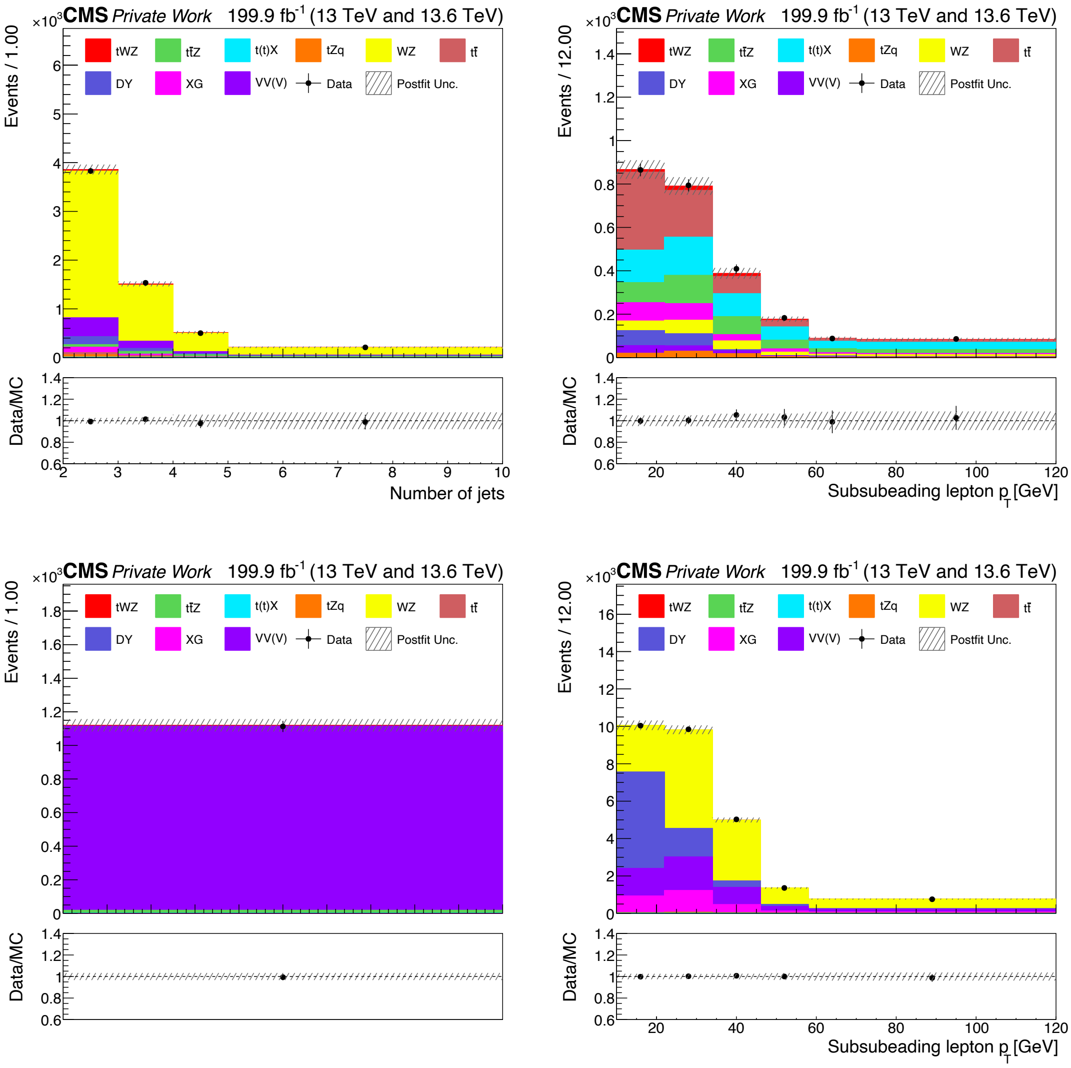

Figure 10.10: Post-fit distributions for the simultaneous fit on Run 2 and Run 3 data. The jet multiplicity distribution is shown in the WZ CR (top left), the event yields in the ZZ CR (bottom left), and the subsubleading lepton transverse momentum in the ttX CR (top right) and DY CR (bottom right). The black markers represent the data, while the solid stacked histogram shows the MC predictions for the various background processes after the fit to data. The dashed band indicates the post-fit uncertainty. The lower panel displays the ratio between data and simulation.

Good agreement is observed in all distributions. In particular, the *max TTZ output* distribution does not show significant fluctuations, as the observed fluctuations in Run 2 and Run 3 compensate each other, resulting in no discrepancies larger than one standard deviation when accounting for both post-fit and data statistical uncertainties.

Table 10.3: Prefit and postfit yields in the different SRs combining Run 2 and Run 3. The uncertainty on the event yields includes only the normalisation uncertainty. The tWZ process has no normalisation uncertainty, as it is the POI. Uncertainties smaller than 0.5 are omitted.

	3 ℓ SR *TWZ* node		3 ℓ SR *TTZ* node		3 ℓ SR *others* node		4 ℓ SR	
	Prefit	Postfit	Prefit	Postfit	Prefit	Postfit	Prefit	Postfit
tWZ	114	194	31	53	21	35	20	33
$t\bar{t}Z$	450 ± 32	428 ± 18	747 ± 32	716 ± 31	152 ± 11	145 ± 6	150 ± 6	143 ± 6
t(t)X	62 ± 12	66 ± 13	54 ± 10	57 ± 11	74 ± 14	81 ± 15	13 ± 3	14 ± 3
tZq	68 ± 7	66 ± 6	28 ± 3	28 ± 3	279 ± 25	262 ± 24	-	-
WZ	295 ± 30	296 ± 11	36 ± 3	37 ± 1	395 ± 40	396 ± 15	1	1
$t\bar{t}$	65 ± 3	88 ± 4	24 ± 1	31 ± 1	115 ± 6	154 ± 7	2	3
DY	54 ± 5	58 ± 5	13 ± 1	14 ± 1	183 ± 16	197 ± 18	1	1
X+γ	21 ± 2	23 ± 2	11 ± 1	12 ± 1	75 ± 7	78 ± 7	1	1
VV(V)	68 ± 7	71 ± 3	11 ± 1	10 ± 1	143 ± 7	143 ± 7	38 ± 2	39 ± 2
All bkgs	1083 ± 39	1096 ± 21	923 ± 34	904 ± 25	1415 ± 45	1456 ± 32	206 ± 9	201 ± 9
All SM	1197 ± 39	1290 ± 21	954 ± 34	957 ± 25	1436 ± 45	1491 ± 32	226 ± 9	234 ± 9
Data	1307	1307	961	961	1457	1457	225	225

Table 10.3 shows the pre- and post-fit event yields in the Run 2 plus Run 3 dataset for the 3ℓ and 4ℓ SRs. The pre-fit yields correspond to the sum of the Run 2 and Run 3 yields, while the post-fit yields are obtained from the simultaneous fit showing good agreement between data and simulation

The GOF test yields a p-value of 13%; therefore, also in this case, the model describes the data accurately. The impacts and pulls of the nuisance parameters, shown in Figure 10.11, reports similar results to those observed in the individual Run 2 and Run 3 fits. In particular, the pulls of the uncertainties related to $t\bar{t}Z$ and WZ+b lie between the values observed in Run 2 and Run 3. As in the previous fits, no one-sided impacts are observed, apart from the DR modelling uncertainty.

The measured signal strength is $1.77 \pm 0.23\,(\text{stat}) \pm 0.22\,(\text{syst})$, representing the most precise tWZ measurement to date. The signal strength is measured with an observed statistical significance of 5.8 s.d. and expected one of 3.5 s.d.. The results are consistent with the previous tWZ measurement and a discrepancy of about 2.3 s.d. between data and prediction is observed, similar to that observed in the previous analysis.

The likelihood scan of the signal strength and the breakdown of the uncertainty into statistical and systematic components are shown in Figure 10.12. In this case, the statistical and systematic uncertainties contribute equally to the total uncertainty.

To study the correlation between the tWZ and the $t\bar{t}Z$ process, a maximum likelihood fit where the signal strengths of both processes are treated as POIs is performed. The

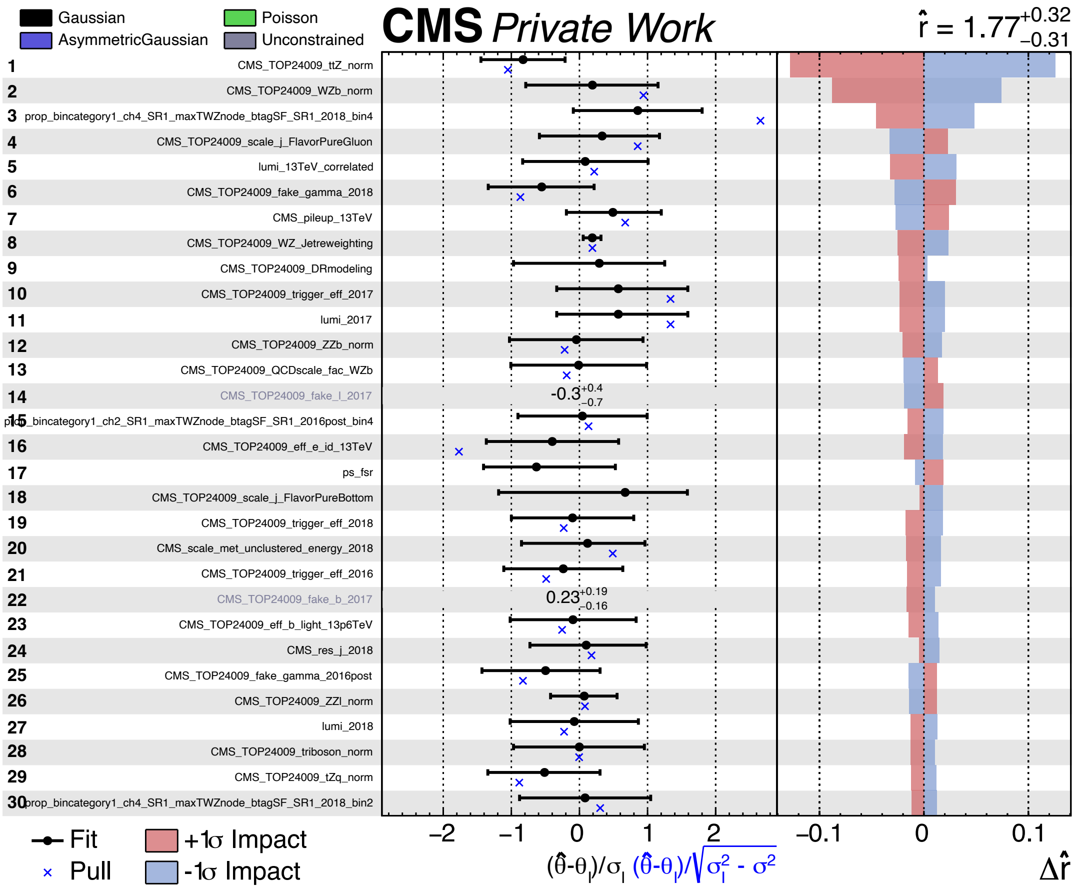

Figure 10.11: Pulls and impacts of the nuisance parameters for the Run 2 and Run 3 data simultaneous fit.

result is shown in Figure 10.13.

The correlation between the two processes is found to be significantly smaller compared to the previous analysis [108]. The signal strength of the tWZ and $t\bar{t}Z$ processes are measured to be

$$\begin{aligned} \mu_{\mathrm{tWZ}} &= 1.88 \pm 0.30\,(\mathrm{stat}) \pm 0.15\,(\mathrm{syst}), \\ \mu_{\mathrm{t\bar{t}Z}} &= 0.91 \pm 0.04\,(\mathrm{stat}) \pm 0.03\,(\mathrm{syst}). \end{aligned} \tag{10.3}$$

The value of the $t\bar{t}Z$ signal strength is in good agreement with that obtained when treating the normalisation uncertainty as a nuisance parameter, and the GOF test yields a p-value of 12%, similar to the nominal configuration. The measured $t\bar{t}Z$ signal strength is compatible within two s.d. with the most recent theoretical prediction

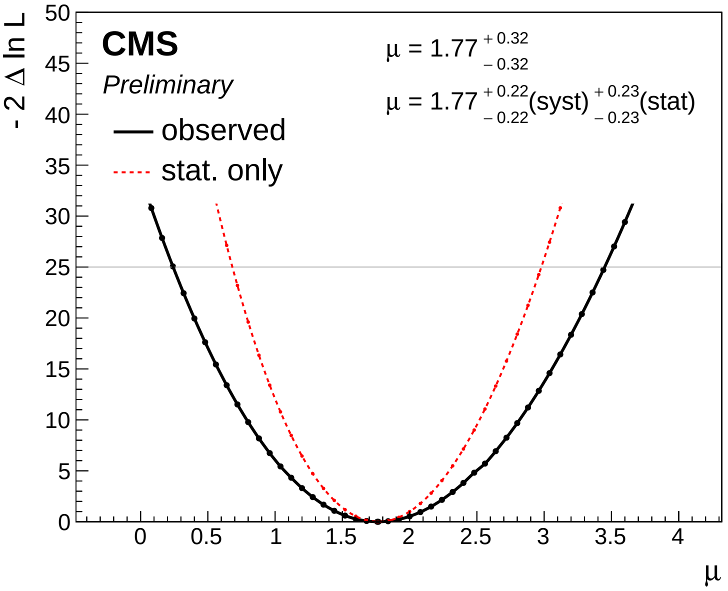

Figure 10.12: Likelihood scan of the tWZ signal strength for the simultaneous fit on Run 2 and Run 3 data. The solid black line represents the likelihood scan considering the total uncertainty, while the dotted red line includes only the statistical component. Published in [209].

at aN^{3}LO QCD and NLO EW [112]. This constitutes the first $\mathrm{t\bar{t}Z}$ measurement using the new theoretical computation, which predicts a cross section 12% larger than previous theoretical estimates. The value of $\mu_{\mathrm{t\bar{t}Z}}$ is consistent with previous $\mathrm{t\bar{t}Z}$ results [102, 103, 122] when accounting for the higher predicted cross section relative to that used in those measurements.

Additional compatibility checks are performed by comparing the signal strength measured for the different data taking periods and leptonic channels. These results are obtained performing dedicated fits for each data taking period or leptonic channel; therefore, the correlation among the systematic uncertainties is not taken into account. The left plot of Figure 10.14 displays the values of the tWZ signal strength measured on the single data-taking periods, showing good agreement. The right image of Figure 10.14 compares the different leptonic channels, combining Run 2 and Run 3, with the nominal result. The different channels are obtained analysing the flavour of the three leading leptons (e = electron, m = muon) and they are in good agreement with the nominal value, proving that the result doesn't depend on the flavour of the leptons in the final state.

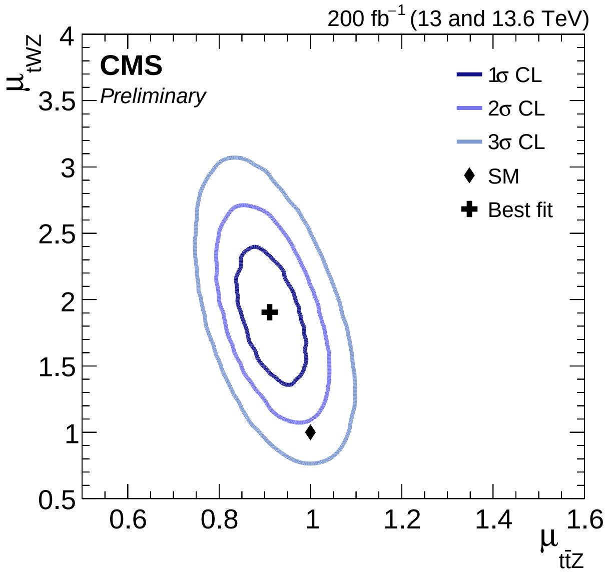

Figure 10.13: Likelihood scan of the signal strengths for tWZ and $t\bar{t}Z$ production. The black cross shows the best fit value, while the black diamond indicates the SM expected value. The contours in different shades of blue correspond to the 68, 95, and 99% confidence level. Published in [109].

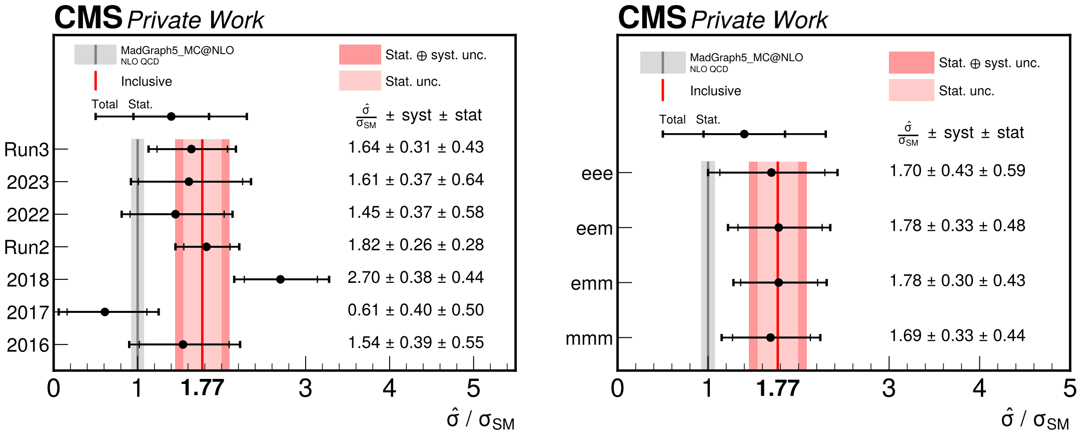

Figure 10.14: Values of the signal strengths for tWZ production obtained from the different data-taking periods (left), and from events with different lepton flavours (right): three electrons (eee), two electrons and one muon (eem), one electron and two muons (emm), and three muons (mmm). If there are more than three leptons in an event, the three p_T-leading leptons are used to determine the flavour. The result from the combined fit to 13 and 13.6 TeV data is shown as a red line with the corresponding uncertainty shown as a red band. The SM prediction is shown as a grey band.

Chapter 11

Conclusions

This thesis presents the first observation of single top quark production in association with a WZ boson pair (tWZ) [109]. The tWZ process is an essential channel to probe the top-quark-electroweak interaction, as it offers strong sensitivity to potential deviations from Standard Model (SM) predictions via the bW → tZ vertex. This distinctive feature can reveal unitarity-violating effects induced by modified electroweak interactions, which can be encoded in the SM Effective Field Theory (SMEFT) framework, making tWZ a key process to probe possible beyond the SM (BSM) scenarios.

Computing SMEFT predictions involves several challenges to accurately describe the effect of higher-dimensional operators and enable the interpretation of measurements as probes for new physics [120]. These have been addressed in this thesis, resulting in SMEFT predictions for the tWZ and $\mathrm{t\bar{t}Z}$ processes, allowing a SMEFT interpretation of the first tWZ measurement [108]. This study provides new constraints for the Wilson coefficients of the $\mathcal{O}_{tZ}$ and $\mathcal{O}_{\phi Q}^{(3)}$ operators and their projections for the High-Luminosity LHC [130]. The results show that a precise experimental identification of the tWZ process, along with differential measurements of relevant observables, will be crucial to improve the current constraints on top-quark-electroweak interaction.

A new measurement of the tWZ process has been presented, analysing data collected by the CMS experiment at centre-of-mass energies of 13 and 13.6 TeV between 2016 and 2023 [109]. The analysis addresses several challenges related to the experimental identification of tWZ. The main difficulty is that the tWZ process has very small predicted cross section, so the measurement targets multi-lepton final states and exploits b-tag information to improve the signal-to-background ratio. Accurate analysis of multi-lepton final states requires efficient identification of the leptons, including precise corrections to account for possible discrepancies between reconstructed and simulated electron quantities [182]. However, even with a dedicated physics object selection, tWZ constitutes only a small fraction of the total number of events, with the main contributions coming from $\mathrm{t\bar{t}Z}$, WZ, and ZZ processes, as well as background involving misidentified leptons. To improve the modelling and reduce the normalisation uncertainties of the WZ and ZZ backgrounds, dedicated control regions are defined. This also results in a significant improvement in the description of the emission of additional jets for the WZ process. Dedicated control regions are also defined to improve the description of background processes involving the presence of misidentified leptons. These processes are not perfectly modelled by the simulation, therefore templates are constructed and fitted to the data in a maximum likelihood fit. A critical element for the identification of the tWZ process is the use of machine learning algorithms capable of efficiently separating signal from background. These algorithms include dedicated output nodes for the identification of tWZ, $\mathrm{t\bar{t}Z}$, WZ, and remaining backgrounds, so that the output distributions can be used not only to separate signal from background, but also to define different regions enriched in tWZ, $\mathrm{t\bar{t}Z}$, and remaining backgrounds. This approach was crucial to constrain the normalisation uncertainty of the $\mathrm{t\bar{t}Z}$ process, which represents the leading systematic uncertainty in the measurement.

The analysis measures the inclusive production cross section of the tWZ process, extracting its value from dedicated maximum likelihood fits to the 13 and 13.6 TeV datasets, resulting in

$$\begin{aligned}\sigma_{\mathrm{tWZ}}(13\,\mathrm{TeV}) &= 248 \pm 38\,(\mathrm{stat}) \pm 35\,(\mathrm{syst})\ \mathrm{fb},\\ \sigma_{\mathrm{tWZ}}(13.6\,\mathrm{TeV}) &= 242 \pm 62\,(\mathrm{stat}) \pm 46\,(\mathrm{syst})\ \mathrm{fb}.\end{aligned} \tag{11.1}$$

From a simultaneous fit to both datasets, the signal strength of tWZ is measured to be $1.77 \pm 0.23\,(\mathrm{stat}) \pm 0.22\,(\mathrm{syst})$, with an observed statistical significance of 5.8 standard deviations (s.d.). This marks the first observation of the tWZ process, establishing it as an experimentally accessible probe of the top-quark-electroweak interaction. The simultaneous fit of tWZ and $\mathrm{t\bar{t}Z}$ shows a significant reduction in the correlation between the two processes with respect to the previous analysis, in particular the signal strengths of the two processes are measured to be

$$\begin{aligned}\mu_{\mathrm{tWZ}} &= 1.88 \pm 0.30\,(\mathrm{stat}) \pm 0.15\,(\mathrm{syst}),\\ \mu_{\mathrm{t\bar{t}Z}} &= 0.91 \pm 0.04\,(\mathrm{stat}) \pm 0.03\,(\mathrm{syst}).\end{aligned} \tag{11.2}$$

The improvement in this measurement can be quantified by comparing the expected sensitivity to that of an earlier analysis [108], using the same dataset (Run 2). The analysis presented in this thesis results in an expected significance of 3.0 s.d., compared to 1.4 s.d. of the previous work, corresponding to an improvement by a factor of two.

This measurement provides the most precise determination to date of the tWZ inclusive cross section and represents a major step forward in our understanding of the top-quark-electroweak sector. A discrepancy of about 2 s.d. between data and the SM prediction is observed, consistent with the tension reported in the previous analysis and opening up exciting perspectives for future measurements. With the additional data collected at the LHC, it will become possible to perform a differential measurement of the tWZ process, enabling a more detailed characterisation of the observed excess and an interpretation within the SMEFT framework to probe possible BSM scenarios.

Acknowledgements

Completing a PhD is a long journey, and what made mine special were the many people I met along the way. I am deeply grateful to my supervisors, Roman Kogler and Katerina Lipka. Roman guided me closely while always giving me the independence to grow as a researcher, and I am sincerely thankful for his support. I am also very grateful to Katerina for believing in my potential from the beginning and for always being available for questions and clarifications. I want to thank the whole DESY-CMS group, and especially the Top group, for creating such a stimulating and supportive environment. Finally, a very special thanks goes to the young colleagues I met over the years, many of whom I'm fortunate to call friends. For every tough goodbye, there was always a warm new hello, and this ever-changing mix of people made these years truly special. I am grateful for the company of so many diverse and remarkable individuals, and I hope to continue sharing this journey with them in the years to come.

Bibliography

[1] S. Weinberg, "The Quantum theory of fields. Vol. 1: Foundations". Cambridge University Press, 6, 2005.

[2] S. Weinberg, "The quantum theory of fields. Vol. 2: Modern applications". Cambridge University Press, 8, 2013.

[3] M. E. Peskin and D. V. Schroeder, "An Introduction to quantum field theory". Addison-Wesley, Reading, USA, 1995.

[4] A. Einstein, "Die Grundlage der allgemeinen Relativitätstheorie", *Annalen der Physik* **354** (1916), no. 7, 769–822, `doi:https://doi.org/10.1002/andp.19163540702`.

[5] G. 't Hooft and M. J. G. Veltman, "Regularization and Renormalization of Gauge Fields", *Nucl. Phys. B* **44** (1972) 189–213, `doi:10.1016/0550-3213(72)90279-9`.

[6] E. Noether, "Invariant Variation Problems", *Gott. Nachr.* **1918** (1918) 235–257, `doi:10.1080/00411457108231446`, `arXiv:physics/0503066`.

[7] C. Burgard, "Standard model of physics".

[8] Particle Data Group Collaboration, "Review of particle physics", *Phys. Rev. D* **110** (2024), no. 3, 030001, `doi:10.1103/PhysRevD.110.030001`.

[9] ALEPH, DELPHI, L3, OPAL, SLD, LEP Electroweak Working Group, SLD Electroweak Group, SLD Heavy Flavour Group Collaboration, "Precision electroweak measurements on the Z resonance", *Phys. Rept.* **427** (2006) 257–454, `doi:10.1016/j.physrep.2005.12.006`, `arXiv:hep-ex/0509008`.

[10] P. W. Higgs, "Broken Symmetries and the Masses of Gauge Bosons", *Phys. Rev. Lett.* **13** (1964) 508–509, `doi:10.1103/PhysRevLett.13.508`.

[11] F. Englert and R. Brout, "Broken Symmetry and the Mass of Gauge Vector Mesons", *Phys. Rev. Lett.* **13** (1964) 321–323, `doi:10.1103/PhysRevLett.13.321`.

[12] M. Gell-Mann, "Symmetries of baryons and mesons", *Phys. Rev.* **125** (1962)

1067–1084, `doi:10.1103/PhysRev.125.1067`.

[13] TASSO Collaboration, “Evidence for Planar Events in e+ e- Annihilation at High-Energies”, *Phys. Lett. B* **86** (1979) 243–249, `doi:10.1016/0370-2693(79)90830-X`.

[14] JADE Collaboration, “Observation of Planar Three Jet Events in e+ e- Annihilation and Evidence for Gluon Bremsstrahlung”, *Phys. Lett. B* **91** (1980) 142–147, `doi:10.1016/0370-2693(80)90680-2`.

[15] PLUTO Collaboration, “Evidence for Gluon Bremsstrahlung in e+ e- Annihilations at High-Energies”, *Phys. Lett. B* **86** (1979) 418–425, `doi:10.1016/0370-2693(79)90869-4`.

[16] D. P. Barber et al., “Discovery of Three Jet Events and a Test of Quantum Chromodynamics at PETRA Energies”, *Phys. Rev. Lett.* **43** (1979) 830, `doi:10.1103/PhysRevLett.43.830`.

[17] JADE Collaboration, “A Study of event shapes and determinations of alpha-s using data of e+ e- annihilations at $\sqrt{s} = 22$ GeV to 44 GeV”, *Eur. Phys. J. C* **1** (1998) 461–478, `doi:10.1007/s100520050096`, `arXiv:hep-ex/9708034`.

[18] C. S. Wu et al., “Experimental Test of Parity Conservation in β Decay”, *Phys. Rev.* **105** (1957) 1413–1414, `doi:10.1103/PhysRev.105.1413`.

[19] S. L. Glashow, “Partial Symmetries of Weak Interactions”, *Nucl. Phys.* **22** (1961) 579–588, `doi:10.1016/0029-5582(61)90469-2`.

[20] S. Weinberg, “A Model of Leptons”, *Phys. Rev. Lett.* **19** (1967) 1264–1266, `doi:10.1103/PhysRevLett.19.1264`.

[21] A. Salam and J. C. Ward, “Weak and electromagnetic interactions”, *Nuovo Cim.* **11** (1959) 568–577, `doi:10.1007/BF02726525`.

[22] M. Gell-Mann, “The interpretation of the new particles as displaced charge multiplets”, *Nuovo Cim.* **4** (1956), no. S2, 848–866, `doi:10.1007/BF02748000`.

[23] T. Nakano and K. Nishijima, “Charge Independence for V-particles”, *Prog. Theor. Phys.* **10** (1953) 581–582, `doi:10.1143/PTP.10.581`.

[24] UA1 Collaboration, “Experimental Observation of Lepton Pairs of Invariant Mass Around 95-GeV/c**2 at the CERN SPS Collider”, *Phys. Lett. B* **126** (1983) 398–410, `doi:10.1016/0370-2693(83)90188-0`.

[25] UA1 Collaboration, “Experimental Observation of Isolated Large Transverse Energy Electrons with Associated Missing Energy at $\sqrt{s} = 540$ GeV”, *Phys. Lett. B* **122** (1983) 103–116, `doi:10.1016/0370-2693(83)91177-2`.

[26] UA2 Collaboration, "Evidence for $Z^0 \to e^+e^-$ at the CERN $\bar{p}p$ Collider", *Phys. Lett. B* **129** (1983) 130–140, `doi:10.1016/0370-2693(83)90744-X`.

[27] UA2 Collaboration, "Observation of Single Isolated Electrons of High Transverse Momentum in Events with Missing Transverse Energy at the CERN anti-p p Collider", *Phys. Lett. B* **122** (1983) 476–485, `doi:10.1016/0370-2693(83)91605-2`.

[28] R. P. Feynman, "Quantum Electrodynamics". W.A. Benjamin Inc., 1961.

[29] J. Ellis, M. K. Gaillard, and D. V. Nanopoulos, "A Historical Profile of the Higgs Boson", pp. 255–274. World Scientific, 2016. `arXiv:1504.07217`. `doi:10.1142/9789814733519_0014`.

[30] CMS Collaboration, "Observation of a New Boson at a Mass of 125 GeV with the CMS Experiment at the LHC", *Phys. Lett. B* **716** (2012) 30–61, `doi:10.1016/j.physletb.2012.08.021`, `arXiv:1207.7235`.

[31] ATLAS Collaboration, "Observation of a new particle in the search for the Standard Model Higgs boson with the ATLAS detector at the LHC", *Phys. Lett. B* **716** (2012) 1–29, `doi:10.1016/j.physletb.2012.08.020`, `arXiv:1207.7214`.

[32] CMS Collaboration, "A portrait of the Higgs boson by the CMS experiment ten years after the discovery.", *Nature* **607** (2022), no. 7917, 60–68, `doi:10.1038/s41586-022-04892-x`, `arXiv:2207.00043`. [Erratum: Nature 623, (2023)].

[33] ATLAS Collaboration, "A detailed map of Higgs boson interactions by the ATLAS experiment ten years after the discovery", *Nature* **607** (2022), no. 7917, 52–59, `doi:10.1038/s41586-022-04893-w`, `arXiv:2207.00092`. [Erratum: Nature 612, E24 (2022)].

[34] N. Cabibbo, "Unitary Symmetry and Leptonic Decays", *Phys. Rev. Lett.* **10** (1963) 531–533, `doi:10.1103/PhysRevLett.10.531`.

[35] M. Kobayashi and T. Maskawa, "CP Violation in the Renormalizable Theory of Weak Interaction", *Prog. Theor. Phys.* **49** (1973) 652–657, `doi:10.1143/PTP.49.652`.

[36] Super-Kamiokande Collaboration, "Evidence for oscillation of atmospheric neutrinos", *Phys. Rev. Lett.* **81** (1998) 1562–1567, `doi:10.1103/PhysRevLett.81.1562`, `arXiv:hep-ex/9807003`.

[37] A. Baha Balantekin and B. Kayser, "On the Properties of Neutrinos", *Ann. Rev. Nucl. Part. Sci.* **68** (2018) 313–338,

`doi:10.1146/annurev-nucl-101916-123044`, `arXiv:1805.00922`.

[38] B. Pontecorvo, “Inverse beta processes and nonconservation of lepton charge”, *Zh. Eksp. Teor. Fiz.* **34** (1957) 247.

[39] Z. Maki, M. Nakagawa, and S. Sakata, “Remarks on the unified model of elementary particles”, *Prog. Theor. Phys.* **28** (1962) 870–880, `doi:10.1143/PTP.28.870`.

[40] KATRIN Collaboration, “Direct neutrino-mass measurement based on 259 days of KATRIN data”, *Science* **388** (2025), no. 6743, adq9592, `doi:10.1126/science.adq9592`, `arXiv:2406.13516`.

[41] KATRIN Collaboration, “The design, construction, and commissioning of the KATRIN experiment”, *JINST* **16** (2021), no. 08, T08015, `doi:10.1088/1748-0221/16/08/T08015`, `arXiv:2103.04755`.

[42] A. D. Sakharov, “Violation of CP Invariance, C asymmetry, and baryon asymmetry of the universe”, *Pisma Zh. Eksp. Teor. Fiz.* **5** (1967) 32–35, `doi:10.1070/PU1991v034n05ABEH002497`.

[43] J. H. Christenson, J. W. Cronin, V. L. Fitch, and R. Turlay, “Evidence for the 2π Decay of the K_2^0 Meson”, *Phys. Rev. Lett.* **13** (1964) 138–140, `doi:10.1103/PhysRevLett.13.138`.

[44] BaBar Collaboration, “Observation of CP violation in the B^0 meson system”, *Phys. Rev. Lett.* **87** (2001) 091801, `doi:10.1103/PhysRevLett.87.091801`, `arXiv:hep-ex/0107013`.

[45] LHCb Collaboration, “Observation of CP Violation in Charm Decays”, *Phys. Rev. Lett.* **122** (2019), no. 21, 211803, `doi:10.1103/PhysRevLett.122.211803`, `arXiv:1903.08726`.

[46] LHCb Collaboration, “Observation of charge-parity symmetry breaking in baryon decays”, `arXiv:2503.16954`.

[47] F. Zwicky, “Die Rotverschiebung von extragalaktischen Nebeln”, *Helv. Phys. Acta* **6** (1933) 110–127, `doi:10.1007/s10714-008-0707-4`.

[48] Planck Collaboration, “Planck 2018 results. VI. Cosmological parameters”, *Astron. Astrophys.* **641** (2020) A6, `doi:10.1051/0004-6361/201833910`, `arXiv:1807.06209`. [Erratum: Astron.Astrophys. 652, C4 (2021)].

[49] J. C. Collins, D. E. Soper, and G. F. Sterman, “Factorization of Hard Processes in QCD”, *Adv. Ser. Direct. High Energy Phys.* **5** (1989) 1–91, `doi:10.1142/9789814503266_0001`, `arXiv:hep-ph/0409313`.

[50] G. Altarelli and G. Parisi, “Asymptotic Freedom in Parton Language”, *Nucl.*

Phys. B **126** (1977) 298–318, `doi:10.1016/0550-3213(77)90384-4`.

[51] V. N. Gribov and L. N. Lipatov, “Deep inelastic e p scattering in perturbation theory”, *Sov. J. Nucl. Phys.* **15** (1972) 438–450.

[52] Y. L. Dokshitzer, “Calculation of the Structure Functions for Deep Inelastic Scattering and e+ e- Annihilation by Perturbation Theory in Quantum Chromodynamics.”, *Sov. Phys. JETP* **46** (1977) 641–653.

[53] H1, ZEUS Collaboration, “Combination of measurements of inclusive deep inelastic $e^{\pm}p$ scattering cross sections and QCD analysis of HERA data”, *Eur. Phys. J. C* **75** (2015), no. 12, 580, `doi:10.1140/epjc/s10052-015-3710-4`, `arXiv:1506.06042`.

[54] CMS Collaboration, “Measurement of $\mathrm{t\bar{t}}$ normalised multi-differential cross sections in pp collisions at $\sqrt{s} = 13$ TeV, and simultaneous determination of the strong coupling strength, top quark pole mass, and parton distribution functions”, *Eur. Phys. J. C* **80** (2020), no. 7, 658, `doi:10.1140/epjc/s10052-020-7917-7`, `arXiv:1904.05237`.

[55] CMS Collaboration, “Determination of the strong coupling and its running from measurements of inclusive jet production”, `arXiv:2412.16665`.

[56] ATLAS Collaboration, “Determination of the parton distribution functions of the proton from ATLAS measurements of differential W and Z/γ^* and $t\bar{t}$ cross sections”,.

[57] S. Alekhin, J. Blümlein, S. Moch, and R. Placakyte, “Parton distribution functions, α_s, and heavy-quark masses for LHC Run II”, *Phys. Rev. D* **96** (2017), no. 1, 014011, `doi:10.1103/PhysRevD.96.014011`, `arXiv:1701.05838`.

[58] T.-J. Hou et al., “New CTEQ global analysis of quantum chromodynamics with high-precision data from the LHC”, *Phys. Rev. D* **103** (2021), no. 1, 014013, `doi:10.1103/PhysRevD.103.014013`, `arXiv:1912.10053`.

[59] S. Bailey et al., “Parton distributions from LHC, HERA, Tevatron and fixed target data: MSHT20 PDFs”, *Eur. Phys. J. C* **81** (2021), no. 4, 341, `doi:10.1140/epjc/s10052-021-09057-0`, `arXiv:2012.04684`.

[60] NNPDF Collaboration, “Parton distributions from high-precision collider data”, *Eur. Phys. J. C* **77** (2017), no. 10, 663, `doi:10.1140/epjc/s10052-017-5199-5`, `arXiv:1706.00428`.

[61] NNPDF Collaboration, “The path to proton structure at 1% accuracy”, *Eur. Phys. J. C* **82** (2022), no. 5, 428, `doi:10.1140/epjc/s10052-022-10328-7`,

`arXiv:2109.02653`.

[62] S. Höche, "Introduction to parton-shower event generators", in *Theoretical Advanced Study Institute in Elementary Particle Physics: Journeys Through the Precision Frontier: Amplitudes for Colliders*, pp. 235–295. 2015. `arXiv:1411.4085`. `doi:10.1142/9789814678766_0005`.

[63] S. Hoeche, F. Krauss, M. Schonherr, and F. Siegert, "QCD matrix elements + parton showers: The NLO case", *JHEP* **04** (2013) 027, `doi:10.1007/JHEP04(2013)027`, `arXiv:1207.5030`.

[64] J. Alwall et al., "Comparative study of various algorithms for the merging of parton showers and matrix elements in hadronic collisions", *Eur. Phys. J. C* **53** (2008) 473–500, `doi:10.1140/epjc/s10052-007-0490-5`, `arXiv:0706.2569`.

[65] R. Frederix and S. Frixione, "Merging meets matching in MC@NLO", *JHEP* **12** (2012) 061, `doi:10.1007/JHEP12(2012)061`, `arXiv:1209.6215`.

[66] J. Alwall et al., "The automated computation of tree-level and next-to-leading order differential cross sections, and their matching to parton shower simulations", *JHEP* **07** (2014) 079, `doi:10.1007/JHEP07(2014)079`, `arXiv:1405.0301`.

[67] P. Nason, "A New method for combining NLO QCD with shower Monte Carlo algorithms", *JHEP* **11** (2004) 040, `doi:10.1088/1126-6708/2004/11/040`, `arXiv:hep-ph/0409146`.

[68] S. Frixione, P. Nason, and C. Oleari, "Matching NLO QCD computations with Parton Shower simulations: the POWHEG method", *JHEP* **11** (2007) 070, `doi:10.1088/1126-6708/2007/11/070`, `arXiv:0709.2092`.

[69] G. Marchesini et al., "HERWIG: A Monte Carlo event generator for simulating hadron emission reactions with interfering gluons. Version 5.1 - April 1991", *Comput. Phys. Commun.* **67** (1992) 465–508, `doi:10.1016/0010-4655(92)90055-4`.

[70] B. Andersson, G. Gustafson, G. Ingelman, and T. Sjostrand, "Parton Fragmentation and String Dynamics", *Phys. Rept.* **97** (1983) 31–145, `doi:10.1016/0370-1573(83)90080-7`.

[71] GEANT4 Collaboration, "GEANT4 - A Simulation Toolkit", *Nucl. Instrum. Meth. A* **506** (2003) 250–303, `doi:10.1016/S0168-9002(03)01368-8`.

[72] M. L. Perl et al., "Evidence for Anomalous Lepton Production in e+ - e- Annihilation", *Phys. Rev. Lett.* **35** (1975) 1489–1492,

`doi:10.1103/PhysRevLett.35.1489`.

[73] E288 Collaboration, "Observation of a Dimuon Resonance at 9.5-GeV in 400-GeV Proton-Nucleus Collisions", *Phys. Rev. Lett.* **39** (1977) 252–255, `doi:10.1103/PhysRevLett.39.252`.

[74] CDF Collaboration, "Observation of top quark production in $\bar{p}p$ collisions", *Phys. Rev. Lett.* **74** (1995) 2626–2631, `doi:10.1103/PhysRevLett.74.2626`, `arXiv:hep-ex/9503002`.

[75] D0 Collaboration, "Observation of the top quark", *Phys. Rev. Lett.* **74** (1995) 2632–2637, `doi:10.1103/PhysRevLett.74.2632`, `arXiv:hep-ex/9503003`.

[76] I. I. Y. Bigi et al., "Production and Decay Properties of Ultraheavy Quarks", *Phys. Lett. B* **181** (1986) 157–163, `doi:10.1016/0370-2693(86)91275-X`.

[77] G. Mahlon and S. J. Parke, "Spin Correlation Effects in Top Quark Pair Production at the LHC", *Phys. Rev. D* **81** (2010) 074024, `doi:10.1103/PhysRevD.81.074024`, `arXiv:1001.3422`.

[78] CMS Collaboration, "Measurement of the top quark Yukawa coupling from $\mathrm{t\bar{t}}$ kinematic distributions in the dilepton final state in proton-proton collisions at $\sqrt{s} = 13$ TeV", *Phys. Rev. D* **102** (2020), no. 9, 092013, `doi:10.1103/PhysRevD.102.092013`, `arXiv:2009.07123`.

[79] A. Andreassen, W. Frost, and M. D. Schwartz, "Scale Invariant Instantons and the Complete Lifetime of the Standard Model", *Phys. Rev. D* **97** (2018), no. 5, 056006, `doi:10.1103/PhysRevD.97.056006`, `arXiv:1707.08124`.

[80] M. Czakon, P. Fiedler, and A. Mitov, "Total Top-Quark Pair-Production Cross Section at Hadron Colliders Through $O(\alpha_S^4)$", *Phys. Rev. Lett.* **110** (2013) 252004, `doi:10.1103/PhysRevLett.110.252004`, `arXiv:1303.6254`.

[81] CDF, D0 Collaboration, "Combination of Measurements of the Top-Quark Pair Production Cross Section from the Tevatron Collider", *Phys. Rev. D* **89** (2014), no. 7, 072001, `doi:10.1103/PhysRevD.89.072001`, `arXiv:1309.7570`.

[82] ATLAS Collaboration, "Measurement of the $t\bar{t}$ production cross-section in pp collisions at $\sqrt{s} = 5.02$ TeV with the ATLAS detector", *JHEP* **06** (2023) 138, `doi:10.1007/JHEP06(2023)138`, `arXiv:2207.01354`.

[83] CMS Collaboration, "Measurement of the inclusive $\mathrm{t\bar{t}}$ cross section in final states with at least one lepton and additional jets with 302 pb^{-1} of pp collisions at $\sqrt{\mathrm{s}} = 5.02$ TeV", *JHEP* **04** (2025) 099, `doi:10.1007/JHEP04(2025)099`, `arXiv:2410.21631`.

[84] ATLAS, CMS Collaboration, "Combination of inclusive top-quark pair

production cross-section measurements using ATLAS and CMS data at $\sqrt{s} =$ 7 and 8 TeV", *JHEP* **07** (2023) 213, `doi:10.1007/JHEP07(2023)213`, `arXiv:2205.13830`.

[85] ATLAS Collaboration, "Inclusive and differential cross-sections for dilepton $t\bar{t}$ production measured in $\sqrt{s} = 13$ TeV pp collisions with the ATLAS detector", *JHEP* **07** (2023) 141, `doi:10.1007/JHEP07(2023)141`, `arXiv:2303.15340`.

[86] CMS Collaboration, "Measurement of the $\mathrm{t\bar{t}}$ production cross section, the top quark mass, and the strong coupling constant using dilepton events in pp collisions at $\sqrt{s} = 13$ TeV", *Eur. Phys. J. C* **79** (2019), no. 5, 368, `doi:10.1140/epjc/s10052-019-6863-8`, `arXiv:1812.10505`.

[87] ATLAS Collaboration, "Measurement of the $t\bar{t}$ production cross-section in the lepton+jets channel at $\sqrt{s} = 13$ TeV with the ATLAS experiment", *Phys. Lett. B* **810** (2020) 135797, `doi:10.1016/j.physletb.2020.135797`, `arXiv:2006.13076`.

[88] CMS Collaboration, "Measurement of differential $t\bar{t}$ production cross sections in the full kinematic range using lepton+jets events from proton-proton collisions at $\sqrt{s} = 13$ TeV", *Phys. Rev. D* **104** (2021), no. 9, 092013, `doi:10.1103/PhysRevD.104.092013`, `arXiv:2108.02803`.

[89] ATLAS Collaboration, "Measurement of the $t\bar{t}$ cross section and its ratio to the Z production cross section using pp collisions at s=13.6 TeV with the ATLAS detector", *Phys. Lett. B* **848** (2024) 138376, `doi:10.1016/j.physletb.2023.138376`, `arXiv:2308.09529`.

[90] CMS Collaboration, "First measurement of the top quark pair production cross section in proton-proton collisions at $\sqrt{s} = 13.6$ TeV", *JHEP* **08** (2023) 204, `doi:10.1007/JHEP08(2023)204`, `arXiv:2303.10680`.

[91] LHCTOPWG, "LHCTopWG Summary Plots", 2024.

[92] J. Campbell, T. Neumann, and Z. Sullivan, "Single-top-quark production in the t-channel at NNLO", *JHEP* **02** (2021) 040, `doi:10.1007/JHEP02(2021)040`, `arXiv:2012.01574`.

[93] ATLAS Collaboration, "Measurement of t-channel production of single top quarks and antiquarks in pp collisions at 13 TeV using the full ATLAS Run 2 data sample", *JHEP* **05** (2024) 305, `doi:10.1007/JHEP05(2024)305`, `arXiv:2403.02126`. [Erratum: JHEP 06, 024 (2024)].

[94] CMS Collaboration, "Measurement of the single top quark and antiquark production cross sections in the t channel and their ratio in proton-proton

collisions at $\sqrt{s} = 13$ TeV”, *Phys. Lett. B* **800** (2020) 135042, `doi:10.1016/j.physletb.2019.135042`, `arXiv:1812.10514`.

[95] N. Kidonakis and N. Yamanaka, “Higher-order corrections for tW production at high-energy hadron colliders”, *JHEP* **05** (2021) 278, `doi:10.1007/JHEP05(2021)278`, `arXiv:2102.11300`.

[96] ATLAS Collaboration, “Measurement of the cross-section for producing a W boson in association with a single top quark in pp collisions at $\sqrt{s} = 13$ TeV with ATLAS”, *JHEP* **01** (2018) 063, `doi:10.1007/JHEP01(2018)063`, `arXiv:1612.07231`.

[97] CMS Collaboration, “Measurement of inclusive and differential cross sections for single top quark production in association with a W boson in proton-proton collisions at $\sqrt{s} = 13$ TeV”, *JHEP* **07** (2023) 046, `doi:10.1007/JHEP07(2023)046`, `arXiv:2208.00924`.

[98] ATLAS Collaboration, “Measurement of single top-quark production in the s-channel in proton–proton collisions at $\sqrt{s} = 13$ TeV with the ATLAS detector”, *JHEP* **06** (2023) 191, `doi:10.1007/JHEP06(2023)191`, `arXiv:2209.08990`.

[99] ATLAS Collaboration, “Measurement of the total and differential cross-sections of $t\bar{t}W$ production in pp collisions at $\sqrt{s} = 13$ TeV with the ATLAS detector”, *JHEP* **05** (2024) 131, `doi:10.1007/JHEP05(2024)131`, `arXiv:2401.05299`.

[100] CMS Collaboration, “Measurement of the cross section of top quark-antiquark pair production in association with a W boson in proton-proton collisions at $\sqrt{s} = 13$ TeV”, *JHEP* **07** (2023) 219, `doi:10.1007/JHEP07(2023)219`, `arXiv:2208.06485`.

[101] CMS Collaboration, “Measurement of the ttW differential cross section and charge asymmetry at $\sqrt{s} = 13$ TeV”, technical report, CERN, Geneva, 2025.

[102] CMS Collaboration, “Measurement of top quark pair production in association with a Z boson in proton-proton collisions at $\sqrt{s} = 13$ TeV”, *JHEP* **03** (2020) 056, `doi:10.1007/JHEP03(2020)056`, `arXiv:1907.11270`.

[103] CMS Collaboration, “Measurements of inclusive and differential cross sections for top quark production in association with a Z boson in proton-proton collisions at $\sqrt{s} = 13$ TeV”, *JHEP* **02** (2025) 177, `doi:10.1007/JHEP02(2025)177`, `arXiv:2410.23475`.

[104] ATLAS Collaboration, “Observation of the associated production of a top

quark and a Z boson in pp collisions at $\sqrt{s} = 13$ TeV with the ATLAS detector", *JHEP* **07** (2020) 124, `doi:10.1007/JHEP07(2020)124`, `arXiv:2002.07546`.

[105] CMS Collaboration, "Inclusive and differential cross section measurements of single top quark production in association with a Z boson in proton-proton collisions at $\sqrt{s} = 13$ TeV", *JHEP* **02** (2022) 107, `doi:10.1007/JHEP02(2022)107`, `arXiv:2111.02860`.

[106] ATLAS Collaboration, "Observation of Single-Top-Quark Production in Association with a Photon Using the ATLAS Detector", *Phys. Rev. Lett.* **131** (2023), no. 18, 181901, `doi:10.1103/PhysRevLett.131.181901`, `arXiv:2302.01283`.

[107] CMS Collaboration, "Evidence for the associated production of a single top quark and a photon in proton-proton collisions at $\sqrt{s} = 13$ TeV", *Phys. Rev. Lett.* **121** (2018), no. 22, 221802, `doi:10.1103/PhysRevLett.121.221802`, `arXiv:1808.02913`.

[108] CMS Collaboration, "Evidence for tWZ production in proton-proton collisions at s=13 TeV in multilepton final states", *Phys. Lett. B* **855** (2024) 138815, `doi:10.1016/j.physletb.2024.138815`, `arXiv:2312.11668`.

[109] CMS Collaboration, "Observation of tWZ production at the CMS experiment", technical report, CERN, Geneva, 2025.

[110] H. E. Faham, F. Maltoni, K. Mimasu, and M. Zaro, "Single top production in association with a WZ pair at the LHC in the SMEFT", *JHEP* **01** (2022) 100, `doi:10.1007/JHEP01(2022)100`, `arXiv:2111.03080`.

[111] F. Maltoni, L. Mantani, and K. Mimasu, "Top-quark electroweak interactions at high energy", *JHEP* **10** (2019) 004, `doi:10.1007/JHEP10(2019)004`, `arXiv:1904.05637`.

[112] N. Kidonakis and C. Foster, "Higher-order soft-gluon corrections for $t\bar{t}Z$ cross sections", *Phys. Lett. B* **860** (2025) 139146, `doi:10.1016/j.physletb.2024.139146`, `arXiv:2410.01214`.

[113] E. Fermi, "An attempt of a theory of beta radiation. 1.", *Z. Phys.* **88** (1934) 161–177, `doi:10.1007/BF01351864`.

[114] B. Grzadkowski, M. Iskrzynski, M. Misiak, and J. Rosiek, "Dimension-Six Terms in the Standard Model Lagrangian", *JHEP* **10** (2010) 085, `doi:10.1007/JHEP10(2010)085`, `arXiv:1008.4884`.

[115] CMS Collaboration, "Combined effective field theory interpretation of Higgs

boson, electroweak vector boson, top quark, and multi-jet measurements", `arXiv:2504.02958`.

[116] ATLAS Collaboration, "Combined effective field theory interpretation of Higgs boson and weak boson production and decay with ATLAS data and electroweak precision observables",.

[117] J. Ellis et al., "Top, Higgs, Diboson and Electroweak Fit to the Standard Model Effective Field Theory", *JHEP* **04** (2021) 279, `doi:10.1007/JHEP04(2021)279`, `arXiv:2012.02779`.

[118] SMEFiT Collaboration, "Combined SMEFT interpretation of Higgs, diboson, and top quark data from the LHC", *JHEP* **11** (2021) 089, `doi:10.1007/JHEP11(2021)089`, `arXiv:2105.00006`.

[119] I. Brivio et al., "O new physics, where art thou? A global search in the top sector", *JHEP* **02** (2020) 131, `doi:10.1007/JHEP02(2020)131`, `arXiv:1910.03606`.

[120] A. Belvedere et al., "LHC EFT WG note: SMEFT predictions, event reweighting, and simulation", `doi:10.21468/SciPostPhysCommRep.4`, `arXiv:2406.14620`.

[121] ATLAS Collaboration, "Measurement of the $t\bar{t}Z$ and $t\bar{t}W$ cross sections in proton-proton collisions at $\sqrt{s} = 13$ TeV with the ATLAS detector", *Phys. Rev. D* **99** (2019), no. 7, 072009, `doi:10.1103/PhysRevD.99.072009`, `arXiv:1901.03584`.

[122] ATLAS Collaboration, "Inclusive and differential cross-section measurements of $t\bar{t}Z$ production in pp collisions at $\sqrt{s} = 13$ TeV with the ATLAS detector, including EFT and spin-correlation interpretations", *JHEP* **07** (2024) 163, `doi:10.1007/JHEP07(2024)163`, `arXiv:2312.04450`.

[123] CMS Collaboration, "Probing effective field theory operators in the associated production of top quarks with a Z boson in multilepton final states at $\sqrt{s} = 13$ TeV", *JHEP* **12** (2021) 083, `doi:10.1007/JHEP12(2021)083`, `arXiv:2107.13896`.

[124] CMS Collaboration, "Search for CP violation in events with top quarks and Z bosons", technical report, CERN, Geneva, 2025.

[125] I. Brivio, "SMEFTsim 3.0 — a practical guide", *JHEP* **04** (2021) 073, `doi:10.1007/JHEP04(2021)073`, `arXiv:2012.11343`.

[126] C. Degrande et al., "Automated one-loop computations in the standard model effective field theory", *Phys. Rev. D* **103** (2021), no. 9, 096024,

`doi:10.1103/PhysRevD.103.096024`, `arXiv:2008.11743`.

[127] T. Sjöstrand et al., "An introduction to PYTHIA 8.2", *Comput. Phys. Commun.* **191** (2015) 159–177, `doi:10.1016/j.cpc.2015.01.024`, `arXiv:1410.3012`.

[128] S. Frixione et al., "Automated simulations beyond the Standard Model: supersymmetry", *JHEP* **12** (2019) 008, `doi:10.1007/JHEP12(2019)008`, `arXiv:1907.04898`.

[129] A. Belvedere, "Results and prospects on an EFT interpretation of the tWZ process", *PoS* **ICHEP2024** (2025) 362, `doi:10.22323/1.476.0362`.

[130] A. Belvedere, C. Englert, R. Kogler, and M. Spannowsky, "Dispelling the $\sqrt{\mathcal{L}}$ myth for the High-Luminosity LHC", *Eur. Phys. J. C* **84** (2024), no. 7, 715, `doi:10.1140/epjc/s10052-024-13032-w`, `arXiv:2402.07985`.

[131] "LHC Design Report Vol.1: The LHC Main Ring", `doi:10.5170/CERN-2004-003-V-1`.

[132] "LHC Design Report. 2. The LHC infrastructure and general services", `doi:10.5170/CERN-2004-003-V-2`.

[133] "LHC Design Report. 3. The LHC injector chain", `doi:10.5170/CERN-2004-003-V-3`.

[134] "LEP Design Report Vol.1: The LEP Injector Chain",.

[135] "LEP Design Report: Vol.2. The LEP Main Ring",.

[136] "LEP Design Report: Vol.3: LEP2",.

[137] CERN, "The CERN Accelerator Complex", 2022. Accessed: June 2025.

[138] ALICE Collaboration, "The ALICE experiment at the CERN LHC", *JINST* **3** (2008) S08002, `doi:10.1088/1748-0221/3/08/S08002`.

[139] ATLAS Collaboration, "The ATLAS Experiment at the CERN Large Hadron Collider", *JINST* **3** (2008) S08003, `doi:10.1088/1748-0221/3/08/S08003`.

[140] CMS Collaboration, "The CMS Experiment at the CERN LHC", *JINST* **3** (2008) S08004, `doi:10.1088/1748-0221/3/08/S08004`.

[141] LHCb Collaboration, "The LHCb Detector at the LHC", *JINST* **3** (2008) S08005, `doi:10.1088/1748-0221/3/08/S08005`.

[142] CERN, "LHC/HL-LHC Plan", 2025. Accessed: June 2025.

[143] CMS Collaboration, "CMS luminosity - Public Result".

[144] CERN, CMS, "The CMS Experiment at CERN", 2025. Accessed: June 2025.

[145] CMS Collaboration, S. R. Davis, "Interactive Slice of the CMS detector", 2016. Accessed: June 2025.

[146] CMS Collaboration, "The CMS tracker system project: Technical Design Report",.

[147] CMS Collaboration, "Description and Performance of Track and Primary-Vertex Reconstruction with the CMS Tracker", *JINST* **9** (2014), no. 10, P10009, `doi:10.1088/1748-0221/9/10/P10009`, `arXiv:1405.6569`.

[148] CMS Tracker Group Collaboration, "The CMS Phase-1 Pixel Detector Upgrade", *JINST* **16** (2021), no. 02, P02027, `doi:10.1088/1748-0221/16/02/P02027`, `arXiv:2012.14304`.

[149] CMS Collaboration, "The CMS electromagnetic calorimeter project: Technical Design Report",.

[150] CMS Collaboration, "The CMS ECAL performance with examples", *JINST* **9** (2014) C02008, `doi:10.1088/1748-0221/9/02/C02008`.

[151] P. Adzic et al., "Energy resolution of the barrel of the CMS electromagnetic calorimeter", *JINST* **2** (2007) P04004, `doi:10.1088/1748-0221/2/04/P04004`.

[152] CMS Collaboration, "Electron and photon reconstruction and identification with the CMS experiment at the CERN LHC", *JINST* **16** (2021), no. 05, P05014, `doi:10.1088/1748-0221/16/05/P05014`, `arXiv:2012.06888`.

[153] CMS Collaboration, "The CMS hadron calorimeter project: Technical Design Report",.

[154] C. Collaboration, "Performance of the CMS hadron calorimeter with cosmic ray muons and LHC beam data", *Journal of Instrumentation* **5** (March, 2010) T03012–T03012, `doi:10.1088/1748-0221/5/03/t03012`.

[155] CMS Collaboration, "CMS, the magnet project: Technical design report",.

[156] CMS Collaboration, "The CMS muon project: Technical Design Report",.

[157] CMS Collaboration, "Performance of the CMS muon detector and muon reconstruction with proton-proton collisions at $\sqrt{s} = 13$ TeV", *JINST* **13** (2018), no. 06, P06015, `doi:10.1088/1748-0221/13/06/P06015`, `arXiv:1804.04528`.

[158] CMS Collaboration, "CMS Physics: Technical Design Report Volume 1: Detector Performance and Software", `doi:10.2172/2510878`.

[159] CMS Collaboration, "Particle-flow reconstruction and global event description with the CMS detector", *JINST* **12** (2017), no. 10, P10003, `doi:10.1088/1748-0221/12/10/P10003`, `arXiv:1706.04965`.

[160] R. E. Kalman, "A New Approach to Linear Filtering and Prediction

Problems", *J. Fluids Eng.* **82** (1960), no. 1, 35–45, `doi:10.1115/1.3662552`.

[161] K. Rose, "Deterministic annealing for clustering, compression, classification, regression, and related optimization problems", *IEEE Proc.* **86** (1998), no. 11, 2210–2239, `doi:10.1109/5.726788`.

[162] W. Adam, R. Frühwirth, A. Strandlie, and T. Todorov, "Reconstruction of electrons with the Gaussian-sum filter in the CMS tracker at the LHC", *Journal of Physics G: Nuclear and Particle Physics* **31** (July, 2005) N9–N20, `doi:10.1088/0954-3899/31/9/n01`.

[163] CMS Collaboration, "Muon identification using multivariate techniques in the CMS experiment in proton-proton collisions at $\sqrt{s} = 13$ TeV", *JINST* **19** (2024), no. 02, P02031, `doi:10.1088/1748-0221/19/02/P02031`, `arXiv:2310.03844`.

[164] CMS Collaboration, "Observation of four top quark production in proton-proton collisions at $\sqrt{s}$=13TeV", *Phys. Lett. B* **847** (2023) 138290, `doi:10.1016/j.physletb.2023.138290`, `arXiv:2305.13439`.

[165] CMS Collaboration, "Measurement of the inclusive WZ production cross section in pp collisions at $\sqrt{s} = 13.6$ TeV", *JHEP* **04** (2025) 115, `doi:10.1007/JHEP04(2025)115`, `arXiv:2412.02477`.

[166] M. Cacciari, G. P. Salam, and G. Soyez, "The anti-k_t jet clustering algorithm", *JHEP* **04** (2008) 063, `doi:10.1088/1126-6708/2008/04/063`, `arXiv:0802.1189`.

[167] M. Cacciari, G. P. Salam, and G. Soyez, "FastJet User Manual", *Eur. Phys. J. C* **72** (2012) 1896, `doi:10.1140/epjc/s10052-012-1896-2`, `arXiv:1111.6097`.

[168] CMS Collaboration, "Jet energy scale and resolution in the CMS experiment in pp collisions at 8 TeV", *JINST* **12** (2017), no. 02, P02014, `doi:10.1088/1748-0221/12/02/P02014`, `arXiv:1607.03663`.

[169] CMS Collaboration, "Pileup Removal Algorithms",.

[170] CMS Collaboration, "Pileup mitigation at CMS in 13 TeV data", *JINST* **15** (2020), no. 09, P09018, `doi:10.1088/1748-0221/15/09/P09018`, `arXiv:2003.00503`.

[171] D. Bertolini, P. Harris, M. Low, and N. Tran, "Pileup Per Particle Identification", *JHEP* **10** (2014) 059, `doi:10.1007/JHEP10(2014)059`, `arXiv:1407.6013`.

[172] CMS Collaboration, "Jet algorithms performance in 13 TeV data",.

[173] CMS Collaboration, “Pileup Jet Identification”,.

[174] CMS Collaboration, “Identification of heavy-flavour jets with the CMS detector in pp collisions at 13 TeV”, *JINST* **13** (2018) P05011, `doi:10.1088/1748-0221/13/05/P05011`, `arXiv:1712.07158`.

[175] E. Bols et al., “Jet flavour classification using DeepJet”, *JINST* **15** (2020) P12012, `doi:10.1088/1748-0221/15/12/P12012`, `arXiv:2008.10519`.

[176] CMS Collaboration, “Performance summary of AK4 jet b tagging with data from proton-proton collisions at 13 TeV with the CMS detector”, CMS Detector Performance Note CMS-DP-2023-005, 2023.

[177] H. Qu, C. Li, and S. Qian, “Particle transformer for jet tagging”, in *Proc. 39th International Conference on Machine Learning (ICML 2022): Baltimore MD, USA, July 17–23, 2022.* 2022. `arXiv:2202.03772`. [PMLR 162 (2022) 18281].

[178] CMS Collaboration, “Transformer models for heavy flavor jet identification”, CMS Detector Performance Note CMS-DP-2022-050, 2022.

[179] CMS Collaboration, “Adversarial training for b-tagging algorithms in CMS”, CMS Detector Performance Note CMS-DP-2022-049, 2022.

[180] CMS Collaboration, “Run 3 commissioning results of heavy-flavor jet tagging at $\sqrt{s} = 13.6$ TeV with CMS data using a modern framework for data processing”, CMS Detector Performance Note CMS-DP-2022-024, 2024.

[181] CMS Collaboration, “Performance summary of AK4 jet b tagging with data from 2022 proton-proton collisions at 13.6 TeV with the CMS detector”, CMS Detector Performance Note CMS-DP-2022-025, 2024.

[182] CMS Collaboration, “Electron and photon reconstruction and identification performance at CMS in 2022 and 2023”,.

[183] CMS Collaboration, “Extraction and validation of a new set of CMS PYTHIA8 tunes from underlying-event measurements”, *Eur. Phys. J. C* **80** (2020), no. 1, 4, `doi:10.1140/epjc/s10052-019-7499-4`, `arXiv:1903.12179`.

[184] P. Artoisenet, R. Frederix, O. Mattelaer, and R. Rietkerk, “Automatic spin-entangled decays of heavy resonances in Monte Carlo simulations”, *JHEP* **03** (2013) 015, `doi:10.1007/JHEP03(2013)015`, `arXiv:1212.3460`.

[185] S. Frixione, P. Nason, and G. Ridolfi, “A Positive-weight next-to-leading-order Monte Carlo for heavy flavour hadroproduction”, *JHEP* **09** (2007) 126, `doi:10.1088/1126-6708/2007/09/126`, `arXiv:0707.3088`.

[186] S. Alioli, P. Nason, C. Oleari, and E. Re, “A general framework for implementing NLO calculations in shower Monte Carlo programs: the

POWHEG BOX", *JHEP* **06** (2010) 043, `doi:10.1007/JHEP06(2010)043`, `arXiv:1002.2581`.

[187] E. Re, "Single-top Wt-channel production matched with parton showers using the POWHEG method", *Eur. Phys. J.* **C71** (2011) 1547, `doi:10.1140/epjc/s10052-011-1547-z`, `arXiv:1009.2450`.

[188] L. Breiman, "Random Forests", *Machine Learning* **45** (2001), no. 1, 5–32, `doi:10.1023/A:1010933404324`.

[189] Y. Freund and R. E. Schapire, "A Decision-Theoretic Generalization of On-Line Learning and an Application to Boosting", *Journal of Computer and System Sciences* **55** (1997), no. 1, 119–139, `doi:https://doi.org/10.1006/jcss.1997.1504`.

[190] W. S. McCulloch and W. Pitts, "A Logical Calculus of the Ideas Immanent in Nervous Activity", *The Bulletin of Mathematical Biophysics* **5** (1943) 115–133, `doi:10.1007/BF02478259`.

[191] F. Rosenblatt, "The Perceptron: A Probabilistic Model for Information Storage and Organization in the Brain", *Psychological Review* **65** (1958), no. 6, 386–408, `doi:10.1037/h0042519`.

[192] I. Goodfellow, Y. Bengio, and A. Courville, "Deep Learning". MIT Press, 2016. `http://www.deeplearningbook.org`.

[193] A. Vaswani et al., "Attention Is All You Need", in *31st International Conference on Neural Information Processing Systems.* 6, 2017. `arXiv:1706.03762`.

[194] S. S. Wilks, "The Large-Sample Distribution of the Likelihood Ratio for Testing Composite Hypotheses", *Annals Math. Statist.* **9** (1938), no. 1, 60–62, `doi:10.1214/aoms/1177732360`.

[195] CMS Collaboration, "Precision luminosity measurement in proton-proton collisions at $\sqrt{s} = 13\,\text{TeV}$ in 2015 and 2016 at CMS", *Eur. Phys. J. C* **81** (2021) 800, `doi:10.1140/epjc/s10052-021-09538-2`, `arXiv:2104.01927`.

[196] CMS Collaboration, "CMS luminosity measurement for the 2017 data-taking period at $\sqrt{s} = 13\,\text{TeV}$", CMS Physics Analysis Summary CMS-PAS-LUM-17-004, 2018.

[197] CMS Collaboration, "CMS luminosity measurement for the 2018 data-taking period at $\sqrt{s} = 13\,\text{TeV}$", CMS Physics Analysis Summary CMS-PAS-LUM-18-002, 2019.

[198] CMS Collaboration, "Luminosity measurement in proton-proton collisions at

13.6 TeV in 2022 at CMS", CMS Physics Analysis Summary CMS-PAS-LUM-22-001, 2024.

[199] CMS Collaboration, "Measurement of the offline integrated luminosity for the CMS proton-proton collision dataset recorded in 2023", CMS Detector Performance Note CMS-DP-2024-068, 2024.

[200] R. J. Barlow and C. Beeston, "Fitting using finite Monte Carlo samples", *Comput. Phys. Commun.* **77** (1993) 219–228, `doi:10.1016/0010-4655(93)90005-W`.

[201] W. S. Cleveland, "Robust locally weighted regression and smoothing scatterplots", *Journal of the American statistical association* **74** (1979), no. 368, 829–836.

[202] CMS Collaboration, "Measurement of the inclusive and differential WZ production cross sections, polarization angles, and triple gauge couplings in pp collisions at $\sqrt{s} = 13$ TeV", *JHEP* **07** (2022) 032, `doi:10.1007/JHEP07(2022)032`, `arXiv:2110.11231`.

[203] CMS Collaboration, "Observation of the production of three massive gauge bosons at $\sqrt{s} = 13\,\text{TeV}$", *Phys. Rev. Lett.* **125** (2020) 151802, `doi:10.1103/PhysRevLett.125.151802`, `arXiv:2006.11191`.

[204] ATLAS Collaboration, "Observation of Wgg triboson production in proton-proton collisions at $\sqrt{s} = 13\,\text{TeV}$ with the ATLAS detector", *Phys. Lett. B* **848** (2024) 138400, `doi:10.1016/j.physletb.2023.138400`, `arXiv:2308.03041`.

[205] ATLAS Collaboration, "Observation of WZg Production in pp collisions at $\sqrt{s} = 13\,\text{TeV}$ with the ATLAS detector", *Phys. Rev. Lett.* **132** (2024) 021802, `doi:10.1103/PhysRevLett.132.021802`, `arXiv:2305.16994`.

[206] CMS Collaboration, "Observation of WWg production and search for Hg production in proton-proton collisions at $\sqrt{s} = 13\,\text{TeV}$", *Phys. Rev. Lett.* **132** (2024) 121901, `doi:10.1103/PhysRevLett.132.121901`, `arXiv:2310.05164`.

[207] M. Czakon and A. Mitov, "Top++: A Program for the Calculation of the Top-Pair Cross-Section at Hadron Colliders", *Comput. Phys. Commun.* **185** (2014) 2930, `doi:10.1016/j.cpc.2014.06.021`, `arXiv:1112.5675`.

[208] J. Butterworth et al., "PDF4LHC recommendations for LHC Run II", *J. Phys. G* **43** (2016) 023001, `doi:10.1088/0954-3899/43/2/023001`, `arXiv:1510.03865`.

[209] CMS Collaboration, "Observation of tWZ production at the CMS

experiment", 2025.

Appendices

A.1 Input variables for the training in the 3ℓ SR

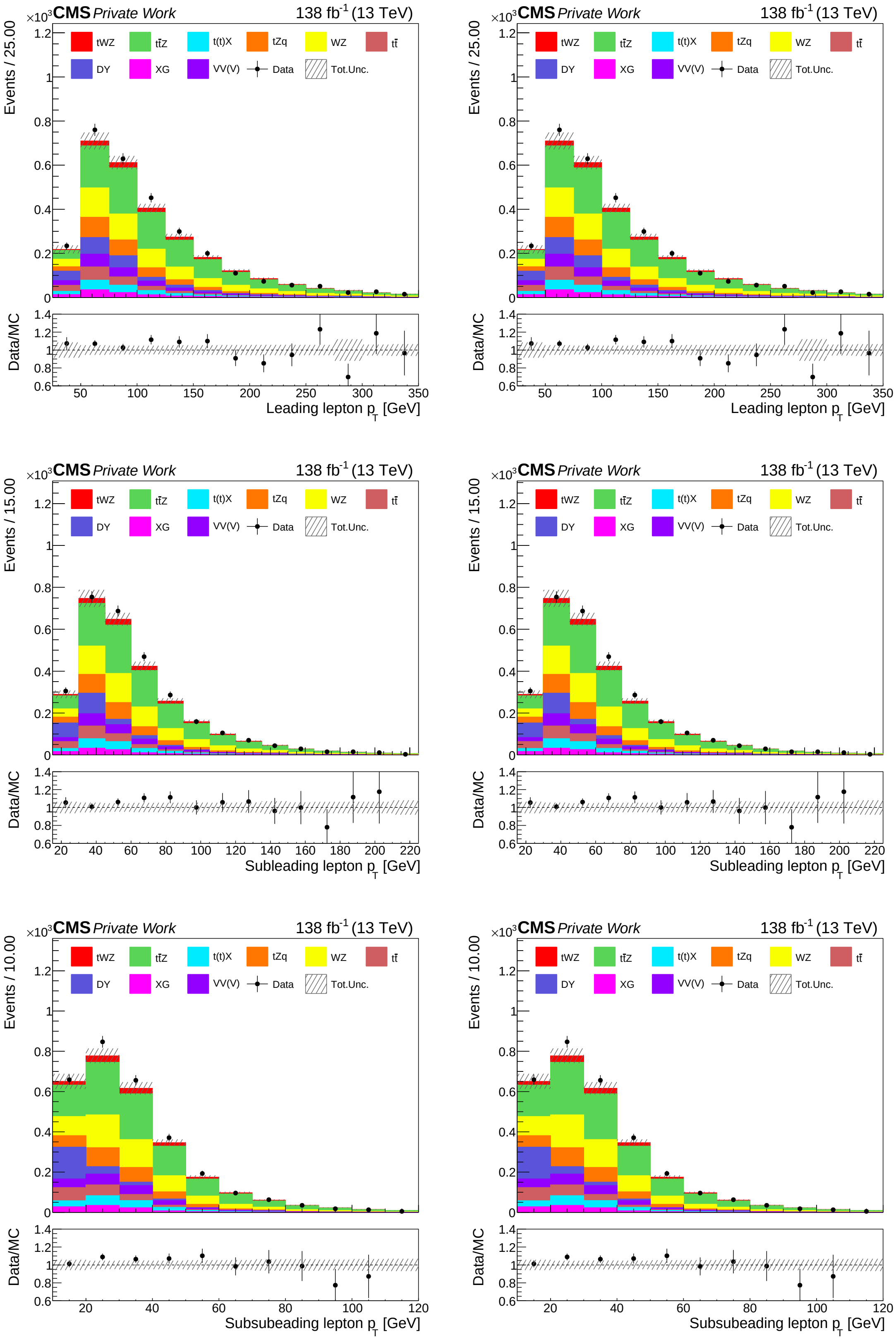

Figure A.1: Control plots for the ML algorithm employed in the SL SR. The left column shows plots with Run 2 data, while the right one contains distributions with Run 3 data.

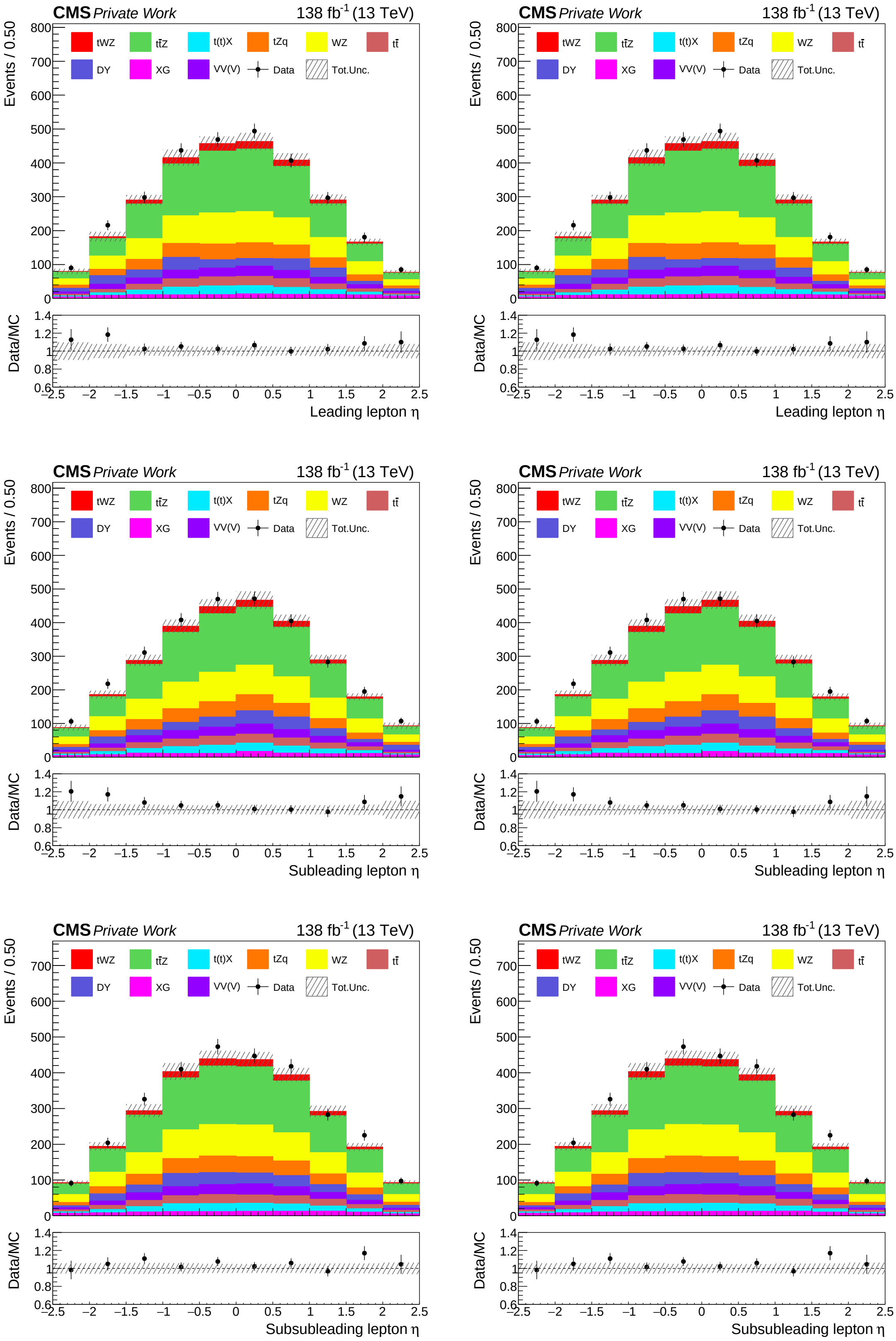

Figure A.2: Control plots for the ML algorithm employed in the SL SR. The left column shows plots with Run 2 data, while the right one contains distributions with Run 3 data.

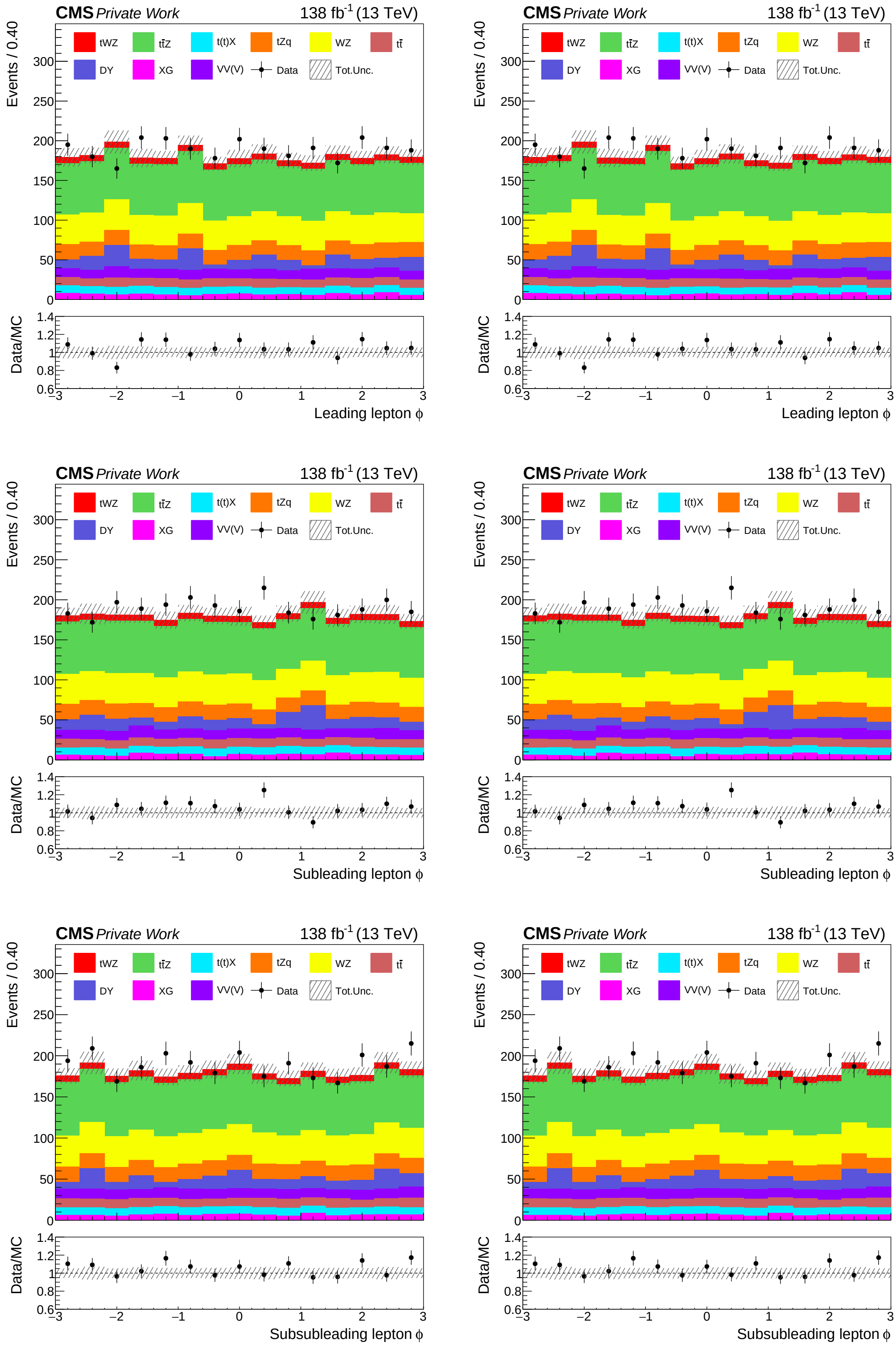

Figure A.3: Control plots for the ML algorithm employed in the SL SR. The left column shows plots with Run 2 data, while the right one contains distributions with Run 3 data.

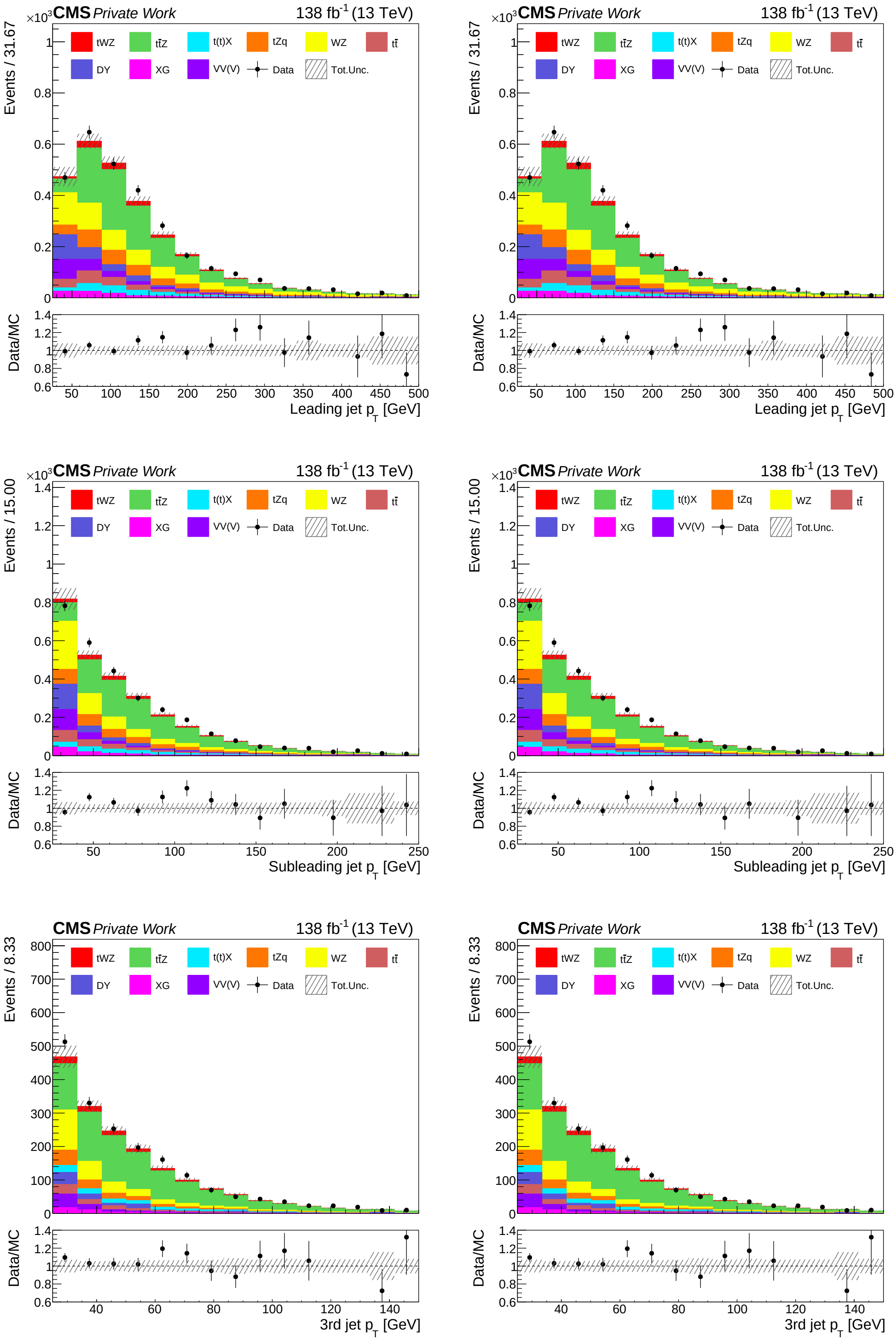

Figure A.4: Control plots for the ML algorithm employed in the SL SR. The left column shows plots with Run 2 data, while the right one contains distributions with Run 3 data.

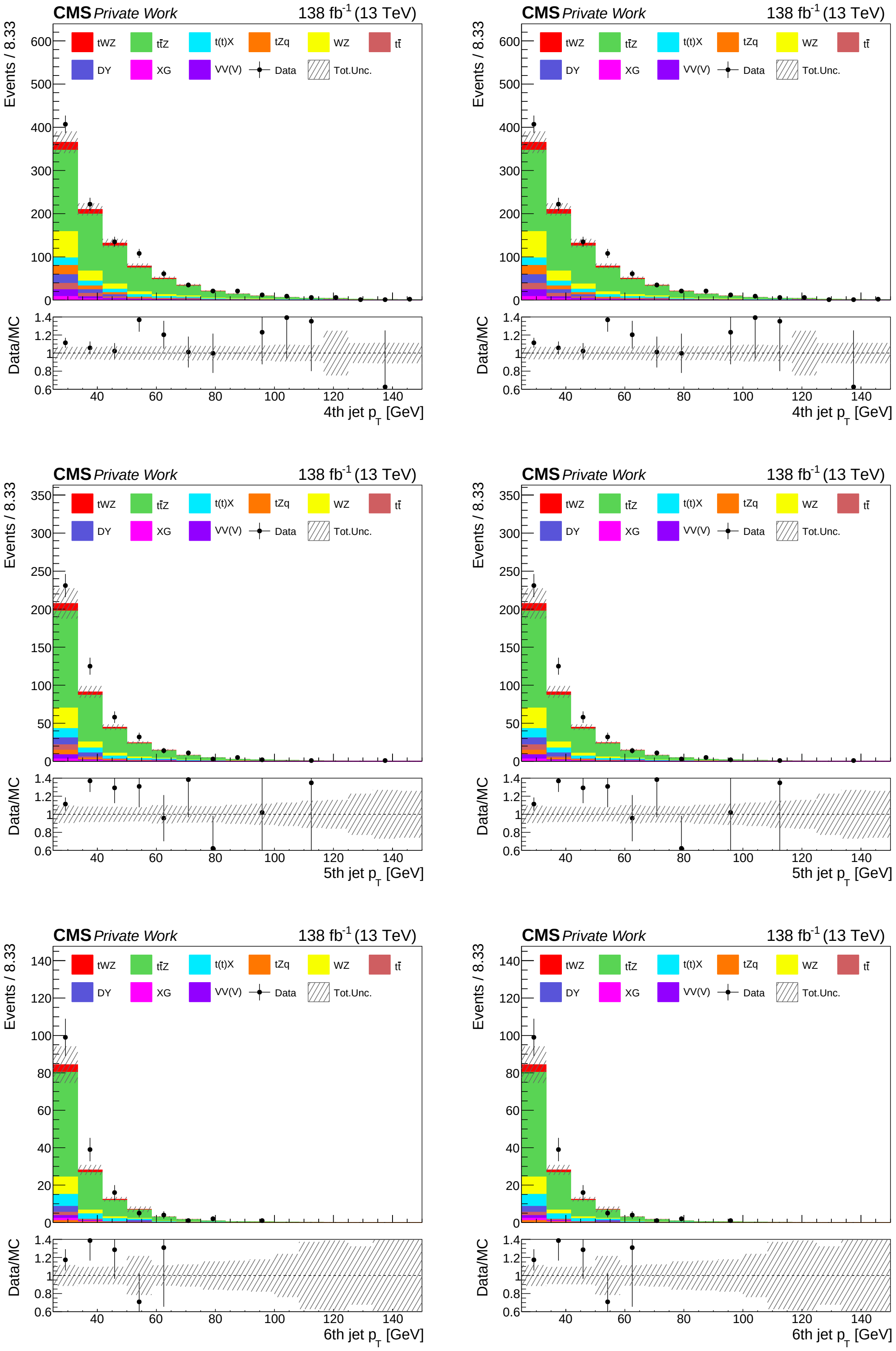

Figure A.5: Control plots for the ML algorithm employed in the SL SR. The left column shows plots with Run 2 data, while the right one contains distributions with Run 3 data.

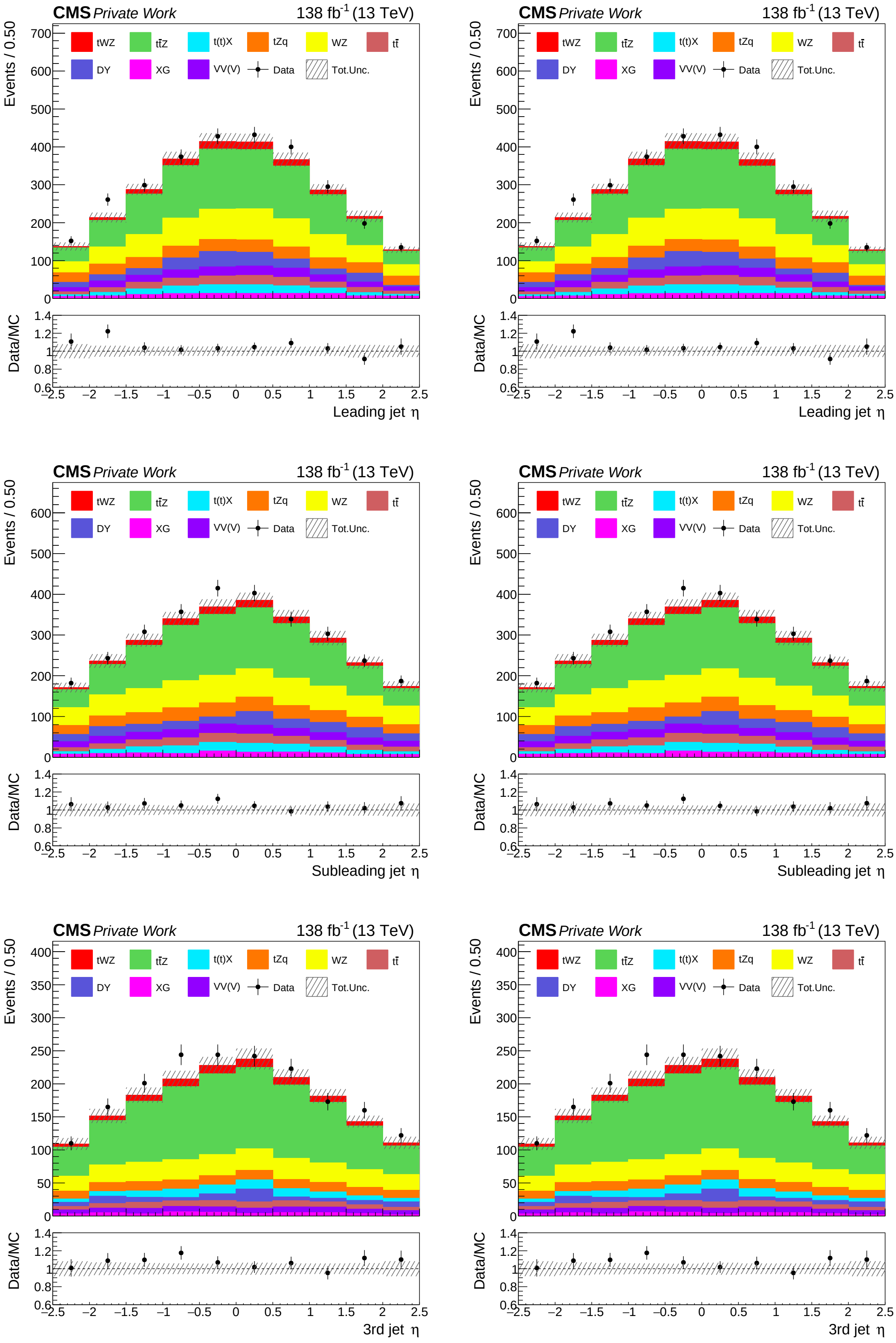

Figure A.6: Control plots for the ML algorithm employed in the SL SR. The left column shows plots with Run 2 data, while the right one contains distributions with Run 3 data.

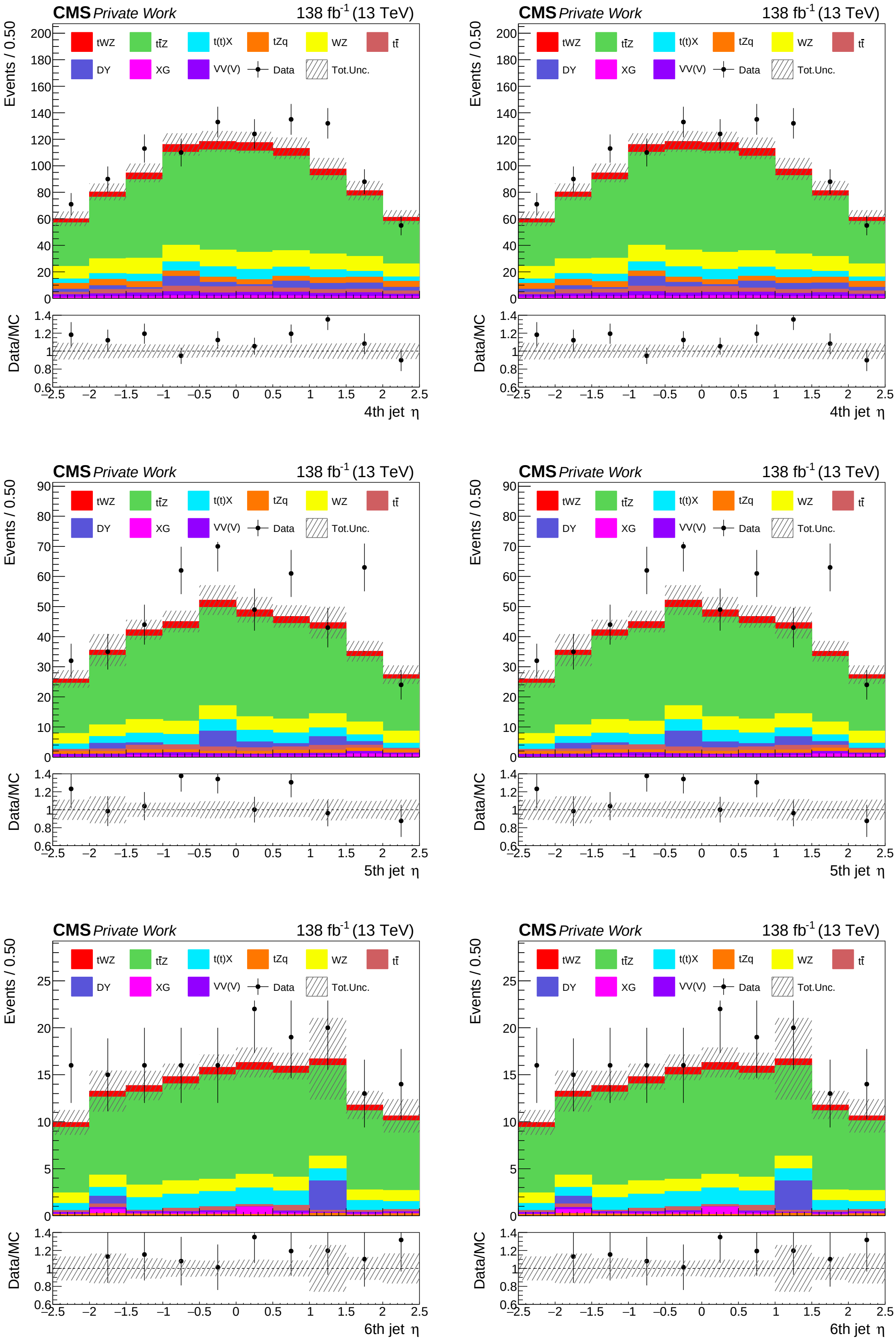

Figure A.7: Control plots for the ML algorithm employed in the SL SR. The left column shows plots with Run 2 data, while the right one contains distributions with Run 3 data.

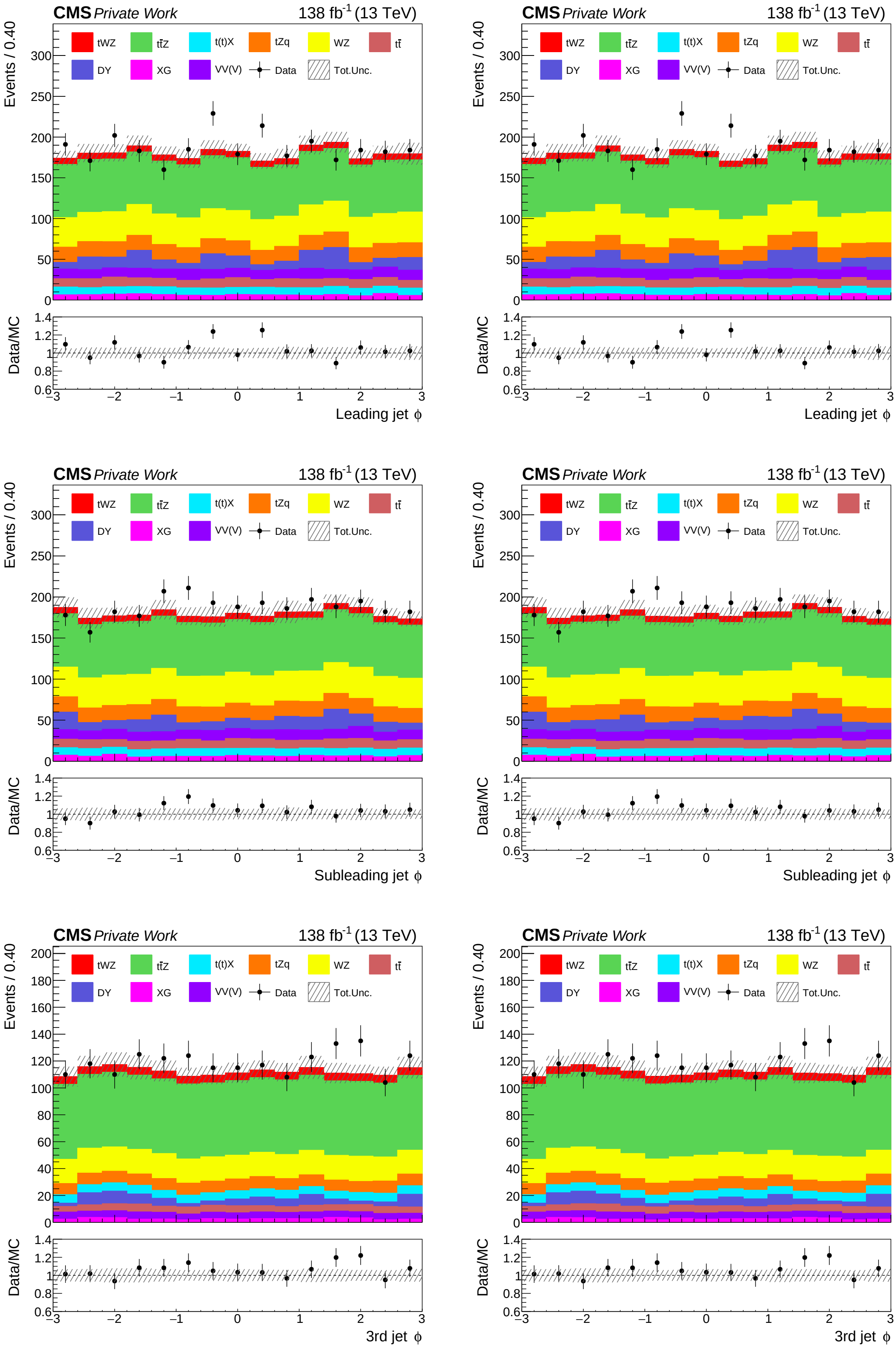

Figure A.8: Control plots for the ML algorithm employed in the SL SR. The left column shows plots with Run 2 data, while the right one contains distributions with Run 3 data.

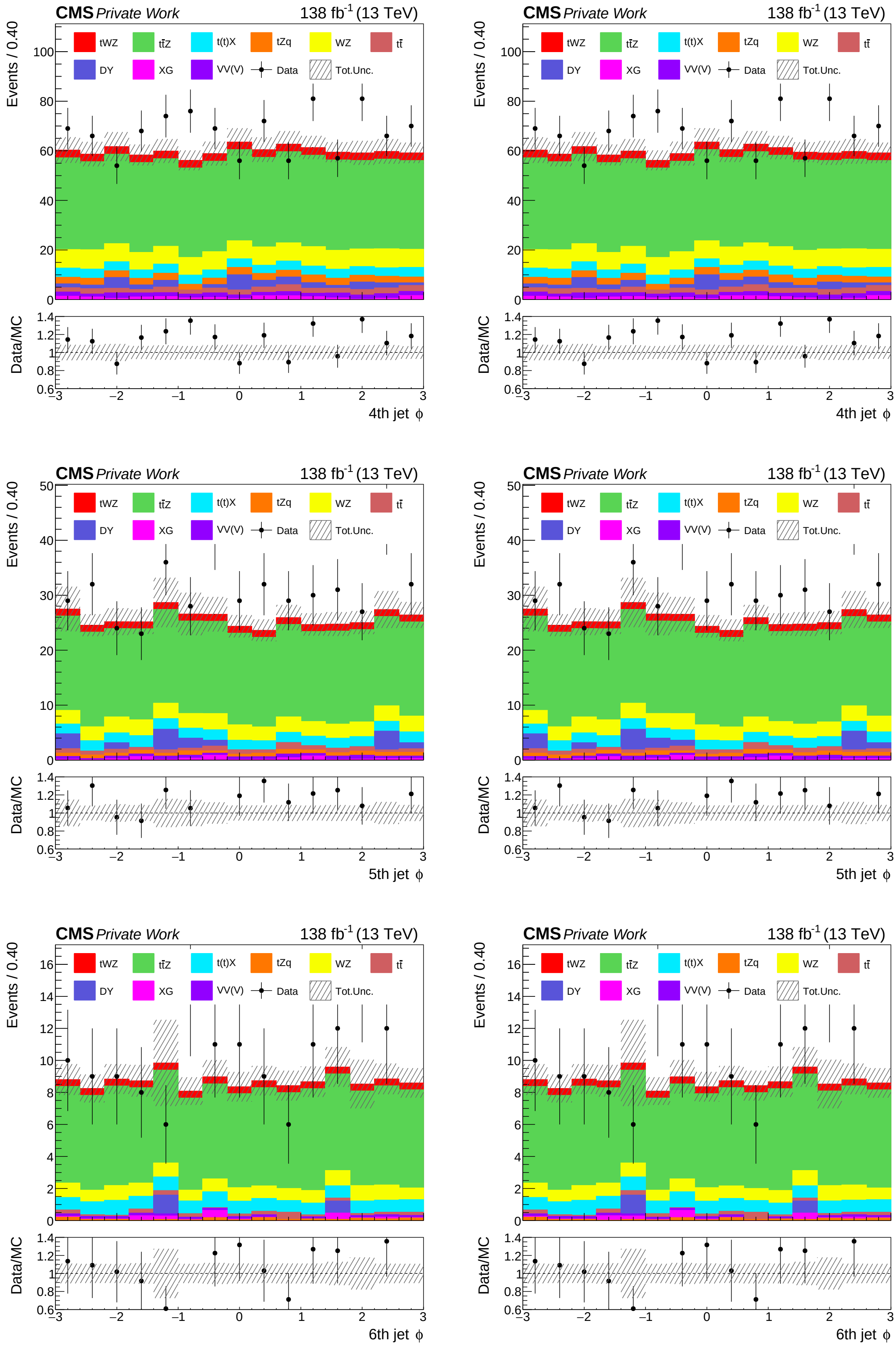

Figure A.9: Control plots for the ML algorithm employed in the SL SR. The left column shows plots with Run 2 data, while the right one contains distributions with Run 3 data.

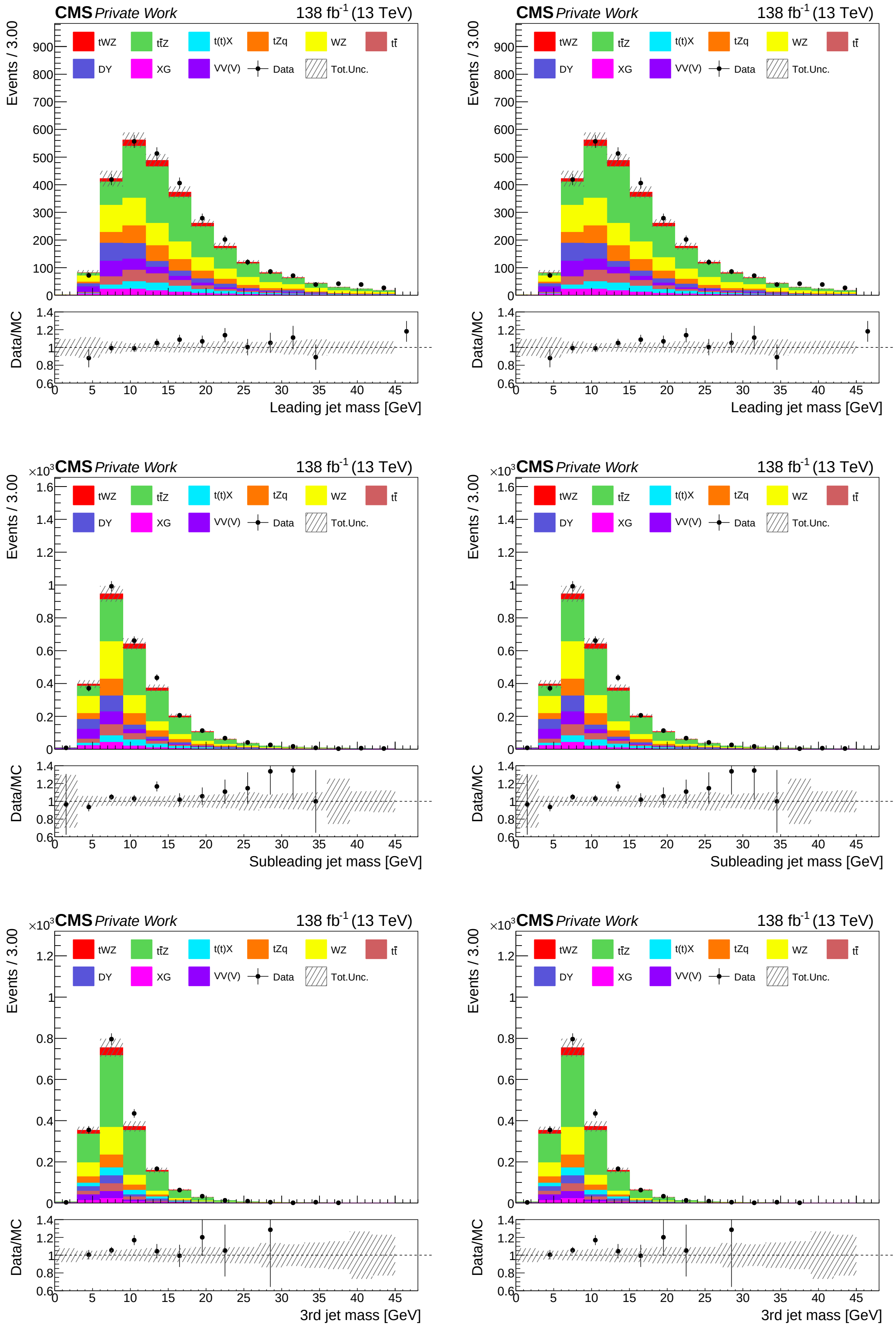

Figure A.10: Control plots for the ML algorithm employed in the SL SR. The left column shows plots with Run 2 data, while the right one contains distributions with Run 3 data.

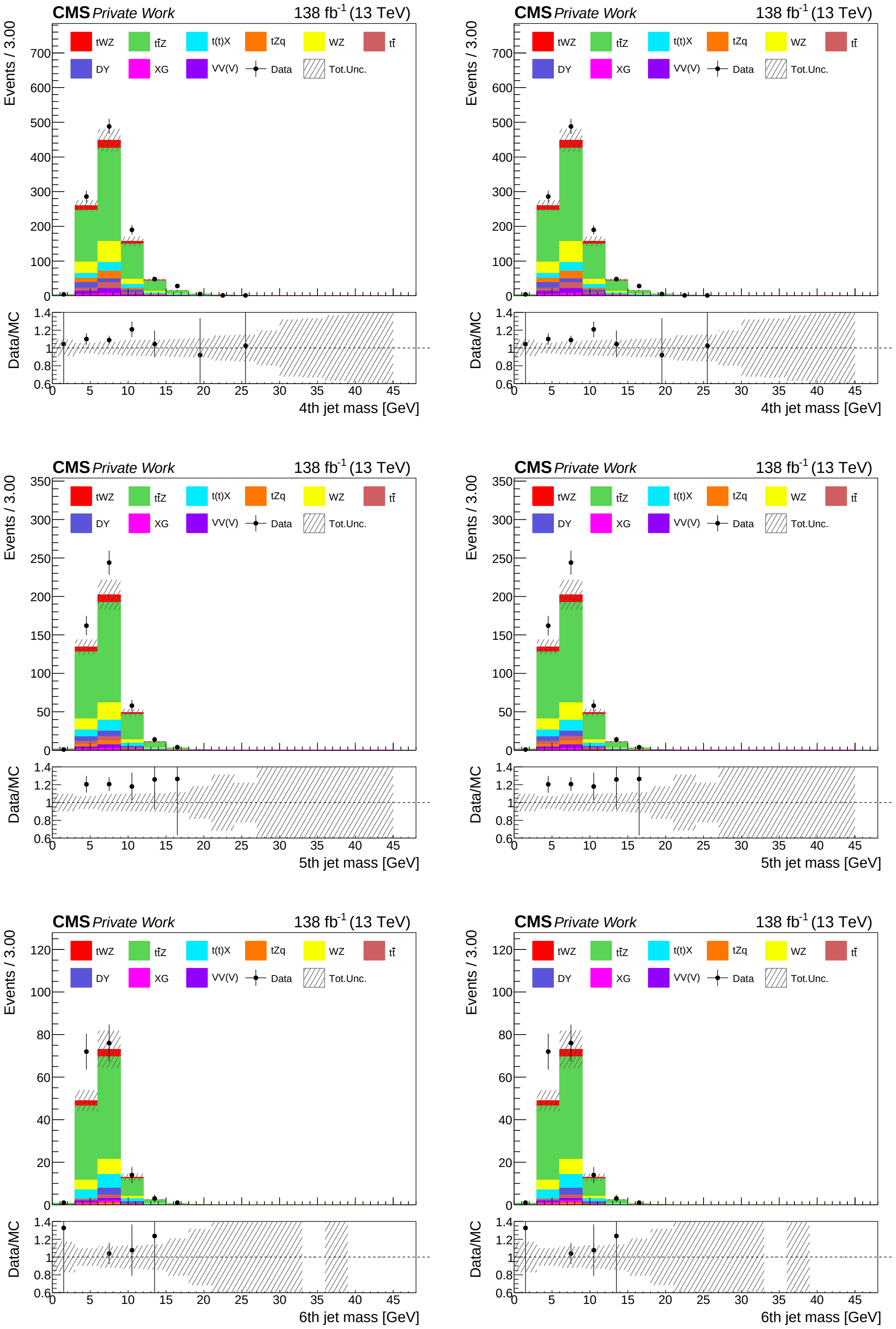

Figure A.11: Control plots for the ML algorithm employed in the SL SR. The left column shows plots with Run 2 data, while the right one contains distributions with Run 3 data.

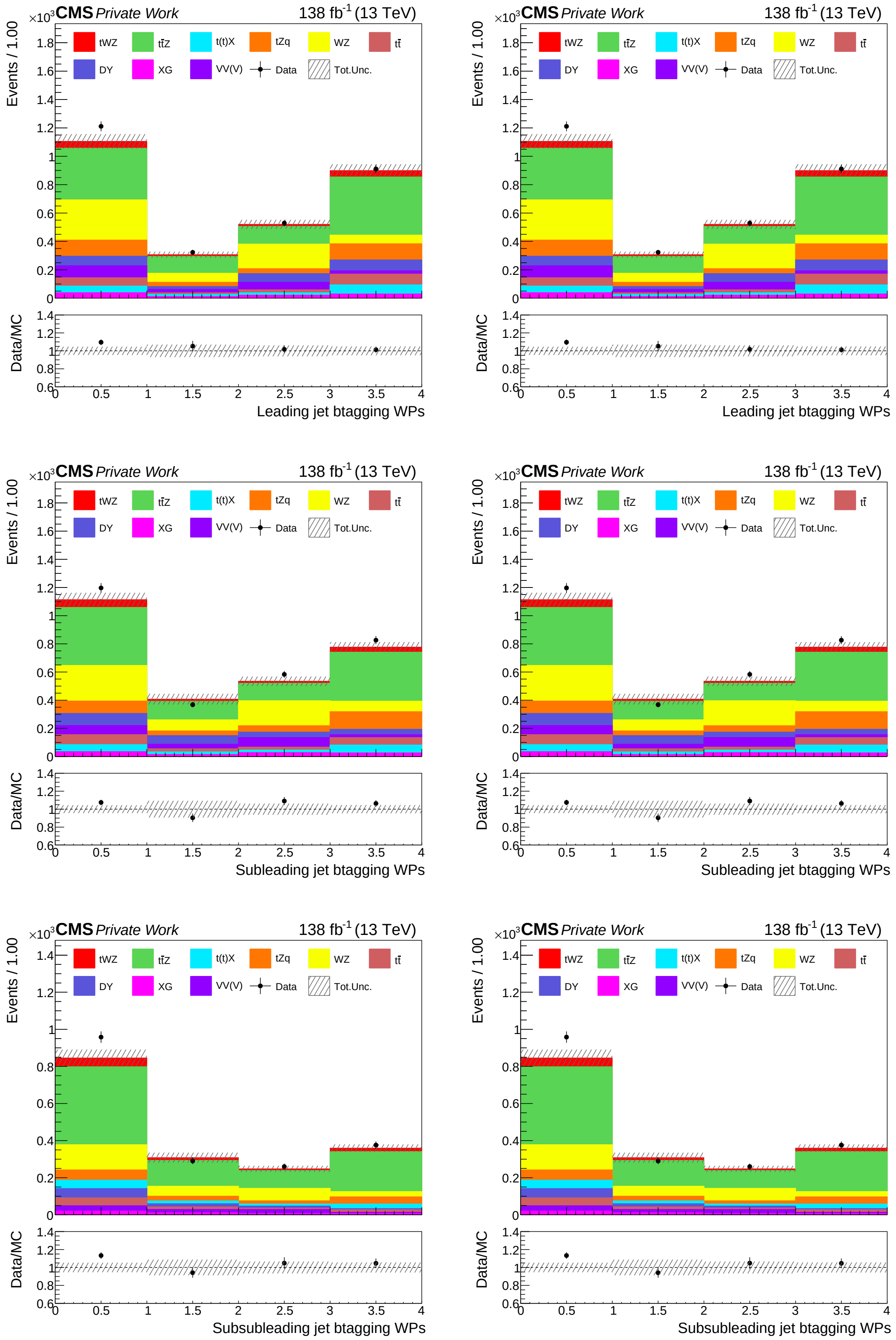

Figure A.12: Control plots for the ML algorithm employed in the SL SR. The left column shows plots with Run 2 data, while the right one contains distributions with Run 3 data.

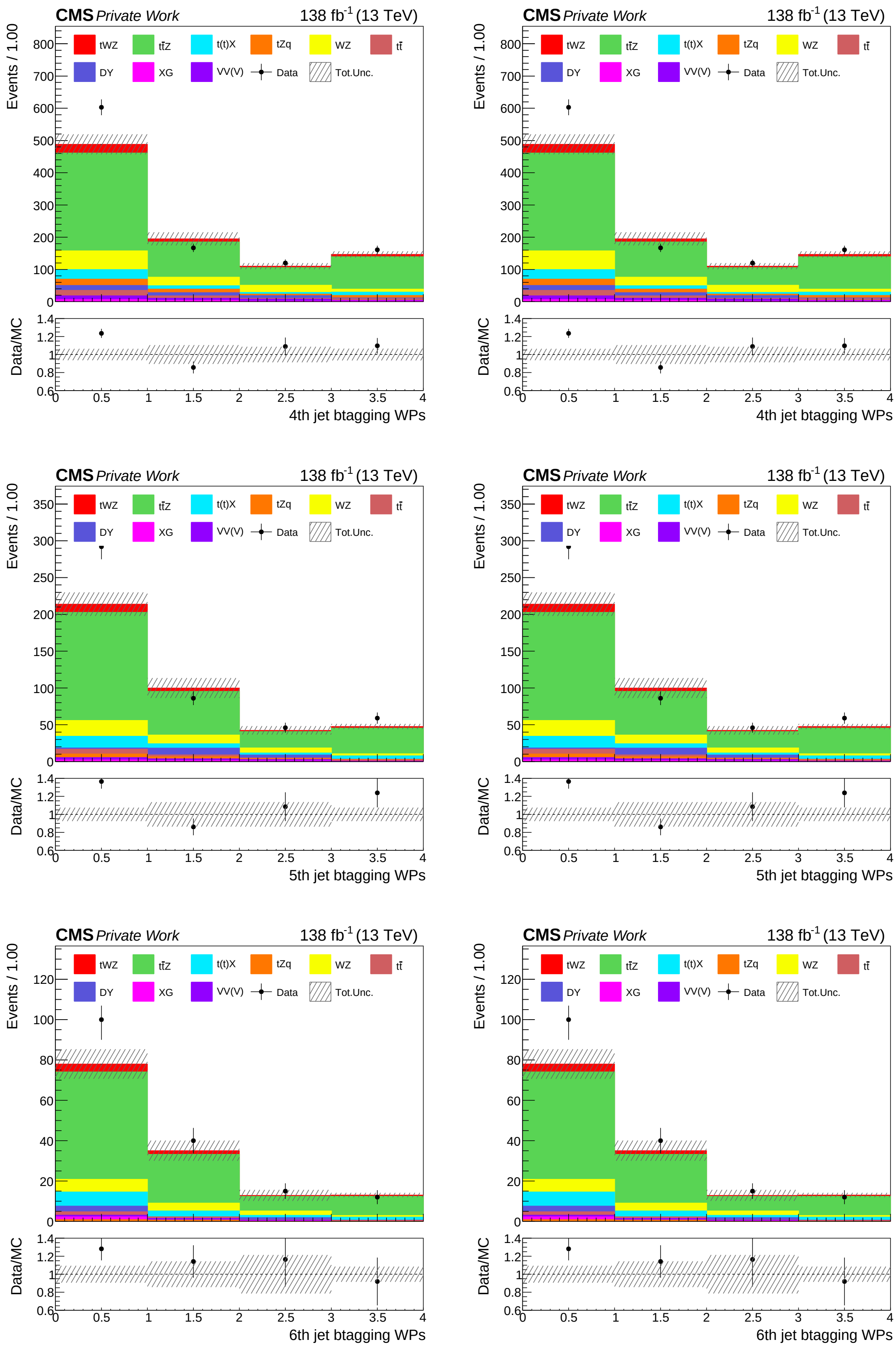

Figure A.13: Control plots for the ML algorithm employed in the SL SR. The left column shows plots with Run 2 data, while the right one contains distributions with Run 3 data.

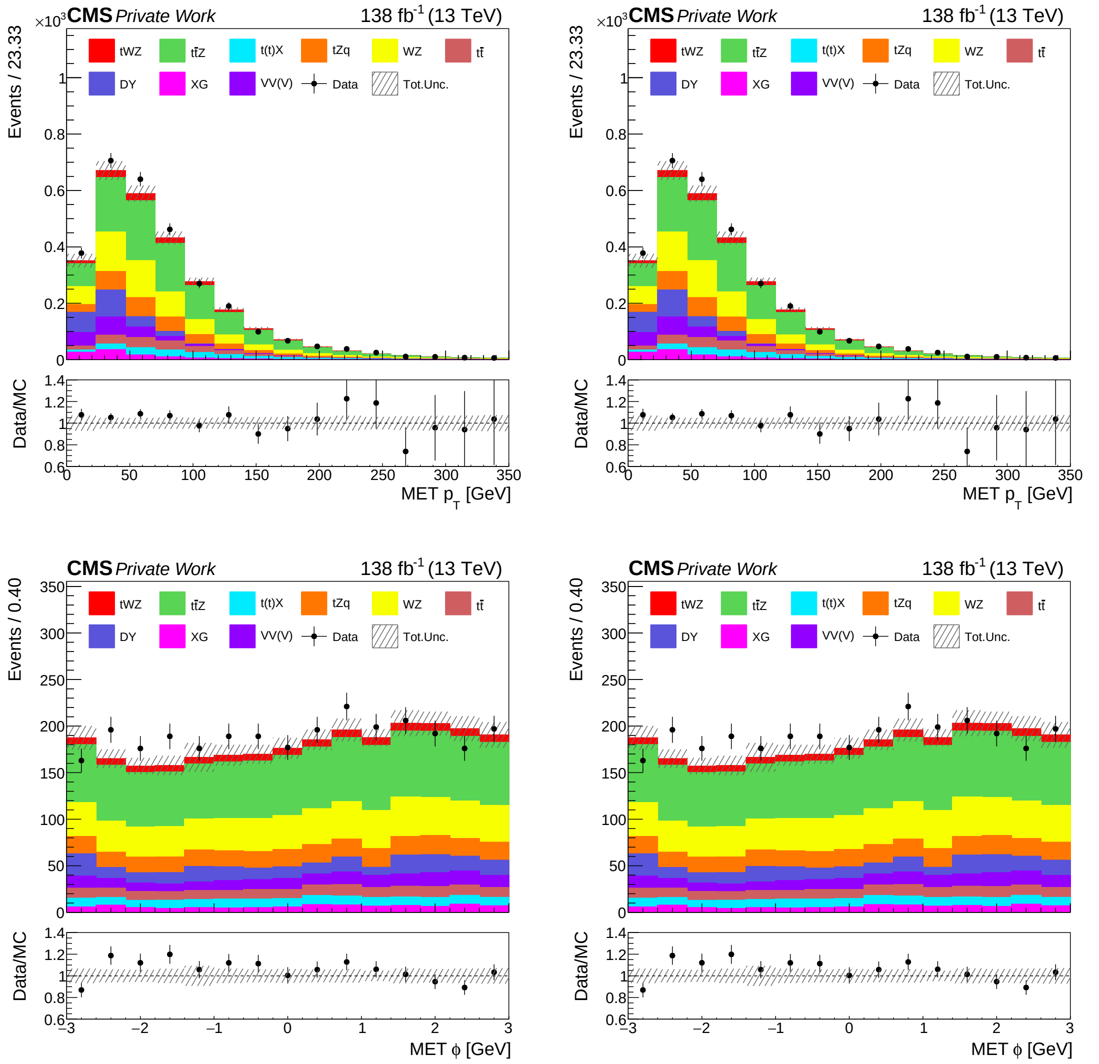

Figure A.14: Control plots for the ML algorithm employed in the SL SR. The left column shows plots with Run 2 data, while the right one contains distributions with Run 3 data.

A.2 Input variables for the training in the 4ℓ SR

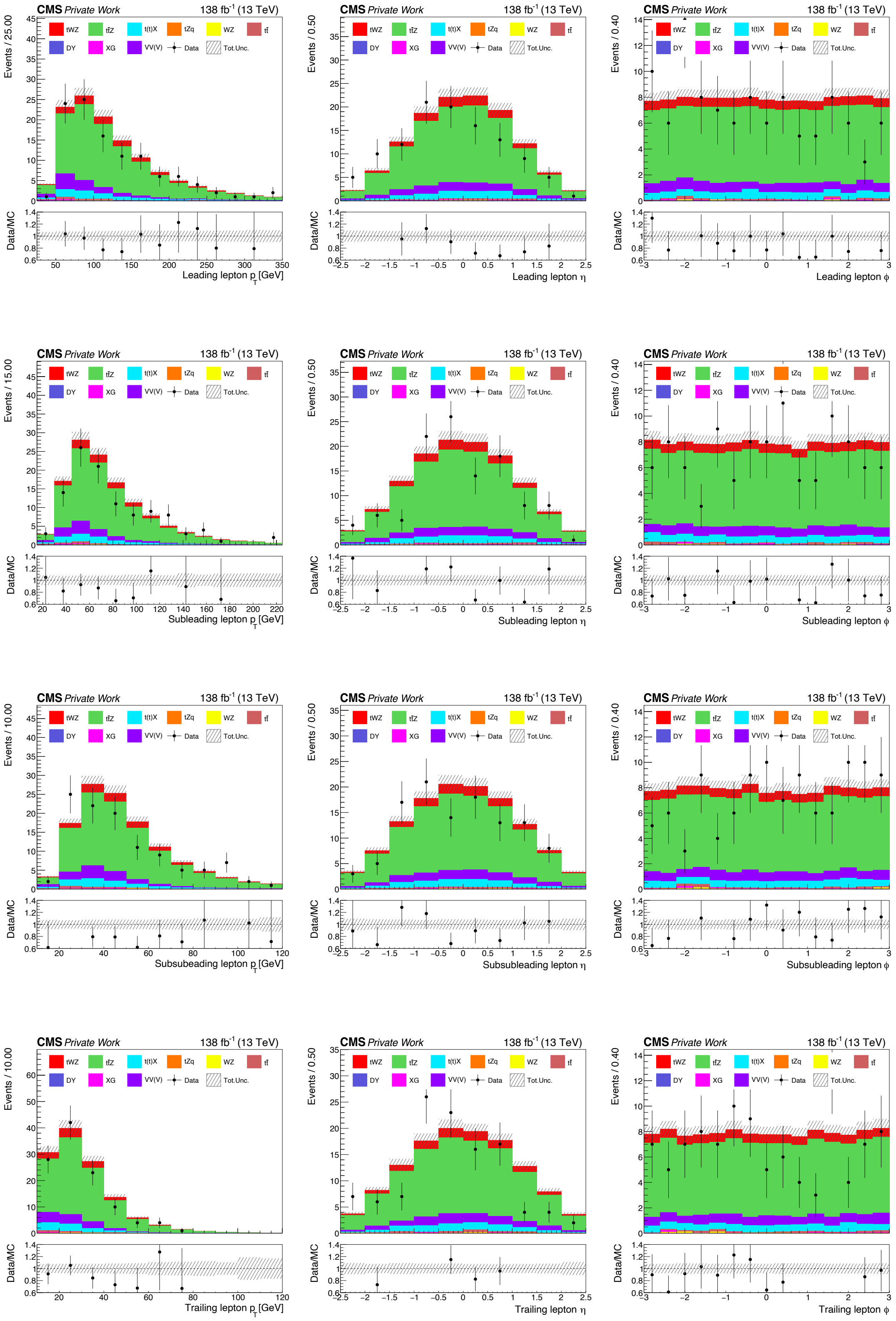

Figure A.15: Lepton control plots for the ML algorithm employed in the FL SR.

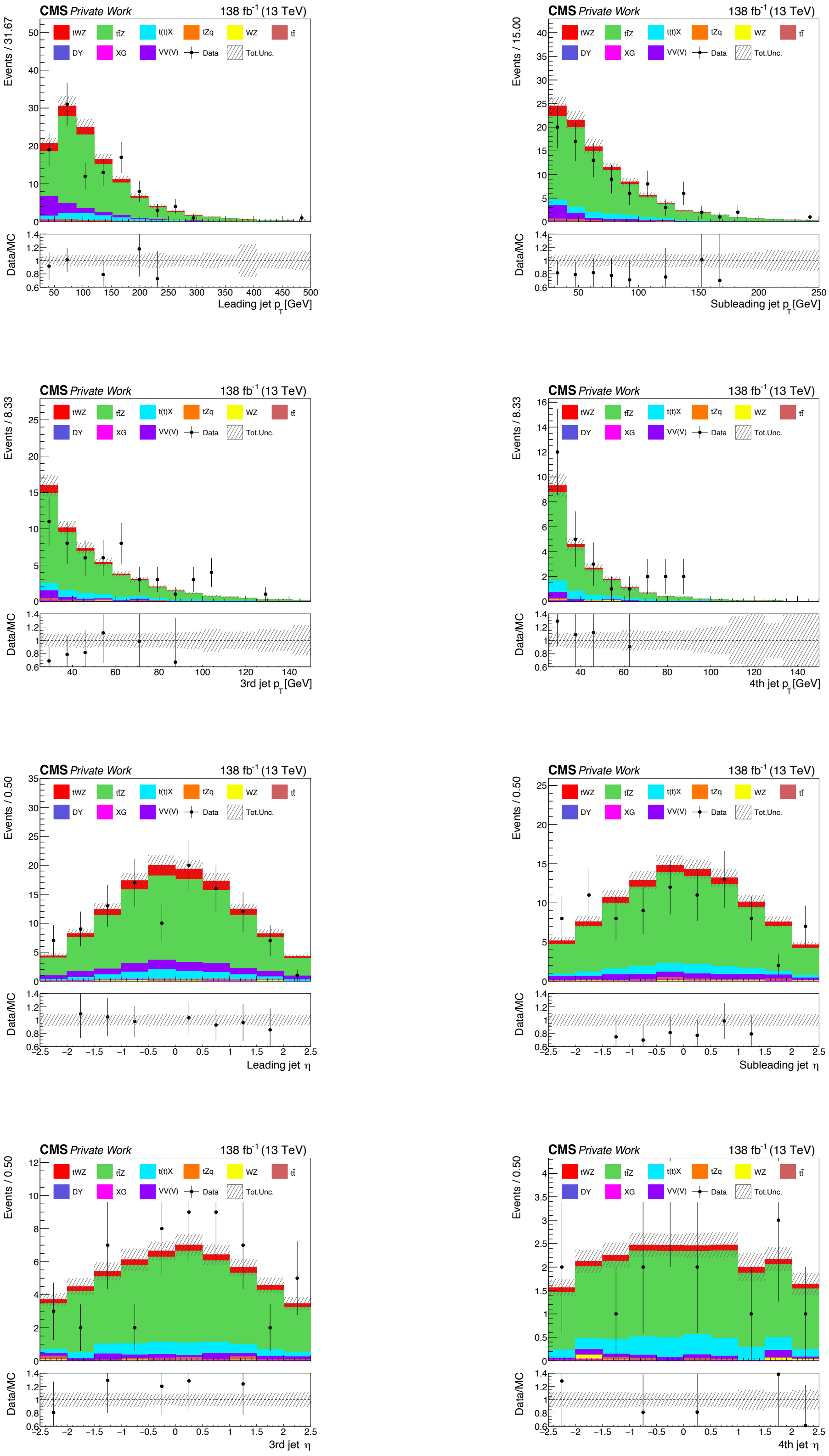

Figure A.16: Jets control plots for the ML algorithm employed in the FL SR.

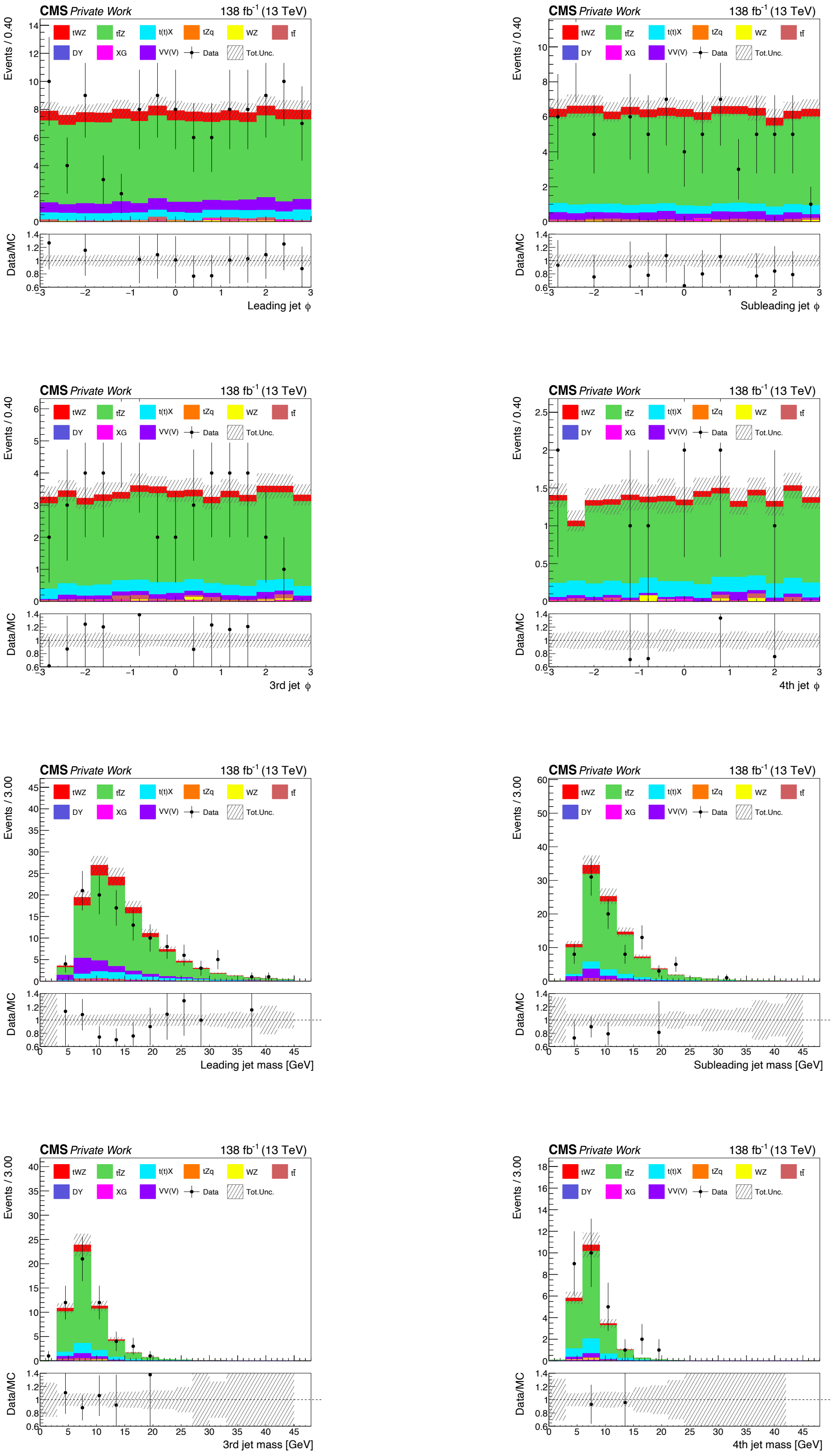

Figure A.17: Jets control plots for the ML algorithm employed in the FL SR.

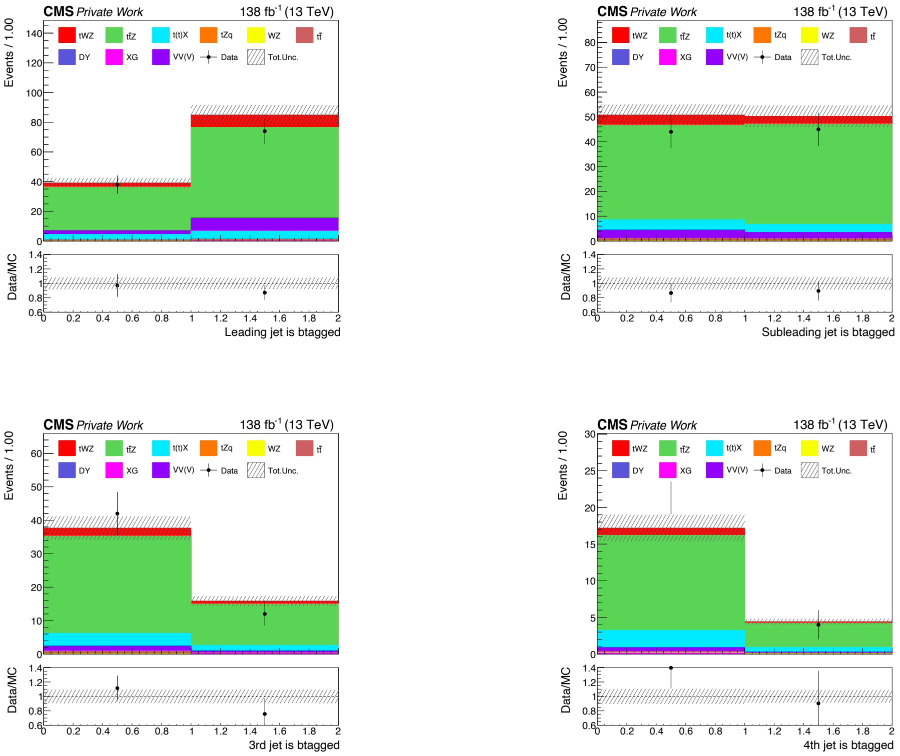

Figure A.18: Jets control plots for the ML algorithm employed in the FL SR.

A.3 Fake nuisances templates for Run 2

2016pre

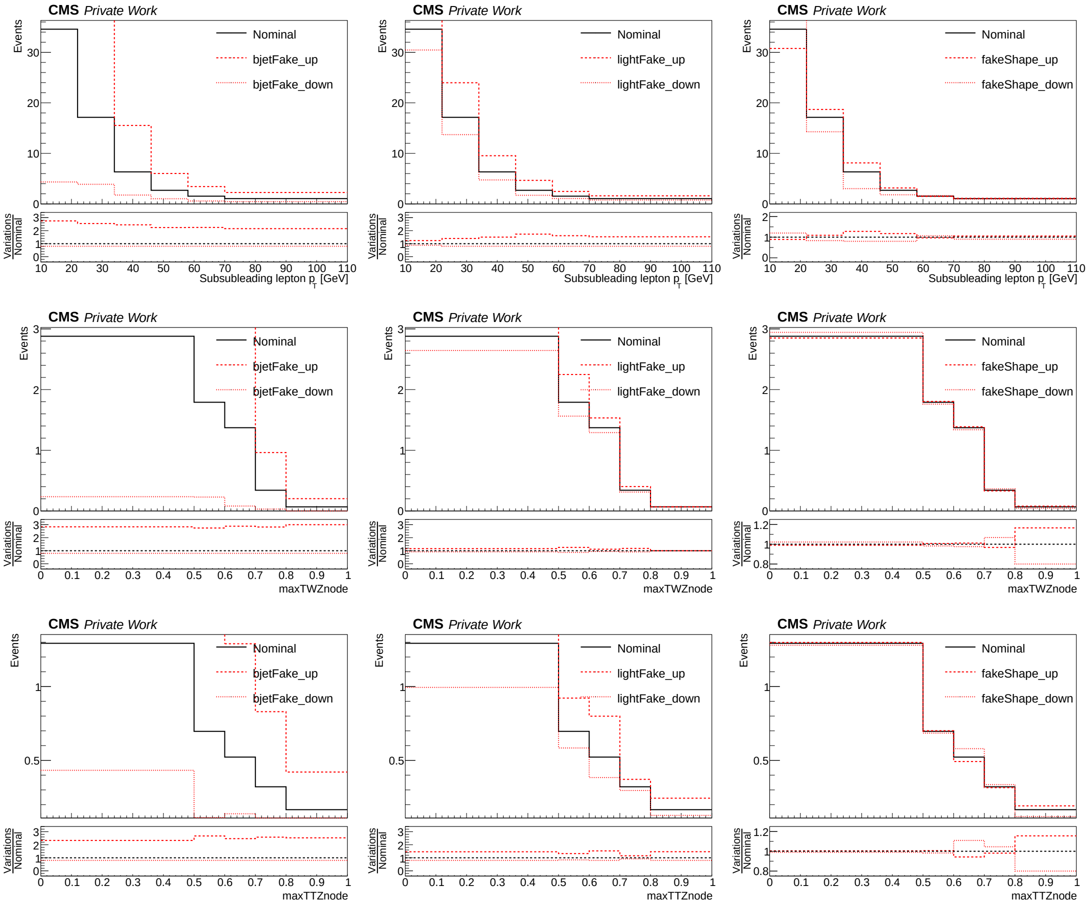

Figure A.19: Nominal event yields and fake lepton nuisances variations for the $t\bar{t}$ background in the 2016pre data-taking year. The subsubleading lepton p_T, the *max TWZ output*, and the *max TTZ output* distributions are shown from the first to the last row respectively. In particular, the subsubleading lepton p_T distribution is shown in the ttX control region, while the two ML output distributions correspond to the semi-leptonic signal region. The first two columns show the templates of the *b-jets fakes* and *light-jets fakes* uncertainties respectively, while in the third column the templates of the *fakes shape* nuisance is presented. The black line represents the nominal distribution, while the dotted red lines indicate the up and down variations. The range in the ratio plot is adjusted to display the entire distributions.

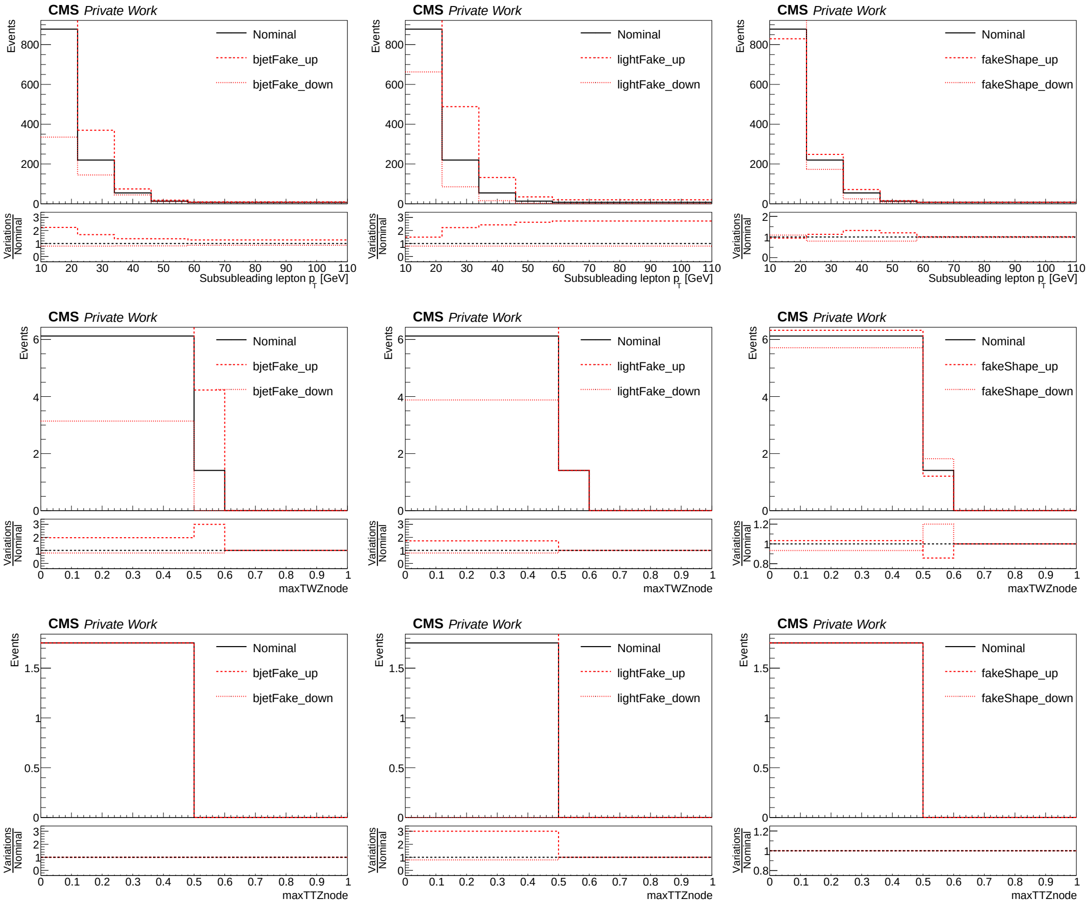

Figure A.20: Nominal event yields and fake lepton nuisances variations for the DY background in the 2016pre data-taking year. The subsubleading lepton p_T, the *max TWZ output*, and the *max TTZ output* distributions are shown from the first to the last row respectively. In particular, the subsubleading lepton p_T distribution is shown in the DY control region, while the two ML output distributions correspond to the semi-leptonic signal region. The first two columns show the templates of the *b-jets fakes* and *light-jets fakes* uncertainties respectively, while in the third column the templates of the *fakes shape* nuisance is presented. The black line represents the nominal distribution, while the dotted red lines indicate the up and down variations. The range in the ratio plot is adjusted to display the entire distributions.

2016post

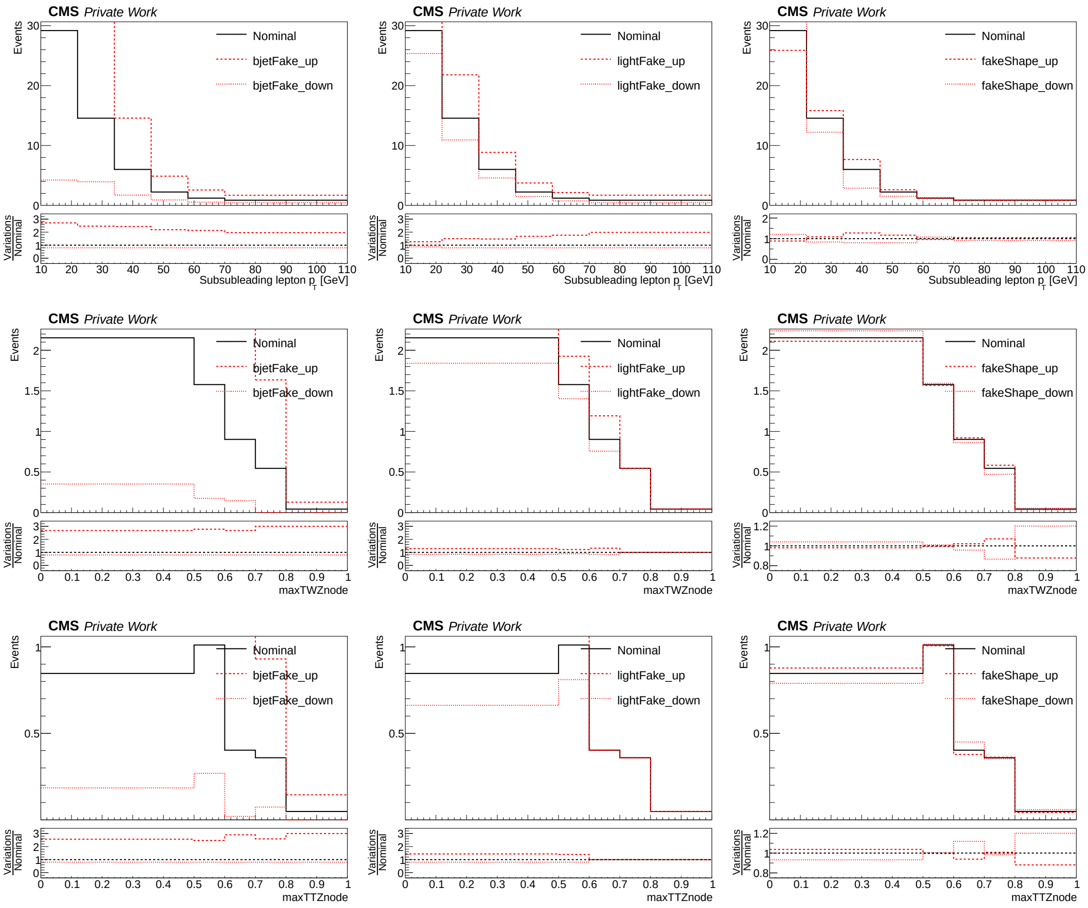

Figure A.21: Nominal event yields and fake lepton nuisances variations for the $t\bar{t}$ background in the 2016post data-taking year. The subsubleading lepton p_T, the *max TWZ output*, and the *max TTZ output* distributions are shown from the first to the last row respectively. In particular, the subsubleading lepton p_T distribution is shown in the ttX control region, while the two ML output distributions correspond to the semi-leptonic signal region. The first two columns show the templates of the *b-jets fakes* and *light-jets fakes* uncertainties respectively, while in the third column the templates of the *fakes shape* nuisance is presented. The black line represents the nominal distribution, while the dotted red lines indicate the up and down variations. The range in the ratio plot is adjusted to display the entire distributions.

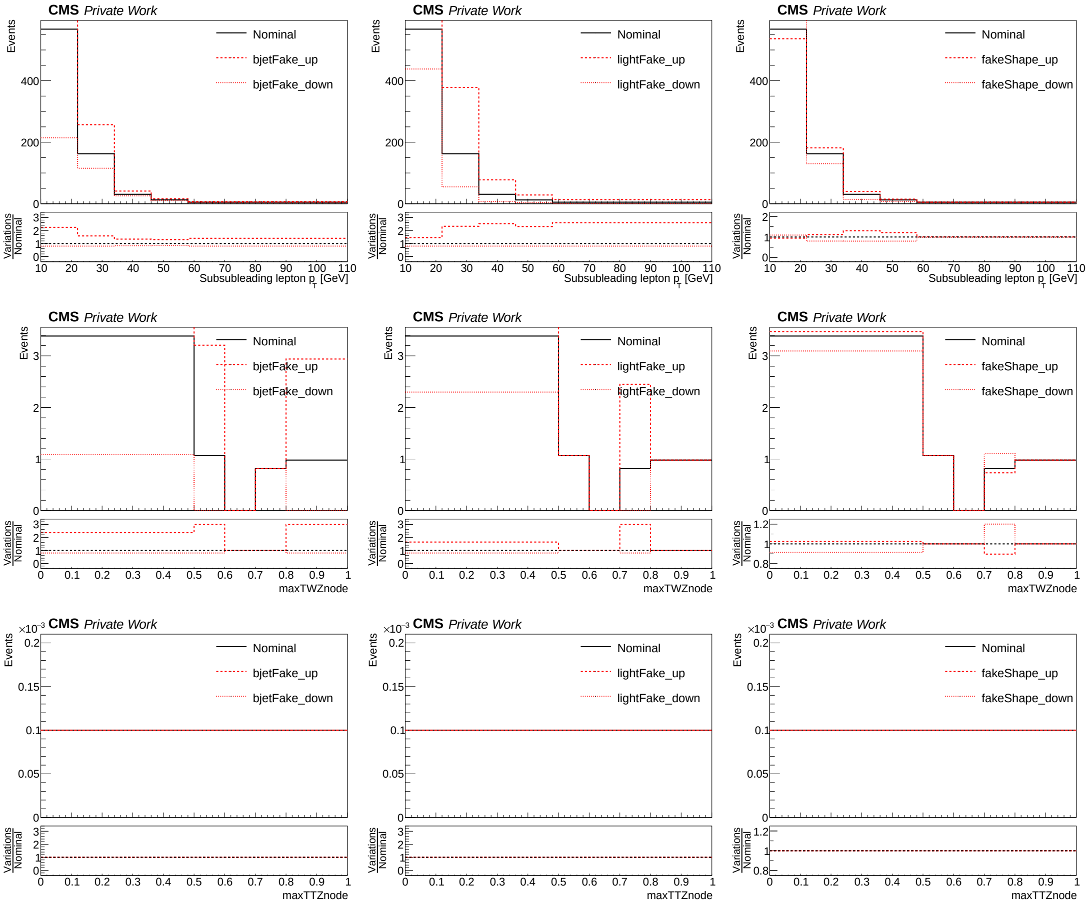

Figure A.22: Nominal event yields and fake lepton nuisances variations for the DY background in the 2016post data-taking year. The subsubleading lepton p_T, the *max TWZ output*, and the *max TTZ output* distributions are shown from the first to the last row respectively. In particular, the subsubleading lepton p_T distribution is shown in the DY control region, while the two ML output distributions correspond to the semi-leptonic signal region. The first two columns show the templates of the *b-jets fakes* and *light-jets fakes* uncertainties respectively, while in the third column the templates of the *fakes shape* nuisance is presented. The black line represents the nominal distribution, while the dotted red lines indicate the up and down variations. The range in the ratio plot is adjusted to display the entire distributions.

2017

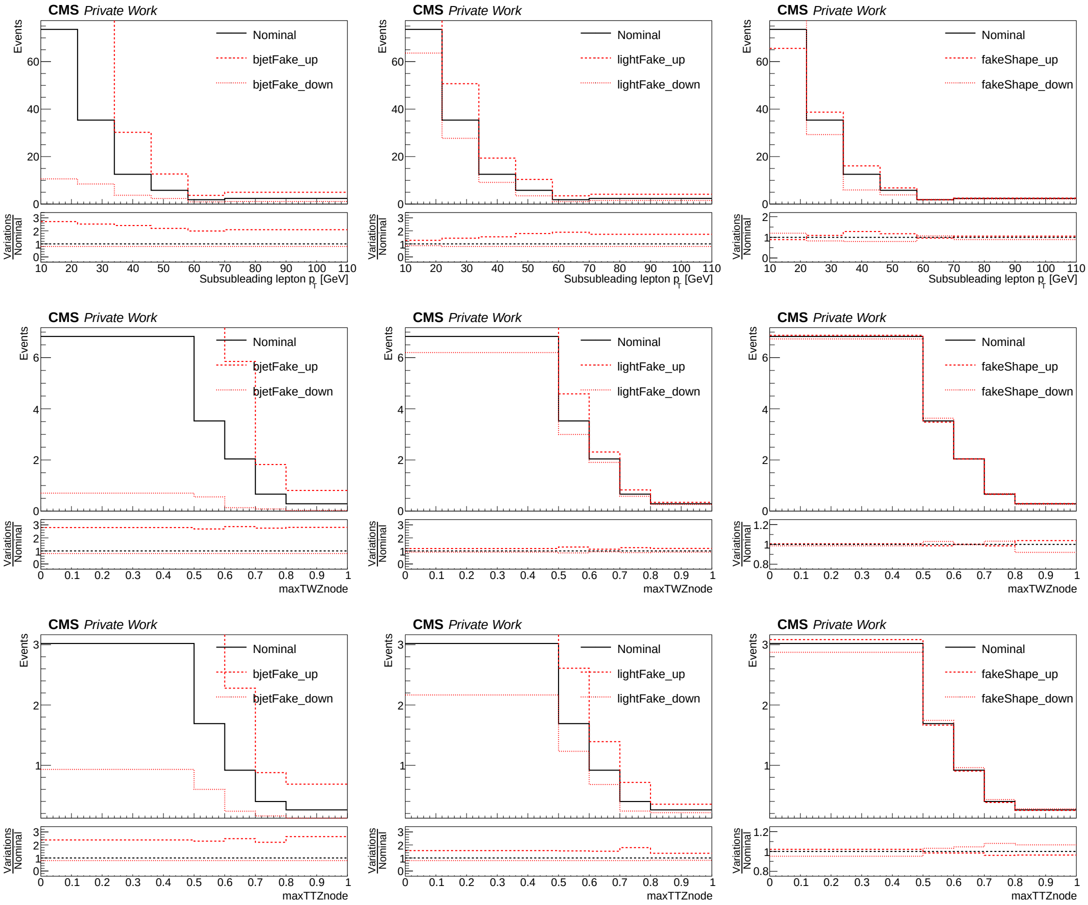

Figure A.23: Nominal event yields and fake lepton nuisances variations for the $t\bar{t}$ background in the 2017 data-taking year. The subsubleading lepton p_T, the *max TWZ output*, and the *max TTZ output* distributions are shown from the first to the last row respectively. In particular, the subsubleading lepton p_T distribution is shown in the ttX control region, while the two ML output distributions correspond to the semi-leptonic signal region. The first two columns show the templates of the *b-jets fakes* and *light-jets fakes* uncertainties respectively, while in the third column the templates of the *fakes shape* nuisance is presented. The black line represents the nominal distribution, while the dotted red lines indicate the up and down variations. The range in the ratio plot is adjusted to display the entire distributions.

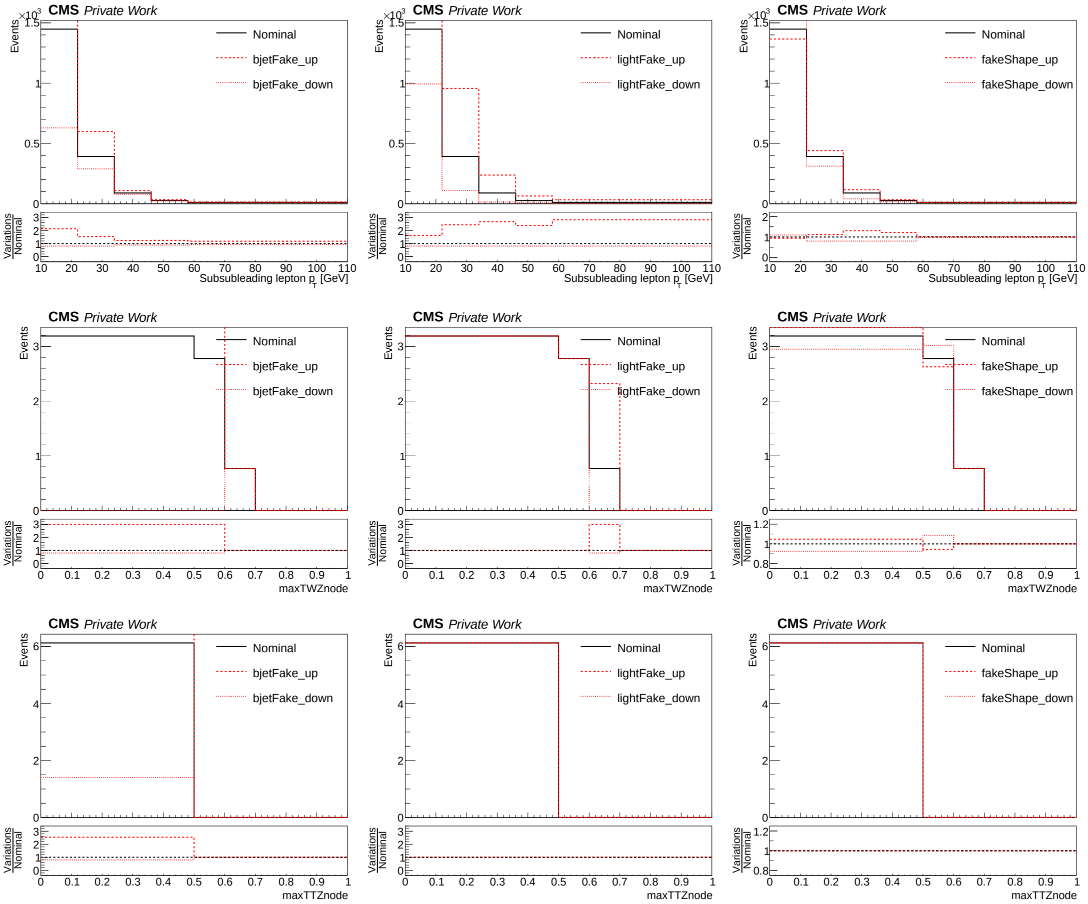

Figure A.24: Nominal event yields and fake lepton nuisances variations for the DY background in the 2017 data-taking year. The subsubleading lepton p_T, the *max TWZ output*, and the *max TTZ output* distributions are shown from the first to the last row respectively. In particular, the subsubleading lepton p_T distribution is shown in the DY control region, while the two ML output distributions correspond to the semi-leptonic signal region. The first two columns show the templates of the *b-jets fakes* and *light-jets fakes* uncertainties respectively, while in the third column the templates of the *fakes shape* nuisance is presented. The black line represents the nominal distribution, while the dotted red lines indicate the up and down variations. The range in the ratio plot is adjusted to display the entire distributions.

A.4 Fake nuisances templates for Run 3

2022pre

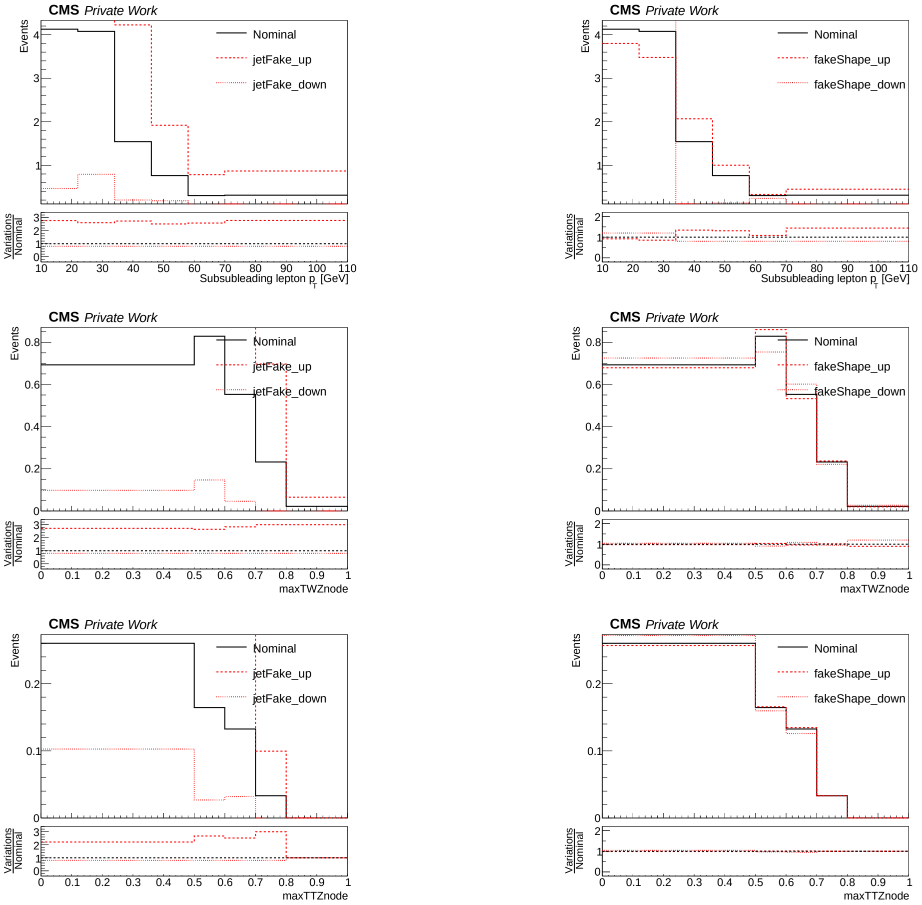

Figure A.25: Nominal event yields and fake lepton nuisances variations for the $t\bar{t}$ background in the 2022pre data-taking year. The subsubleading lepton p_T, the *max TWZ output*, and the *max TTZ output* distributions are shown from the first to the last row respectively. In particular, the subsubleading lepton p_T distribution is shown in the ttX control region, while the two ML output distributions correspond to the semi-leptonic signal region. The first column shows the templates of the *jets fakes* uncertainty, while in the second column the templates of the *fakes shape* nuisance is presented. The black line represents the nominal distribution, while the dotted red lines indicate the up and down variations. The range in the ratio plot is adjusted to display the entire distributions.

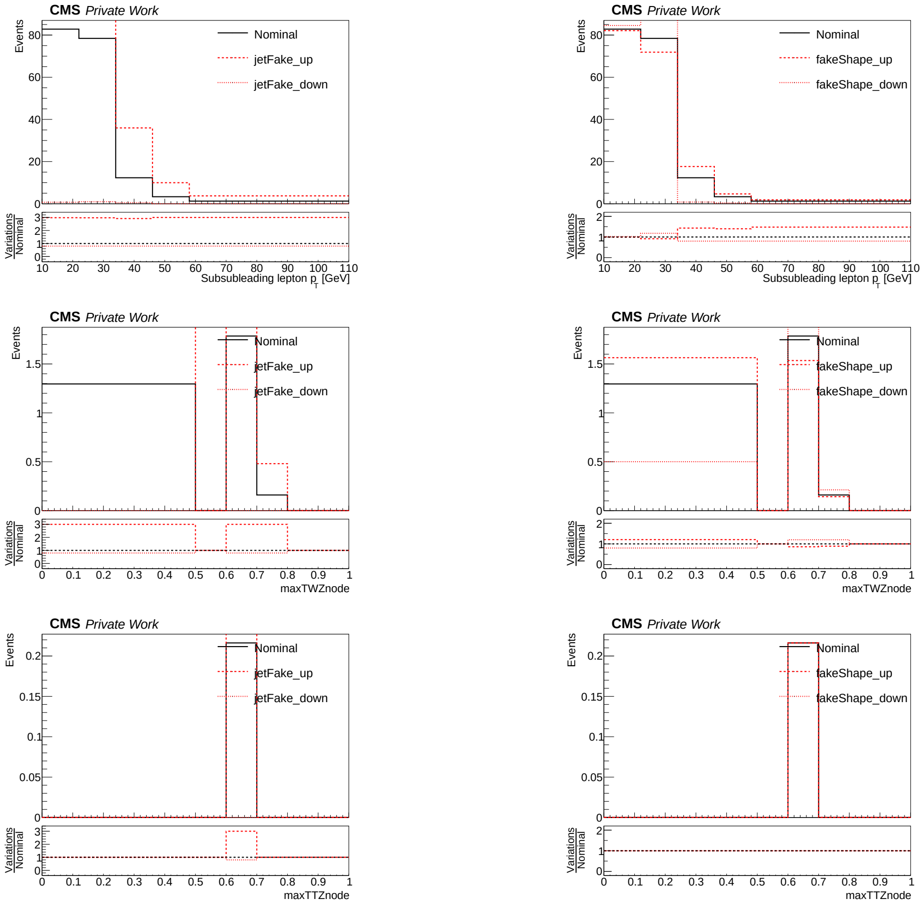

Figure A.26: Nominal event yields and fake lepton nuisances variations for the DY background in the 2022pre data-taking year. The subsubleading lepton p_T, the *max TWZ output*, and the *max TTZ output* distributions are shown from the first to the last row respectively. In particular, the subsubleading lepton p_T distribution is shown in the DY control region, while the two ML output distributions correspond to the semi-leptonic signal region. The first column shows the templates of the *jets fakes* uncertainty, while in the second column the templates of the *fakes shape* nuisance is presented. The black line represents the nominal distribution, while the dotted red lines indicate the up and down variations. The range in the ratio plot is adjusted to display the entire distributions.

2022post

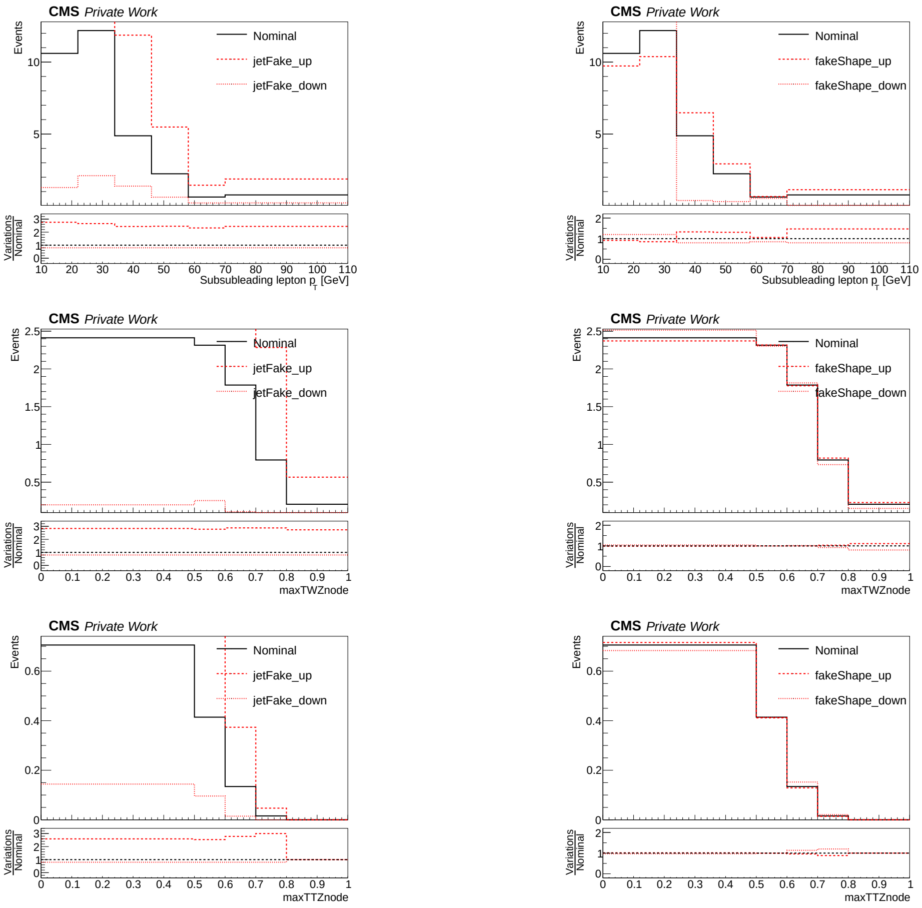

Figure A.27: Nominal event yields and fake lepton nuisances variations for the $t\bar{t}$ background in the 2022post data-taking year. The subsubleading lepton p_T, the *max TWZ output*, and the *max TTZ output* distributions are shown from the first to the last row. The subsubleading lepton p_T distribution is presented in the ttX CR, while the ML output distributions in the 3ℓ SR. The first column shows the templates of the *jet fakes* uncertainty, while in the second column the templates of the *fakes shape* nuisance is presented. The black line represents the nominal distribution, while the dotted red lines indicate the up and down variations. The range in the ratio plot is adjusted to display the entire distributions.

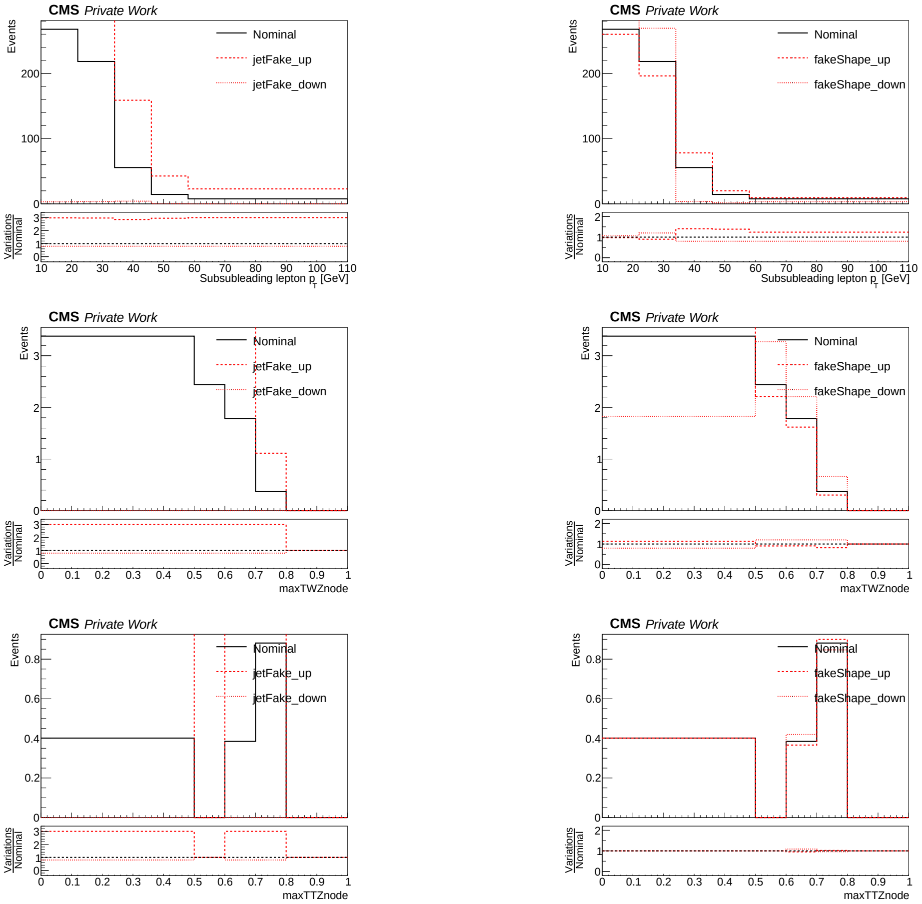

Figure A.28: Nominal event yields and fake lepton nuisances variations for the DY background in the 2022post data-taking year. The subsubleading lepton p_{T}, the *max TWZ output*, and the *max TTZ output* distributions are shown from the first to the last row. The subsubleading lepton p_{T} distribution is presented in the DY CR, while the ML output distributions in the 3ℓ SR. The first column shows the templates of the *jet fakes* uncertainty, while in the second column the templates of the *fakes shape* nuisance is presented. The black line represents the nominal distribution, while the dotted red lines indicate the up and down variations. The range in the ratio plot is adjusted to display the entire distributions.

2023pre

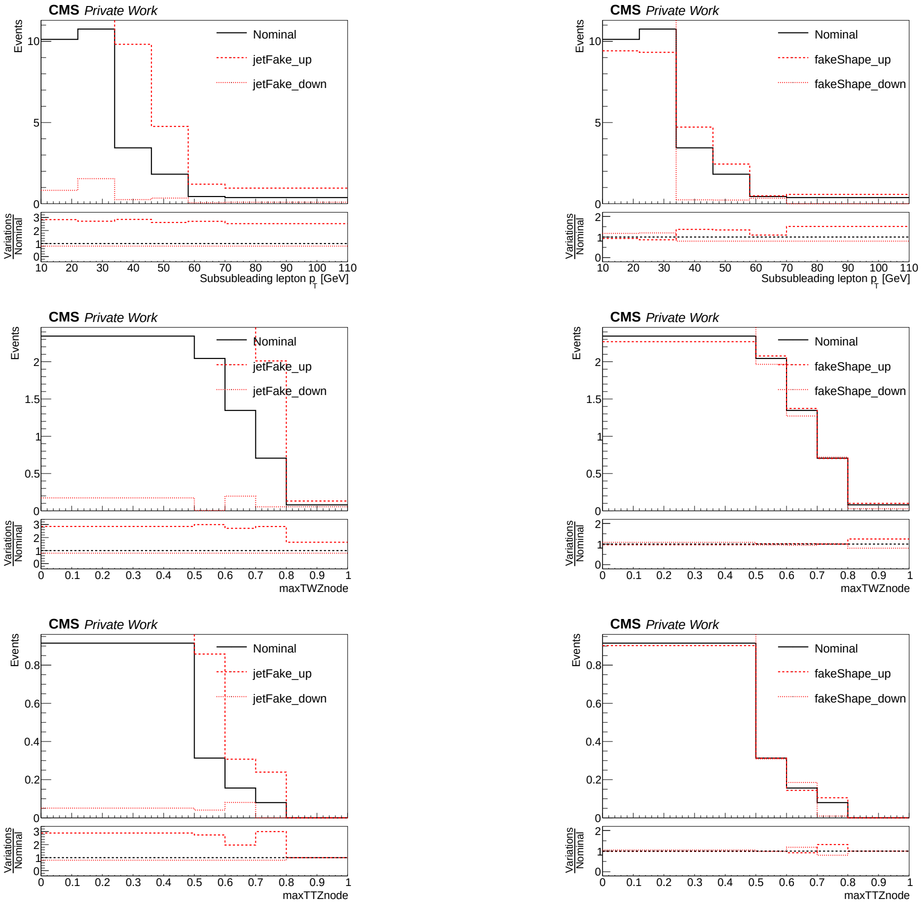

Figure A.29: Nominal event yields and fake lepton nuisances variations for the $t\bar{t}$ background in the 2023pre data-taking year. The subsubleading lepton p_T, the *max TWZ output*, and the *max TTZ output* distributions are shown from the first to the last row respectively. In particular, the subsubleading lepton p_T distribution is shown in the ttX control region, while the two ML output distributions correspond to the semi-leptonic signal region. The first column shows the templates of the *jets fakes* uncertainty, while in the second column the templates of the *fakes shape* nuisance is presented. The black line represents the nominal distribution, while the dotted red lines indicate the up and down variations. The range in the ratio plot is adjusted to display the entire distributions.

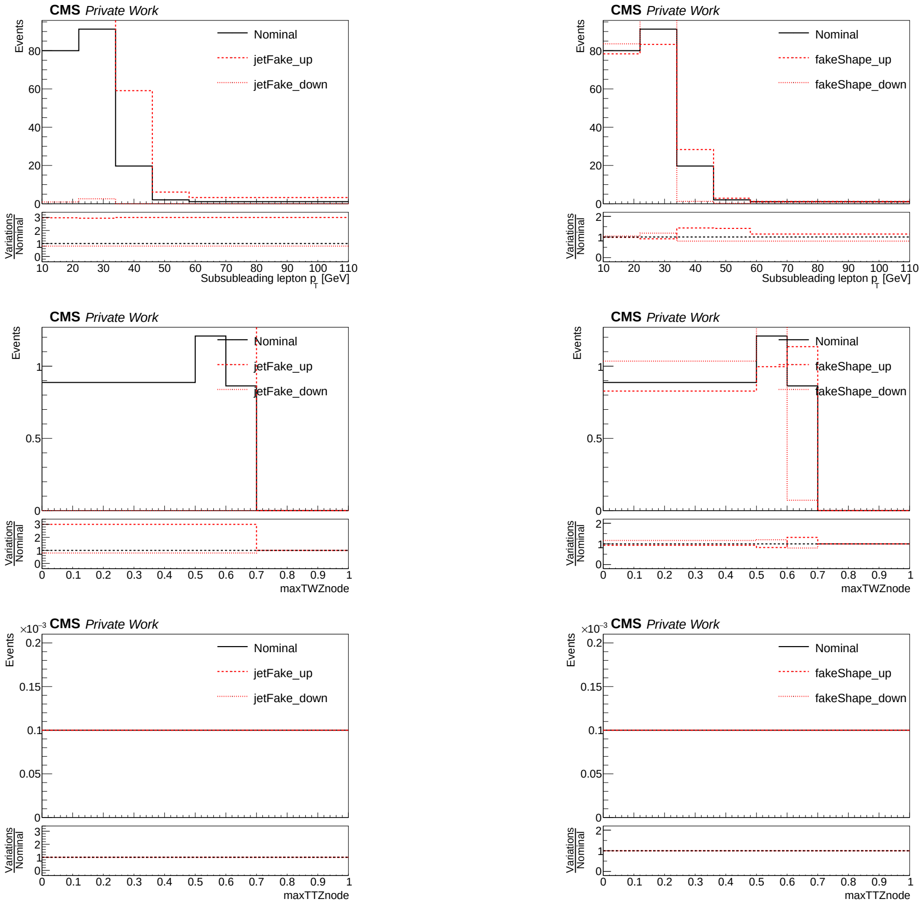

Figure A.30: Nominal event yields and fake lepton nuisances variations for the DY background in the 2023pre data-taking year. The subsubleading lepton p_T, the *max TWZ output*, and the *max TTZ output* distributions are shown from the first to the last row respectively. In particular, the subsubleading lepton p_T distribution is shown in the DY control region, while the two ML output distributions correspond to the semi-leptonic signal region. The first column shows the templates of the *jets fakes* uncertainty, while in the second column the templates of the *fakes shape* nuisance is presented. The black line represents the nominal distribution, while the dotted red lines indicate the up and down variations. The range in the ratio plot is adjusted to display the entire distributions.

2023post

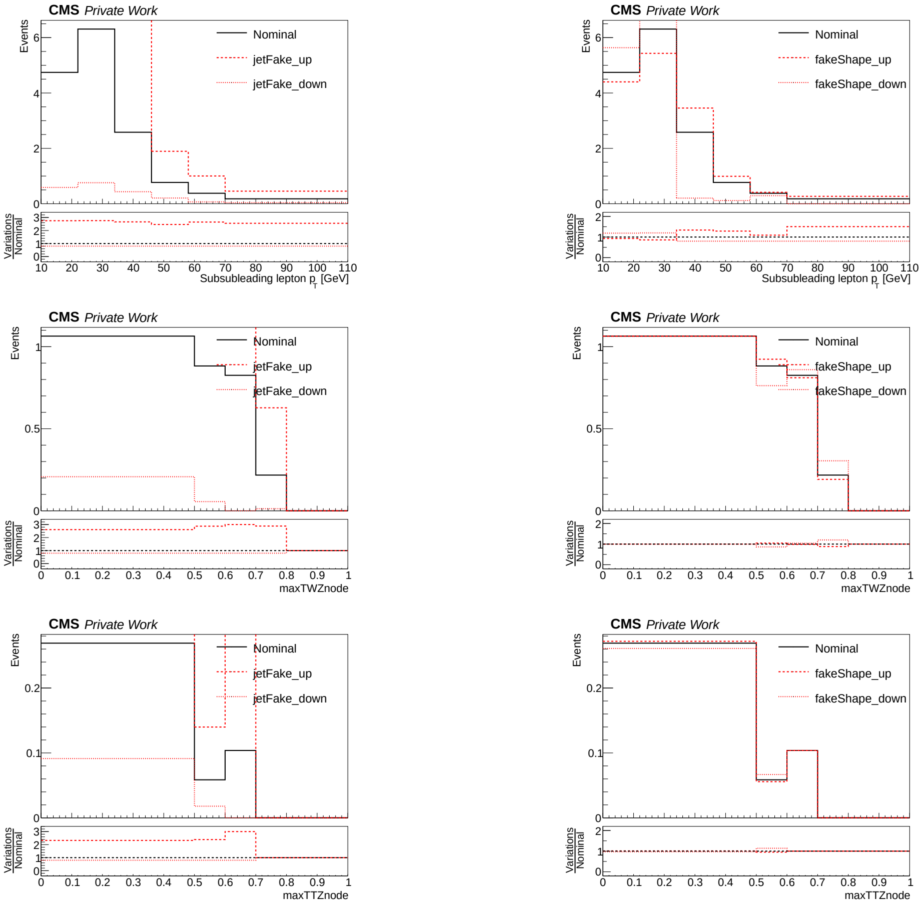

Figure A.31: Nominal event yields and fake lepton nuisances variations for the $t\bar{t}$ background in the 2023post data-taking year. The subsubleading lepton p_T, the *max TWZ output*, and the *max TTZ output* distributions are shown from the first to the last row respectively. In particular, the subsubleading lepton p_T distribution is shown in the ttX control region, while the two ML output distributions correspond to the semi-leptonic signal region. The first column shows the templates of the *jets fakes* uncertainty, while in the second column the templates of the *fakes shape* nuisance is presented. The black line represents the nominal distribution, while the dotted red lines indicate the up and down variations. The range in the ratio plot is adjusted to display the entire distributions.

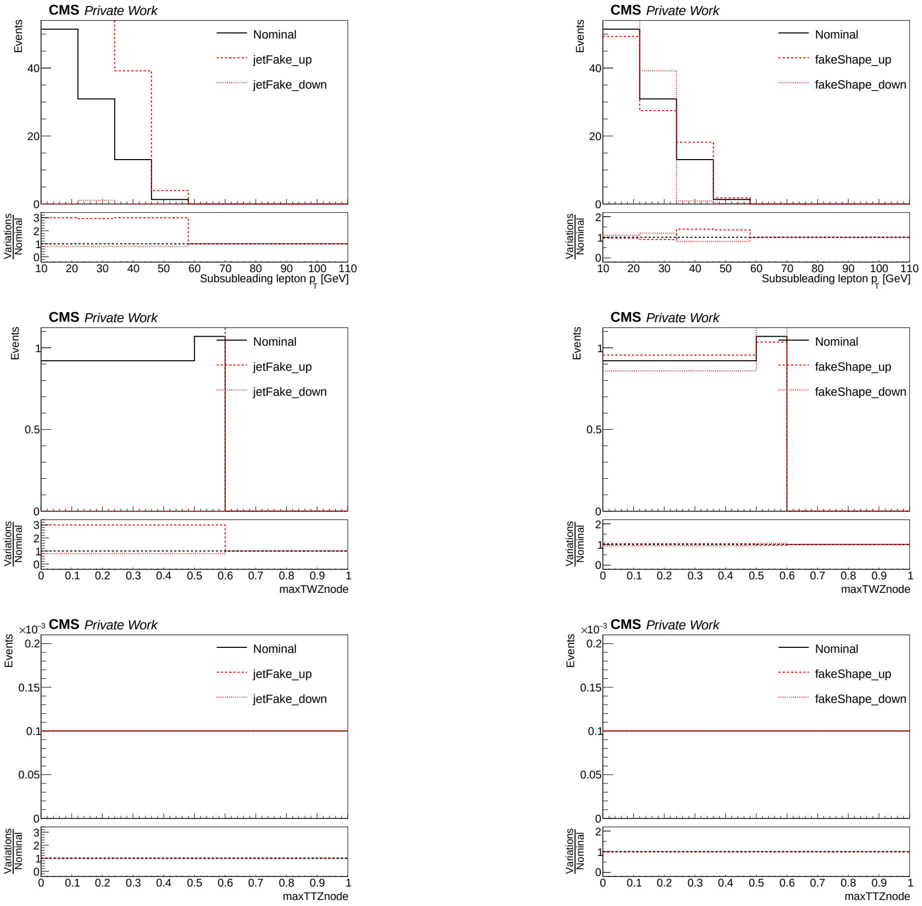

Figure A.32: Nominal event yields and fake lepton nuisances variations for the DY background in the 2023post data-taking year. The subsubleading lepton p_T, the *max TWZ output*, and the *max TTZ output* distributions are shown from the first to the last row respectively. In particular, the subsubleading lepton p_T distribution is shown in the DY control region, while the two ML output distributions correspond to the semi-leptonic signal region. The first column shows the templates of the *jets fakes* uncertainty, while in the second column the templates of the *fakes shape* nuisance is presented. The black line represents the nominal distribution, while the dotted red lines indicate the up and down variations. The range in the ratio plot is adjusted to display the entire distributions.

A.5 Pre-fit distributions Run 2

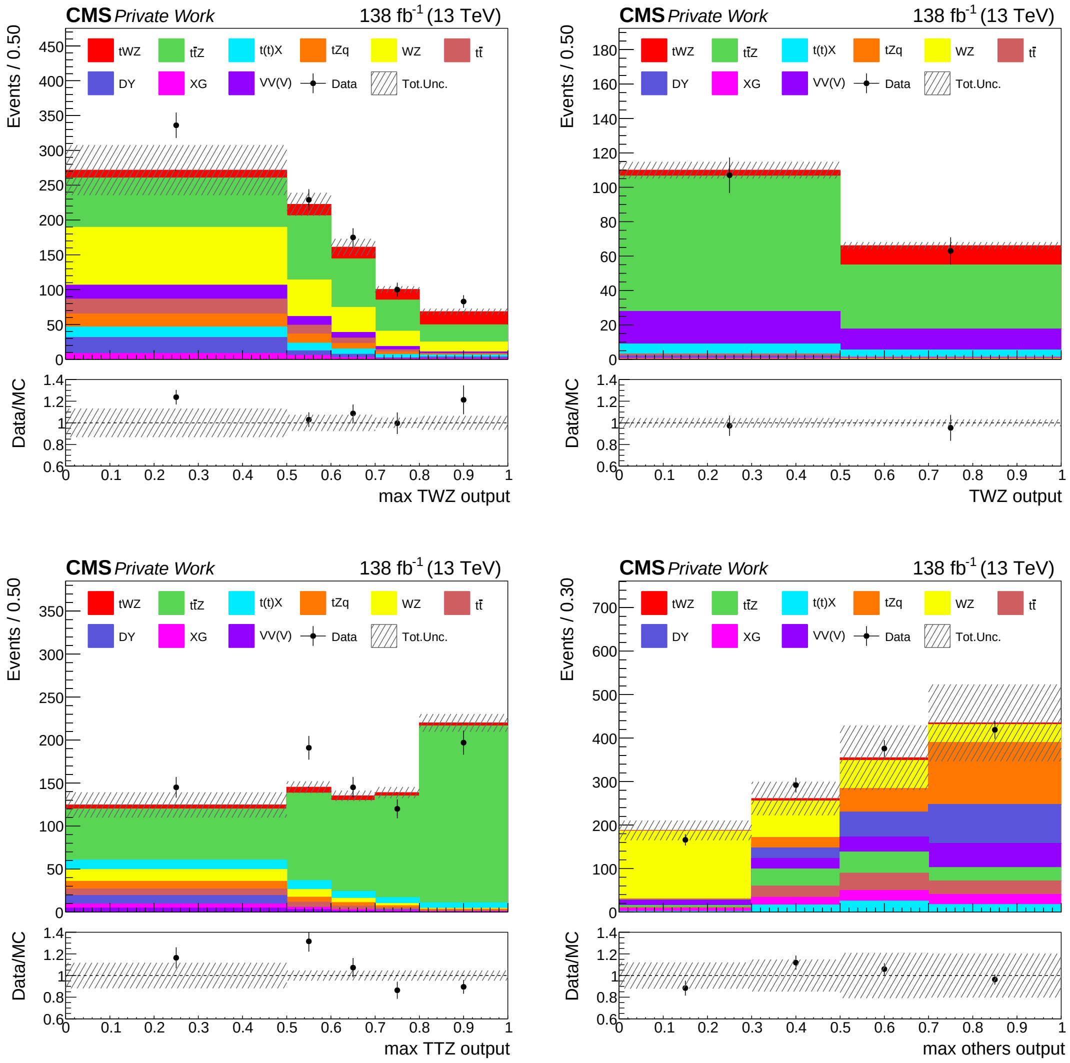

Figure A.33: Pre-fit distributions in the SRs for the fit on Run 2 data. The *max TWZ output* (top left), *max TTZ output* (bottom left), and *max others output* (bottom right) distributions are shown in the 3ℓ SR, while the tWZ ML output node distribution (top right) is shown in the 4ℓ SR. The black markers represent the data, while the solid stacked histogram shows the MC predictions for the various background processes. The dashed band indicates the total uncertainty. The lower panel displays the ratio between data and simulation.

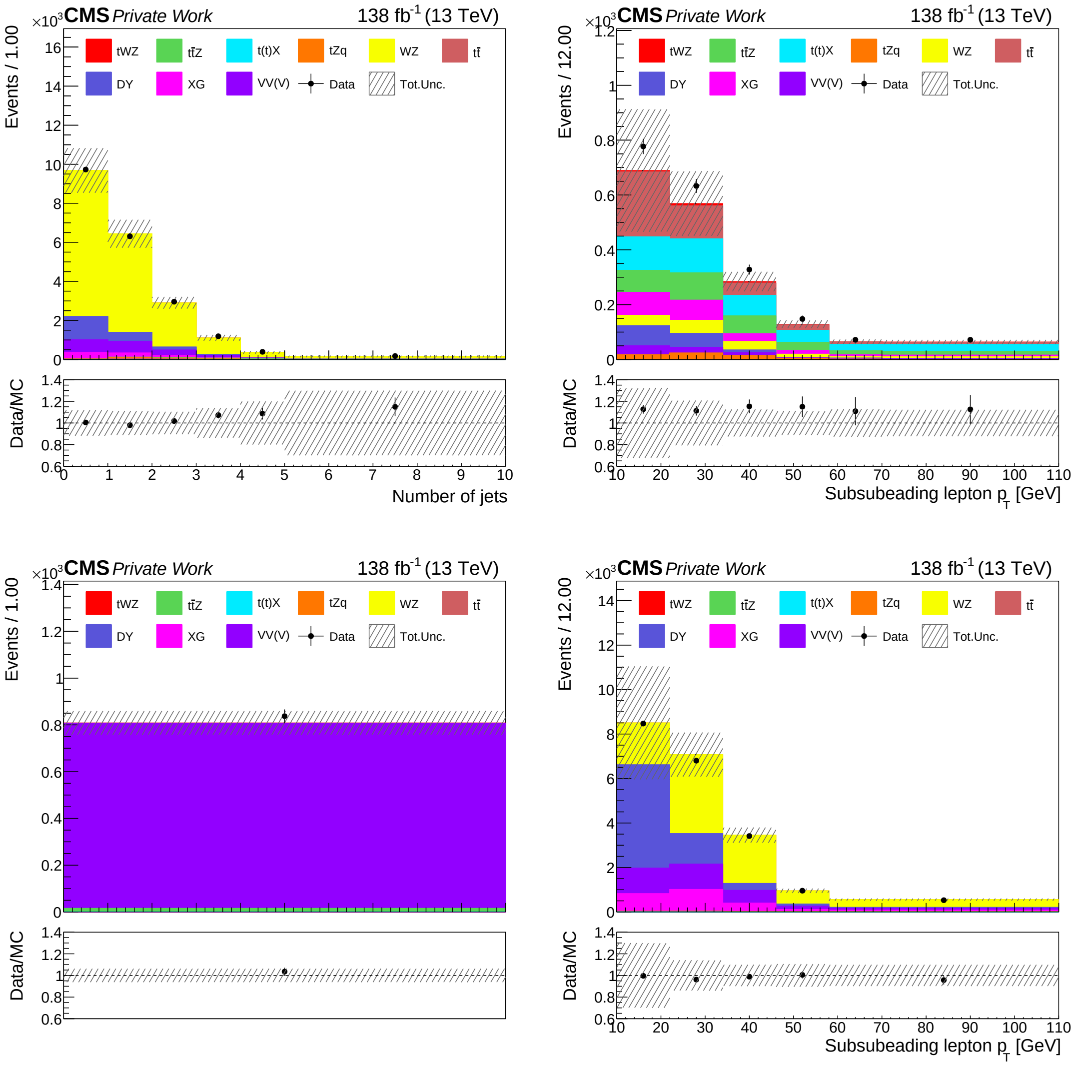

Figure A.34: Pre-fit distributions in the CRs for the fit on Run 2 data. The jet multiplicity distribution is shown in the WZ CR (top left), the event yields in the ZZ CR (bottom left), and the subsubleading lepton transverse momentum in the ttX CR (top right) and DY CR (bottom right). The black markers represent the data, while the solid stacked histogram shows the MC predictions for the various background processes. The dashed band indicates the total uncertainty. The lower panel displays the ratio between data and simulation.

A.6 Pre-fit distributions Run 3

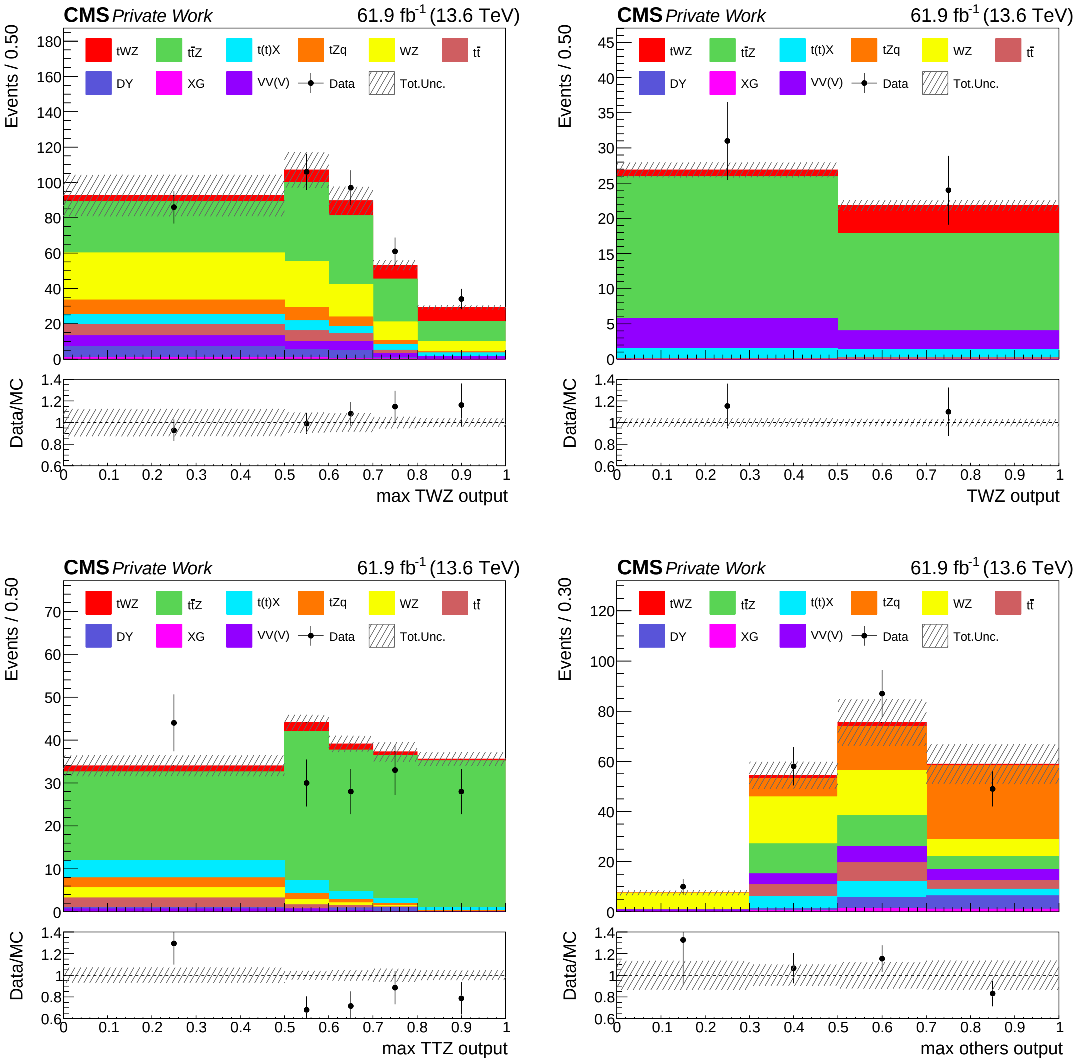

Figure A.35: Pre-fit distributions for the fit on Run 3 data. The *max TWZ output* (top left), *max TTZ output* (bottom left), and *max others output* (bottom right) distributions are shown in the 3ℓ SR, while the tWZ ML output node distribution (top right) is shown in the 4ℓ SR. The black markers represent the data, while the solid stacked histogram shows the MC predictions for the various background processes. The dashed band indicates the total uncertainty. The lower panel displays the ratio between data and simulation.

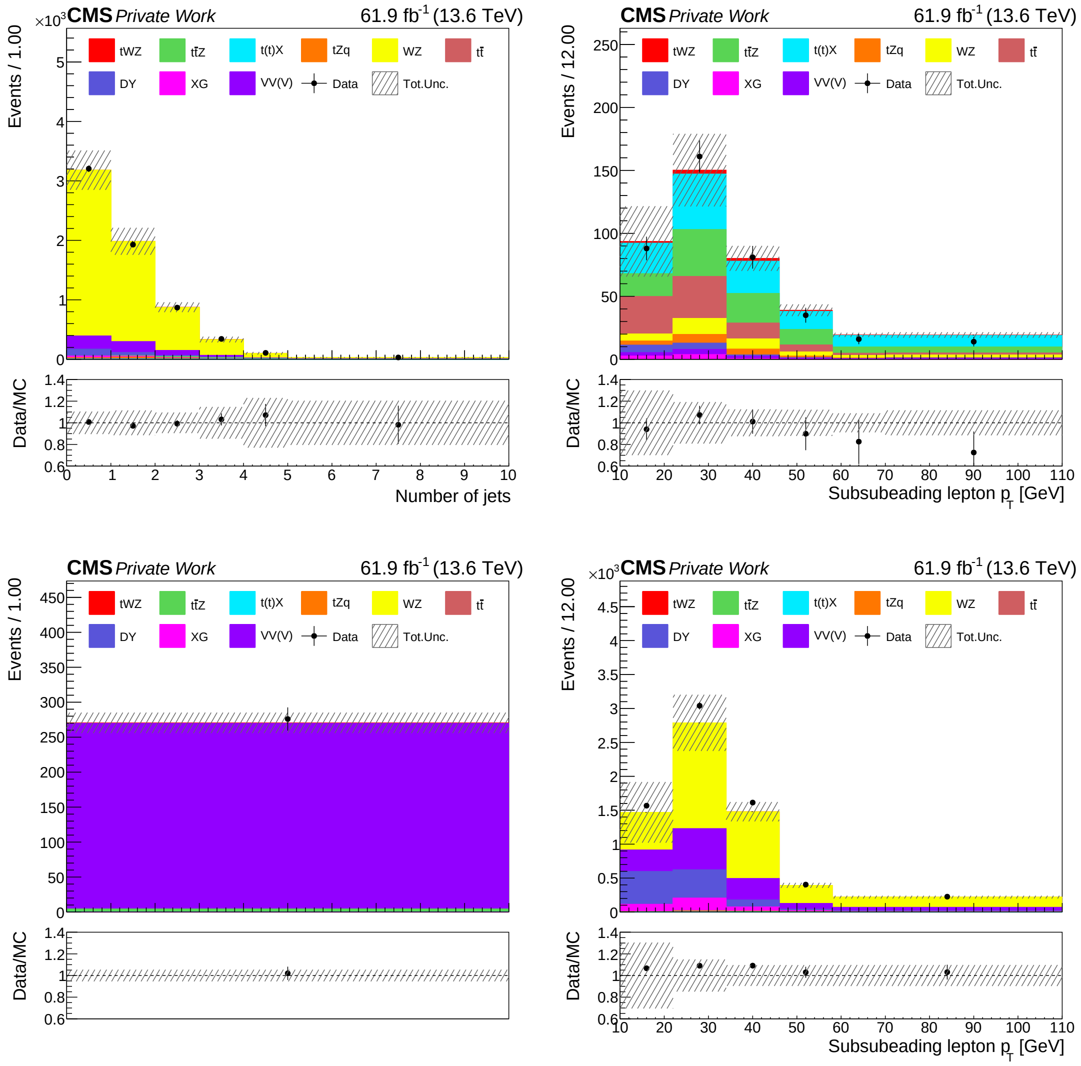

Figure A.36: Pre-fit distributions for the fit on Run 3 data. The jet multiplicity distribution is shown in the WZ CR (top left), the event yields in the ZZ CR (bottom left), and the subsubleading lepton transverse momentum in the ttX CR (top right) and DY CR (bottom right). The black markers represent the data, while the solid stacked histogram shows the MC predictions for the various background processes. The dashed band indicates the total uncertainty. The lower panel displays the ratio between data and simulation.